Synthesis and Analytical Centrifugation of Magnetic Model Colloids

Universiteit Utrecht

Cover design: Bob Luigjes.

Printed by: Proefschriftmaken.nl || Printyourthesis.com.

ISBN 978-90-393-5711-8
Subject headings: Magnetic/magnetite/colloids/emulsions/nanoparticles/dipoles/colloidal synthesis/analytical centrifugation/osmotic equation of state.

Synthesis and Analytical Centrifugation of Magnetic Model Colloids

Synthese en Analytische Centrifugatie van Magnetische Model Colloïden

(met een samenvatting in het Nederlands)

Proefschrift

ter verkrijging van de graad van doctor aan de
Universiteit Utrecht op gezag van de rector magnificus,
prof. dr. G.J. van der Zwaan, ingevolge het besluit van het
college voor promoties in het openbaar te verdedigen
op woensdag 1 februari 2012 des middags te 12.45 uur

door

Bob Luigjes

geboren op 9 augustus 1984 te Barneveld

Promotor: Prof. dr. A.P. Philipse

Co-promotor: Dr. B.H. Erné

Het in dit proefschrift beschreven onderzoek werd gefinancierd door het gebied Chemische Wetenschappen (CW) van de Nederlandse Organisatie voor Wetenschappelijk Onderzoek (NWO).

Contents

1

General Introduction

1.1. Magnetic colloids

Colloids are important not only for numerous applications, but also as model systems in fundamental physical chemistry research [1–5]. Colloids are particles with at least one of their dimensions in the range of 1–1000 nm, such that the Brownian motion of colloids dispersed in a liquid medium can be sufficient to counteract gravity. Liquid dispersions of colloids display similar phase behavior as atoms and molecules with, for instance, a colloidal gas-liquid coexistence, but diffusion is considerably slower, and due to the larger particle size colloids can be more easily studied by various microscopic techniques. Moreover, colloids can be prepared in many sizes and shapes [4], with a variety of tunable interactions, and they may self-assemble into complex structures. For these reasons, colloids and clusters of colloids are used as model systems for atoms and molecules [6–9].

In this thesis, the focus is on magnetic colloids, *i.e.*, colloids with a magnetic dipole moment. Two general types of particles are investigated. The first class of magnetic colloids consists of ferrofluids, colloidal dispersions of single-domain magnetic nanoparticles in a liquid. Ferrofluids are stabilized against aggregation by electric charges (aqueous ferrofluids) and/or a layer of polymeric surfactants (apolar ferrofluids). The second class of magnetic colloids comprises composite particles with a number of nanoparticles embedded in a solid matrix.

Magnetic colloids offer great potential for a variety of applications, such as in magnetic data storage, magnetic inks, as lubricants in loudspeakers, and in ferrofluid-sealed rotary shafts [10–14]. In the latter case, ferrofluids are kept in place using a magnet, whereas friction forces are low due to the fact that the seal is a liquid. In chemical catalysis magnetic colloids are studied as catalytic metals for the Fischer-Tropsch synthesis [15], for example, or as a magnetic support material to enable recovery of the catalyst by magnetic separation [16–19].

Furthermore, magnetic colloids are promising for biomedical applications, in imaging, drug delivery, and hyperthermia [10, 20–28]. For instance, they can be used as a contrast enhancing agent for magnetic resonance imaging (MRI). By functionalizing the magnetic particles with specific antibodies, specific types of cells can be targeted and visualized by MRI. Magnetic nanoparticles can also be used for hyperthermia treatment, in which the nanoparticles are heated by an alternating magnetic field and tumor tissue is destroyed by hyperthermia. The magnetic nanoparticles can be delivered by directly introducing them in the tissue to be treated, or by targeting them to the tumor cells specifically by antibody functionalization.

In this thesis magnetic colloids are not primarily studied for any commercial applications, but rather for their use as a colloidal model system for dipolar hard spheres, as is further explained in Section 1.5. First, magnetic material properties are briefly reviewed

in Section 1.2; the alternating gradient magnetization technique used to characterize the colloids is explained in Section 1.3. Subsequently, the synthesis of magnetic colloids is reviewed in Section 1.4, followed by an overview of the phase behavior of dipolar hard-sphere fluids (Section 1.5). How the equation of state can be measured by analytical centrifugation is explained in Section 1.6. The scope of the thesis is described in Section 1.7, followed by the outline of the thesis in Section 1.8.

1.2. Magnetic properties of materials

A major part of this thesis is devoted to the chemical synthesis of magnetic model colloids. Therefore, magnetic material properties are now briefly explained, with special attention to the magnetic substances that are studied in this work.

Magnetism originates from the motion of electrical charges [13, 29]. The total magnetic field, or magnetic induction, B (in T), consists of the contribution of the external magnetic field, H (in A/m), and the magnetization, M (in A/m), of the sample, and is given by $B = \mu_0(H + M)$, with $\mu_0 = 4\pi \times 10^{-7}$ T/(Am^{-1}) the permeability of vacuum. The magnetization of a sample originates from the spins and orbital angular momenta of electrons in the material (contributions from the nuclei can be neglected). For atoms with unpaired electron spins, this results in a permanent atomic magnetic moment. The magnetization upon applying an external magnetic field is given by $M = \chi H$, with χ the magnetic susceptibility.

Figure 1.1 schematically depicts the different types of magnetism that are discussed below. When an external field is applied to a substance, the orbital motion of the electrons is changed and a small opposing field is induced. This response is called diamagnetism and the response to the magnetic field is linear. The corresponding magnetic susceptibility is negative and of the order $|\chi| = 10^{-6}$–10^{-5}. Diamagnets are materials with only a diamagnetic response to an external field. Paramagnetic substances, such as oxygen, have permanent atomic dipoles due to unpaired electron spins that align only upon applying an external magnetic field. This paramagnetic response has a positive magnetic susceptibility of order $\chi = 10^{-5}$–10^{-3}, which is larger than the diamagnetic response.

In some substances, the unpaired spins are strongly coupled, resulting in a permanent magnetic moment already without the presence of an external field. These materials are called ferromagnetic: iron, nickel, and cobalt are among the best known examples. In anti-ferromagnetic materials such as nickel oxide, the neighboring dipoles are aligned anti-parallel, which results in a zero net magnetization. For ferrimagnetic materials, there is also an anti-parallel alignment, but these substances do exhibit a permanent magnetic moment, as the contribution of the dipole moments in one direction outweighs the oppositely directed moments. Magnetite (Fe_3O_4) and cobalt ferrite ($CoFe_2O_4$) are examples of ferrimagnetic materials used in this thesis. Finally, it should be noted that

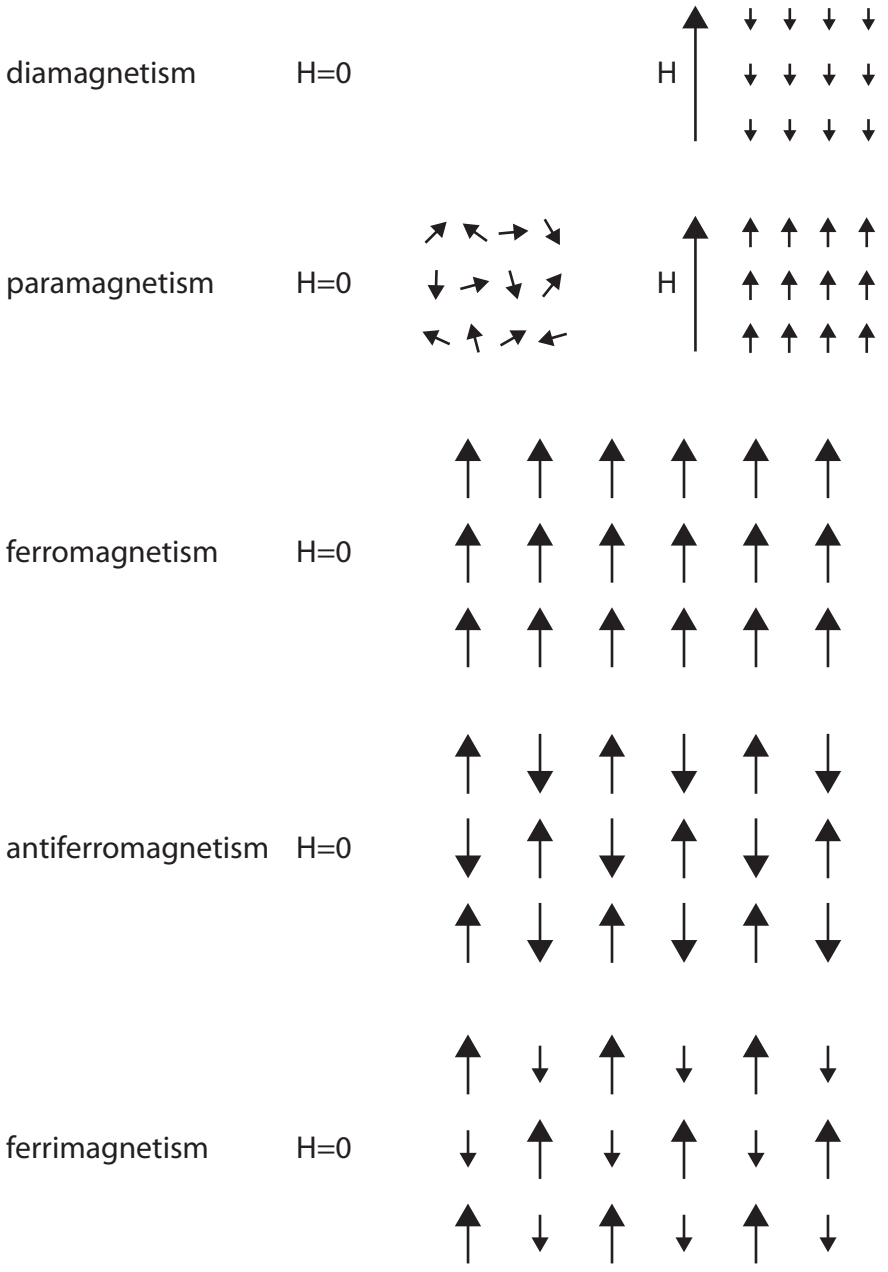

Figure 1.1. Schematic illustration of different types of magnetism, in which the arrows represent atomic magnetic moments. For diamagnetism, dipole moments are only induced by a magnetic field, and these induced dipole moments are opposite to the field direction. For paramagnets, the randomly oriented dipole moments in zero field are aligned parallel in an external magnetic field. For ferromagnetism, antiferromagnetism, and ferrimagnetism, the magnetic moments already spontaneously align without the application of a magnetic field.

there are also non-collinear magnetic materials, in which the spins are not parallel and there is no universal direction of magnetization, such as in certain phases of manganese.

On the macroscopic scale, ferro- and ferri-magnets are composed of multiple domains, where each domain has a permanent magnetic moment due to the strong coupling of the spins. When these domains are randomly oriented, the net magnetization of the material is zero in the demagnetized state. It is only below a certain critical size, which is on the order of several tens of nanometers, that these materials consist of a single magnetic domain.

In ferrofluids, the magnetic nanoparticles are small enough for each particle to possess a single magnetic domain. Consequently, the dispersion essentially behaves as a large paramagnet, each particle having a permanent dipole moment that is randomly oriented in the absence of a magnetic field. Upon employing an external magnetic field, the magnetic response is orders of magnitude larger than for typical molecular paramagnets, and therefore these magnetic colloids are classified as superparamagnetic.

There are two types of orientational relaxation mechanisms for the magnetic dipole moments of the colloids in dispersion. The first is Brownian rotation of the particles in the liquid, with a relaxation time, τ_B, in the case of spherical particles given by [30]:

$$\tau_B = \frac{4\pi R_H^3 \eta}{kT} \tag{1.1}$$

where R_H is the hydrodynamic radius of the particle, η is the solvent viscosity, k is the Boltzmann constant, and T is the absolute temperature. The second relaxation mechanism is the internal rotation of the effective dipole moment, by the simultaneous rotation of the coupled spins of all the atoms. This is called Néel relaxation, for which the relaxation time, τ_N, is given by:

$$\tau_N = \tau_0 \exp\left(\frac{Kv}{kT}\right) \tag{1.2}$$

in which τ_0 is of order 10^{-9} s or smaller, K is the magneto-crystalline anisotropy constant, and v is the volume of the single-domain particle. When the magneto-crystalline energy Kv is much larger than the thermal energy kT, the dipole moment is fixed along the so-called crystallographic 'easy axis', which has the lowest magneto-crystalline energy. When Kv is much smaller than the thermal energy, the dipole moment is essentially free to rotate inside the crystal. For nanoparticles in dispersion, relaxation occurs mainly via the fastest relaxation mechanism.

In composite magnetic colloids, with the nanoparticles embedded in a solid matrix, there is no Brownian relaxation of the individual nanoparticles. Depending on the type of material, the time-averaged net dipole moment of composite particles will only be non-zero if Néel relaxation inside the nanoparticles is sufficiently slow. For example, for magnetite nanoparticles the anisotropy constant is generally still low enough to allow

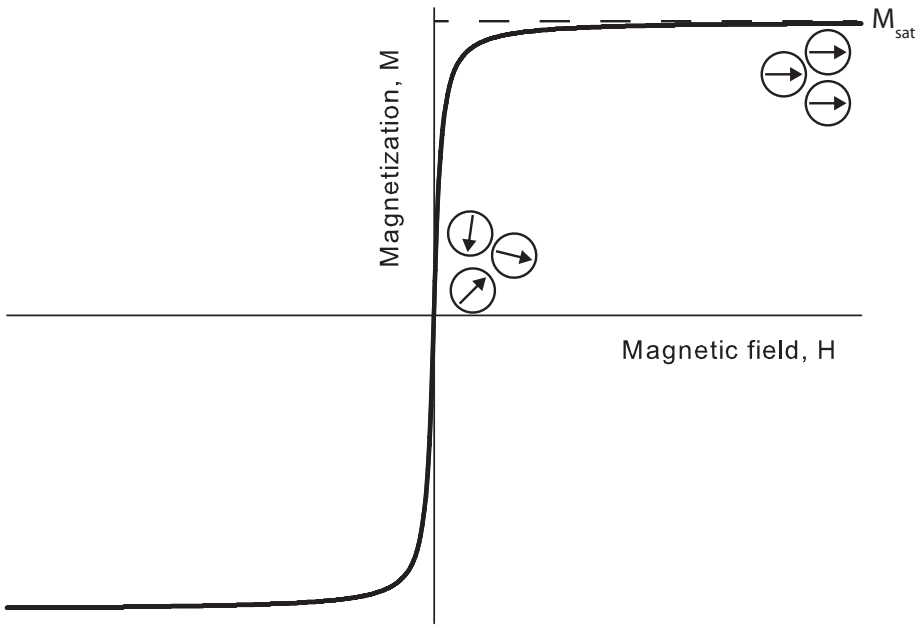

Figure 1.2. Magnetization as a function of the magnetic field strength for a dispersion of superparamagnetic colloids. At low field strengths, the magnetic moments are randomly oriented. When all magnetic dipoles are aligned, the saturation magnetization, M_{sat}, is reached.

relaxation of the dipole moments, whereas for cobalt ferrite colloids with a diameter larger than about 10 nm the relaxation time becomes so large that the dipole moments are effectively fixed along their crystallographic easy axis. Therefore, cobalt ferrite nanoparticles can be used to obtain permanently magnetized composite colloids.

1.3. Magnetization measurements

Figure 1.2 shows a typical magnetization curve for superparamagnetic colloids, in which the magnetization, M, is shown as a function of the magnetic field strength, H. The magnetic susceptibility, $\chi = M/H$, is given by the slope of the curve. When all magnetic dipoles are aligned with the field, the saturation magnetization, M_{sat}, is reached, as indicated in Figure 1.2. The dipole moment, μ (Am^2), can be obtained from analysis of the magnetization curve (detailed in Chapter 5).

The magnetization of magnetic colloids can be measured with different techniques. In this thesis, an alternating gradient magnetometer (AGM) is employed [31]. In an AGM, the sample is attached to a sample holder that is positioned in the homogeneous magnetic field of an electromagnet (Figure 1.3). This field is used to magnetize the sample, and the magnetization is simultaneously measured by applying a small alternating field gradient. The alternating field gradient exerts an alternating force on the sample, which is converted to a voltage by a piezoelectric crystal. The AGM gives the

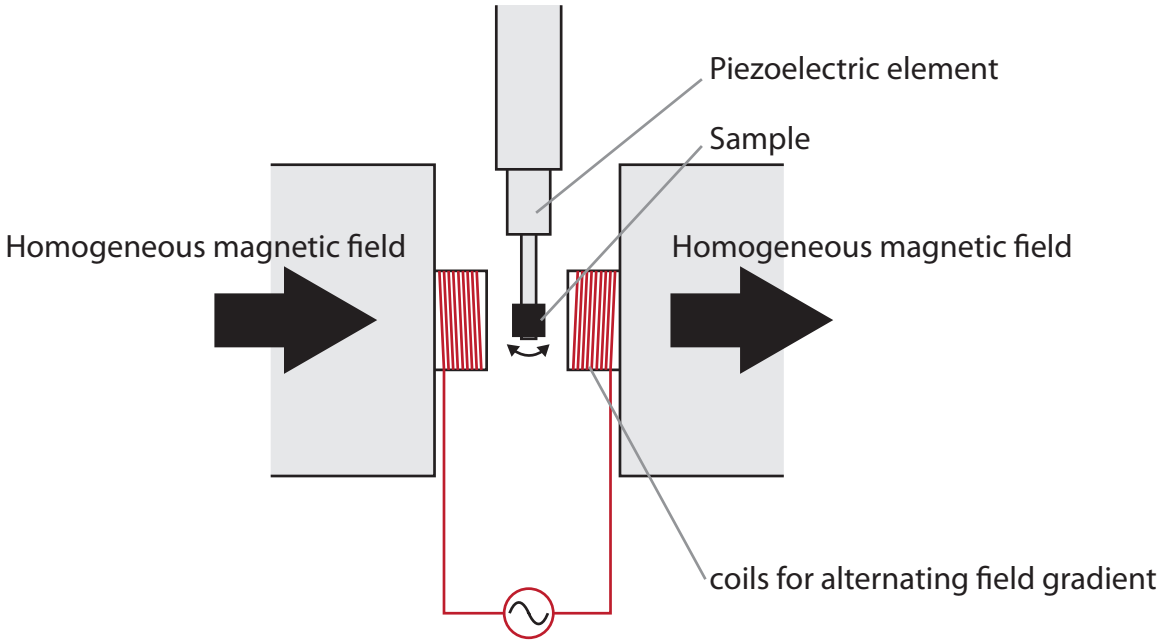

Figure 1.3. Schematic illustration of a sample in the alternating gradient magnetometer, in which the sample is magnetized by a homogeneous magnetic field. The magnetization is measured using a small alternating field gradient, which applies an alternating force on the sample that is converted to a voltage by a piezoelectric crystal.

total magnetic dipole moment of the sample, MV (Am^2), as a function of the magnetic field, H (A/m), where V is the sample volume.

1.4. Magnetic colloid synthesis

In this section, the synthesis of magnetic colloids is briefly reviewed. First the progress in the synthesis of magnetic composite colloids is discussed, followed by a concise overview of the preparation of iron oxide nanoparticles.

Earlier work on magnetic composite colloids comprises the preparation of silica spheres with one or several magnetite nanoparticles in their core [32–34]. The disadvantage of this approach is the very low dipole moment of the composite particles, as a result of the small amount of embedded magnetic particles. Due the small magnetic volume, even a very thin silica shell screens the dipole-dipole interactions between the magnetic composite spheres [35].

Composite particles with a higher magnetic loading have been prepared using a surface coverage of magnetite [35], clusters of magnetic nanoparticles [36–42], microemulsions [43], or magnetomicelles [44]. Despite the progress in the preparation of composite

magnetic colloids, control of both the magnetic content and monodispersity remains limited.

It has previously been shown in our group that monodisperse thermodynamically stable Pickering emulsions [45–47] of 3-methacryloxypropyl trimethoxysilane (TPM) oil in water, stabilized by magnetic nanoparticles, can be polymerized to obtain magnetic composite colloids [48, 49]. In these studies, mostly magnetite (Fe_3O_4) nanoparticles were used, which results in composite colloids without a permanent magnetic moment in zero field, although it was shown that the method can also be applied using cobalt ferrite ($CoFe_2O_4$) [46,47,49]. Claesson showed that by using cobalt ferrite nanoparticles to prepare composite silica colloids, particles with a permanent magnetic moment can be obtained by exposing them to a magnetic field [50]. In this thesis, Pickering emulsions are further investigated to obtain composite particles with a permanent magnetic moment that is larger than in previous works [50, 51].

A variety of synthesis methods is available for the preparation of magnetic nanoparticles [10, 11, 21, 23, 52–54]. A well-known and simple method is aqueous co-precipitation of iron chloride salts [55, 56]. However, this method results in a high polydispersity due to the simultaneous nucleation and growth of the nanoparticles. Magnetite crystals have also been prepared by harvesting them from magnetotactic bacteria [57]. A drawback here is the low yield and the poor control of crystal size and shape [57].

Monodisperse iron oxide nanocrystals have been prepared by thermal decomposition of organometallic precursors in a solvent with a high boiling point, in which nucleation and growth are well separated. For example, the method reported by Hyeon and coworkers can be used to prepare monodisperse iron oxide nanocrystals in a single step, and the size can be controlled by using solvents with different boiling points [58, 59]. A similar method was reported by Jana *et al.* [60].

Another way to prepare monodisperse iron oxide nanoparticles is by separating the synthesis of nuclei and the subsequent growth of those nuclei by using multiple synthesis steps. Sun *et al.* first reported this seed-mediated growth of magnetite nanoparticles [61, 62], and it has been modified by Klokkenburg *et al.* [63, 64] to prepare a series of magnetite colloids with different particle sizes. Although the seed-mediated growth method can be used to prepare magnetic nanoparticles with well-defined properties, it is a laborious procedure and the yield is rather low. In this thesis, several of these thermal decomposition methods are further investigated to improve size and shape control, also in view of our interest in dipolar phase behavior.

1.5. Phase behavior of dipolar hard spheres

The dipolar hard-sphere (DHS) potential is one of the simplest potentials for modeling simple polar liquids, such as ethanol and hydrogen fluoride, or ferrofluids. The DHS-potential only involves dipole-dipole interactions and at contact an infinite, hard-sphere

repulsion. Despite the model's simplicity, the phase behavior of DHS-fluids is still under debate, as the possibility of liquid-gas coexistence is still unresolved, both for the Van der Waals-like liquid-gas criticality and for phases with chain-like structures [65–68].

In 1970, de Gennes and Pincus conjectured that the orientational average of weak dipolar interactions yields an isotropic attraction, analogous to Van der Waals attractions, which enables the coexistence of an isotropic gas and an isotropic liquid phase [69]. This scenario was supported by other theoretical work [70] and by Monte Carlo simulations of a small system of 32 particles [71].

However, Monte Carlo simulations performed in the nineties failed to find the liquid-gas transition, and chaining of the particles was found instead [72–75]. Theoretical work by Sear [76] and van Roij [77] supported this scenario: the anisotropic nature of the dipolar hard spheres favors chaining of particles and no liquid-gas phase separation was found. The formation of chain-like structures for particles with a relatively large dipole moment was already theoretically predicted by de Gennes and Pincus [69] and by the Monte Carlo method by Chantrell *et al.* [78]. The formation of dipolar chains has been experimentally confirmed by cryogenic TEM experiments performed in our laboratory [63, 79–81].

In 2000, Tlusty and Safran argued that coexistence of two phases with different chain morphologies is possible [82], which concurs with computer simulations by Camp *et al.* in that same year [83]. One of the challenges in simulating DHS-fluids is that the association into chains may be enhanced by periodic boundary conditions. Additionally, the chain-like structures are energetically very stable, which greatly reduces the probability of successful Monte Carlo moves. Therefore, computer simulations have been performed in which the limit of dipolar hard spheres is approached, for example by starting from charged dumbbells comprising two oppositely charged hard spheres of which the separation distance is decreased [84]. Most of these simulations [84–86], though not all of them [87], provide evidence for a phase separation with different chain morphologies. So there seems to be no final verdict yet on the existence of Van der Waals-like liquid-gas criticality, at least not unambiguously from simulations. To obtain more insight into the phase behavior of dipolar hard spheres, experiments seem indispensable.

The experimental approach adopted here is to study a model system of magnetic colloids. Besides the chemical preparation of magnetic model systems, a second challenge is to find a technique to analyze the thermodynamics of concentrated magnetic dispersions. The aim here is to measure the osmotic pressure as a function of concentration to obtain the osmotic equation of state. At sufficiently strong interactions and high concentrations, phase separation would be revealed by a concentration jump at constant pressure.

The osmotic equation of state of a colloidal dispersion can generally be expressed in terms of a virial series, in which the second virial coefficient, B_2, is the first-order

deviation from ideal behavior. This B_2 can be correlated to the magnetic interactions of dipolar hard spheres, via the dipolar coupling parameter, λ. The relation between λ and B_2 has recently been calculated for a wide range of λ's [88]. Also an estimate was made of the critical value of B_2 and the corresponding λ for a Van der Waals-like liquid-gas phase separation, if any, to occur in a system of dipolar hard spheres [88]. How the osmotic equation of state can be obtained experimentally is discussed in the next section.

1.6. Analytical centrifugation

We use apolar dispersions of sterically stabilized magnetic colloids as an experimental approach of dipolar hard spheres. However, even for well-defined magnetic particles measuring the osmotic equation of state is challenging.

Osmotic pressures have previously been determined for aqueous ferrofluids, in which the magnetic colloids were small and electrostatic and Van der Waals forces were significant if not dominant [89–92]. In these studies, osmotic pressures were measured directly, using a membrane osmometer or the osmotic stress method [93], which is particularly difficult for very low pressures [89]. Moreover, for the apolar solvents to be used in our systems, no suitable flexible dialysis membranes are available.

Another method to determine osmotic pressures employs light scattering, and this technique has been applied to determine the second virial coefficient in dispersions of attractive (non-magnetic) silica colloids [5,94,95]. However, in the case of concentrated dispersions of magnetic colloids, light is strongly absorbed, and light scattering becomes unfeasible; X-rays or neutrons might be used as an alternative [90].

In this thesis, the osmotic equation of state of dispersions of magnetic colloids is determined by analytical centrifugation. It has been shown that the osmotic equation of state of colloidal systems in general can be determined from the sedimentation-diffusion equilibrium measured in an analytical ultracentrifuge (AUC) [96–99]. The basics of AUC measurements have been described in detail in the PhD thesis of Planken [100], in which both sedimentation velocity measurements and sedimentation-diffusion equilibrium measurements are explained. In colloid science, the AUC has mainly been employed for sedimentation velocity experiments [99]. For example, Planken *et al.* [101] have recently shown for diluted ferrofluids that the sedimentation velocity increases with an increasing dipolar coupling parameter. The velocity increase can be correlated to the second virial coefficient by modeling the interaction between two attractive particles as a reversible dimerization [101].

A more direct way to determine the second virial coefficient is from the osmotic equation of state, obtained from sedimentation-diffusion equilibrium measurements. In a typical experiment, a colloidal dispersion is centrifuged and the concentration profile of the colloids is recorded *in situ*. When sedimentation-diffusion equilibrium is reached,

the osmotic pressure is calculated by integration of the concentration profile. However, concentrated dispersions of magnetic colloids cannot be measured using conventional AUC sample cells, which have an optical path length of 3–12 mm, due to the strong light absorption of the particles. Another limitation of the AUC are the high rotation rates, which restricts its utilization in equilibrium measurements to small nanoparticles (typically d $<$ 10 nm) only; at lower rotation rates the rotor motion becomes unstable.

The approach adopted here is to implement a LUMiFuge stability analyzer, originally designed to study sedimentation kinetics of industrial colloids such as anti-settling agents (*e.g.* organoclays [102]), as an analytical centrifuge for concentrated ferrofluids, using homebuilt sample cells with thin capillaries with an optical path length of only 50 μm. Since for small magnetic colloids an AUC can still be employed, be it at its lowest rotation rates, we designed ultra-thin sedimentation centerpieces to enable measurements of concentrated ferrofluids. The AUC can be used to obtain independent measurements of the equation of state and compare the results with the results from the LUMiFuge.

1.7. Scope of the thesis

To investigate the thermodynamics of dipolar fluids, magnetic model colloids are required with a sufficiently large permanent magnetic moment. Although many synthesis methods for magnetic colloids have been reported, as described in Section 1.4, it remains a challenge to obtain monodisperse particles with a significant magnetic dipole moment leading to magnetic attractions up to about 10 kT.

The thermodynamically stable Pickering emulsions discovered by Sacanna *et al.* [45–47] are practically monodisperse and can be used to prepare composite particles [48, 49]. Preparing these colloids with cobalt ferrite nanoparticles would render them permanently magnetic after treatment in a magnetic field. An advantage of such colloids is that they can be made fluorescent [46], which would enable studies of dipolar interactions by confocal microscopy on a single-particle level. The Pickering emulsions stabilized by cobalt ferrite nanoparticles are investigated in this thesis, to enhance control over the emulsion droplet size by varying experimental parameters such as the amount of oil or the salt concentration. Nevertheless, the nanoparticles are confined to a shell and the magnetic content of the resulting composite particles remains limited. Therefore, the transfer of magnetic nanoparticles to the TPM-oil will be investigated, since that should allow embedding of the nanoparticles in the core of the composite particle as well, and the magnetic content could be tuned via the concentration of nanoparticles in the TPM-oil.

The dispersions of magnetite nanoparticles prepared by Klokkenburg *et al.* using a seed-mediated growth method have already proven to be a suitable model system to study the chaining of dipolar colloids [63, 64, 81]. In principle, particles with a larger

magnetic moment can be obtained by applying additional growth steps. However, the seeded-growth of such colloids is laborious and in addition, the yield is fairly low. Therefore, we further investigate this seeded-growth method on a larger scale in this thesis. Another promising method, from Hyeon's group [58, 59], in which large iron oxide nanoparticles can be prepared in a single synthesis with high yields, will also be studied in this thesis. The aim here is to compare the Hyeon method to the seed-mediated growth synthesis and apply the most suitable method to obtain single-domain monodisperse iron oxide particles with a large magnetic moment.

Once magnetic colloids have been obtained, a suitable method of analytical centrifugation is required to study the thermodynamics of these strongly light absorbing colloids. Since the LUMiFuge stability analyzer has never been used (and neither was designed) for studying sedimentation-diffusion equilibria of colloids, it must be adapted to enable measurements of the osmotic equation of state. This involves the preparation of homebuilt sample cells, in which thin capillaries of ferrofluid can be incorporated to measure on concentrated colloidal dispersions. The limitations of the LUMiFuge will be examined, and the data analysis procedure to obtain the osmotic pressure from raw LUMiFuge data will be developed. For sufficiently small nanoparticles, an AUC can be employed, which would be a suitable technique to acquire independent results to compare to the LUMiFuge data. However, conventional centerpieces are unsuitable and thinner AUC centerpieces will be specially designed in this thesis.

Finally, the magnetic model colloids that possess the largest magnetic moment as well as a high colloidal stability will be chosen and studied by analytical centrifugation, comparing the equations of state determined by the LUMiFuge and AUC. If the magnetic interactions are strong enough, predictions of the Van der Waals-like liquid-gas coexistence of dipolar hard spheres may be tested. Moreover, the first-order deviation from ideal behavior can be quantified by the osmotic second virial coefficient and information about the particle interactions can be obtained.

1.8. Thesis outline

In **Part 1** of this thesis, a route towards composite colloids is examined. Thermodynamically stable Pickering emulsions of 3-methacryloxypropyl trimethoxysilane (TPM) oil in water, stabilized by magnetic nanoparticles, can be polymerized to obtain magnetic composite colloids. Therefore, the tunability of the emulsion droplet sizes is investigated in **Chapter 2**, by variation of the amount of oil, the concentration of salt, and the evolution of emulsions over time. In **Chapter 3**, a simple method to transfer aqueous magnetic nanoparticles to the functional TPM oil is described. The use of the resulting TPM ferrofluid to increase the magnetic loading of the composite particles is investigated, together with other potential applications.

Part 2 concerns the preparation of magnetic nanoparticles as a colloidal model system. The dipole moment of single-domain nanoparticles strongly depends on the size of the particles. Therefore, three synthesis routes to prepare a size series of magnetite nanoparticles are investigated in **Chapter 4**. All methods used involve the thermal decomposition of organometallic precursors in an apolar solvent, to obtain a low polydispersity in particle size. That the polydispersity in the geometric size is not sufficient to characterize the magnetic properties of the nanoparticles is shown in **Chapter 5**. In this chapter, the magnetic properties of nanoparticles prepared by different synthesis methods are compared. Depending on the synthesis method, a different amount of defects may be present in the nanocrystals, which has vital consequences for the magnetic properties of the particles.

In **Part 3**, analytical centrifugation is employed to examine the thermodynamics of concentrated dispersions of magnetic colloids. In **Chapter 6**, a LUMiFuge stability analyzer with homebuilt measurement cells is utilized as an analytical centrifuge and the data analysis procedure required to obtain the equation of state and the instrumental limitations are explored. **Chapter 7** describes the measurement of concentrated dispersions of nanoparticles with an analytical ultracentrifuge, using novel ultra-thin sedimentation centerpieces. Finally, in **Chapter 8** the osmotic equations of state of the concentrated ferrofluids obtained by the LUMiFuge and AUC are compared. The osmotic second virial coefficient is extracted from the data and converted to an effective dipolar coupling parameter [88].

Part 1

Magnetic Emulsions

2

Tunability of Thermodynamically Stable Magnetic Pickering Emulsions

Abstract

Pickering emulsions of 3-methacryloxypropyl trimethoxysilane (TPM) oil in water stabilized by magnetite or cobalt ferrite nanoparticles and the tunability of their thermodynamically determined droplet sizes are investigated. First, the influence of the oil-colloid weight ratio is discussed. The emulsion droplet size can be increased by addition of oil, up to a certain limit where an excess oil phase appears. Another way of tuning the size of emulsion droplets is by the added amount of salt: by screening the charges on the emulsion droplets the average interfacial area per colloid decreases, resulting in droplet growth. At larger salt concentrations the emulsions become unstable. Finally, investigations on emulsions over time show the gradual transfer of interfacial nanoparticles to the oil phase; the emulsion droplets grow until they eventually destabilize. The time scale of this particle transfer is determined by the relative amount of oil. During the gradual transfer, the degrees of wetting of the colloids by water and TPM oil change, which changes the corresponding thermodynamically determined droplet size. This evolution of the emulsions in time may be utilized to control the droplet size.

2.1. Introduction

Pickering emulsions are emulsions stabilized by solid particles [103, 104]. Generally, these emulsions are not thermodynamically stable, as they require energy input to create the unfavorable bare parts of the oil-water surface. The high interfacial tension is nevertheless reduced by the absorption of colloidal particles at the interface, which can prevent droplet coalescence and hence kinetically stabilize the emulsions. However, on the long term these emulsions will phase separate, as they are not the thermodynamically most favorable state [105, 106]. So far the only emulsions that were considered thermodynamically stable are microemulsions, in which very low interfacial tensions are obtained by the presence of surfactants at the oil-water interface. Microemulsions can form spontaneously due to the increase in entropy which compensates for the energy cost for creating the extra oil-water surface.

Recently, however, a specific type of Pickering emulsions has been discovered that does display thermodynamic stability. These emulsions consist of droplets of a particular oil, 3-methacryloxypropyl trimethoxysilane (TPM), in water, stabilized by colloidal particles such as magnetite, cobalt ferrite or Ludox silica [45, 46]. It was found that these emulsions form spontaneously, and an average size in the range of 30–150 nm could be obtained depending on the quantity of the various components in water. The thermodynamic stability was demonstrated by mixing two emulsions with droplets of different sizes that evolved to an intermediate size, as dictated by the total amount of the components present in the system [45]. Additionally, confocal microscopy and time-resolved dynamic light scattering confirmed the spontaneous emulsification of the system [46].

A systematic study of the conditions for the formation of thermodynamically stable Pickering emulsions has been published recently [47]. It was shown that a combination of conditions is required for emulsion stability: solid colloidal particles with a size below 200 nm and a preferential wettability by the oil phase, amphiphilic ions adsorbed at the surface of the droplet, and interfacial tensions of the bare-oil-water interface of about 10 mN/m or lower [47]. Theoretical studies of these emulsions have also been reported [107, 108].

Although some trends governing the emulsion droplet size were indicated in [45] and [47], the main focus was on the specific requirements for thermodynamic stability. In this chapter, several factors governing the emulsion droplet size that were partially addressed previously, such as the amount of oil and salt, are studied in more detail. In addition, the time evolution of emulsions, a factor that had not been investigated yet, is described here. The tunability of the emulsion droplet size is of importance for future applications, such as in the preparation of magnetic composite particles that can be obtained from such emulsions [48, 49]. First, the tunability of the emulsion size by

variation of the oil-colloid weight ratio is reviewed and extended. Second, the influence of salt on the emulsions is investigated. Finally, the evolution of these emulsions in time is examined and shown to be an important parameter for the state of the emulsions.

2.2. Experimental

2.2.1. Materials

Cobalt(II) chloride hexahydrate ($CoCl_2.6H_2O$; purum p.a., Fluka), iron(II) chloride tetrahydrate ($FeCl_2.4H_2O$; p.a. 99+%, Fluka), iron(III) chloride hexahydrate ($FeCl_3.6H_2O$; purum p.a., Sigma-Aldrich), iron(III) nitrate nonahydrate ($Fe(NO_3)_3.9H_2O$; p.a., Merck), ammonia (25%, extra pure, Acros Organics), sodium chloride (NaCl; p.a., Merck), sodium hydroxide pellets (NaOH; p.a., Acros), nitric acid (HNO_3; 65%, Merck), hydrochloric acid (HCl; 35%, Merck), aqueous tetramethylammonium hydroxide solution (TMAH; 25%, Aldrich), 3-methacryloxypropyl trimethoxysilane (TPM; 98%, Acros Organics) and potassium persulfate (KPS, 99+%, Acros Organics) were all used as received. TPM was stored in the dark at 4 °C after opening. In all experiments deionized water was used, obtained with a Millipore Synergy water purification system.

2.2.2. Synthesis of magnetite nanoparticles

Magnetite (Fe_3O_4) nanoparticles were prepared by the co-precipitation method described by Massart [55]. 3.98 g (0.02 mol) of $FeCl_2.4H_2O$ was dissolved in 10 mL of 2 M hydrochloric acid and mixed with 10.81 g (0.04 mol) of $FeCl_3.6H_2O$ in 40 mL of water. The mixture was ultrasonicated briefly (several seconds) and quickly added to 500 mL of 0.7 M ammonia under vigorous stirring. The mixture turned black immediately and was stirred for at least 10 minutes. The resulting magnetite particles were easily sedimented using a magnet and subsequently redispersed in 50 mL of 1 M TMAH overnight under stirring. Finally, the particles were sedimented on a magnet to remove the excess of TMAH, and redispersed in approximately 50 mL of H_2O. Stable dispersions of magnetite colloids were obtained with an average diameter of 8 nm ($\pm$ 28 %) or 11 nm ($\pm$ 28 %) as determined by transmission electron microscopy (TEM).

2.2.3. Synthesis of cobalt ferrite nanoparticles

Cobalt ferrite ($CoFe_2O_4$) nanoparticles were prepared by the co-precipitation of iron chloride and cobalt chloride salts, as described by Claesson *et al.* [35], based on the procedure developed by Tourinho *et al.* [55,56]. First, 2.38 g (0.01 mol) of $CoCl_2.6H_2O$ was dissolved in a solution of 1 mL of HCl (37%) in 4 mL of water, and 5.406 g (0.02 mol) of $FeCl_3.6H_2O$ was dissolved in 40 mL of water. These solutions were both heated to 50 °C, subsequently mixed and quickly added to a 200 mL solution of boiling 1.0 M

NaOH under vigorous stirring. After stirring for 30 minutes at 100 °C the black mixture was cooled down to room temperature. The particles precipitated within minutes and were collected with a magnet; next the supernatant was decanted, and the black sediment was redispersed in 100 mL of H_2O. This procedure was used to rinse the particles 4 times with 100 mL of H_2O. The resulting sediment was redispersed in 30 mL of 2.0 M HNO_3 and stirred for 5 minutes, upon which 30 mL of 0.35 M $Fe(NO_3)_3.9H_2O$ was added. The reaction mixture was refluxed for 45 minutes, after which it was cooled down to room temperature. After sedimentation of the particles with a magnet and removal of the supernatant, they were repeptized in 50 mL of 1 M TMAH overnight under stirring. Finally, the particles were sedimented on a magnet to remove the excess of TMAH, and redispersed in approximately 60 mL of H_2O. Stable dispersions of cobalt ferrite colloids were obtained with an average diameter of 23 nm (± 28 %) or 20 nm (± 27 %) as determined by TEM.

2.2.4. Preparation of emulsions

In general, emulsions were prepared as follows: a certain amount of oil, 3-methacryloxypropyl trimethoxysilane (TPM), was added to a dispersion of 1.2 g/L magnetite or cobalt ferrite colloids in water in a glass vial. The samples were mixed by gentle swirling of the vials, and stored on a vibration-free table in a dark, temperature-controlled room at 20 °C. Emulsion droplets were polymerized by addition of 60 μL of a 10 mM potassium persulfate (KPS) stock solution to 1.5 mL of sample to obtain a final initiator concentration of 0.4 mM, and heating for at least 8 hours in a pre-heated oil bath at 70–80 °C.

To investigate the influence of the fraction of oil on the emulsion droplet size, increasing volumes of oil were added with a Finn pipette and weighed to determine the actual oil-colloid weight ratios ($m_{\mathrm{oil}}/m_{\mathrm{colloid}}$).

To investigate the influence of salt on the emulsion droplet size in regime I (emulsions with no excess oil phase), a stock solution of an emulsion was prepared and divided over several vials in 10 mL portions. Subsequently, 1 mL of a series of stock solutions of salt (sodium chloride) was added to obtain the desired final concentration ranging between 0 and 20 mM.

Since in regime II (emulsions with an excess oil phase) the excess oil phase cannot be equally divided over the vials, no stock solution of emulsion could be used. Instead, several emulsions with the same number of colloids and TPM were prepared in separate vials. Subsequently, 1 mL of a series of stock solutions of salt (sodium chloride) was added to obtain the desired final concentration, ranging between 0 and 20 mM.

Since the emulsions destabilized upon increasing concentration of salt, the influence of the salt on the colloidal stability of magnetite and cobalt ferrite particles was investigated. Therefore, 0.1 grams of the same stock solutions of salt used for the salt experiments described above were added to 1 g of the 1.2 g/L stock solutions of magnetite and cobalt ferrite colloids and monitored over time.

To investigate the long term stability of the emulsions, two emulsions were prepared by the addition of 0.104 g and 0.466 g of TPM to 44.45 g and 42.17 g of 1.2 g/L cobalt ferrite dispersions in water, to obtain oil-colloid weight ratios $m_{\text{oil}}/m_{\text{colloid}}$ of 2.0 and 9.2, respectively. The emulsions were monitored for 20 days by visual observation, and aliquots of 1.5 mL were taken and polymerized for investigation by TEM. The emulsion was homogenized by shaking before a sample was taken.

A series of magnetite-stabilized TPM emulsions was prepared to investigate the emulsion stability at high oil concentrations. Each sample contained 2.0 g of a 0.125% w/w magnetite dispersion and different TPM volumes, such that the corresponding weight ratios $m_{\text{oil}}/m_{\text{colloid}}$ were 100, 150, 200, 250, 300, 350, 400, 500, 600, and 1000. The samples were gently homogenized several times a day during the first three days to separate emulsion stability from effects due to sedimentation. Furthermore, three samples containing 2.0 g of a 0.125% w/w magnetite dispersion with weight ratios $m_{\text{oil}}/m_{\text{colloid}}$ of 160, 240, and 400 were prepared. These samples were not shaken during the observation.

2.2.5. Characterization

Transmission electron microscopy (TEM) was performed using a Philips Tecnai 10 or Tecnai 12, typically operating at 100 kV or 120 kV, respectively. TEM samples were prepared by drying a drop of diluted dispersion on a formvar-coated copper grid. Particle diameter and polydispersity (standard deviation divided by average size) of at least 100 particles were determined from analysis of the TEM images. Polymerized sediment was sputter-coated with platinum/palladium prior to imaging by scanning electron microscopy (SEM, XL FEG 30, Philips).

Dynamic light scattering was performed on diluted emulsions at 25 °C using an argon ion laser ($\lambda = 641.7$ nm, 400 mW, Spectra Physics). Samples were diluted immediately before measurement to minimize any effect of dilution on the thermodynamic state of the emulsion.

2.3. Results and discussion

Upon addition of TPM oil to aqueous, charge stabilized dispersions of magnetite or cobalt ferrite colloids, thermodynamically stable emulsions are formed. These emulsions consist of droplets of oil in water, stabilized by the colloids at the interface, as visualized by electron microscopy pictures of the polymerized droplets in for example Figures 2.1b–d and 2.2a–c. The size of these emulsion droplets can be changed by several parameters, such as the fraction of oil (discussed in Section 2.3.1), the addition of salt (Section 2.3.2) and the evolution of emulsions over time (Section 2.3.3).

2.3.1. Size tunability by amount of oil

The size of the emulsion droplets can be tuned by the amount of oil added to the system. Upon increasing the oil-colloid weight ratio two regimes can be distinguished, as displayed in Figure 2.1e for magnetite-stabilized emulsions and Figure 2.2e for cobalt ferrite-stabilized emulsions. In Regime I, the size of the colloids increases by uptake of the added oil into the droplets. This is evident by emulsions turning lighter and increasingly turbid, due to stronger light scattering of larger objects as shown in Figures 2.1a (magnetite) and 2.2d (cobalt ferrite). The increase in size upon increasing the oil-colloid weight ratio $m_{\text{oil}}/m_{\text{colloid}}$ is quantified by polymerization of the droplets and TEM analysis (Figures 2.1b–d and 2.2a–c), and the resulting diameter is given as a function of $m_{\text{oil}}/m_{\text{colloid}}$ in Figures 2.1e (magnetite) and 2.2e (cobalt ferrite). At larger oil-colloid weight ratios, indicated as Regime II, the growth of the emulsions levels off by expulsion of the oil to an excess phase at the bottom of the sample (see Figures 2.1a and 2.2d).

These observations have been made and explained previously for emulsions stabilized by magnetite [46]. It should be noted that although the trends for magnetite observed here are qualitatively the same as reported previously, the size of an emulsion droplet cannot be predicted very precisely based on the oil-colloid weight ratio if a different batch of colloids is used. In a similar experiment comparing two batches of magnetite, where the only difference is the age of the magnetite colloids and all other conditions are the same, there are significant differences in emulsion size for fixed oil-colloid weight ratios (see Appendix). These differences can be explained by the concentration of ions present in the system. At the end of the synthesis of the colloids, there is a magnetic decantation step where it is difficult to distinguish the sediment from the supernatant. Therefore, there is insufficient control over the number of ions present in the aqueous colloid dispersions, as also discussed for colloids with different quaternary ammonium salts [47].

For cobalt ferrite stabilized emulsions the same trends as for magnetite are observed. The influence of $m_{\text{oil}}/m_{\text{colloid}}$ on the droplet size was unpublished so far for cobalt ferrite,

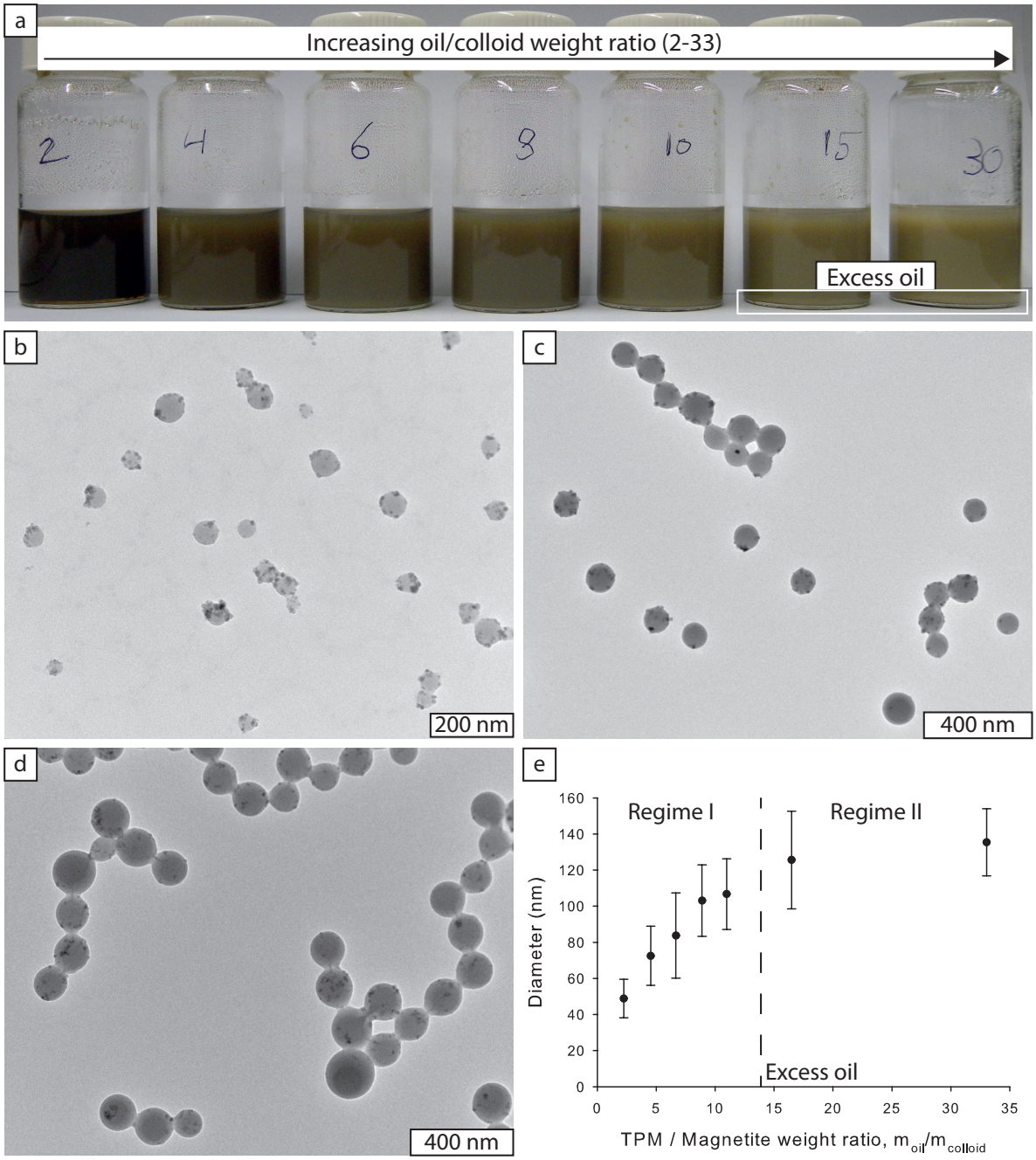

Figure 2.1. Magnetite-stabilized emulsions with increasing volumes of TPM oil, as indicated by the change in turbidity and color upon increasing TPM content (**a**). The presence of an excess oil phase for $m_{\text{oil}}/m_{\text{colloid}} = 16$ and 33 is indicated by the box. It should be noted that the horizontal white lines in the other samples are simply reflections of the glass bottom of the vial. TEM images of polymerized emulsion droplets for $m_{\text{oil}}/m_{\text{colloid}} = 2.2$ (**b**), 8.9 (**c**) and 33 (**d**) are shown. The diameter from polymerized emulsion droplets as a function of the oil-colloid weight ratio, $m_{\text{oil}}/m_{\text{colloid}}$, is shown in (**e**). The oil-colloid weight ratio's indicated on the flasks in (a) were the desired values, the actual values for $m_{\text{oil}}/m_{\text{colloid}}$ in (e) were determined by weighing the added amounts.

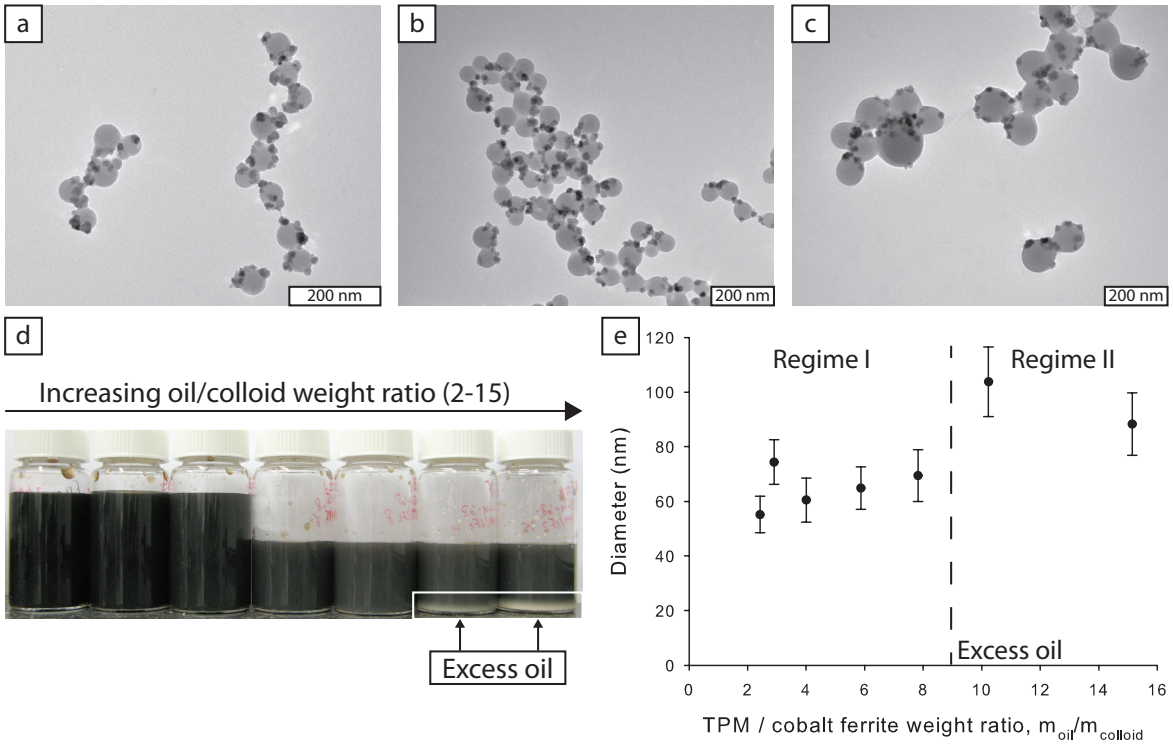

Figure 2.2. Polymerized emulsion droplets for increasing TPM/cobalt ferrite weight ratios: ratio 2.4 (**a**), ratio 4.0 (**b**) and ratio 10 (**c**). The picture (**d**) shows the change in turbidity upon increasing TPM content, as well as the presence of an excess oil phase for $m_{\text{oil}}/m_{\text{colloid}} = 10$ and 15 as indicated by the arrows. As in Figure 2.1, the horizontal white lines in the other samples are simply reflections of the glass bottom of the vial. The diameter from polymerized emulsion droplets as a function of the oil-colloid weight ratio, $m_{\text{oil}}/m_{\text{colloid}}$, is also shown (**e**).

but are in line of expectation, since it had been shown that thermodynamically stable emulsions can also be formed using aqueous cobalt ferrite colloids [46, 47].

2.3.2. Size tunability by salt concentration

A preliminary experiment by Sacanna *et al.* [45] showed that the size of magnetite-stabilized TPM oil in water Pickering emulsion droplets can be influenced by the salt concentration. Here, the influence of salt on the emulsion droplet size is investigated quantitatively by variation of the salt concentrations in emulsions prepared with different oil-colloid weight ratios, to investigate both regimes (Regime I: no excess oil and Regime II: excess oil phase present). First, emulsions were prepared and salt (NaCl) was added only after the emulsions had equilibrated. Upon addition of salt, the emulsion droplets clearly increased in size as observed from the change in turbidity and color of the samples. The increase in size was quantified by polymerization of the emulsion

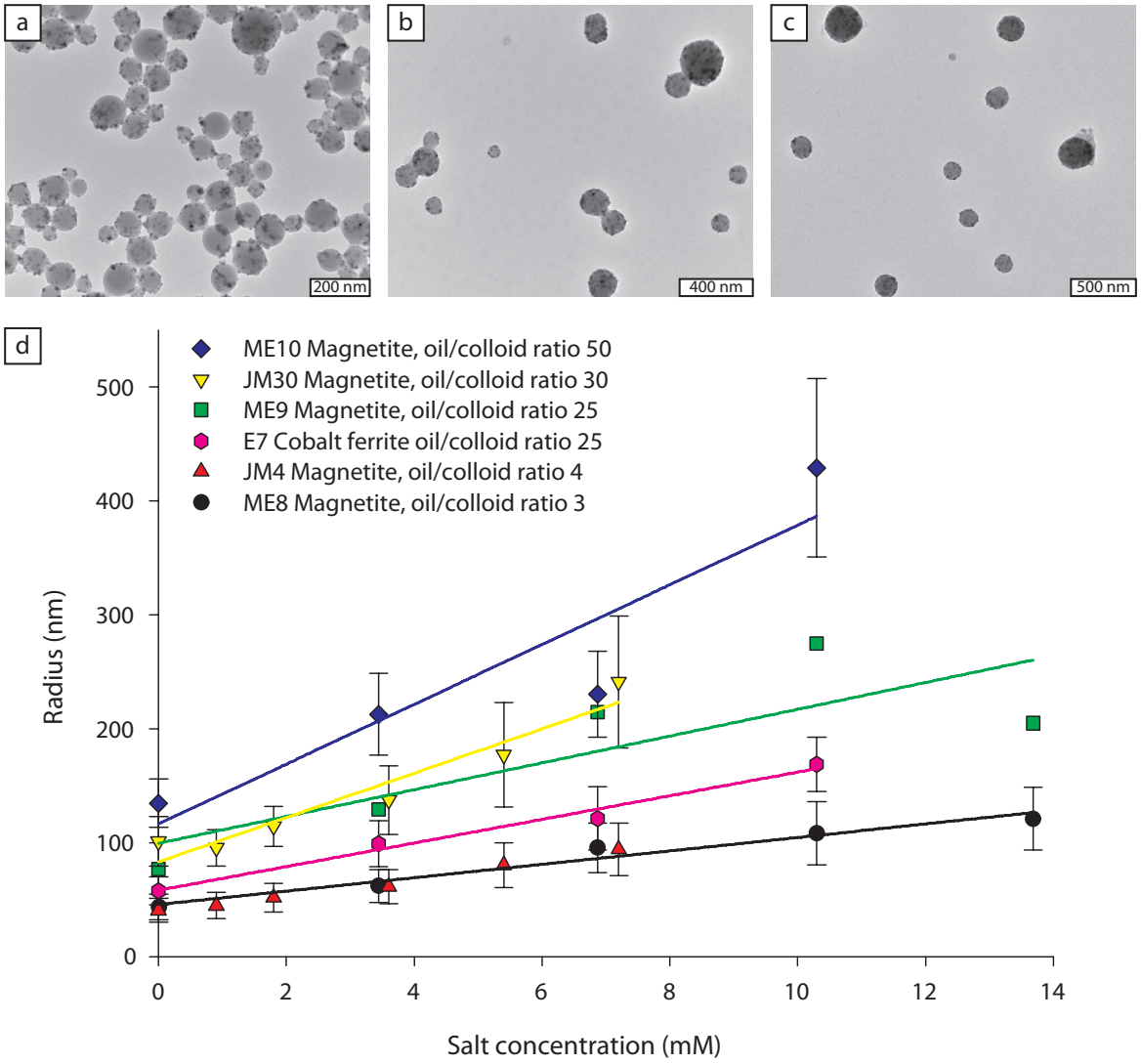

Figure 2.3. Influence of salt concentration on the emulsion droplets. TEM images are shown for polymerized emulsions stabilized by magnetite colloids with an oil-colloid weight ratio of 4, for salt concentrations of 0 mM (**a**), 3.6 mM (**b**) and 7.2 mM (**c**). The bottom graph displays the droplet radius as a function of salt concentration for magnetite stabilized emulsions with oil-colloid weight ratio 3 (dots), ratio 4 (triangles), ratio 25 (squares), ratio 30 (inverse triangles) and ratio 50 (diamonds). Data for a cobalt ferrite emulsion series with oil-colloid weight ratio of 25 are also shown (hexagons). All sizes were determined by TEM on polymerized droplets, except for the emulsions with added salt in series ME9, where emulsion droplet sizes were determined by DLS because polymerization was unsuccessful. The solid lines are fits to guide the eye, where the color corresponds to the symbols of the data.

droplets and investigation by TEM. The results are summarized in Figure 2.3 for different emulsions and salt concentrations and clearly demonstrate that the size of emulsion droplets increases with increasing salt concentration.

The increase in size of the emulsion droplets is limited to low concentrations of salt, since at higher concentrations the colloids themselves become unstable, as merely colloids in water with the same salt concentrations also became unstable over time. This is shown for a batch of magnetite and cobalt ferrite colloids at the same concentration of NaCl as in the emulsion experiments, but without any oil (Figure 2.4). The absolute concentration of added salt at which the emulsions become unstable varies per batch of colloids, as the number of ions present in the aqueous colloidal dispersions varies per synthesis, as explained in Section 2.3.1.

In Figure 2.3 the change of the average emulsion droplet radius with salt concentration is compared for several batches of magnetite stabilized emulsions and one cobalt ferrite stabilized emulsion. Two independent series of emulsions in Regime I (no excess oil present) were prepared using different batches of magnetite, but almost the same oil-colloid weight ratio ($m_{\text{oil}}/m_{\text{colloid}} = 3$ for ME8 and $m_{\text{oil}}/m_{\text{colloid}} = 4$ for JM4). As

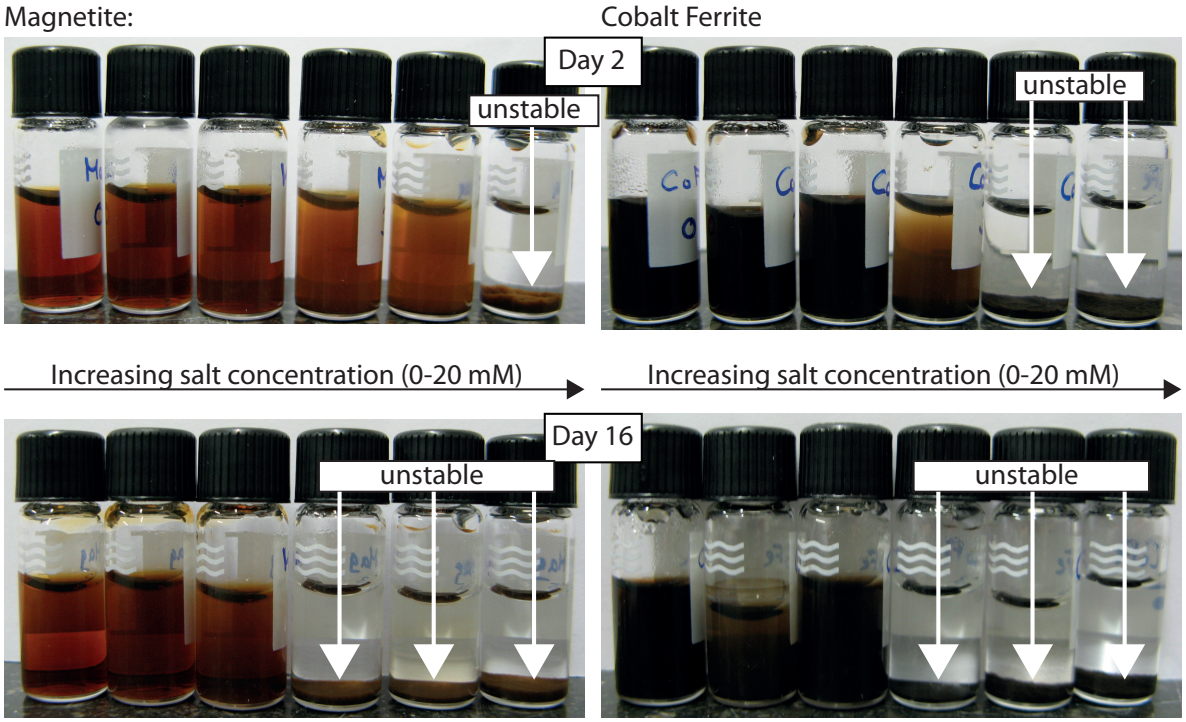

Figure 2.4. Magnetite colloids (**left**) and cobalt ferrite colloids (**right**) in water become unstable upon increasing salt concentration and time, as indicated by the white arrows. Concentrations of colloids and salt are the same as in the emulsion experiments ME8, ME9, ME10, and E7 in Figure 2.3, but without any oil present. The salt concentrations due to addition of NaCl solutions are from left to right 0, 3.4, 6.9, 10.3, 13.7, and 20.6 mM in each picture.

displayed by the black line in Figure 2.3, the points of both series follow the same trend, and the emulsion droplet size increases linearly with increasing salt concentration. In Regime I, the size of the emulsion droplets is determined purely by geometry. Assuming a narrow size distribution, the radius, R, of the emulsion droplets is given by

$$R = \frac{3V_{oil}}{A} = \frac{3V_{oil}}{N_c\sigma_c} \tag{2.1}$$

where V_{oil} is the total volume of oil in the system and A is the total area of the oil-water interface, which is determined by the number of colloids, N_c, times the average interfacial area per colloid, σ_c. In each series of increasing salt concentration, the number of colloids as well as the volume of oil are kept constant, and thus the radius of the droplets is determined by σ_c. As the ionic strength increases, the repulsion between the colloids is decreased. The colloids come closer together, which decreases σ_c and hence requires an increase in the droplet radius, according to Equation 2.1, in the regime where charge renormalization is not dominant. In its new equilibrium state, each emulsion droplet now contains a larger volume of oil and number of colloids, whereas the total number of emulsion droplets has decreased.

In Regime II more effects can play a role. As can be seen from the lines to guide the eye in Figure 2.3, the increase in emulsion size is larger upon salt addition compared to Regime I. Here not only the average interfacial area per colloid, σ_c, is changed by the salt concentration, but also the curvature of the emulsion droplets can be modified by the presence of salt. The charges at the oil-water interface are asymmetrically distributed between the oil and water sides, bending the interface around the oil-phase. By addition of salt, the curvature decreases and the emulsion droplets can grow by uptake of oil from the excess phase. Note that this preferred curvature effect does not play a role in Regime I, since there is no excess oil present and the emulsion size is merely dictated by geometry. Nevertheless, the major contribution to the increase in emulsion size is caused by the decrease of the emulsion interfacial area per colloid in Regime II as well.

To look at the average interfacial area per colloid, σ_c, in more detail, the values of σ_c are calculated using Equation 2.1, and shown as a function of salt concentration in Figure 2.5 for emulsions in Regime I (no excess oil). Clearly, σ_c decreases with increasing salt concentration, due to the colloids coming closer together. The actual average areas taken up by the magnetite colloids, calculated from $\pi r^2_{colloid}$, are 95 nm^2 for magnetite colloids of 5.5 nm in radius (ME8) and 50 nm^2 for magnetite colloids of 4 nm in radius (JM4). This is considerably smaller than the average interfacial area σ_c available per colloid on the oil-water interface. The fraction of occupied surface, ϕ_s, can be estimated by dividing the actual average areas that the colloids occupy ($\pi r^2_{colloid}$) by the average interfacial area that is available per colloid (σ_c). The estimated occupied surface fractions are for ME8: $0.1 \lesssim \phi_s \lesssim 0.4$, and for JM4: $0.1 \lesssim \phi_s \lesssim 0.25$. Although

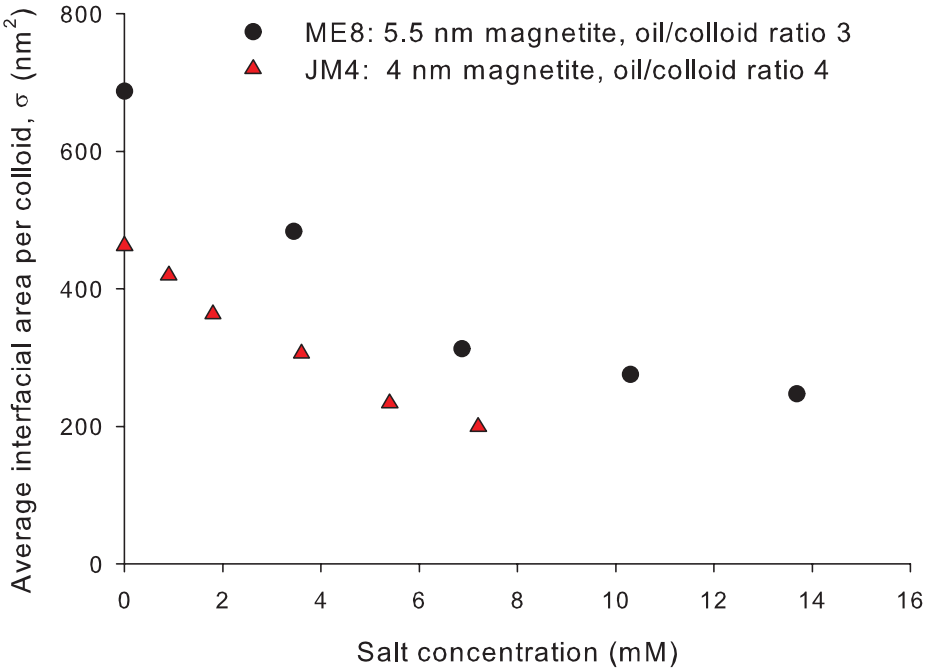

Figure 2.5. The average interfacial area available per colloid, σ_c, decreases as a function of increasing salt concentration for emulsions stabilized by magnetite colloids with an average colloid radius of 5.5 nm (ME8, dots) and 4 nm (JM4, triangles).

these values of ϕ_s are estimates since the nanoparticles on the emulsion droplets are rather polydisperse, these numbers clearly show that there is a significant fraction of oil-water interface unoccupied by colloids, which concurs with the TEM pictures in Figure 2.3. This observation is important for theoretical considerations: in [107] close-packing of the colloids on the droplet surface is assumed, whereas in [108] a thermodynamic equilibrium size is found for droplets on which the colloids are not close-packed.

2.3.3. Size tunability by time evolution

After formation, the Pickering emulsions remain stable for days to months, with the time scale of stability depending on the specific composition of the emulsion. Macroscopically, a change in the droplet size can be noticed by the color of the emulsions turning lighter, manifesting larger light scattering objects and thus growth of the emulsion droplets. An emulsion consisting of TPM and cobalt ferrite colloids at oil-colloid weight ratio $m_{\text{oil}}/m_{\text{colloid}}$ of 2 turned from black/grey to grey/brown within 20 days (Figure 2.6). From TEM images of polymerized aliquots of this emulsion we quantified the size increase in time. Over the course of 20 days, the size of these emulsion droplets increased roughly from 50 to 90 nm, whereas polydispersity increased only slightly (see Figure 2.7C). TEM images after 2 and after 15 days show that the size of the droplets

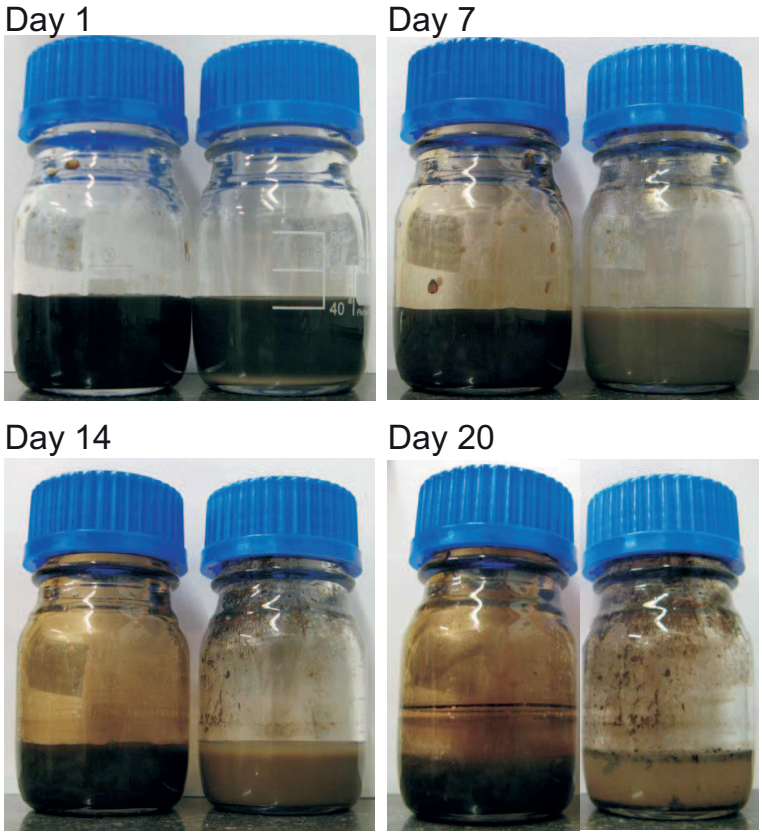

Figure 2.6. Cobalt ferrite stabilized TPM emulsions in time. Left: $m_{oil}/m_{colloid} = 2$. Right: $m_{oil}/m_{colloid} = 9$. The changes in color and turbidity indicate the growth of the emulsion droplets. The emulsion with $m_{oil}/m_{colloid} = 9$ is fully destabilized after 20 days.

had increased while the effective surface area per colloid decreased from $3.2{\cdot}10^3$ nm^2 after 2 days to $2.3{\cdot}10^3$ nm^2 after 20 days (Figure 2.7 A,B). In other words, more colloidal particles are present per droplet and they are more closely packed at the interface after 20 days than after 2 days.

This denser surface occupation implies that the effective charge of the colloidal particles has decreased allowing for closer approach which in turn leads to droplet growth because the colloidal particles can stabilize less oil-water surface area. In other words, the average interfacial area per colloid decreases, which results in droplet growth as explained in Section 2.3.2. If this droplet size increase would be due to Ostwald ripening [109, 110], the radius should grow as $r \propto t^{1/3}$ with time t. Fitting the experimental data with $r = a \cdot t^b$ yields $a = 44$ nm and $b = 0.25 \pm 0.02$, which is not in good agreement with Ostwald ripening. In light of our conclusion that the emulsion droplet size is thermodynamically determined, the slow droplet growth is more likely due to chemical changes such as the gradual transfer of the colloidal particles to the oil phase as discussed below. We have observed droplet growth in time in various solid-stabilized

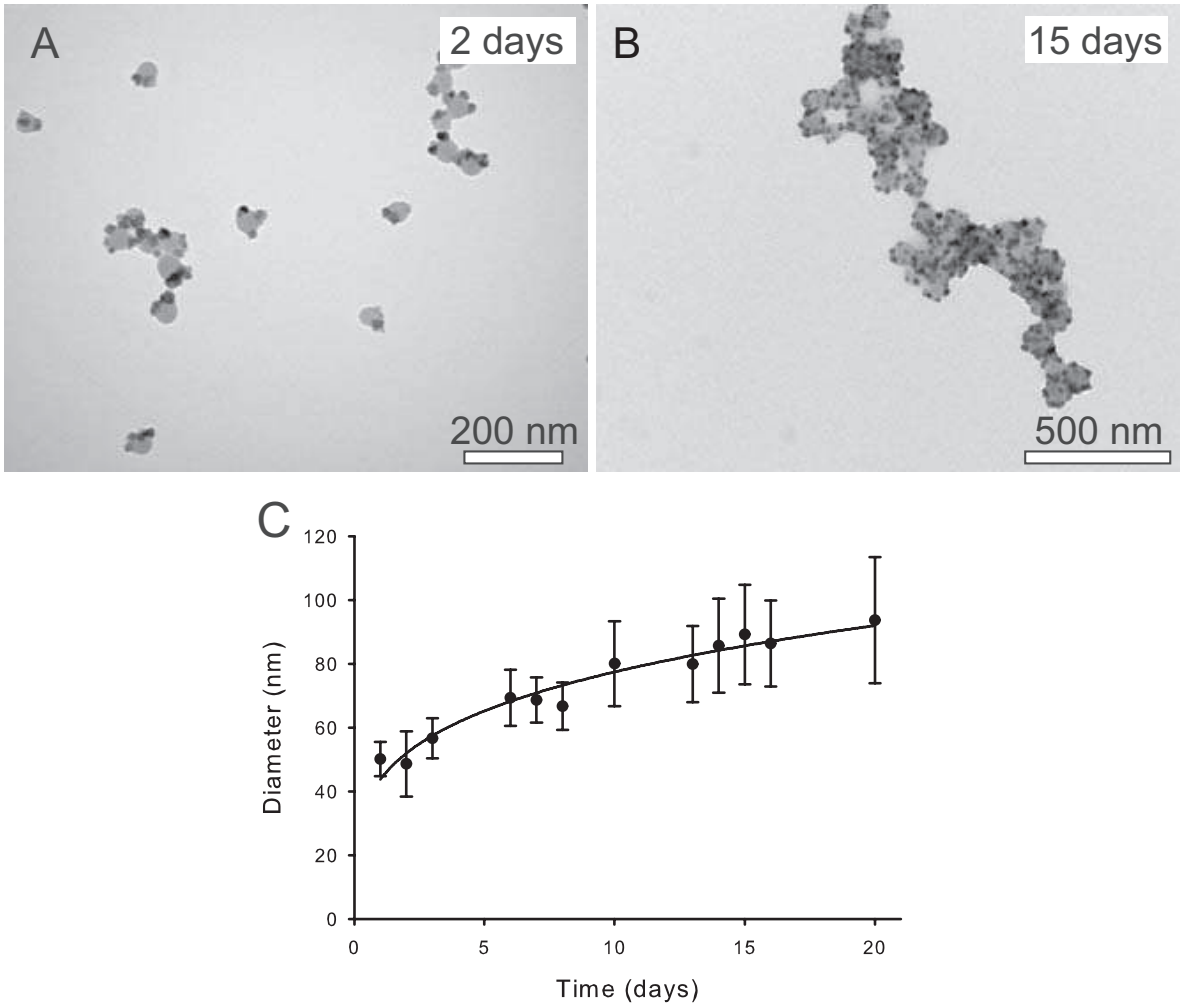

Figure 2.7. Over the course of 20 days, the emulsion droplet size grows up to double the diameter without a significant increase in polydispersity. TEM images of polymerized aliquots after A) 2 days and B) 15 days. C) Diameter of cobalt ferrite stabilized TPM emulsion droplets as measured from TEM images of polymerized samples. The solid line is the corresponding fit of $r = a \cdot t^b$ yielding $a = 44$ nm and $b = 0.25$.

equilibrium emulsions. Also for a cobalt ferrite stabilized TPM emulsion with an oil-colloid weight ratio of $m_{\text{oil}}/m_{\text{colloid}} = 9$, that is in the presence of an excess phase, the average droplet diameter increased from 80 ± 15 nm to 191 ± 73 nm over the course of two weeks.

Eventually, the emulsions become unstable and form brown sediment. By polymerizing a magnetite- as well as a cobalt ferrite-stabilized emulsion that had been allowed to settle to the bottom of the flask we could image the sediment with scanning electron microscopy (SEM). The sediment consists of a continuous phase with attached and partly coalesced droplets as can be seen in Figure 2.8. Droplets and continuous phase are

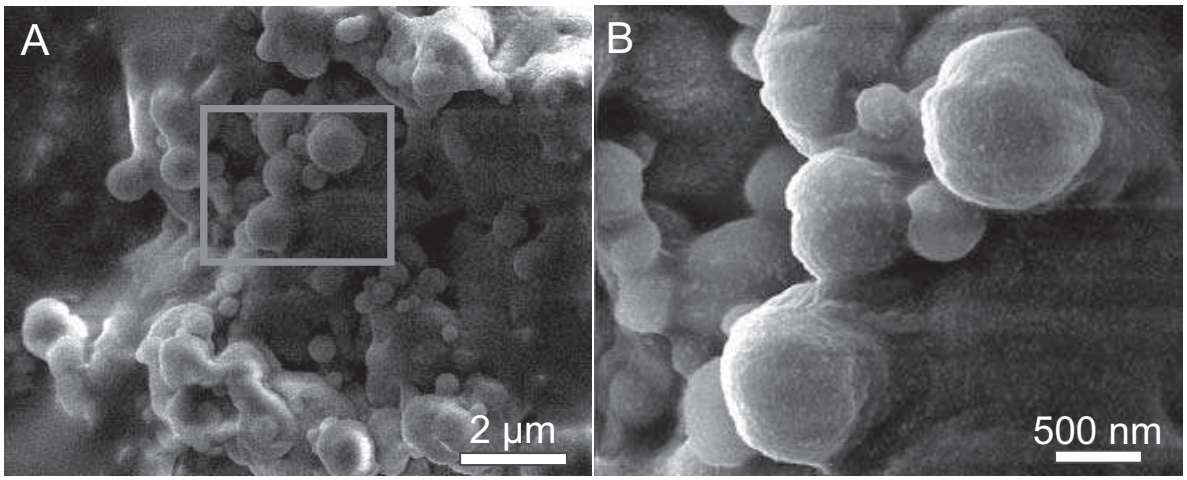

Figure 2.8. SEM micrographs of polymerized sediment of a cobalt ferrite stabilized TPM emulsion. (**A**) A continuous phase with attached and partly coalesced droplets is visible. (**B**) Magnified image of rectangle in (**A**): the surface is covered with cobalt ferrite colloids.

covered with magnetite colloids. The color of the macroscopic sediment was identical to that of the colloidal suspension, whereas the supernatant became fully transparent. Similar experiments with magnetite colloids led to comparable observations.

The time scale of sedimentation and coalescence, and ultimately transfer of magnetite to the oil phase, is linked to the relative amounts of oil and colloidal particles. To illustrate this dependence we prepared a series of magnetite stabilized TPM emulsions with oil-colloid weight ratios ranging from 100 to 1000 and observed the transfer macroscopically in time (Figure 2.9). All samples contained an equal volume of a 0.125% w/w magnetite colloidal suspension, yet different volumes of TPM. 10 hours after preparation of the samples all flasks exhibit two distinguishable phases: an aqueous upper phase consisting of colloid stabilized oil droplets and an excess oil phase at the bottom of the sample flask. The oil phase of samples with weight ratio $m_{\mathrm{oil}}/m_{\mathrm{colloid}} = 400$ and above appears slightly brownish, whereas samples below 400 exhibit a transparent oil phase. Since TPM by itself is a colorless liquid, the brown color of the oil phase indicates the presence of magnetite colloids. This is corroborated further by the response of the emulsion and excess phase to the presence of a magnet. After 2 days, the bottom phase of the sample with oil-colloid weight ratio 250 does not yet strongly respond to the magnet, whereas the sample with oil-magnetite weight ratio 500 does (Figure 2.10A and B, respectively). After 5 days the transfer of magnetite particles has proceeded to the point that the oil phase of all samples has turned brown/black and is magnetically responsive (Figure 2.9 and 2.10D). Note that before particle migration, the magnet attracts the magnetite stabilized emulsion phase more strongly (Figure 2.10C). Homogenization of the system by gentle shaking several times a day does not influence

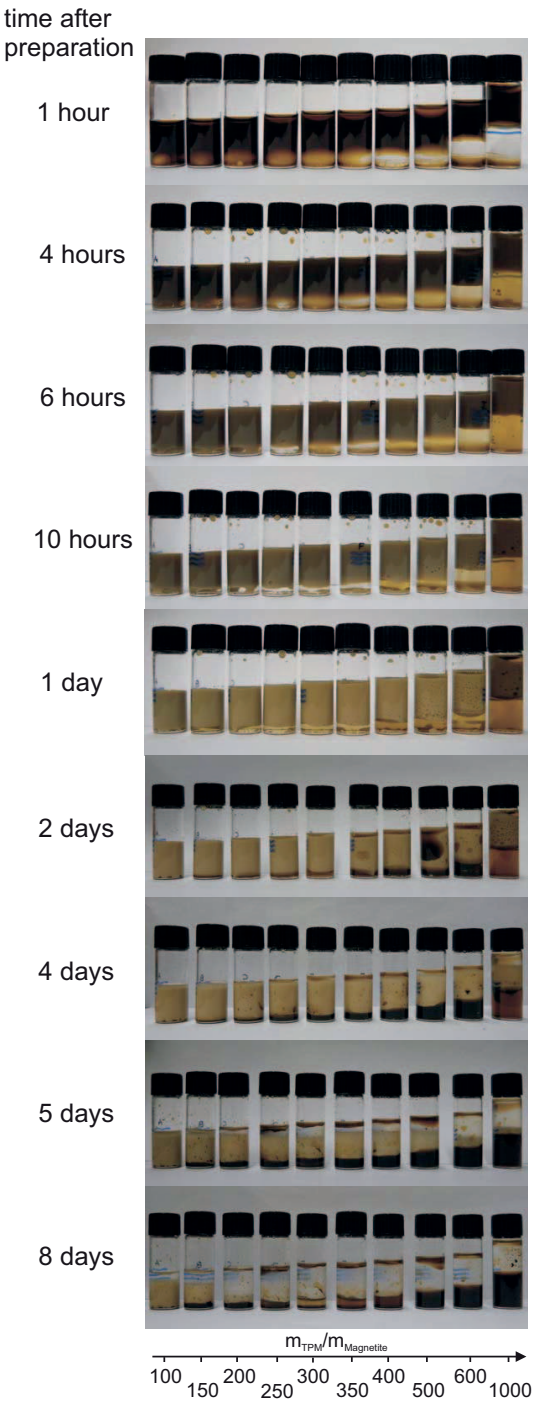

Figure 2.9. Emulsions containing magnetite colloidal particles and increasing volumes of TPM in the presence of an excess oil phase over time. Samples were gently homogenized several times a day. After several hours, emulsification of the aqueous top phase is visible by the increased turbidity. Samples above a TPM-magnetite weight ratio of 400 already show coloring of the bottom (TPM) phase due to migration of magnetite. After several days, most of the magnetite particles have transferred to the bottom phase, indicated by the brown color. In the upper phase, emulsion droplets sediment with a sharp interface. Sedimentation occurs faster with larger relative oil volumes.

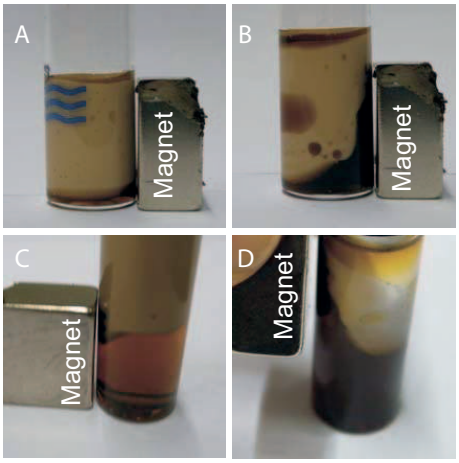

Figure 2.10. Emulsions 2 days after preparation. (**A**) With an oil-magnetite weight fraction of 250 the emulsion does not show significant attraction of the bottom phase to the magnet, whereas (**B**) with an oil-magnetite weight ratio of 500 the dark brown oil phase strongly reacts to the magnet. (**C**) Before migration, the magnetite stabilized aqueous emulsion phase is attracted more strongly to the magnet than the oil phase ($m_{\mathrm{oil}}/m_{\mathrm{colloid}} = 1000$). (**D**) After phase separation (5 days) the oil phase is strongly magnetic.

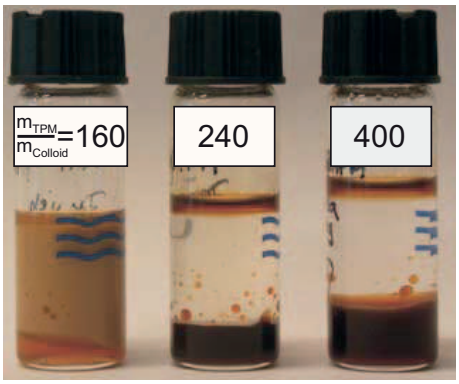

Figure 2.11. Samples of TPM and magnetite in different oil-colloid weight ratios, not homogenized by gentle shaking.

the relative time scales of particle transfer: the colloids migrate more quickly to the oil phase with higher relative oil volumes (Figure 2.11). However, the regularly mixed samples show with increasing oil volume a less abrupt transition between an emulsified and a phase separated state than the undisturbed samples. Possibly this difference originates from sedimentation of the emulsion droplets to the excess oil phase, which is prohibited by shaking.

The influence of shaking upon the formation of cobalt ferrite-stabilized emulsions was also monitored. In Figure 2.12 two identical series of emulsions are shown over time. The series shown in the left column was homogenized by shaking, whereas the right

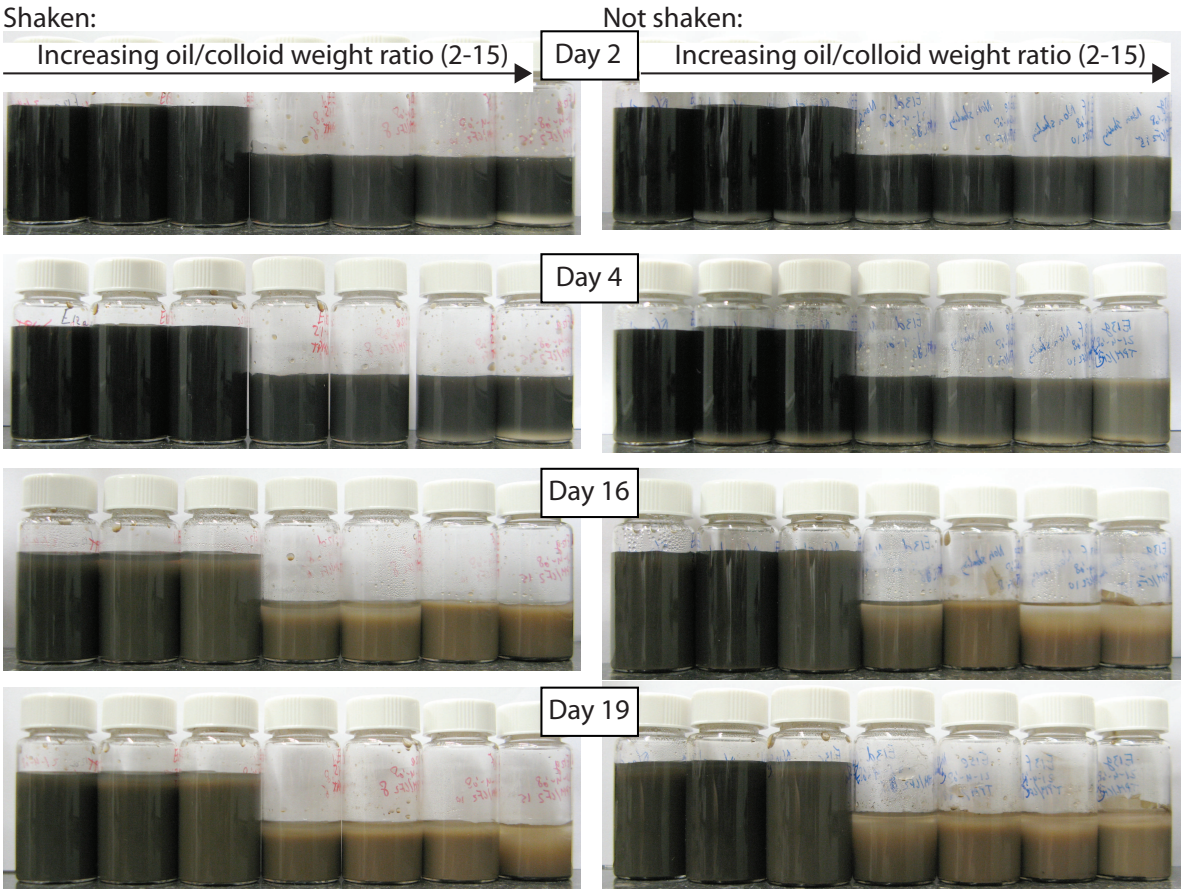

Figure 2.12. The evolution of two identical emulsion series with increasing oil-colloid weight ratios. The left series was homogenized by shaking during preparation, whereas the emulsions on the right were left undisturbed. The unshaken emulsions on the right initially contain an excess oil phase for many samples, whereas the shaken emulsions only display an excess oil phase for the largest two $m_{\mathrm{oil}}/m_{\mathrm{colloid}}$ ratios. Note that the excess oil phase becomes more brownish in time, making their visibility in these pictures more difficult. For the sake of clarity, the optical contrast has been slightly adjusted for all pictures in the same manner.

column shows emulsions formed without any shaking. The emulsions on the left change color in time more rapidly than on the right. Moreover, the emulsions on the right display an excess oil phase even at low oil-colloid weight ratios, which disappears only after more than 4 days. Nevertheless, the emulsions after 19 days look rather similar. It seems that shaking mainly influences the kinetics of emulsion formation, as shaking alleviates diffusion limitations within the aqueous phase for example for dissolved TPM molecules, and it may increase the oil surface exposed to the aqueous phase leading to more hydrolyzed TPM molecules.

Although in the experiments shown in Figure 2.9 the transfer of colloids to the oil phase takes place in a matter of days, for much smaller relative oil volumes the time scale of particle transfer lengthens significantly. Magnetite emulsions have been reported to be stable for months [45] and the cobalt ferrite stabilized TPM emulsion with oil-colloid weight ratio of 2 (Figure 2.7) still exhibit emulsion droplets with a uniform size after 20 days (Figure 2.7B). For cobalt ferrite emulsions with oil-colloid weight ratio of 9 (Figure 2.6) phase transfer has completed after 20 days as indicated by the black sediment on the bottom of the flask. The gradual emergence of the magnetic response of the TPM phase at different times in the samples (Figure 2.10) again demonstrates the oil volume dependent time scale of colloidal migration to the oil phase.

The migration of colloidal particles to TPM likely occurs because of a slow condensation of hydrolyzed TPM molecules on the colloidal surface, rendering the colloids gradually more hydrophobic over the course of time. Silica particles deliberately coated with TPM support this scenario: the colloids were found to be stable in organic solvents, yet less stable in weakly polar organic solvents and unstable in water [111]. Self-condensation of alkoxysilanes is known to happen on oxides of iron, such as magnetite, and certainly is expected for silica surfaces [111–113]. Indications for this condensation reaction were found in infrared absorbance spectra on colloidal magnetite that was removed from a stable TPM emulsion by washing with ethanol [48]. Infrared absorbance spectra showed a strong absorbance peak typical for TPM, indicating that TPM is still present on the magnetite surface. Furthermore, colloidal magnetite in ethanol as well as in TPM forms a stable dispersion, suggesting steric stabilization by the adsorbed TPM. The time scale governing the emulsion droplet growth therefore must be comparable to the one governing the condensation of TPM on the colloidal particles. The time scale of condensation is set by various factors, such as temperature and pH [112, 114]. As the colloidal particles are gradually coated by TPM, they are increasingly wetted by the oil, until they eventually have completely migrated to the oil phase. Therefore, the eventual phase separation into a transparent aqueous and an oil phase containing colloidal particles is a consequence of particle transfer to TPM.

Nevertheless, it is surprising that the migration of colloidal particles is faster with increasing relative oil volume. A likely scenario for explaining this behavior is that the number of hydrolyzed TPM molecules is higher for larger relative oil volumes, for example due to more oil-water interfacial contact, or dissolution of water molecules in the oil phase. If more hydrolyzed TPM molecules are dissolved in the aqueous phase, faster coverage of the colloidal surface and therefore transfer to the oil phase is expected.

The oil-volume dependent time scale of particle coating has another surprising consequence: in the magnetite stabilized TPM emulsions with large excess oil phase, sedimentation of the emulsion droplets of the aqueous upper phase occurs with a sharp interface between the transparent aqueous phase and the turbid light brown emulsion

phase. The larger the relative oil volume, the faster the emulsion sediments, and hence the larger the emulsion droplets must be. This observation is surprising, because the solid-stabilized emulsions, in analogy with the preferred curvature of microemulsions, are expected to have a constant droplet size in the presence of an excess oil phase, independent of the volume thereof [45, 115]. However, through faster condensation of TPM on the particle surface, the charge on the colloidal particles decreases, and the emulsion droplets grow despite the presence of an excess oil phase with an increasing oil volume.

Also in the absence of an excess oil phase, the coating with TPM leads to droplet growth in time (Figure 2.7). Here, it is not a preferred curvature that determines the droplet size, because of an absence of excess oil. The radius of the droplets is given by Equation 2.1. From this relationship, droplet growth in time can be explained by either a decrease in the number of colloidal particles at the interface, N_c, or the effective surface area per colloid, σ_c. For cobalt ferrite stabilized emulsions, the droplet radius slowly increases while the effective surface area of the colloidal particles continuously decreases in time as mentioned earlier (Figure 2.7C). From the TEM images we deduce that it is rather a lowering of the colloidal charge by coating with TPM that induces an effectively smaller area per colloidal particle than transfer of whole particles to the oil phase that accounts for the droplet growth.

From our observations on droplet size growth and chemical changes leading to different wetting properties of the stabilizing particles, thermodynamic stability of the Pickering emulsions may come into question. However, there are convincing experiments that demonstrate thermodynamic stability and point to a more intricate equilibrium: spontaneous emulsification occurs only in the presence of colloidal particles [47] and reproducibly leads to a specific droplet size depending on the oil volume relative to the number of colloidal particles [45]. Even more so, an intermediate droplet size is obtained from mixing two emulsions with a different equilibrium droplet size [45], and these experiments are reproduced as shown in the Appendix. Also, the sequence of addition of the constituents does not influence the outcome. These observations strongly suggest that a thermodynamic equilibrium exists towards which the system develops depending on the total amounts of the components.

Along that line, we consider this system to be in thermodynamic equilibrium, despite the slow chemical changes taking place over time. Thermodynamic equilibrium implies that any changes in an equilibrated system are much slower than the experimental observation time. The slow process here is formation and condensation of surface-active molecules onto the particles surfaces. This changes the particle wetting properties and the system moves to a new equilibrium state, with a minimum in free energy for the chemical conditions in this state. If another oil-colloid system is found that does not rely on *in situ* generation of surfactants that can condense on the particle surface,

the change in the wetting properties of the colloids due to the chemical processes of hydrolysis and condensation will be prevented. In the presented oil-colloid system, the emulsion adapts to the change in the wetting properties of the colloids. Yet, it does so in a controlled way, that is, the droplets collectively grow in size without becoming polydisperse. The latter suggests a minimum in the free energy, which determines the state towards which the emulsion evolves. Hence, the presented type of stable Pickering emulsions exhibits an intricate equilibrium emulsion whose evolution depends on the time scale of the condensation of the oil molecules.

2.4. Conclusions

Thermodynamically stable Pickering emulsions of TPM oil in water, stabilized by magnetite or cobalt ferrite nanoparticles, can be tuned in several ways. The emulsion droplet size can be increased by addition of oil (TPM), up to a certain limit where excess oil is expelled. Although known already for magnetite-stabilized emulsions, it is shown that the same tunability can be obtained in cobalt ferrite-stabilized emulsions. The precise window of sizes that can be obtained for certain oil-colloid weight ratios depends on the synthesis batch, since the number of ions present may vary.

Another way of tuning the emulsion droplet size is by the addition of salt to the system. Upon increasing the salt concentration, larger emulsion droplets are formed. This is mainly due to the screening of the charge on the colloids, reducing their average interfacial surface area and resulting droplet growth, also in the regime where an excess oil phase is present and curvature effects can play a role. From calculating the average interfacial area per colloid on the oil-water interface it can be concluded that there is a significant oil-water interface unoccupied by colloids. The tunability of the emulsions by the amount of salt is limited to low salt concentrations, since at higher concentrations the colloids themselves become increasingly unstable.

Interestingly, emulsion droplets increase in size over time to adjust to the chemical changes in the system: the colloids are gradually coated by TPM, as a result of which they transfer slowly from the aqueous to the oil phase. The transfer depends on whether the system is shaken or not, and the rate of transfer is increased by larger volumes of TPM present. The changes in these emulsions over time can be used to obtain a desired size by polymerizing the droplets after a certain time, since the emulsions adapt to the equilibrium size belonging to the chemical conditions at that specific time.

2.5. Acknowledgements

Daniela Kraft is thanked for collaboration on many experiments and discussions. Willem Kegel is also thanked for much input. Joen Hermans is thanked for work on several experiments, and he and Sonja Castillo are thanked for analyzing many of the

TEM images. Stefano Sacanna and Julius de Folter are acknowledged for discussions. Part of this chapter is reprinted with permission from [47].

Appendix: Thermodynamic stability of Pickering emulsions

Introduction

Thermodynamic stability of the Pickering emulsions such as studied in this chapter has been demonstrated previously by Sacanna *et al.* [45]. In a crucial experiment, two emulsions with droplets of a different size were mixed and shown to spontaneously evolve to an intermediate size distribution. However, the observations reported in this chapter in which the emulsions grow in time may cast doubt on the thermodynamic stability, and it was found difficult to reproduce this crucial experiment. Therefore, a thorough attempt to reproduce the experiment by Sacanna is made and described in detail in this appendix. Additionally, the use of freshly synthesized magnetite colloids to prepare emulsions is compared to the use of colloids of four months old.

Experimental

Two batches of magnetite colloids were used for the experiments, both prepared by the method described in Section 2.2.2. Emulsions prepared using a fresh batch of magnetite, synthesized one day prior to the experiments (series E41), were compared to emulsions prepared using a batch four months older (series E42). Dispersions of 1.2 g/L magnetite colloids in water were prepared in vials, and increasing volumes of TPM were added with a Finn pipette to obtain oil-colloid weight ratios ($m_{\mathrm{oil}}/m_{\mathrm{colloid}}$) of 2, 4, 6, 8, 10, 15, and 30. The amounts of TPM were weighed to determine the actual $m_{\mathrm{oil}}/m_{\mathrm{colloid}}$ values. All samples were mixed by gentle swirling of the vials, and they were stored on a vibration-free table in a dark, temperature-controlled room overnight. After one day, 3 mL of the samples with $m_{\mathrm{oil}}/m_{\mathrm{colloid}} = 2$ and $m_{\mathrm{oil}}/m_{\mathrm{colloid}} = 10$ were mixed, which was done for both series. All the samples in the series, including the mixed emulsions were polymerized at three different times: a few minutes after mixing the emulsions, after 1 day and after 6 days. Samples were polymerized by addition of 60 μL of a 10 mM KPS stock solution to 1.5 mL of sample to obtain a final initiator concentration of 0.4 mM, and heating for at least 8 hours in a pre-heated oil bath at 70–80 °C.

Results

Pickering emulsions were prepared using freshly synthesized colloids (series E41) as well as magnetite colloids of four months old (series E42). Stable emulsions were formed for all samples, and the size increased upon an increasing fraction of oil. This was observed by the color of the emulsions turning lighter as well as by analysis of TEM images of polymerized samples. The results from TEM analysis of both series for all

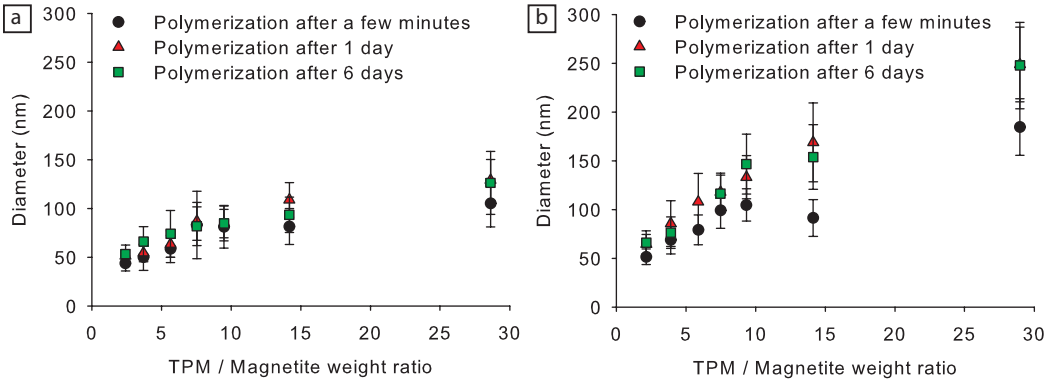

Figure 2.13. The change in droplet diameter as a function of TPM/magnetite weight ratio $m_{\text{oil}}/m_{\text{colloid}}$ using fresh magnetite (E41, **a**) and using four months old magnetite (E42, **b**). The emulsion droplets were polymerized after a few minutes (dots), 1 day (triangles) and 6 days (squares).

$m_{\text{oil}}/m_{\text{colloid}}$ ratios are shown in Figure 2.13. The sizes of the emulsion droplets using magnetite colloids of four months old are larger than the emulsion droplets prepared using fresh magnetite. As explained in Section 2.3.1, this size difference can be caused by the different number of ions present per synthesis batch. Also to be noted is that the emulsion droplets do not grow significantly in 6 days, confirming that the time evolution described in Section 2.3.3 indeed takes place over a longer period of time for relatively low fractions of oil.

The results shown in Figure 2.14 clearly demonstrate the thermodynamic stability of all the emulsions investigated here. If emulsions would not be thermodynamically stable, as is the case for most commonly known emulsions, a binary mixture of emulsions would spontaneously evolve to a mixture with an average droplet size larger than the average size of the largest droplets in the initial mixture, due to coalescence or Ostwald ripening. However, here the size distributions of all binary emulsion mixtures evolve toward the intermediate equilibrium distribution, clearly confirming their thermodynamic stability. This happens on a time scale of minutes as shown by the top row in Figure 2.14, as has been reported previously [45]. Additionally, it can be concluded that both freshly prepared magnetite colloids and four months old magnetite colloids result in thermodynamically stable emulsions.

Conclusion

The thermodynamic stability of Pickering emulsions stabilized using magnetite colloids has been confirmed by repeating the experiments of mixing two emulsions with droplets of different sizes. The size distribution of the binary mixture evolves to the intermediate average size within minutes, both for emulsions using freshly prepared magnetite colloids and magnetite colloids of four months old.

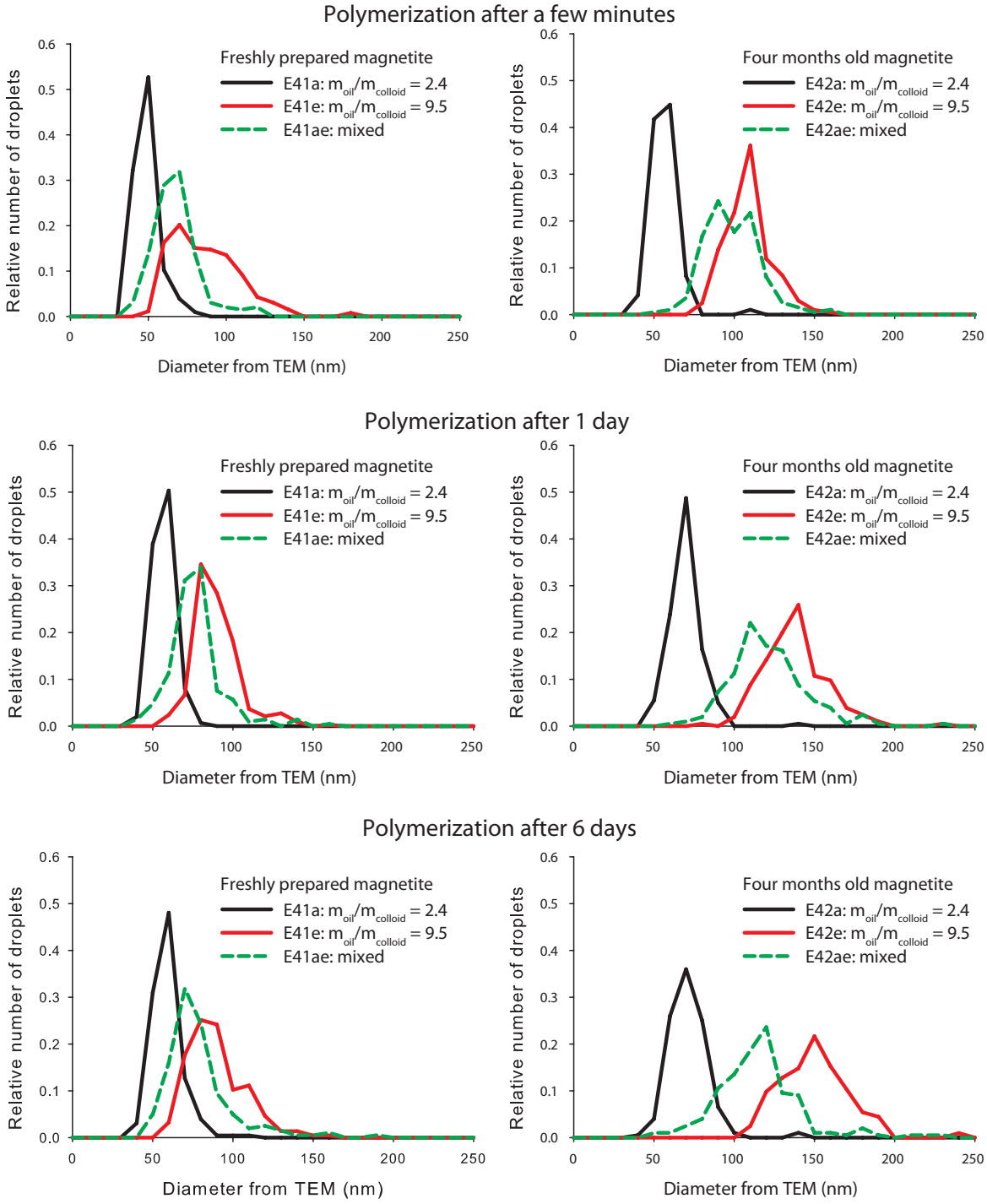

Figure 2.14. Size distributions of emulsions made using fresh magnetite (E41, left column) and using four months old magnetite (E42, right column). Small emulsions droplets (black solid lines) and large emulsion droplets (red solid lines) were mixed (green dashed lines) and polymerized after a few minutes (top row), 1 day (middle row) and 6 days (bottom row). All the size distributions after mixing are in between the small and large droplets, confirming the thermodynamic stability of the emulsions.

3

Preparation and Properties of a Polymerizable Ferrofluid

Abstract

Stable ferrofluids were prepared by transferring aqueous magnetic nanoparticles to a polymerizable oil, TPM (3-methacryloxypropyl trimethoxysilane). A convenient transfer procedure has been found, in which TPM oil was added to aqueous dispersions of cobalt ferrite ($CoFe_2O_4$) or magnetite (Fe_3O_4) nanoparticles, which were subsequently centrifuged into the denser oil phase. The particles were successfully transferred, with the surface of the nanoparticles being modified by a layer of grafted TPM. Several applications of these magnetic ferrofluids have been explored, such as the preparation of magnetic TPM gels.

3.1. Introduction

The dispersion of functional nanoparticles into polymers is an important challenge in materials science [116–119]. Polymer nanocomposites combine properties of the nanoparticles and the polymers, resulting in valuable mechanical, electrical, optical, and other properties. However, dispersing nanoparticles into polymers is difficult, for instance due to strong interactions between the nanoparticles [116] and entropic effects depending on the relative size of the nanoparticles and the polymer chains [117]. Recently, the polymerization of a monomer-based ferrofluid has been reported, although little detail is given on the colloidal stability [120]. In this chapter, a polymerizable ferrofluid is investigated, by using as the ferrofluid solvent medium a silane coupling agent. Not only can the resulting ferrofluids be used to investigate polymer nanocomposites, it also has additional functionalities being a magnetic silane coupling agent.

To obtain a dispersion of nanoparticles in a functional oil, the idea is to graft those same oil molecules to the surface of the nanoparticles. In this way, a good chemical compatibility between the sterical stabilization layer and the solvent is expected, and a dispersion of the free nanoparticles should have a good colloidal stability. Therefore, the same molecules function as monomer precursor to enable polymerization, as stabilizer of the nanoparticles, as solvent for the nanoparticles, and as silane coupling agent to use the ferrofluids in different types of applications.

Our choice of a functional oil that can both be polymerized and grafted to nanoparticles is 3-methacryloxypropyl trimethoxysilane (TPM). In a recent paper by De Palma et al. [121], several silane ligand exchange agents to transfer hydrophobic nanoparticles to water were examined. One of the molecules that was used to replace adsorbed oleic acid ligands was TPM, which failed to result in water solubility but did yield TPM-grafted nanoparticles. We will present a different procedure that yields TPM-grafted nanoparticles that are significantly more stable in TPM oil and at much higher concentrations than obtained in the method by De Palma et al. TPM is a well-known silane coupling agent, used as an additive in composite materials such as fiberglass, mineral filled thermoset resin and thermoplastic polymers [112, 113].

The addition of a magnetic functionality to this TPM oil may be useful for a range of applications, for which some preliminary investigations will be carried out here. First, the use of these ferrofluids to prepare magnetic composite particles is investigated. There is a growing interest in magnetic composite particles for applications ranging from separation technologies [12, 34, 40] and catalysis [19, 122] to biomedical applications [20, 123, 124]. Several methods to prepare magnetic composite particles are available. For example, particles with a high magnetic loading can be prepared by making clusters of magnetic nanoparticles [36–41], microemulsions [43], or magnetomicelles [44]. Unfortunately, control of both the magnetic content and monodispersity

of composite magnetic colloids remains moderate to poor. It was recently shown that thermodynamically stable Pickering emulsions can be used to prepare magnetic composite particles [48, 49]. This method is based on the discovery that the addition of non-magnetic TPM oil to a dispersion of magnetic nanoparticles in water leads to a thermodynamically stable oil-in-water Pickering emulsion, with an inherently low polydispersity [45,46]. In our approach we will attempt to prepare composite particles from Pickering emulsions with TPM ferrofluid. By varying the concentration of nanoparticles in the oil, control over the magnetic content may be obtained.

Another application for the functional ferrofluids is in the preparation of thin magnetic polymer layers, which are of interest for instance to prepare magnetic bar codes and other printable product labels. Here, the coating of silica colloids with a layer of this funtional ferrofluid is investigated.

Finally, the application of these functional ferrofluids to prepare magnetic gels is investigated, by polymerization of TPM and investigation of the distribution of the nanoparticles throughout the gel.

3.2. Experimental

3.2.1. Materials

Cobalt(II) chloride hexahydrate ($CoCl_2.6H_2O$; purum p.a., Fluka), iron(II) chloride tetrahydrate ($FeCl_2.4H_2O$; p.a. 99+%, Fluka), iron(III) chloride hexahydrate ($FeCl_3.6H_2O$; purum p.a., Sigma-Aldrich), iron (III) nitrate nonahydrate ($Fe(NO_3)_3.9H_2O$; p.a., Merck), ammonia (25%, extra pure, Acros Organics), sodium chloride (NaCl; p.a., Merck), sodium hydroxide pellets (NaOH; p.a., Acros), nitric acid (HNO_3; 65%, Merck), hydrochloric acid (HCl; 35%, Merck), aqueous tetramethylammonium hydroxide solution (TMAH; 25%, Aldrich), 3-methacryloxypropyl trimethoxysilane (TPM; 98%, Acros Organics), potassium persulfate (KPS, 99+%, Acros Organics), Bis(2,4,6-trimethylbenzoyl)-phenylphosphineoxide (Ciba IRGACURE 819 Photoinitiator) and commercial Epofix resin (Electron Microscopy Sciences) were all used as received. TPM was stored in the dark at 4 °C after opening. In all experiments deionized water was used, obtained with a Millipore Synergy water purification system.

3.2.2. Preparation of cobalt ferrite nanoparticles

Cobalt ferrite ($CoFe_2O_4$) nanoparticles were prepared by the co-precipitation of iron chloride and cobalt chloride salts, as described by Claesson *et al.* [35], based on the procedure developed by Tourinho *et al.* [55,56]. First, 2.38 g (0.01 mol) of $CoCl_2.6H_2O$ was dissolved in a solution of 1 mL of HCl (37%) in 4 mL of water, and 5.406 g (0.02 mol) of $FeCl_3.6H_2O$ was dissolved in 40 mL of water. These solutions were both heated to 50 °C, subsequently mixed and quickly added to a 200 mL solution of boiling 1.0 M NaOH under vigorous stirring. After stirring for 30 minutes at 100 °C the

black mixture was cooled down to room temperature. The particles precipitated within minutes and were collected with a magnet; next the supernatant was decanted, and the black sediment was redispersed in 100 mL of H_2O. This procedure was used to rinse the particles 4 times with 100 mL of H_2O. The resulting sediment was redispersed in 30 mL of 2.0 M HNO_3 and stirred for 5 minutes, upon which 30 mL of 0.35 M $Fe(NO_3)_3.9H_2O$ was added. The reaction mixture was refluxed for 45 minutes, after which it was cooled down to room temperature. After sedimentation of the particles with a magnet and removal of the supernatant, they were repeptized in 50 mL of 1 M TMAH overnight under stirring. Finally, the particles were sedimented on a magnet to remove the excess of TMAH, and redispersed in approximately 60 mL of H_2O.

3.2.3. Preparation of magnetite nanoparticles

Magnetite (Fe_3O_4) nanoparticles were prepared by the co-precipitation method described by Massart [55]. 3.98 g (0.02 mol) of $FeCl_2.4H_2O$ was dissolved in 10 mL of 2 M hydrochloric acid and mixed with 10.81 g (0.04 mol) of $FeCl_3.6H_2O$ in 40 mL of water. The mixture was ultrasonicated briefly (several seconds) and quickly added to 500 mL of 0.7 M ammonia under vigorous stirring. The mixture turned black immediately and was stirred for at least 10 minutes. The resulting magnetite particles were easily sedimented using a magnet and subsequently redispersed in 50 mL of 1 M TMAH overnight under stirring. Finally, the particles were sedimented on a magnet to remove the excess of TMAH, and redispersed in approximately 50 mL of H_2O.

3.2.4. Transfer of nanoparticles to TPM

To transfer aqueous nanoparticles to a functional oil, 3-methacryloxypropyl trimethoxysilane (TPM), typically, 100 g of a 1.2 g/L aqueous cobalt ferrite or magnetite dispersion was added to 24 g of TPM in a centrifuge tube, to obtain a TPM-colloid weight ratio, $m_{\mathrm{TPM}}/m_{\mathrm{colloid}}$, of approximately 200. This system was centrifuged for 1 night – 70 hours at 2500 rpm (1455 g), using a Beckman Coulter Allegra X-12R centrifuge, until all particles had migrated from the water phase to the TPM phase (TPM has a slightly higher density than water) or even sedimented to the bottom of the tube. The clear water phase was removed, and the particles in TPM from 3 or 4 different tubes were added together and centrifuged for several days up to two weeks (1455 g) to obtain a more concentrated dispersion of particles in TPM. The supernatant was removed, and the sedimented particles were redispersed in a small amount of TPM, obtaining a concentration of 10–30 wt%. Lower concentrations of particles in TPM were obtained by dilution.

3.2.5. Preparation of Pickering emulsions

Pickering emulsions stabilized by magnetic nanoparticles were prepared and polymerized as described by Sacanna et al. [48], with some modifications. Typically, a 100 mL

Table 3.1. Amounts of TPM ferrofluid (FeT) used to coat silica colloids.

Sample	FeT (μL)
SiFeT4a	286
SiFeT4b	57.2
SiFeT4c	28.6
SiFeT4d	14.3
SiFeT4e	9.5
SiFeT4f	7.2
SiFeT4g	5.7

dispersion of magnetite nanoparticles in water (1.2 g/L) was mixed with 0.4 mL of 1 M NaCl solution (4 mM in final solution), after which 1.15 mL of TPM was added to obtain a TPM-colloid weight ratio of 10. The resulting mixture was stirred gently for 1 to 24 hours, until an emulsion was formed as observed by the increased turbidity. The emulsion droplets were polymerized by the addition of 4 mL of a 10 mM stock solution of potassium persulfate (KPS) in water to obtain a concentration of 0.4 mM in the reaction mixture, and heating for at least 8 hours at 70–80 °C to ensure complete polymerization. To obtain magnetically loaded emulsion droplets, pure TPM was replaced by a dispersion of magnetite in TPM.

3.2.6. Magnetic TPM coating of silica colloids

An attempt was made to coat silica colloids with a layer of TPM ferrofluid, to see whether magnetite nanoparticles would be incorporated in that TPM layer. Silica colloids with an average diameter of 136 nm and a concentration of 33.4 g/L were used, prepared previously using the Stöber method [125] and stored in the synthesis mixture. To coat the particles with TPM, the procedure from Philipse and Vrij was used [111], with some simplifications. 10 mL of silica dispersion was mixed with decreasing amounts of TPM ferrofluid (30 wt% of magnetite in TPM, labeled FeT), as indicated in Table 3.1, and shaken overnight. To check whether the silica particles were coated with TPM, the solubility of the particles was tested by adding a few drops of the dispersion to a 1:3 ethanol/toluene mixture. All samples were washed with ethanol three times to remove free nanoparticles for investigation by TEM.

3.2.7. Preparation of functional TPM gels

To prepare TPM gels, different amounts of concentrated TPM ferrofluid (30 wt% of magnetite in TPM, labeled FeT) were added to pure TPM. Small amounts of photoinitiator (Irgacure 819) were dissolved in the mixtures by shaking for at least an hour, after which the TPM was polymerized by exposure to UV-light (Sylvania GTE Blacklight blue 8W, F8T5/BLB, wavelength 365 nm) for at least one night. Two types of

Table 3.2. The amounts of TPM, concentrated TPM ferrofluid (FeT) and Irgacure initiator used to prepare different TPM gels. The type of glass container, as described in the main text, is also indicated.

Sample	TPM (mL)	FeT (μL)	initiator (mg)	vessel
TPMp1	3	0	0	vial
TPMp2	2	0	0	test tube
TPMp3	3	0	55.9	vial
TPMp4	3	0	56.7	test tube
FeTp1	3	10	0	vial
FeTp2	2	10	0	test tube
FeTp3	2	10	59.7	vial
FeTp4	2	10	67.4	test tube
FeTp5	2	1000	54.3	vial
FeTp6	2	1000	61.3	test tube
FeTp7	2	500	56.3	test tube
FeTp8	2	250	60.9	test tube
FeTp9	2	100	61.8	test tube
FeTp10	2	50	60.5	test tube
FeTp11	2	100	26.5	test tube
FeTp12	2	100	11.6	test tube
FeTp13	2	100	7.2	test tube

glass vessels were used, as this may influence the penetration depth of the UV-light: vials with a height of 57.5 mm and diameter of 27.30 mm and Schott Duran test tubes of a height of 100 mm and a diameter of 12 mm (borosilicate glass). The compositions of the gels, as well as the type of vessel used, are summarized in Table 3.2.

3.2.8. Characterization

Transmission Electron Microscopy (TEM) was performed using a Philips Tecnai 10 or Tecnai 12 operating at 100 kV or 120 kV, respectively. TEM samples were prepared by drying a drop of diluted dispersion on a polymer-coated copper grid. Particle size and polydispersity of at least 100 particles were determined from TEM image analysis.

Dynamic Light Scattering (DLS) and zeta potential measurements were performed at 25 °C with a Malvern Zetasizer Nano ZS using laser light of 633 nm and detection at an angle of 173 degrees. The particles dispersed in TPM had to be diluted with ethanol, to prevent polymerization of the TPM in the laser beam. The results were analyzed using the Malvern Dispersion Technology Software 5.10, and size distributions were obtained with a Cumulants analysis.

Magnetization curves of the particles were measured at room temperature with a Micromag 2900 alternating gradient magnetometer (Princeton Measurements Corperation). These magnetization curves were fitted based on the Langevin equation assuming a log-normal size distribution of the nanoparticles.

To cut thin sections of the gel for TEM studies, a Leica UCT microtome using a glass knife was used. Small particles of polymerized TPM were mixed with Epofix resin and kept at room temperature overnight to harden completely. The rough polymerized Epofix was mounted in the special microtome holder and trimmed with a razor blade to obtain a small (1×1 mm) surface at which cutting starts. The cutting speed was 3 mm/sec starting with high thickness (2 μm) for a quick approach, ending with 100–300 nm thick sections. The very flexible polymerized TPM particles in the much harder Epofix do not section in the same way as the Epofix itself, giving rise to varying thicknesses for the TPM-part in the Epofix sections. The sections were picked up from the water level with a platinum loop, spread on a polymer coated 200 mesh copper grid and left to dry before imaging in the TEM.

3.3. Results and Discussion

3.3.1. Preparation of a TPM ferrofluid

Aqueous magnetic nanoparticles have been prepared successfully, as shown by TEM in Figure 3.1a for cobalt ferrite ($CoFe_2O_4$) and Figure 3.1c for magnetite (Fe_3O_4). The average diameters are 22 nm and 8 nm for $CoFe_2O_4$ and Fe_3O_4 respectively, and the particles have an irregular shape and a polydispersity of 25–30 % as expected for particles prepared by the Massart procedure [35, 56].

For the transfer of these aqueous nanoparticles to TPM, the relative amounts of TPM oil and aqueous nanoparticles are of great importance, because a mixture of water, $CoFe_2O_4$ or Fe_3O_4 colloids, and TPM results in Pickering emulsions of TPM oil stabilized by the nanoparticles. Upon increase of the TPM oil-colloid weight ratio, the emulsion droplet size grows linearly at first, until a maximum is reached and additional oil is expelled as a separate phase [45, 46]. Moreover, we found that the colloids migrate to the TPM phase in time due to a slow condensation of hydrolyzed TPM molecules on the colloidal surface, gradually rendering the colloids more hydrophobic. Eventually the colloids are completely transferred to the oil phase, and the rate of migration increases with increasing oil volumes [126]. Here, we have used these observations to transfer aqueous nanoparticles controllably from water to TPM using a large excess of TPM, typically using a TPM-colloid weight ratio of 200. Under normal gravity, the transfer took about one month for large reaction mixtures, but this process was significantly accelerated by centrifugation. When aqueous nanoparticles are centrifuged in the presence of a large amount of TPM, the gravitational force pulls the particles

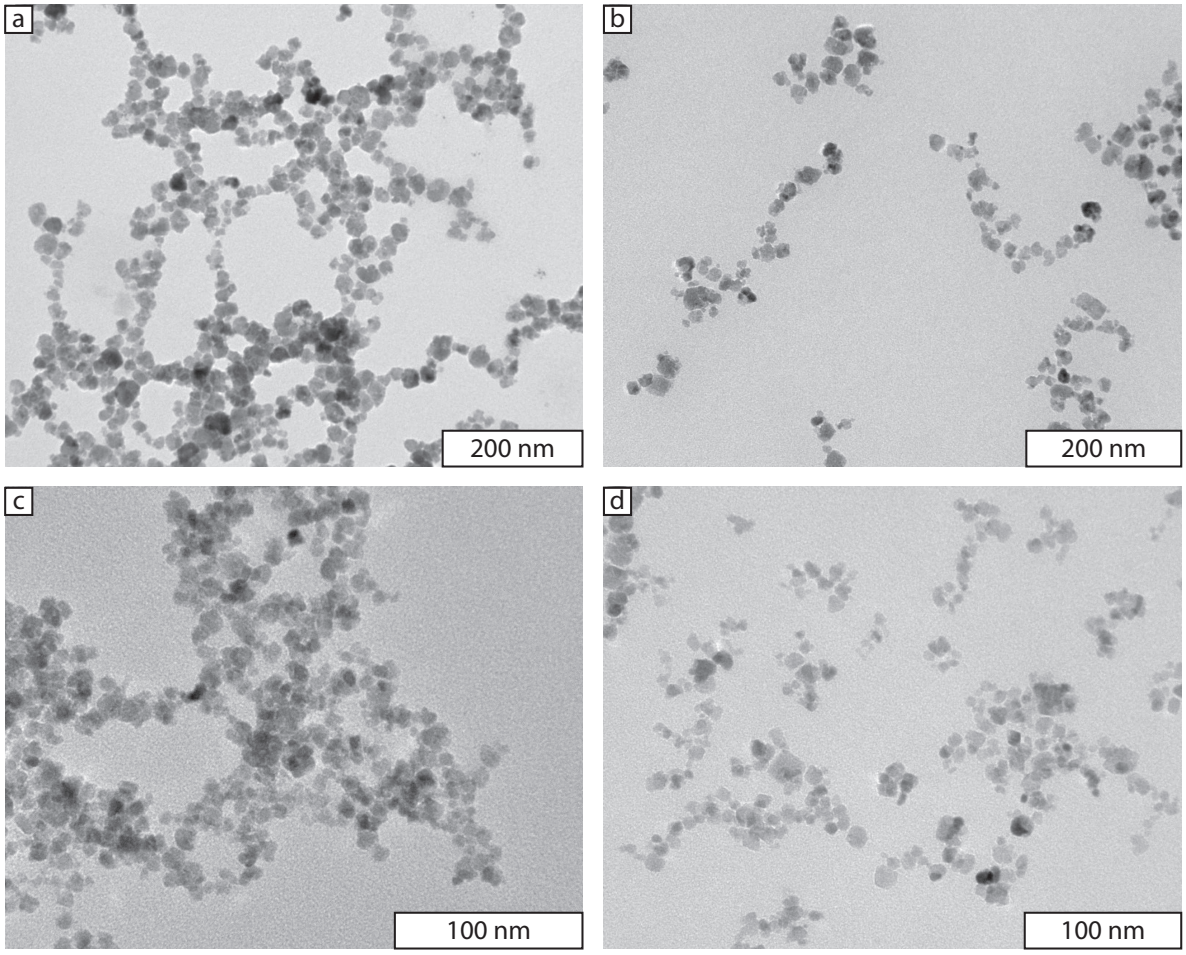

Figure 3.1. TEM images of cobalt ferrite nanoparticles before (**a**) and after transfer from water to TPM (**b**), and magnetite nanoparticles before (**c**) and after transfer from water to TPM (**d**).

towards the TPM phase, which has a slightly higher density than water. Even if initially an emulsion is formed, all the nanoparticles transfer to the TPM phase using this procedure.

The successful transfer of aqueous nanoparticles to TPM is evident from different observations and techniques. First of all, the color of the transparent TPM phase changes to black/brown upon transfer, whereas the dark aqueous phase turns clear, clearly showing the transfer to the TPM oil phase. Visual inspection of the resulting TPM ferrofluids indicates that the samples remain stable for at least several months. Moreover, it takes at least several days of centrifugation at 1455 g to sediment all the particles at the bottom of a 10 cm column of TPM fluid, corresponding to a particle size below 30 nm assuming a viscosity of 2.6 mPa s. This shows that no significant aggregation of the particles occurs during the transfer to TPM.

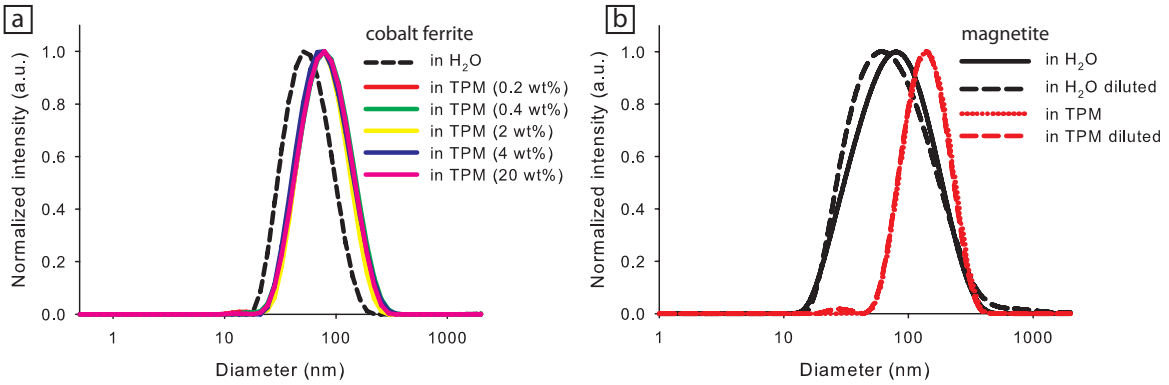

Figure 3.2. Dynamic Light Scattering measurements on cobalt ferrite particles (**a**) and magnetite particles (**b**) in water (dashed lines) and different concentrations in TPM. The concentrations indicated for cobalt ferrite in TPM are the concentrations before dilution with ethanol for DLS measurements.

Secondly, the nanoparticles before and after transfer to TPM were compared using TEM, as shown in Figure 3.1. Analysis of the TEM images reveals that the average diameter of the colloids was unchanged, 22 nm for the cobalt ferrite particles and 8 nm for the magnetite particles. Interestingly, the TEM images suggest that the minimal distance between the particles in TPM has increased. This is due to the grafting of TPM on the particles upon transfer to the TPM phase. Aqueous, charge-stabilized nanoparticles are pushed together upon drying a drop of dispersion on a TEM-grid, whereas a layer of TPM molecules provides a sterical barrier between the particles, keeping them at a distance. The presence of chemisorbed TPM on aqueous magnetite nanoparticles used in the formation of TPM emulsions has been previously shown by infrared spectroscopy [48].

Furthermore, the particle transfer was investigated by Dynamic Light Scattering (DLS) measurements performed on diluted dispersions of the nanoparticles before and after transfer to TPM. The resulting size distributions for different concentrations of TPM ferrofluid diluted with ethanol are displayed in Figure 3.2. The larger average diameter compared to TEM measurements may arise from several origins. Firstly, ferrofluids made by the Massart method as investigated here naturally contain small aggregates, as was shown by cryo-TEM [127]. Secondly, in DLS the hydrodynamic diameter is measured, which is usually larger than (hard sphere) diameters detected by TEM. Moreover, a number-weighted average size is determined from TEM images, whereas in DLS the intensity is proportional to the radius to the power 6, and therefore the larger particles contribute significantly more to the intensity-weighted size distribution. Figure 3.2a shows DLS measurements of cobalt ferrite nanoparticles from different concentrations in TPM, which upon dilution with ethanol result in the same size distribution. This indicates that no irreversible aggregates are formed upon varying the

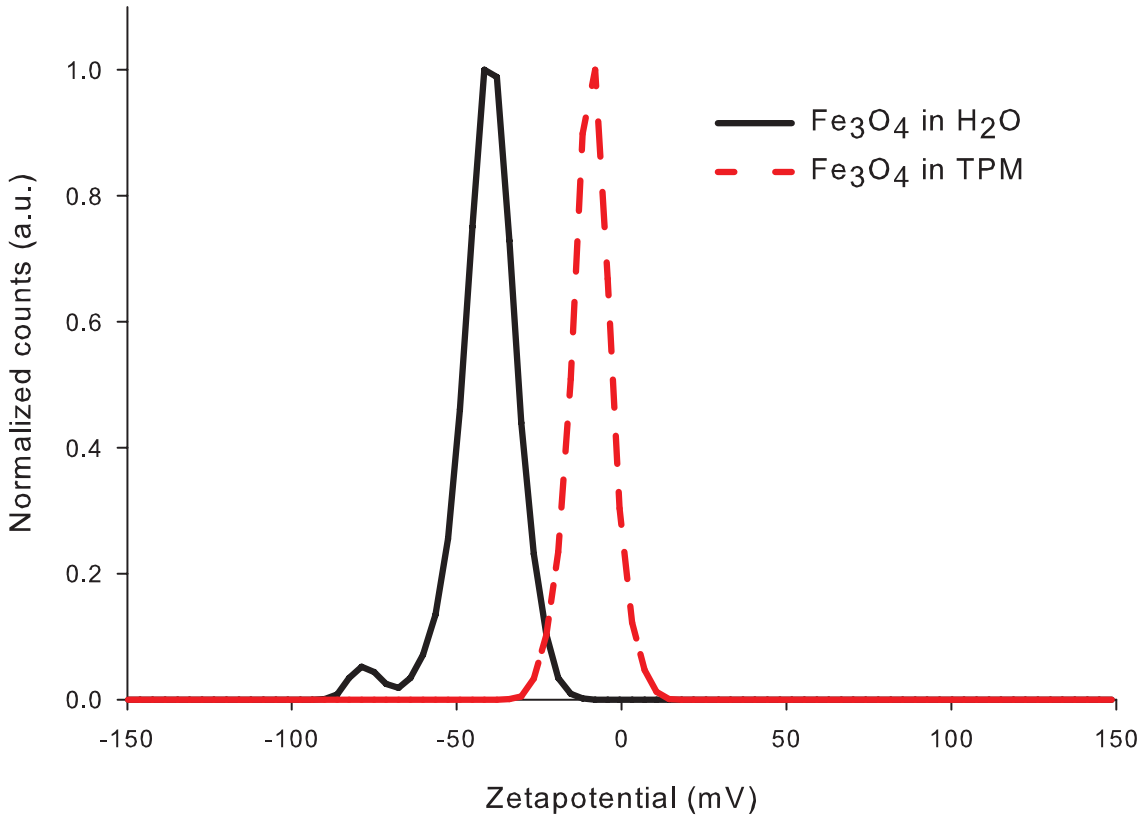

Figure 3.3. Zeta potential measurements on magnetite particles in water (solid line) and TPM (dashed line).

concentration of the nanoparticles in the TPM ferrofluid. Additionally, the hydrodynamic diameter of cobalt ferrite particles in TPM is slightly larger than in water, which can be ascribed to a TPM layer that covers the nanoparticles, corroborating the results from TEM. However, for the magnetite nanoparticles the difference in size before and after transfer to TPM is larger (Figure 3.2b), which cannot be fully accounted for by a TPM layer. During the transfer the particles are concentrated, possibly resulting in reversible aggregates in water, which upon coating with TPM may become irreversibly connected, resulting in a larger average size measured by DLS.

The electrical potential at the surface of a particle can be expressed by the zeta potential, which is the potential at the outside of the thin boundary layer of ions that remains associated with the particle as it moves through the dispersion. The zeta potential of the magnetite particles was measured before and after transfer from water to TPM (Figure 3.3). The zeta potential was measured to be about 40 mV for aqueous magnetite, corresponding to -1.5 kT/e (thermal energy per elementary charge), which is similar to previously reported values [47]. The zeta potential of the particles after

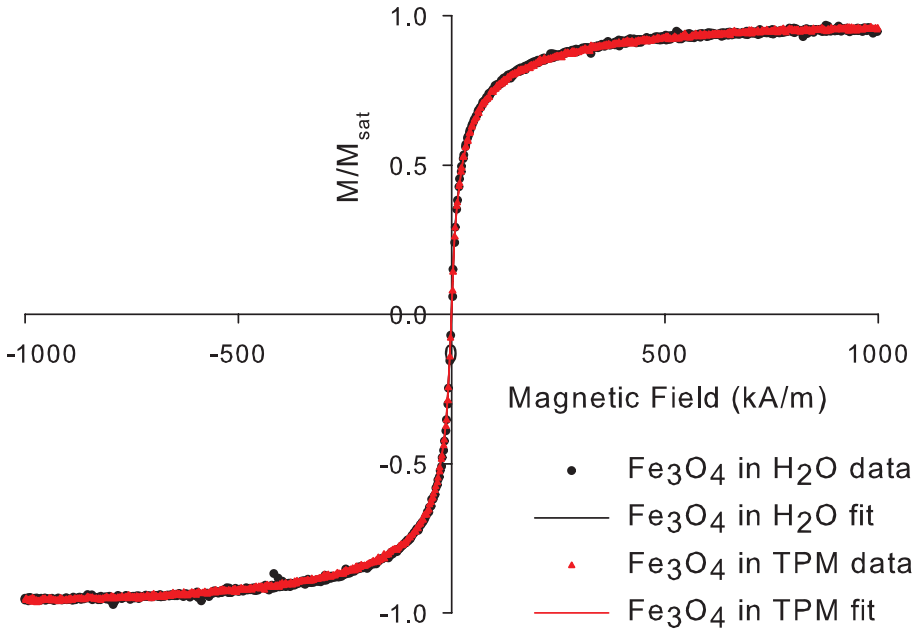

Figure 3.4. Magnetization curves normalized by the saturation magnetization M_{sat} of magnetite particles before (dots) and after (triangles) transfer from water to TPM, and their corresponding fits (lines).

transfer was measured to be 9 mV (-0.3 kT/e). Apparently, the particles remain slightly charged even in a non-aqueous environment.

Finally, magnetization curves of dispersions of magnetite nanoparticles before and after transfer to TPM have been measured. The data can be well fitted by using the Langevin equation and a log-normal distribution in particle size, as shown in Figure 3.4. From these fits an average dipole moment of 8×10^{-20} Am^2 is determined. The magnetization curves before and after transfer to TPM coincide precisely, clearly showing that the magnetic properties are unaffected by the transfer.

From the various measurements it can be concluded that magnetic cobalt ferrite and magnetite particles have been successfully transferred from water to TPM without changing the internal properties of the particles. It was recently discovered that magnetite and cobalt ferrite colloids transfer to TPM, and they do so at an increasing rate if the relative amount of oil is larger [126]. Here, this knowledge was utilized to controllably transfer the colloids to TPM, using centrifugation, which increases the transfer rate. Even if emulsions are initially formed, this transfer rate is increased by centrifugation of the emulsion droplets to the macroscopic water-TPM interface. It was suggested that the colloids migrate to the TPM phase in time due to a slow condensation of hydrolyzed TPM molecules on the colloidal surface [126]. The silane moiety of the TPM-molecule is known to have a strong affinity for the colloid surface [111], and this grafting of TPM onto the surface of the nanoparticles is confirmed by our TEM

and DLS measurements, in agreement with previous findings by IR measurements [48]. Using this method, stable TPM ferrofluids are obtained, offering potential for several applications, which will be further discussed in the next sections.

3.3.2. Pickering emulsions from TPM ferrofluids

Recently, it has been discovered that the addition of TPM oil to an aqueous dispersion of nanoparticles leads to a thermodynamically stable oil-in-water Pickering emulsion [45, 46]. The resulting droplets could be polymerized to prepare magnetic composite particles [48]. However, the magnetic nanoparticles remained confined to the oil-water interface, which limits the tunability of the magnetic content of the composite particles. Here, the preparation of Pickering emulsions using TPM ferrofluid is investigated, with the aim to control the magnetic content of the droplets by variation of the concentration of the nanoparticles in the TPM ferrofluid.

Based on the investigations described in Chapter 2, the conditions to prepare emulsions were chosen in such a way that large emulsion droplets were formed, without oil being expelled to an excess phase. This was achieved by using a TPM-Fe_3O_4 weight ratio of 10 and a NaCl concentration of 4 mM. The concentration of magnetic nanoparticles in the TPM phase was varied from 0 to 30 wt%. When pure TPM was used, stable emulsions were formed which were polymerized and analyzed by TEM. However, when TPM containing magnetic nanoparticles was used, black aggregates were visible in the reaction mixture. Despite the presence of these aggregates, a stable emulsion was formed, which could be polymerized. The nanoparticles in TPM had a strong influence on the equilibration time of the system: the emulsion prepared with pure TPM was formed within an hour, whereas the mixture from TPM ferrofluid had to be stirred overnight before a stable emulsion was formed.

The resulting TEM images for polymerized emulsions from pure TPM and TPM containing 30 wt% of nanoparticles are shown in Figures 3.5a–b and Figures 3.5c–d, respectively. From these TEM images no significant difference in the amount of nanoparticles per composite particle can be detected. The emulsions were also analyzed by magnetic measurements, from which the weight fraction of magnetic nanoparticles per composite particle could be calculated. The results are shown in Figure 3.6, where the fraction of magnetic material in the composite particles is shown as a function of the fraction of magnetic nanoparticles in the TPM ferrofluid that was used (black dots). In this figure the expected increase in magnetic fraction is also displayed assuming that all nanoparticles of the TPM ferrofluid are embedded in the composite particles, and compared to the case where none of the TPM ferrofluid nanoparticles are embedded. Note that for the pure TPM (0 wt% Fe_3O_4 in TPM), the weight fraction of magnetic material in the composite particles is already 8 %, due to the aqueous nanoparticles at the oil-water interface used to stabilize the Pickering emulsion. Clearly, the magnetic

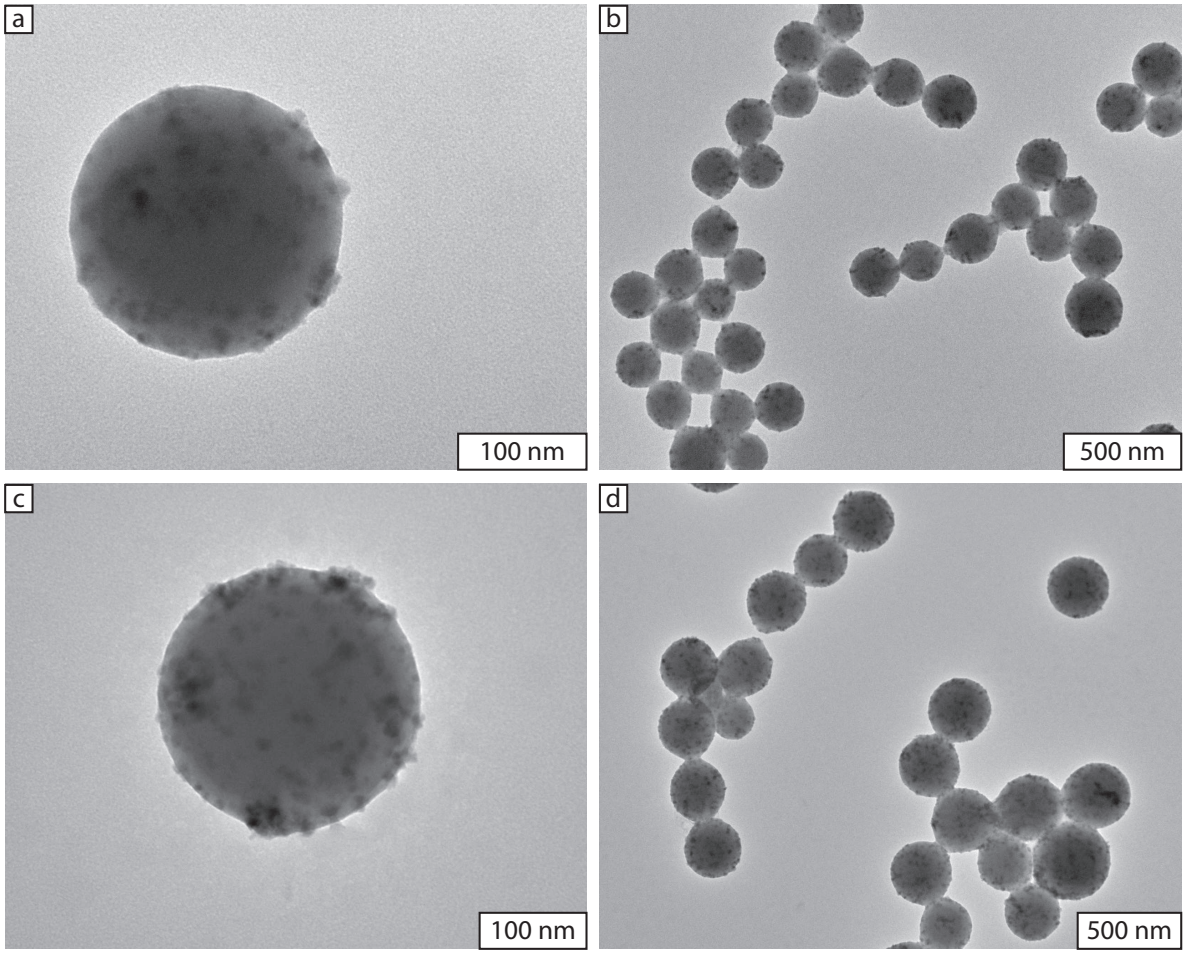

Figure 3.5. TEM images of composite particles prepared with a TPM-Fe_3O_4 weight ratio of 10 and 4 mM NaCl, using (**a**–**b**) pure TPM and (**c**–**d**) TPM with 30 wt% magnetite

loading of the composite particles does not change upon increasing the concentration of magnetic nanoparticles in the initial TPM ferrofluid, which confirms the observations from TEM. The fact that the magnetic loading of the emulsion droplets does not change upon increasing concentration of nanoparticles in TPM suggests that the aggregates visually observed already before polymerization of the emulsions are originating from the TPM phase.

To exclude the possibility that the presence of added salt (NaCl) or a small excess of TPM oil was the origin of the observed aggregation of nanoparticles, emulsions without added salt were prepared, using a TPM-Fe_3O_4 weight ratio of 4. When pure TPM was used, a stable emulsion was formed without aggregates of nanoparticles. However, using TPM containing 30 wt% of magnetite nanoparticles resulted in an emulsion in the presence of aggregates of nanoparticles as before.

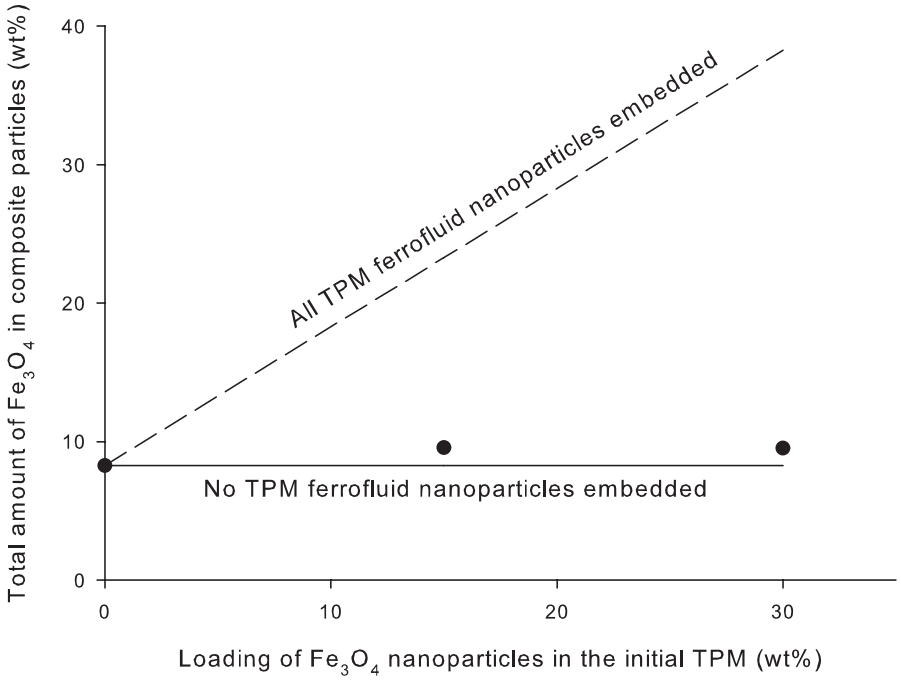

Figure 3.6. Measured magnetic content of the composite particles upon increasing concentration of nanoparticles in the initial TPM ferrofluid (dots). Two theoretical limits are indicated: no TPM ferrofluid particles are embedded, which means that only nanoparticles at the oil-water interface are present (solid line) and all of the particles of the TPM ferrofluid embedded as well (dashed line).

It is surprising that emulsions are formed without aggregates from pure TPM, whereas the use of TPM ferrofluid results in aggregates of nanoparticles in co-existence with stable emulsions. This may be related to the mechanism of emulsion formation. When TPM ferrofluid is used, two types of nanoparticles are present: charge-stabilized aqueous magnetite particles to stabilize the oil-water interface, and TPM-covered nanoparticles in TPM. It is likely that the aggregated nanoparticles originate from the TPM phase, since the magnetic loading of the composite particles remains constant, corresponding to the presence of aqueous nanoparticles (Figure 3.6). However, it seems unlikely that the TPM-covered nanoparticles would be expelled from the TPM phase, since it was seen earlier that the particles spontaneously migrate *to* the TPM oil phase during the water-to-TPM transfer. An explanation may be that not the nanoparticles are expelled, but that the TPM is removed from the TPM ferrofluid upon emulsion formation. If the TPM ferrofluid that is added to the aqueous magnetite dispersion is broken up by the mechanical stirrer into smaller, but still macroscopic blobs of TPM oil with the nanoparticles, it is likely that the surface of these blobs will be covered with nanoparticles from the water phase, to reduce the interfacial tension (see Figure 3.7). Since

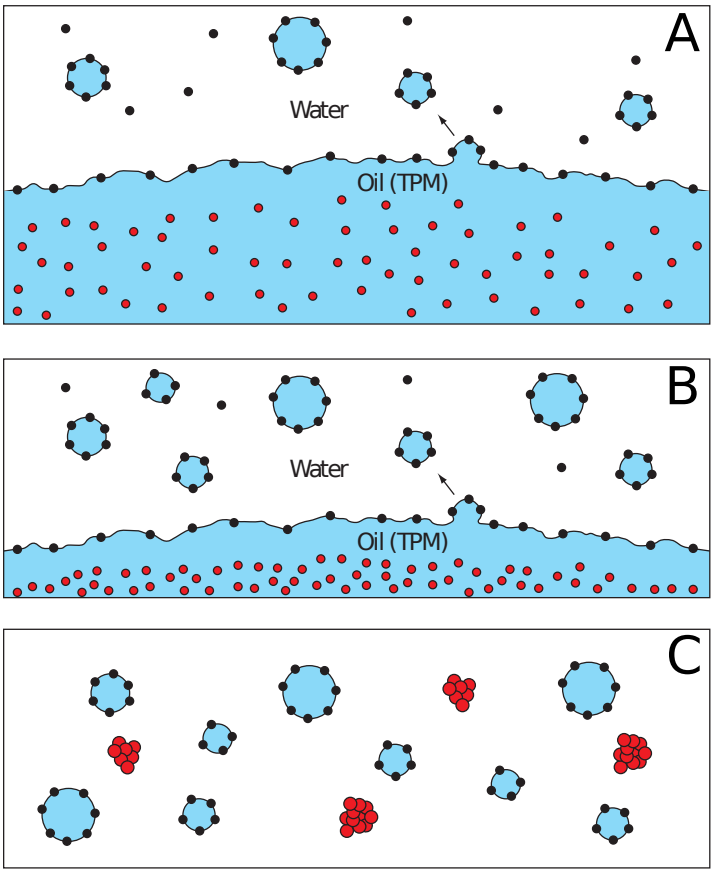

Figure 3.7. The proposed mechanism of emulsion formation when using TPM ferrofluid. **A** and **B**: Fluctuations in the surface of TPM-ferrofluid form small droplets stabilized with nanoparticles from the aqueous dispersion (black dots). **C**: The TPM ferrofluid becomes more and more concentrated, and eventually aggregates of TPM-coated nanoparticles (red dots) are formed.

the nanoparticles in the oil are charged, it may create a colloid free zone close to the interface [128, 129]. Fluctuations at the surface could initiate the 'budding' of a small TPM droplet, already partially covered with aqueous nanoparticles, resulting in a stable emulsion droplet. Magnetite nanoparticles from the TPM ferrofluid are not included in the droplets, due to their distance from the oil-water interface. This budding process could continue until the concentration of TPM-covered nanoparticles in the TPM ferrofluid phase becomes too high, resulting in the observed aggregation. In this scenario, the emulsion droplets will contain (almost) exclusively aqueous nanoparticles at the oil-water interface.

To test the hypothesized mechanism, an emulsion was prepared using a large excess of TPM ferrofluid. If an emulsion is formed according the mechanism displayed in Figure 3.7, part of the TPM would be removed from the TPM ferrofluid to form the emulsion, whereas a TPM ferrofluid phase containing the nanoparticles should remain.

This is in fact what was found: much of the TPM seemed to be taken up by the aqueous phase, whereas concentrated TPM ferrofluid remained at the bottom of the vial. No aggregation was observed in this case due to the large amount of TPM present and not all TPM was taken up in emulsion droplets. It should be noted that after several days the TPM ferrofluid phase started to become more viscous, but this is generally observed for emulsions with an excess oil phase, where the alkaline environment may catalyze the hydrolysis and condensation of the TPM-phase. Attempts were made to influence the mechanism of emulsion, using vigorous stirring or ultrasonication during emulsion formation or the addition of TMACl to screen the charges in the TPM phase, but in all cases the aggregates of nanoparticles were still observed.

Alternatively, it was found that the addition of a concentrated drop of TMAH in water to a TPM-ferrofluid diluted with ethanol results in fast precipitation of the nanoparticles. Possibly the charge of the nanoparticles in TPM is screened by the TMAH, and the TPM-layer on the particles is not sufficient to stabilize these nanoparticles solely by steric repulsion. A similar process may take place in the emulsions, where the presence of TMAH from the aqueous dispersion of nanoparticles destabilizes of the nanoparticles in the TPM ferrofluid.

Altogether, the amount of magnetic nanoparticles in the Pickering emulsions could not be increased using TPM ferrofluids, since aggregates of nanoparticles are formed in co-existence with the emulsion droplets. This is probably caused by the mechanism of emulsion formation, although the presence of TMAH may also play a role. For composite colloids similar to the ones prepared in this chapter, the maximum magnetic interaction between two colloids was reported to be below 1 kT [51]. Hence, the composite colloids prepared from these emulsions without an increased number of magnetic nanoparticles are insufficiently magnetic for our work on the thermodynamics of dipolar fluids. Consequently, an alternative approach was explored: the synthesis of nanoparticles with a single magnetic domain, described in Part 2 of this thesis.

3.3.3. Magnetic TPM coating of silica colloids

TPM is used as a coating material in different applications [112, 113]. Using TPM ferrofluids instead of pure TPM will add a magnetic functionality to such materials. A simple system to investigate this on a colloidal scale is by the coating of silica colloids, since the coating of silica with TPM is well-known [111]. Successful coating of silica colloids with TPM can be qualitatively tested by addition of the dispersion to an ethanol-toluene mixture. Stöber silica without TPM showed (partial) aggregation in this solvent mixture, as did the samples with small amounts of TPM (SiFeT4d–g). The other dispersions (SiFeT4a–c) appeared to be stable in the solvent mixture, indicating that the silica particles were coated with TPM. However, the color of the dispersions changed from brown to white after washing of the samples with ethanol. TEM images of

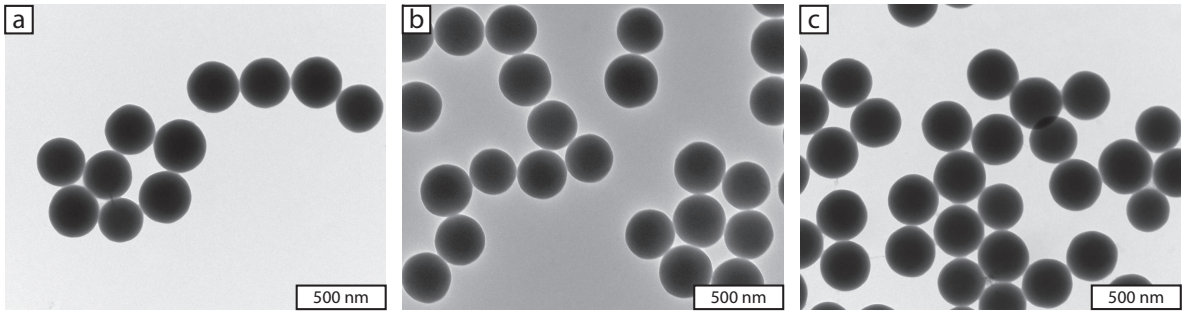

Figure 3.8. TEM images of silica colloids treated with different amounts TPM ferrofluid (FeT): 286 μL (SiFeT4a, **a**), 14.3 μL (SiFeT4d, **b**), 5.7 μL (SiFeT4g, **c**). No magnetite colloids can be found in the images.

several samples are shown in Figure 3.8, and no magnetite nanoparticles on the surface of the silica colloids are observed.

In the original procedure, part of the solvent is removed by distillation, which can promote the condensation of the silanol groups on the silica surface [111]. However, even without this distillation step, the stability of silica colloids is clearly improved due to TPM coating as shown by the qualitative test of adding some drops of the dispersion to an ethanol-toluene mixture. When a large amount of TPM ferrofluid is added, the silica colloids are more stable than the Stöber silica in these mixtures. Nevertheless, no magnetite colloids are incorporated on the surface, as indicated by the white color after purification of the samples and corroborated by the TEM images in Figure 3.8. The magnetic colloids are dispersed in TPM by the coverage of TPM on their surface by condensation of the silanol groups. This implies that the methacrylate groups are on the outside of the particles, whereas the silanol groups are required for attachement to the silica colloids, which explains why the nanoparticles are not incorporated on the silica surface. When the amount of TPM is reduced to promote the incorporation of nanoparticles on the surface, the silica colloids become less stable at the point that not enough TPM is present. Hence, although this method can be investigated more systematically, it is unlikely that the magnetic nanoparticles will be incorporated in a thin TPM layer.

3.3.4. Magnetic TPM gels

Preparation of functional TPM gels. It is difficult to disperse nanoparticles in plastics or gels. Since we have obtained magnetic nanoparticles well dispersed in TPM, this offers a way to obtain gels containing nanoparticles by polymerizing the TPM. This is investigated by polymerization of different TPM ferrofluids using UV light.

First, polymerization of pure TPM was compared to a low concentration of magnetic particles in TPM, using two different glass containers, as shown in Figure 3.9. In this experiment, no photoinitiator was used, and polymerization took several weeks,

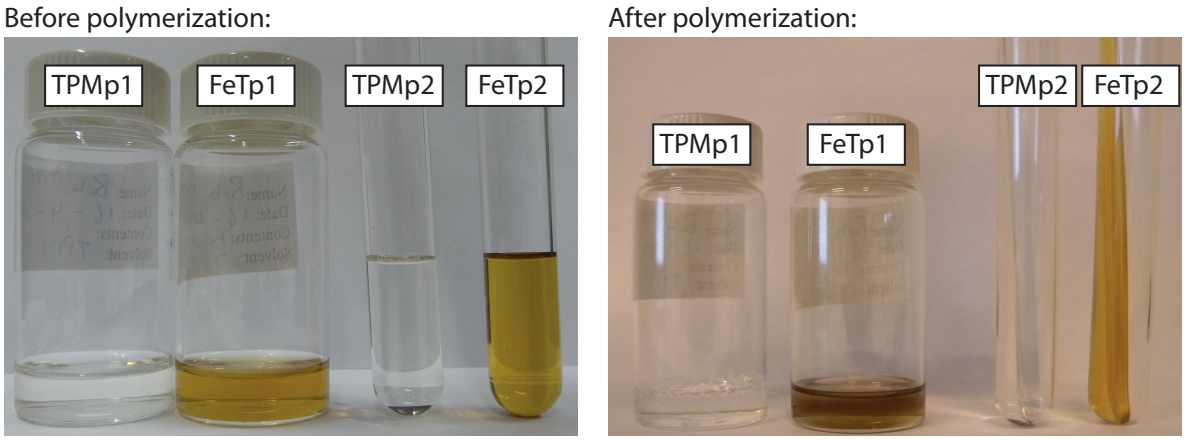

Figure 3.9. TPM gels before (**left**) and after (**right**) polymerization, for pure TPM in a vial (TPMp1), pure TPM in a test tube (TPMp2), TPM ferrofluid in a vial (FeTp1) and TPM ferrofluid in a test tube (FeTp2).

depending on the glass container and the presence of magnetic particles. The sample with pure TPM in the test tube (TPMp2) polymerized faster than the one in the vial (TPM1), possibly due to the presence of the cap or a difference in glass thickness, although this has not been quantified. Polymerization of the samples with magnetic particles present (FeTp1 and FeTp2) took more than a month. Smooth and rather homogeneous gels were formed, although the sample with pure TPM in the vial (TPM1) shows surface roughness of which the origin is unknown.

To enhance the polymerization rate, a photoinitiator, Irgacure 819, was used, which enabled polymerization in one night instead of several weeks. TPM gels with a high concentration of magnetic particles are shown in Figure 3.10. Interestingly, the resulting gels are very rough and irregular. Although most of the sample is very dark in color, some lighter spots are also visible, especially near the glass wall, suggesting an inhomogeneous distribution of the nanoparticles.

To investigate the influence of the nanoparticle concentration, several TPM gels with different concentrations of nanoparticles were prepared. Upon increasing concentration of magnetic nanoparticles in TPM, the irregularities increased (Figure 3.11). Evidently, the irregularities are caused by the presence of the magnetic nanoparticles, which may act as a trapping centre for radicals, or absorb more UV light resulting in local heating.

Another parameter that may have an important influence on the formation of the gels is the concentration of initiator. In Figure 3.12, TPM gels are shown prepared using the same amount of nanoparticles, but different concentrations of initiator. After 2 hours of polymerization, the TPM samples with lower concentration of initiator were more liquid, and as can be seen from Figure 3.12 (left), less irregularities were present. However, after polymerization was finished, all samples looked similar. The initiator

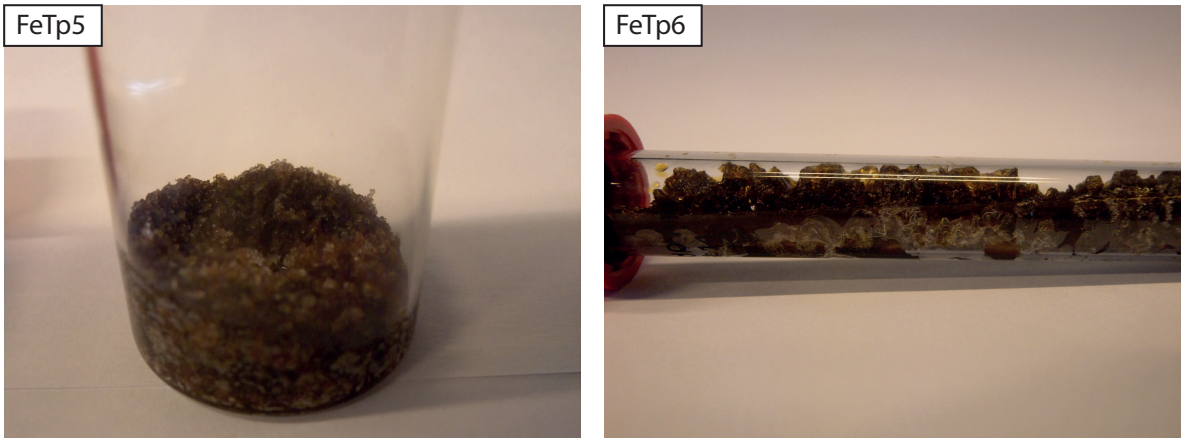

Figure 3.10. TPM gels with a high concentration of magnetic nanoparticles, prepared in a vial (FeTp5) and a test tube (FeTp6).

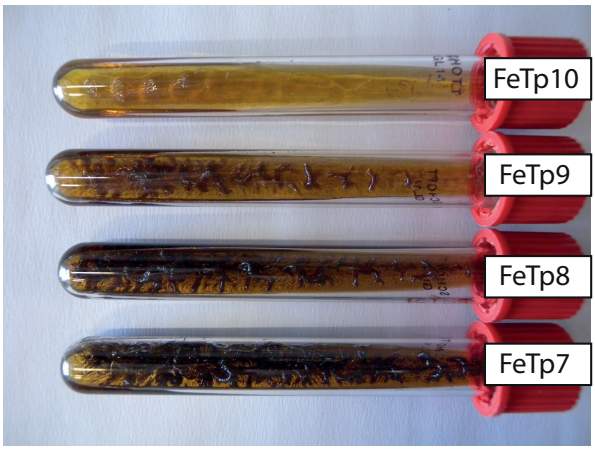

Figure 3.11. TPM gels with increasing concentrations of magnetic nanoparticles from top to bottom, showing an increase in irregularities of the gels.

concentration has a significant influence on the rate of polymerization, but does not seem to have a direct impact on the amount of irregularities.

Distribution of nanoparticles in TPM gels. To investigate the distribution of nanoparticles in the TPM gels in more detail, two TPM gels (FeTp2 and FeTp7) were cut into thin sections to study them with TEM. Small pieces of TPM gels were prepared and embedded in Epofix resin for cutting of the sections.

Figure 3.13 shows TEM images with increasing magnification of the TPM gel with a low concentration of nanoparticles (FeTp2). In general, the Epofix resin looks rather smooth on TEM pictures, whereas the TPM pieces look shredded. This is caused by the softness of the TPM gel, by which the sections are more torn off than neatly cut, opposite to the Epofix regions. The nanoparticles found in the TPM gel consist of small clusters, which may well be the clusters as they are present in aqueous dispersions as found by cryo-TEM [127], as also discussed in section 3.3.1. Since the gel has a rather

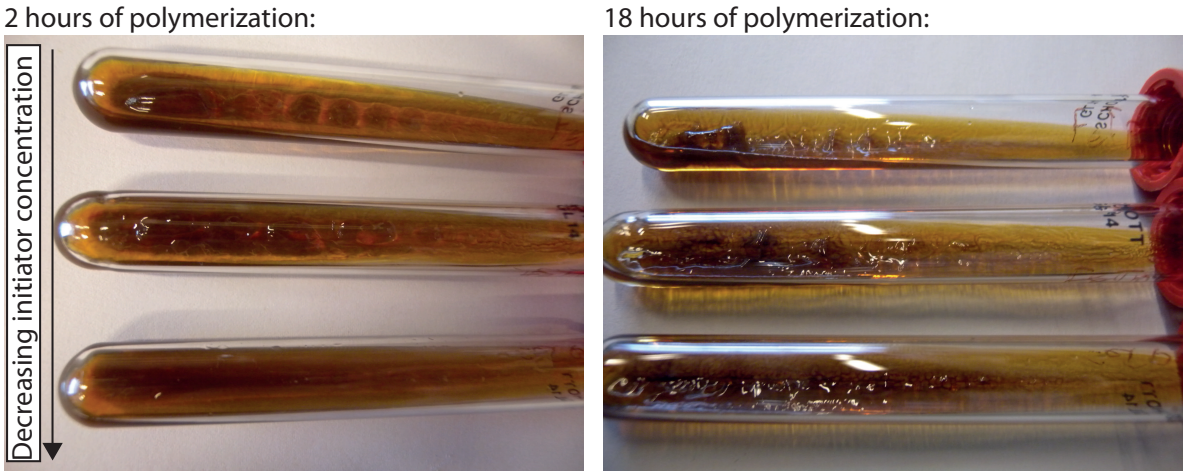

Figure 3.12. TPM gels (FeTp11–13) with decreasing concentration of initiator from top to bottom, after 2 hours of polymerization (left) and 18 hours of polymerization (right). The amount of initiator influences the rate of polymerization, but not the final state of the samples

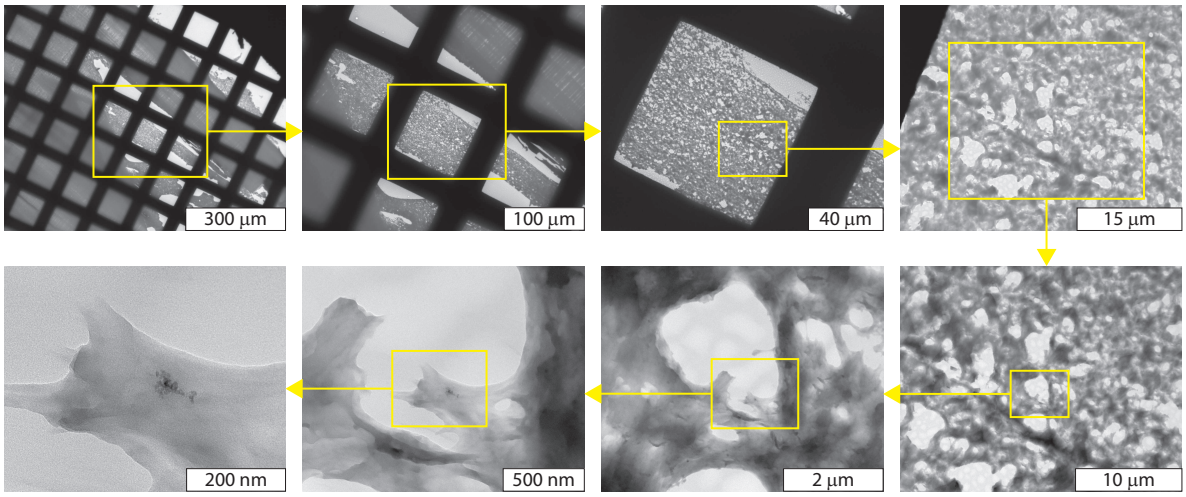

Figure 3.13. TEM images of a TPM gel (FeTp2) embedded in Epofix resin, with increasing magnification.

low concentration of nanoparticles, not many particles can be found in one image, and single particles are even more difficult to distinguish. Nevertheless, investigation of TEM images of several sections never showed any large clusters, indicating that the nanoparticles are dispersed in the TPM gel as in the original TPM ferrofluid.

In Figure 3.14 a picture is shown of pieces of a few mm in size of the TPM gel with a high concentration of nanoparticles (FeTp7). From this picture it can already be seen that the gel consists of transparent regions as well as very dark regions, indicating a phase segregation of the nanoparticles. Several TEM images of the sections of the TPM gel with higher concentration of nanoparticles are shown in Figure 3.15. Small

Figure 3.14. Pieces of a few mm in size of a TPM gel with a high concentration of nanoparticles (FeTp7), showing segregation of the nanoparticles to concentrated regions.

aggregates are observed, similar to the TPM gel with low concentrations. Although a macroscopic segregation of the nanoparticles can be observed, the areas containing many nanoparticles do not consist of large aggregates of hundreds of particles, but of well dispersed small clusters, as for the sample with a low concentration of nanoparticles.

In summary, magnetic nanoparticles are distributed in small clusters throughout the TPM gel, both for a low and high concentration of magnetic nanoparticles. However, for high concentrations of nanoparticles, the TPM macroscopically separates in regions with hardly any nanoparticles and concentrated regions. This may be connected to the irregularities as discussed above, so it is worthwhile investigating and improving the polymerization process, for example by increasing the polymerization rate. Nevertheless, the nanoparticles are homogeneously distributed in the highly concentrated regions, which is promising for future application.

3.4. Conclusions

Stable, concentrated TPM ferrofluids have been successfully prepared via a simple transfer method. DLS measurements and TEM results clearly show that the nanoparticles are transferred from the aqueous phase to TPM-oil, a process initiated by the grafting of TPM-molecules on the nanoparticle surface. Magnetic measurements show that the magnetic properties of the nanoparticles remain unaltered by the transfer.

Several applications of these TPM ferrofluids have been investigated. Use of TPM ferrofluid to prepare composite particles from Pickering emulsions resulted in emulsion droplets of oil without magnetic particles except at the oil-water interface, which we explain by repulsion of oil-dispersed nanoparticles from the oil-water interface. Another possible application of these ferrofluids is in the coating of materials. Preliminary experiments to coat silica colloids with a magnetic TPM layer were unsuccessful, since the magnetic nanoparticles were not incorporated in the TPM layer on the silica. This is attributed to the need for silanol groups to attach to the silica, whereas these silanol groups are attached to the nanoparticles, preventing the incorporation into the thin

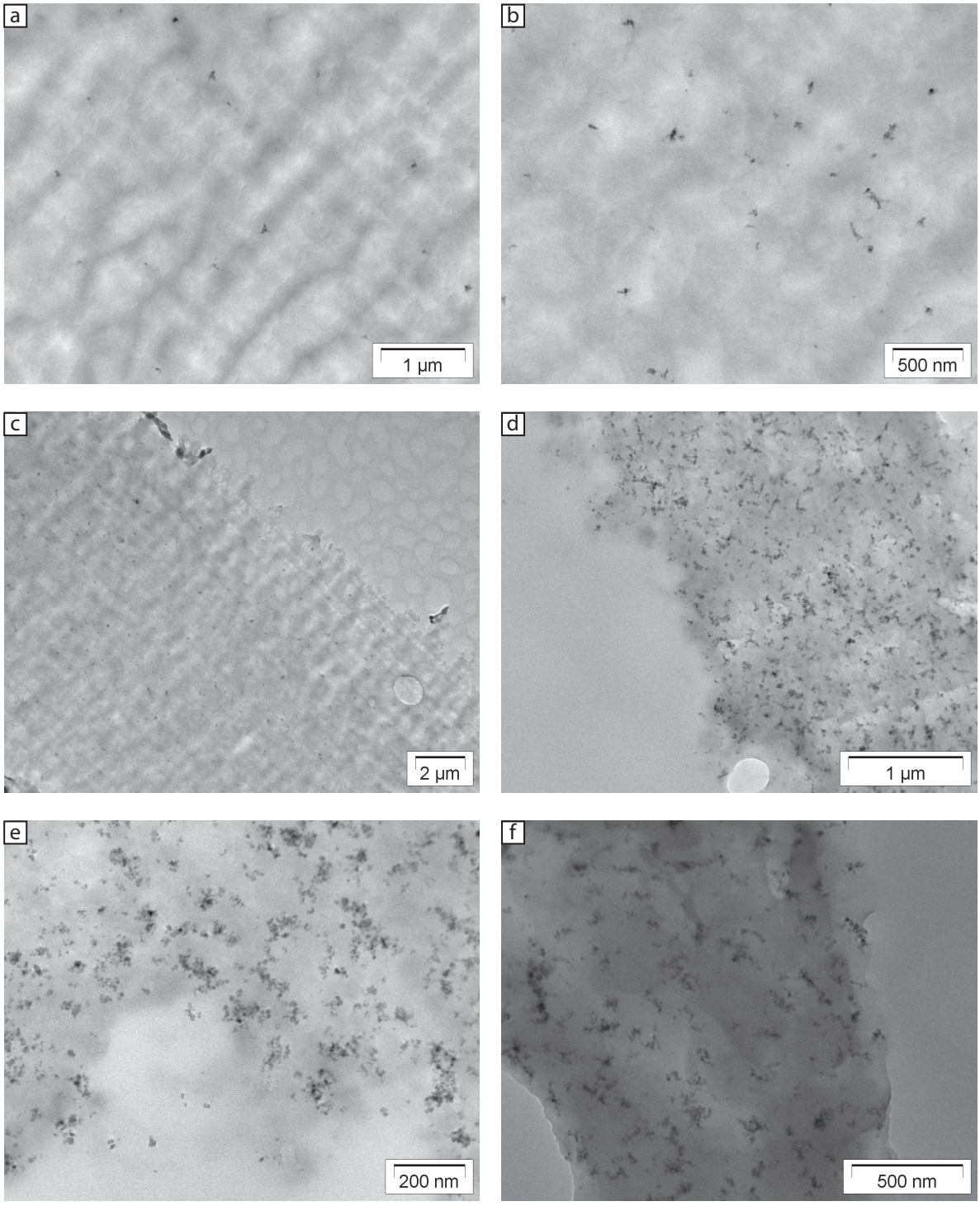

Figure 3.15. TEM images of a TPM gel with a high concentration of nanoparticles (FeTp7), showing small aggregates dispersed throughout the TPM gel. Images **(d)** and **(e)** suggest that a macroscopic phase segregation takes place, as in Figure 3.14. Nevertheless, all pictures display well dispersed small clusters, even in the concentrated regions.

TPM layer. Finally, the use of TPM ferrofluids to prepare functional gels was investigated. TPM gels with a variety of magnetic loadings could be prepared, although an increasing concentration of magnetic nanoparticles resulted in an increasing amount of irregularities. The nanoparticles are distributed throughout the TPM gel in small clusters, as observed from TEM images of sections of TPM gel. For high concentrations of nanoparticles, a segregation in clear TPM regions and regions with high concentrations of nanoparticles is observed. Despite this segregation, the distribution of small clusters of nanoparticles in the concentrated region is still rather homogeneous.

The preparation of stable functional ferrofluids is of great interest for material applications. The facile method to prepare TPM ferrofluids described here may be extended to other materials, since TPM is known to functionalize a variety of materials. Many applications may be envisioned, such as the preparation of thin magnetic polymer layers, although further research is required.

3.5. Acknowledgements

Chiara Cassarini and Joen Hermans are gratefully acknowledge for their experimental contributions. Hans Meeldijk is thanked for the sectioning of the TPM gels.

Part 2

Magnetic Nanoparticles

4

Single-Step and Seeded Growth Synthesis of Size Series of Iron Oxide Nanoparticles

Abstract

Several methods to synthesize size series of magnetic iron oxide nanoparticles are investigated. To obtain a low polydispersity in particle size, the syntheses are all by thermal decomposition of organometallic precursors in apolar solvents. The Hyeon method to synthesize monodisperse nanoparticles of tunable size in a single thermal decomposition step is investigated extensively, sometimes resulting in an extremely low polydispersity, but in general with poorly crystallized particles and limited control of the average size. The Klokkenburg method, a seed-mediated growth method, is modified and scaled up, and results in widespread twinning defects, which are attributed to the change in surfactant concentrations or the change in reducing agent. The Klokkenburg method is also reproduced in all its original details, resulting in faceted particles whose colloidal stability decreases when the average particle diameter reaches 20 nm.

4.1. Introduction

Magnetic nanoparticles offer a great potential for applications such as in the field of magnetic data storage, catalysis, and biomedicine [10, 11, 14, 16, 20, 22–24, 27, 28, 130, 131]. Not only are magnetic nanocrystals promising for many applications, but they can also be used as a model system for the study of dipolar interactions [63, 81, 132]. A variety of syntheses of magnetic nanocrystals has been reported in the last years, as discussed in a number of reviews (see for example [10, 11, 21, 23, 52–54]). Here, several methods to prepare a series of monodisperse magnetic nanoparticles with different sizes are investigated, to enable studies of the thermodynamics of magnetic colloids (see Chapter 8). Since the magnetic properties of the nanocrystals are strongly size dependent, it is important to prepare a series of differently sized particles in order to perform systematic studies as a function of the strength of their magnetic interactions, and the polydispersity of each system should be low.

A well-known method to prepare magnetic nanoparticles, such as magnetite (Fe_3O_4) and maghemite (γ-Fe_2O_3), is by aqueous co-precipitation of iron chloride salts [55, 56]. This aqueous method is simple and easily used on larger scales, but it has the main disadvantage that nucleation and growth of the nanocrystals are not separated in time, resulting in particles with a large polydispersity. To obtain monodisperse magnetic particles, nucleation and growth need to be separated, such that no new nuclei will be formed during the growth stage [133, 134].

The separation of nucleation and growth can be obtained in several ways in the preparation of nanocrystals. The well-known "hot injection" method [135] is widely used for a large variety of nanocrystals and understood using known principles from previous work on larger particles [133, 134]. In the hot-injection method, the precursor materials are quickly injected into a high temperature solvent, causing a large supersaturation, resulting instantaneously in a nucleation burst. This nucleation is quickly quenched due to the fast drop in temperature upon injection of the cooler precursor materials solution and the relief of the supersaturation by the nucleation burst. Subsequently, the size distribution is narrowed (focussed) during the diffusion-limited growth stage (for reasons explained in [4]), until the concentration of monomers comes below a critical threshold and broadening (defocussing) of the size distribution by Ostwald ripening takes place [52, 136–138].

A successful approach to prepare monodisperse iron oxide particles is the thermal decomposition of organometallic precursors in a high-boiling solvent containing stabilizing surfactants. For example, the method reported by Hyeon and coworkers can be used to prepare monodisperse iron oxide nanocrystals in a single step, in which the average particle diameter can be controlled through the boiling point of the solvent [58, 59]. Practically the same method was reported by Jana *et al.* [60]. It was shown by Hyeon's

group that this "heating up" method follows the same kinetics as the hot injection method described above, resulting in effective separation of nucleation and growth [59]. A short nucleation burst was found, followed by rapid growth of the nanocrystals while the size distribution was narrowing.

An alternative strategy to separate nucleation and growth is by physically separating the synthesis of nuclei and the growth of those nuclei to larger particles by using subsequent synthesis steps. In this so-called seed-mediated growth method, the seeds are prepared in a first synthesis step, followed by a number of growth steps to increase the particle size. The conditions in the growth steps (concentration of precursor and surfactants) are chosen such that no new nuclei will be formed. With increasing number of growth steps polydispersity decreases: as long as the monomer concentration is high enough, smaller particles will grow faster than larger particles, resulting in focussing of the size distribution [136]. Sun and co-workers reported a method to prepare iron oxide nanoparticles in the 4–20 nm size range by the reaction of iron(III) acetylacetonate with 1,2-hexadecanediol in the presence of surfactants. The larger particles could be obtained by seed-mediated growth [61, 62]. This method was modified by Klokkenburg *et al.* to obtain a series of nanoparticles with different sizes from seeded growth [63, 64]. The disadvantage of the seeded growth method is that it requires many synthesis steps to reach particle sizes of about 20 nm, whereas the absolute yield of particles is rather low.

In this chapter, three methods to prepare monodisperse nanoparticles are described and discussed. First, the method using the thermal decomposition of iron oleate from Hyeon and co-workers is investigated, which is labelled 'Hyeon method' in this chapter. The advantage of the Hyeon method is reportedly that particles with a very low polydispersities can be obtained in a single synthesis, in which the size can be controlled by simply varying the reaction conditions [58]. Second, the seed-mediated growth of Klokkenburg *et al.* [63, 64] is investigated using modifications to increase the scale of the synthesis using less expensive chemicals. This method is labelled 'twin method', since particles with twinning defects can be produced using this method. Finally, the original seed-mediated growth method from Klokkenburg *et al.* [63, 64] is revisited to prepare a size series of nanoparticles without twinning defects.

4.2. Experimental

4.2.1. Materials

Iron(III) chloride hexahydrate (SW* and RdG*: 95%, Fluka; AB*: 95%, Sigma), sodium oleate (95%, ABCR), ethanol (p.a., Merck), ethanol (technical, LP), acetone (technical, LP), n-hexane (p.a., Merck), 1-octadecene (90%, Sigma-Aldrich), 1-eicosene (90%, Sigma-Aldrich), trioctylamine (98%, Sigma-Aldrich or 99%, Fluka), technical grade oleic acid (techn 90%, Sigma-Aldrich), oleic acid p.a. (>99%, Sigma-Aldrich),

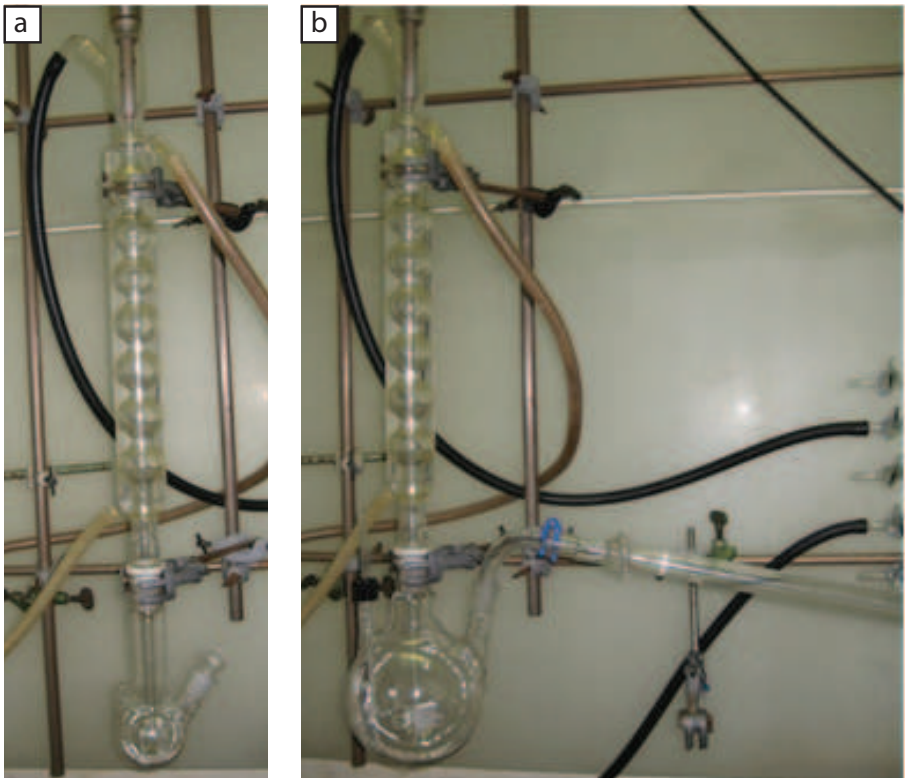

Figure 4.1. Picture of the setup used for the synthesis of the nanoparticles prepared by the Hyeon method (**a**), and in the degassing step of the twin method (**b**).

methanol (p.a., Baker), sodium hydroxide pellets (p.a., Fluka), decahydronaphtalene (decalin; mixture of cis and trans, >99%, Merck), iron(III) acetylacetonate ($Fe(acac)_3$; >99%, Acros), 1,2-dodecanediol (90%, Aldrich), 1,2-hexadecanediol (90%, Aldrich), oleyl amine (>70%, Fluka), phenyl ether (99%, Acros), nitric acid (65%, p.a., Merck), and hydrochloric acid (37%, p.a., Merck) were all used as received. In all experiments deionized water was used, obtained with a Millipore Synergy water purification system. Nitrogen atmosphere was applied using a Schlenk line.

* Codes SW, RdG, and AB refer to the chemists who performed the syntheses as indicated in the acknowledgements.

4.2.2. Hyeon method for preparation of iron oxide nanoparticles

Iron oxide nanocrystals were prepared using the thermal decomposition method described by the group of Hyeon [58, 59], scaled down by a factor of about 13. First, the iron oleate complex was prepared as the precursor for use in several syntheses of nanoparticles. Additionally, a similar method by Jana *et al.* [60] to prepare the precursor was investigated.

'Hyeon' precursor preparation. To prepare the iron oleate complex, typically 2.7 g (10 mmol) of iron(III) chloride hexahydrate and 9.125 g (30 mmol) of sodium oleate

were dissolved in mixture of 15 mL of water, 20 mL of ethanol and 35 mL of hexane. This orange solution was heated to 70 °C with an oil bath and refluxed at that temperature for 4 hours. After cooling down to room temperature, the top layer containing the iron oleate complex was washed three times with 10 mL of water in a separatory funnel. Subsequently, the hexane was removed by evaporation in a rotary evaporator, resulting in a brownish, viscous oil. This was dissolved in 1-octadecene (or another appropriate solvent) to prepare a stock solution with a final concentration of 0.4 M.

'Jana' precursor preparation. To prepare the precursor according to Jana *et al.* [60], 5.40 g (20 mmol) of iron(III) chloride hexahydrate and 15.2 g (54 mmol) of oleic acid were dissolved in 100 mL of methanol. A solution of 2.42 g (60 mmol) of NaOH in 200 mL of methanol was added to this mixture dropwise under magnetic stirring upon which a black precipitate was formed. The precursor was washed 4 times with methanol and dried under vacuum using a rotary evaporator. The iron oleate was dissolved in 1-octadecene to obtain a stock solution with a final concentration of 0.2 M.

Synthesis of nanoparticles. The setup used in the synthesis consisted of a two-necked round bottom flask with an Allihn condenser through which a long glass stirring rod reached into the flask, while being mechanically rotated from above beyond a rotary seal adapter with vacuum and nitrogen inlets. A Teflon sleeve was used to attach the condenser to the flask, to prevent the use of vacuum grease, which could contaminate the reaction mixture. The flask was also equipped with a glass inlet to avoid contact between the thermometer and the reaction mixture. A picture of the setup is shown in Figure 4.1a.

In a typical synthesis, 7.5 mL (3 mmol) of the iron oleate complex and 0.85 g (3 mmol) of oleic acid were mixed in 11.5 mL of 1-octadecene. This mixture was heated with a constant heating rate of 6 °C/min to degas at 120 °C for 1.5 hours under vacuum. Subsequently, the reaction mixture was heated to 320 °C under nitrogen atmosphere to reflux for 30 minutes. After cooling the black mixture to room temperature, the particles were washed 3 times by addition of ethanol, centrifugation at 2000 rpm (912 g) and redispersion in decalin. When particles did not precipitate but the sample phase separated into two liquid phases, an amount of cyclohexane was added equal to the amount of solvent present, upon which precipitation was continued as described above.

It has been reported that the size of the nanoparticles depends on the boiling point of the solvent [58], which we investigated for 3 different solvents here. The size of the nanocrystals has also been reported to be tunable by the amount of oleic acid used in the synthesis [58, 60]. We investigated this by varying the molar ratio of iron oleate to oleic acid, mostly keeping the amount of iron oleate constant. The variations for the different syntheses are given in Table 4.1. When the Jana precursor was used, 4 mL (0.8 mmol) of iron oleate stock solution was used in 16 mL of 1-octadecene.

Table 4.1. Synthesis details of the Hyeon method

Sample	Solvent	Amount of oleic acid (g) [a]	Molar ratio of iron oleate to oleic acid	Precursor method	Degassing step
SW1	1-octadecene	0.42 (p.a.)	1:0.5	Hyeon	no
SW2	1-octadecene	0.85 (p.a.)	1:1	Hyeon	no
SW5	1-octadecene	0.85	1:1	Hyeon	no
SW6	1-octadecene	1.70 (p.a.)	1:2	Hyeon	no
SW8	1-octadecene	2.45	1:3	Hyeon	no
SW9	1-octadecene	8.46	1:10	Hyeon	no
SW10	1-octadecene	4.26	1:5	Hyeon	no
SW11	1-octadecene	0.72	1:1	Hyeon	no
SW14	1-eicosene	0.88	1:1	Hyeon	no
SW15	trioctylamine	0.96	1:1	Hyeon	no
SW18	1-octadecene	1.47	1:1	Hyeon	no
SW20	1-octadecene	0.73	1:3	Jana	yes
SW21	1-octadecene	1.09	1:5	Jana	yes
SW24	tricotylamine	0.85	1:1	Hyeon	yes
SW25	tricotylamine	0.86	1:1	Hyeon	yes
RdG2	trioctylamine	0.85	1:1	Hyeon	yes
AB-NP01	1-octadecene	0.84	1:1	Hyeon	yes
AB-NP03	1-octadecene	0.87	1:1	Hyeon	yes
AB-NP05	1-octadecene	0.86	1:1	Hyeon	yes
AB-NP06	1-octadecene	0.90	1:1	Hyeon	yes

[a] (p.a.) indicates that oleic acid p.a. (>99%) was used. For all other syntheses, technical grade oleic acid (techn. 90%) was used.

4.2.3. Twin method for preparation of iron oxide nanoparticles

A size series of magnetic nanoparticles with well-defined magnetic properties can be prepared by a seeded growth method [61–64]. However, the yield of this procedure is rather low whereas it takes many synthesis steps to obtain particles up to 20 nm in diameter. Therefore, this method was modified to produce particles on a larger scale, using less expensive chemicals. Small seeds are prepared in the first step, which are subsequently grown in a number of repeated steps. The modifications to the original procedure by Mark Klokkenburg are indicated below by (*modifications*). These modifications were tested using a few growth steps before a whole size series was prepared.

The setup used in the synthesis was essentially the same as for the Hyeon method (Section 4.2.2), but with a larger flask. During the degassing step (see below), a condenser was attached to the second neck of the flask as an exit for the nitrogen flow coming from the Allihn condenser, as shown in Figure 4.1b.

Seed particles of a few nanometers in size were prepared by mixing 7.06 g (20 mmol) of $Fe(acac)_3$, 20.23 g (100 mmol) of 1,2-dodecanediol (*modification*), 16.90 g (60 mmol) of technical grade oleic acid (*modification*), and 16.04 g (60 mmol) of oleyl amine in 200 mL of phenyl ether. This reaction mixture was heated to 200 °C under nitrogen flow to degas the dispersion for 30 minutes (*modification*). Subsequently, the mixture was heated to reflux temperature (around 260 °C) for another 30 minutes under nitrogen atmosphere. The resulting seed solution was washed by precipitation with 100 mL ethanol and 30–40 minutes of centrifugation at 2000 rpm (912 g).

The iron oxide particles were grown in repeated seeded growth steps by redispersing the particles in hexane and transferring to a reaction flask containing 7.06 g (20 mmol) of $Fe(acac)_3$, 20.23 g (100 mmol) of 1,2-dodecanediol (*modification*), 5.63 g (20 mmol) of technical grade oleic acid (*modification*), and 5.35 g (20 mmol) of oleyl amine in 200 ml of phenyl ether. The mixture was heated to 200 °C under nitrogen flow for 30 minutes of degassing in which also the hexane was removed (*modification*). Subsequently, the mixture was heated to reflux temperature to reflux for 30 minutes under nitrogen atmosphere. The particles were washed by precipitation using ethanol and centrifugation if necessary, and redispersion in hexane if the next growth step was not done within a day. In later growth steps, particles were stored in decalin for improved stability and transferred to hexane just before the next growth step. Also an attempt was made to store the sample in phenyl ether by crystallization of the solvent, but not all phenyl ether crystallized for these large reaction volumes. If it was difficult to redisperse the particles, a small amount of oleic acid was added and occasionally ultrasonication was used. Since after a certain number of growth steps the particles did not seem to grow any further, the amount of surfactants was decreased to 10 mmol. After each synthesis step 10% of the reaction mixture was taken out for storage in phenyl ether under nitrogen atmosphere at 4 °C at which temperature phenyl ether is solid. In Table 4.2 the variations of the growth steps for this synthesis (RdG series 15) are indicated.

A second seeded growth series was started as well. In this synthesis, the seeds were washed 3 times before the first growth step was initiated. After each growth step, 20% of the reaction mixture was taken out for storage. Further variations in the growth steps of this synthesis (RdG series 16) are shown in Table 4.3.

Table 4.2. Growth steps of the first series of twin-particles (RdG series 15). The amounts of oleic acid and oleyl amine used in each growth step are indicated, as well as the amount of oleic acid that was added in the washing step.

Growth step	Amount of oleic acid (g)	Amount of oleyl amine (g)	Oleic acid for redispersion	Remarks
15.1	5.68	5.39	none	
15.2	5.68	5.35	none	
15.3	5.64	5.45	none	
15.4	5.64	5.40	none	
15.5	5.64	5.37	none	
15.6	5.69	5.35	none	
15.7	5.68	5.40	none	
15.8	5.64	5.35	none	
15.9	5.69	5.35	none	
15.10	5.73	5.36	none	no N_2 atmosphere reaction was stopped prematurely
15.11	5.63	5.50	none	
15.12	5.68	5.35	none	
15.13	5.64	5.35	none	
15.14	5.85	5.45	400 μL	
15.15	5.68	5.35	none	
15.16	5.78	5.36	none	
15.17	5.64	5.35	none	
15.18	5.64	5.35	800 μL	
15.19	5.74	5.40	800 μL	
15.20	5.72	5.40	none	
15.21	2.82	2.69	400 μL	
15.22	2.84	2.69	1 mL	
15.23	2.85	2.68	800 μL	400 μL oleyl amine used for redispersion
15.24	2.81	2.72	none	
15.25	2.84	2.66	none	
15.26	2.86	2.74	none	
15.27	2.84	2.67	none	Redispersion problems

Table 4.3. Growth steps of the second series of twin-particles (RdG series 16). The amounts of oleic acid and oleyl amine used in each growth step are indicated, as well as the amount of oleic acid that was added in the washing step.

Growth step	Amount of oleic acid (g)	Amount of oleyl amine (g)	Oleic acid for redispersion	Remarks
16.1	5.68	5.39	none	
16.2	5.65	5.37	none	
16.3	5.69	5.65	none	
16.4	5.67	5.35	none	
16.5	5.66	5.37	none	
16.6	5.90	5.50	none	
16.7	5.64	5.34	none	
16.8	5.83	5.35	none	
16.9	5.75	5.35	400 μL	
16.10	2.93	2.72	400 μL	
16.11	2.91	2.66	800 μL	200 μL oleyl amine used for redispersion
16.12	2.90	2.67	400 μL	
16.13	2.88	2.76	none	
16.14	2.83	2.64	none	
16.15	3.00	2.69	none	
16.16	2.68	2.69	none	

Table 4.4. Growth steps of revisited Klokkenburg synthesis, RdG series 17. The amounts of oleic acid and oleyl amine used in each growth step are indicated, as well as the amount of ethanol used for precipitation of the particles.

Growth step	Amount of oleic acid (mL)	Amount of oleyl amine (mL)	Amount of ethanol (mL)	Remarks
17.1	0.19	0.19	5	
17.2	0	0	3	
17.3	0	0	3	
17.4	0.19	0.19	0	
17.5	0.38	0.38	0	
17.6	0.38	0.38	0	
17.7	0.095	0.095	0	
17.8	0.095	0.095	0	
17.9	0.19	0.19	3	
17.10	0.38	0.38	7	
17.11	0.38	0.38	0	
17.12	0.19	0.19	0	
17.13	0.19	0.19	0	
17.14	0.19	0.19	0	
17.15	0.19	0.19	0	
17.16	1.9	1.9	0	(sample unstable)

4.2.4. Klokkenburg method for preparation of iron oxide nanoparticles

The synthesis as described by Klokkenburg *et al.* was reproduced [63,64,139]. Before synthesis, glassware was cleaned with *aqua regia*, a mixture of concentrated nitric acid and concentrated hydrochloric acid with molar ratio 1:3. The acid was removed by rinsing with water and subsequent rinsing with acetone to remove water traces. Finally, vacuum was applied to the setup and the glass was heated with a Bunsen burner for several seconds until all condensation from acetone had dissappeared and the setup was put under nitrogen atmosphere.

In a typical synthesis of seed particles, 0.706 g (2 mmol) of $Fe(acac)_3$ was added to the reaction flask via a funnel after which 10 mL of phenyl ether was added. Once the $Fe(acac)_3$ had dissolved, 2.85 g (10 mmol) of 1,2-hexadecanediol was added. Subsequently, 1.90 mL (6 mmol) of oleic acid and 1.93 mL (6 mmol) of oleyl amine were added under nitrogen flow, after which the flow was stopped and the setup was kept under a nitrogen atmosphere. The reaction mixture was heated to reflux at the maximum rate possible (in 10–15 minutes) using a 3-level heating mantle at level 3, and kept at reflux temperature (around 260 °C) for 30 minutes. The heating mantle was

Table 4.5. Growth steps of revisited Klokkenburg syntheses, RdG series 18–20. The amounts of oleic acid and oleyl amine used in each growth step are indicated, as well as the amount of ethanol used for precipitation of the particles.

Growth step	Amount of oleic acid (mL)	Amount of oleyl amine (mL)	Amount of ethanol (mL)	Remarks
18.1	0	0	3	
18.2	0.095	0.095	0	
18.3	0.095	0.95	0	20 % of sample taken
18.4	0.095	0.095	0	(secondary nucleation)
18.5	0.095	0.095	0	(secondary nucleation)
19.1	0	0	2	
19.2	0	0	0	
19.3	0.095	0.095	0	20 % of sample taken
19.4				leaking setup
20.1	0	0	2	
20.2	0	0	0	
20.3	0.095	0.095	0	
20.4	0.095	0.95	0	20 % of sample taken
20.5	0.095	0.095	0	
20.6	0.19	0.19	2	
20.7	0.19	0.19	0	
20.8	0.19	0.19	0	20 % of sample taken
20.9	0.19	0.19	0	20 % of sample taken
20.10	0.38	0.38	0	some aggregates were removed (unstable, only top layer of dispersion used for growth)
20.11	0.19	0.19	0	(unstable)

removed, and after cooling of the reaction mixture the particles were precipitated on a magnet using 5 mL of ethanol.

To grow larger particles, the seed particles were redispersed in 10 mL of phenyl ether and added to 0.706 g (2 mmol) of $Fe(acac)_3$ in the reaction flask. Once the $Fe(acac)_3$ was dissolved, 2.85 g (10 mmol) of 1,2-hexadecanediol and another 10 mL of phenyl ether were added. The nitrogen flow was applied, and different amounts of oleic acid and oleyl amine were added as indicated in Table 4.4, after which the flow was stopped and the setup was kept under a nitrogen atmosphere. In the first growth steps, little to no surfactants were added, to prevent secondary nucleation. In later growth steps, the amount of surfactants was chosen based on the amount of ethanol used to precipitate

the particles after the preceding growth step [139], since ethanol is known to desorb surfactant molecules from the nanoparticles [140]. The reaction mixture was heated very slowly (in 45–60 minutes) to the reflux temperature, at which it was kept for 30 minutes. The particles were washed using a minimal amount of ethanol to precipitate the particles on a magnet and redispersed in 10 mL of phenyl ether for the next growth step using 10 seconds of ultrasonication.

Several series of the Klokkenburg synthesis were performed for which the varying parameters are given in Tables 4.4 and 4.5. In RdG series 17, a 1.3 T hand-held permanent magnet was used for precipitation of the particles, which was replaced by a 0.1 T hand-held permanent magnet in RdG series 18–20. In RdG series 18–20 occasionally a sample of 20% of the reaction volume was taken out, as indicated in Table 4.5.

4.2.5. Characterization

Transmission Electron Microscopy (TEM) was performed using a Philips Tecnai 10 or Tecnai 12, typically operating at 100 kV or 120 kV, respectively. TEM samples were prepared by drying a drop of diluted dispersion on a formvar-coated copper grid. Particle diameter and polydispersity (standard deviation divided by average size) were determined by analysis of at least 100 particles from the TEM images.

4.3. Results and discussion

4.3.1. Hyeon method

Iron oxide nanoparticles were prepared in a single step using the thermal decomposition method of Hyeon's group [58, 59], sometimes yielding monodisperse spherical particles (Figure 4.2a–b), but also polydisperse particles (Figure 4.2c–d). We performed many syntheses varying several parameters, as summarized in Table 4.6 together with the resulting average particle diameters and polydispersities. It should be noted that in the synthesis of SW21 (Table 4.6) cubic particles were found, but these could not be reproduced. Although monodisperse particles were obtained in several syntheses, the control over the average particle size as reported by Hyeon and co-workers could not be reproduced by us.

According to Park *et al.*, the diameter of the particles can be tuned via the boiling point of the solvent [58]. Here, we indeed found larger particles when 1-eicosene (bp = 330 °C) or tricotylamine (bp = 365 °C) were used as a solvent in comparison to 1-octadecene (bp = 317 °C). However, the spread in particles sizes for one particular solvent is large and it proved difficult to reproduce a specific average particle diameter.

It has also been reported that the amount of oleic acid can be used to control the average particle diameter [58, 60]. Here, this was investigated by varying the molar ratio of iron oleate to oleic acid, keeping the amount of iron oleate constant. However, even when the molar ratio of iron oleate to oleic acid is increased by a factor of 20

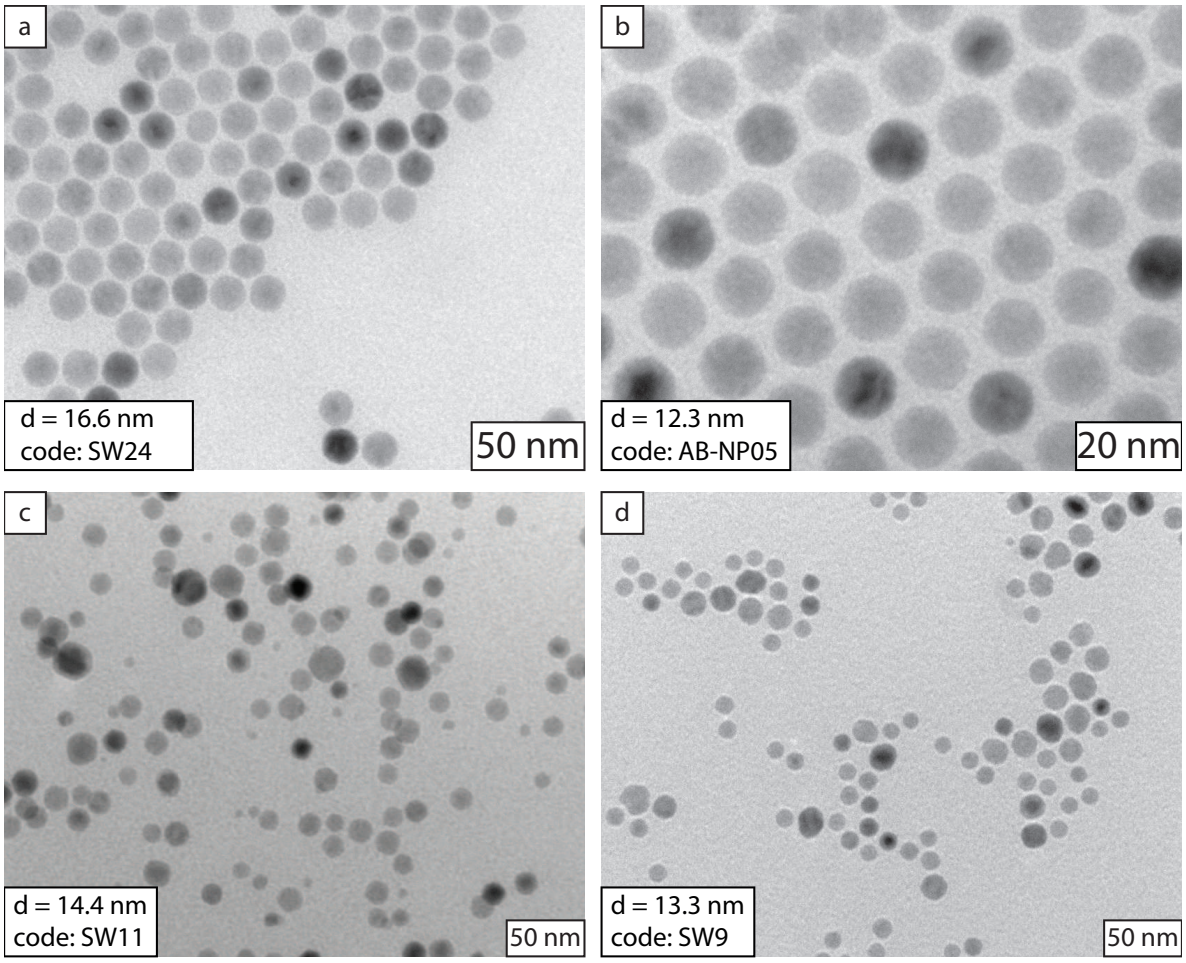

Figure 4.2. TEM images of iron oxide particles prepared by the Hyeon method that have a low polydispersity (**a**–**b**, both 3.5 %) and a high polydispersity (**c**, 23.6 %, and **d**, 16.7 %).

from 1:0.5 (SW1) to 1:10 (SW9), hardly any change in average particle diameter was observed, whereas reproducing a specific experiment resulted in a much larger variation in particle size. Thus, no correlation between the amount of oleic acid and the particle diameter seems to be present. Additionally, no significant difference between the use of technical grade oleic acid or p.a. oleic acid was found. The use of the precursor prepared by the method of Jana *et al.* [60] as described in Section 4.2.2 does not seem to have a significant influence on the size of the nanoparticles either. Variations of other parameters, such as the concentration of iron oleate all resulted in higher polydispersity (not shown).

One possible explanation for the difficulties in reproducibility may be the difference in heating rate of the reaction mixture. Hyeon *et al.* reported a specific heating rate of 3.3 °C/min [58, 59], whereas the heating rate in our experiments was higher (on the order of 6 °C/min) and without the use of a temperature controller. The lack of precise

Table 4.6. Overview of the main parameters in the synthesis using the Hyeon method and the resulting average particle diameters and polydispersities.

Sample	Solvent	Molar ratio iron oleate to oleic acid	Degassing step	Diameter (nm)	Polydispersity (%)
SW1	1-octadecene	1:0.5	no	11.5	20.4
SW2	1-octadecene	1:1	no	10.4	12.3
SW5	1-octadecene	1:1	no	16.3	11.4
SW6	1-octadecene	1:2	no	14.9	20.6
SW8	1-octadecene	1:3	no	11.5	15
SW9	1-octadecene	1:10	no	13.3	16.7
SW10	1-octadecene	1:5	no	11.4	13.9
SW11	1-octadecene	1:1	no	14.4	23.6
SW14	1-eicosene	1:1	no	19.6	11.6
SW15	trioctylamine	1:1	no	22.9	12.5
SW18	1-octadecene	1:1	no	10.7	11.3
SW20	1-octadecene	1:3	yes	8.4	8.8
SW21	1-octadecene	1:5	yes	11.9	9.4
SW24	tricotylamine	1:1	yes	16.6	3.5
SW25	tricotylamine	1:1	yes	16.3	5.7
RdG2	trioctylamine	1:1	yes	19.5	4.6
AB-NP01	1-octadecene	1:1	yes	6.4	9.7
AB-NP03	1-octadecene	1:1	yes	4.6	13.2
AB-NP05	1-octadecene	1:1	yes	12.3	3.5
AB-NP06	1-octadecene	1:1	yes	5.2	9.5

control over the heating rate may have an important influence on the resulting particle sizes. For example, in a study by Bronstein *et al.* [141] the iron oleate precursor was prepared using different methods, resulting in different thermal characteristics, which has an important influence on the size and polydispersity of the particles. Thus, it may very well be that control over the heating rate is crucial for the reproducibility of the synthesis.

Another important factor in the Hyeon method is the degassing of the reaction mixture prior to the thermal decomposition. In a more recent paper by the group of Hyeon about their synthesis it was reported that *"the reaction mixture was degassed under vacuum at 120 °C for 1.5 h"*, prior to the addition of iron-oleate complex and heating to reflux temperature [59]. Therefore, we applied the degassing procedure starting from the synthesis of SW20 and onwards (see Table 4.6), although in our case all reactants were mixed before the degassing step. This degassing step removes impurities such as oxygen and water from the solvent, which is observable by initial bubbling of the solvent under vacuum. Clearly, the polydispersity is significantly lower after applying

the degassing step (see Table 4.6), and the particles with lowest polydispersities were only obtained if this degassing step was applied.

Despite the difficulties with the reproducibility of the synthesis, monodisperse iron oxide nanoparticles of several sizes have been prepared successfully. However, the magnetic properties of the larger nanoparticles are not as expected for particles of this size, as discussed in Chapter 5. While particles of 8 nm in diameter still have magnetic properties on the order of magnitude expected for magnetic iron oxide, for an increasing size of nanoparticles an increasingly large discrepancy was found between the size obtained from TEM and the size from magnetic measurements. Moreover, the larger particles had a higher polydispersity in magnetic size, despite their low polydispersity in geometric size. This is attributed to crystal defects in the larger particles, as shown in Chapter 5.

A possible explanation for the increasing amount of crystal defects in larger particles may be found in the synthesis procedure of these particles. All the nanocrystals prepared by this method are prepared in one step, regardless of their size. As shown by Kwon *et al.*, both nucleation and growth of these particles occur very rapidly [59]. This gives the particles a short time to crystallize. Particles of 8 nm may still have sufficient time to crystallize well, but as the final particle size increases defects are incorporated, which disrupt the magnetic properties of the particles. In contrast, nanoparticles in a seeded growth method have much more time to crystallize, since the particles are grown in an epitaxial manner by a large number of growth steps. This method is further discussed in the next sections.

4.3.2. Twin method

Since the seed-mediated growth procedure [61–64] is very laborious, attempts were made to increase the scale of the synthesis by a factor of 10, and samples were taken from each synthesis to obtain a series of magnetite particles with increasing size.

The obtained sizes as determined by TEM for RdG series 15 and 16 are shown in Figure 4.3, displaying the stepwise seeded growth. Particles with a diameter of 20 nm were prepared in more than 25 growth steps. Since the growth of the particles appeared to stagnate at a diameter of about 14 nm, the amount of surfactants was halved from 15.21 and onwards. If the particles are strongly stabilized by the surfactants and an excess of surfactants is present, there is a larger probability that secondary nuclei are formed. Indeed, upon decrease of the surfactant concentration the particles were grown larger again.

In Figure 4.4 a selection of TEM images of RdG series 15 is shown. Interestingly, the particles of 20 nm appear to have twinning defects, dividing the particles in 2 or 3 crystalline domains. In retrospect, these defects can also be observed for the smaller particles, although it is more difficult to distinguish. In Chapter 5 it is shown that

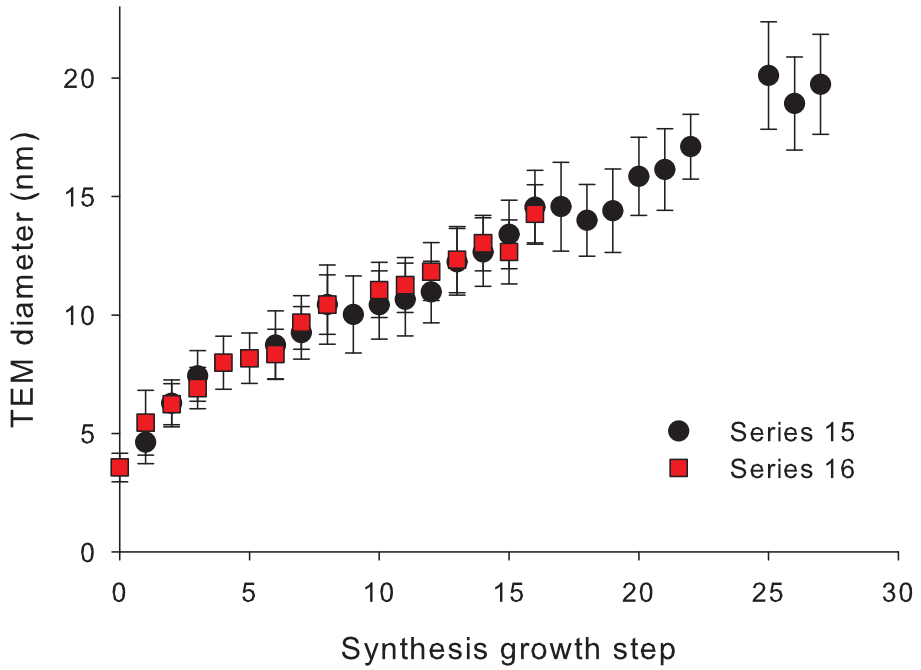

Figure 4.3. Average diameter from TEM versus the synthesis growth steps for magnetite synthesis series 15 (dots) and 16 (squares). The error bars indicate the standard deviation in TEM size.

indeed the crystalline size obtained from XRD is much smaller than the size from TEM. Moreover, these particles have a magnetic size that is considerably smaller than the geometric size from TEM, and the polydispersity in magnetic size (40%) is much larger than the polydispersity resulting from TEM measurements (11%). These differences clearly result from the observed twinning defects.

The same twinning defects are observed for RdG series 16, as shown by TEM in Figure 4.5, which shows the reproducibility of these nanocrystals. The synthesis procedure of these twins is very similar to the synthesis of Klokkenburg *et al.* [63], although some modifications were made to scale the procedure up. The influence of these modifications in increasing the scale of the synthesis was investigated by doing several syntheses of seeds and a few subsequent growth steps before starting a whole series. However, for such small particles, twinning defects are either not present yet, or hardly distinguishable from TEM. To obtain more insight into the origin of the twinning defects, the major differences with the original procedure are now discussed.

In our synthesis, the procedure from Klokkenburg was scaled up by a factor of 10. Although this should in principle not modify the chemistry of the synthesis, it will have scale effects on parameters such as the heat distribution throughout the reaction flask, the mixing of reactants, etcetera. In retrospect, the heating rate was also higher in our

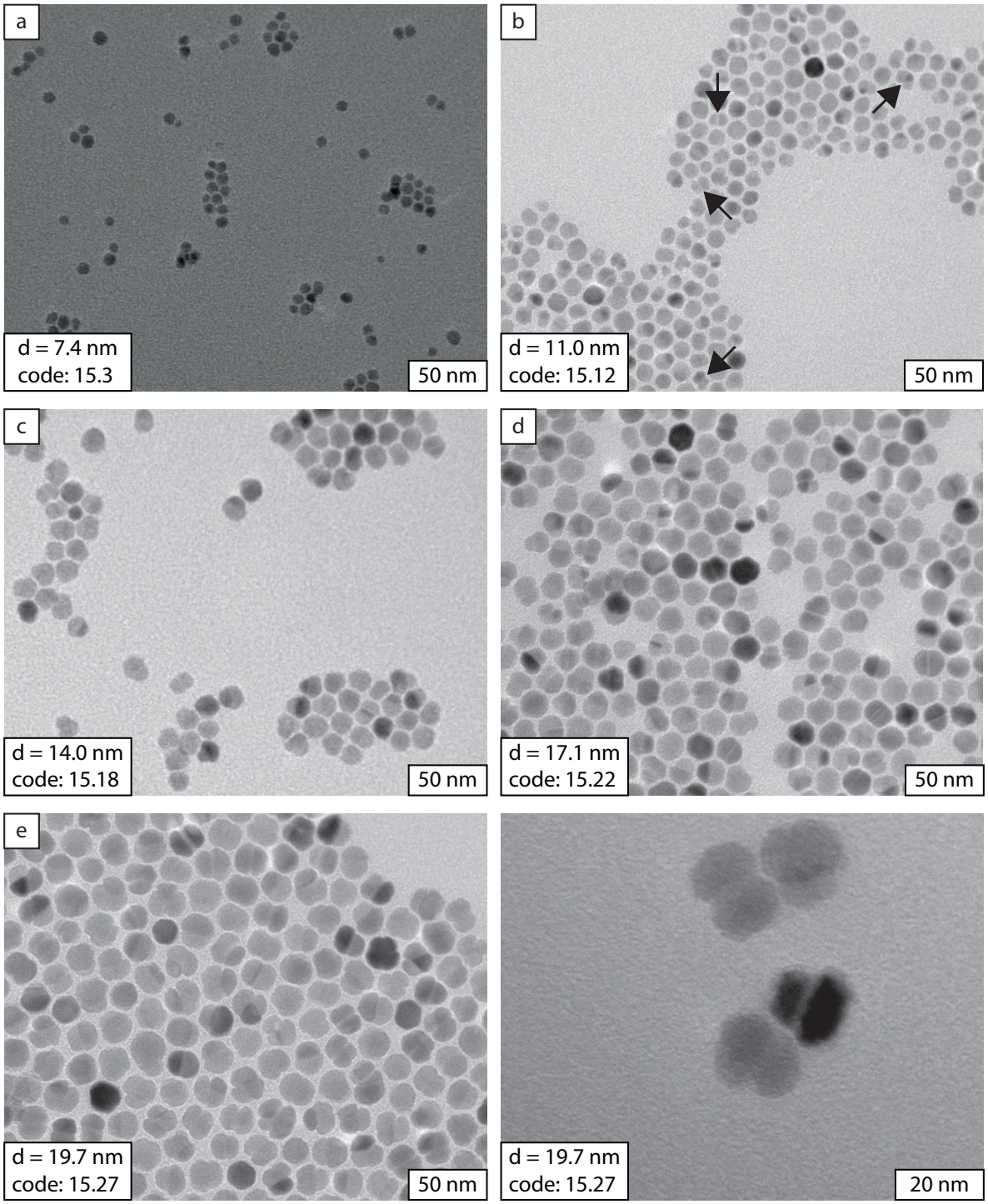

Figure 4.4. TEM pictures of iron oxide nanoparticles prepared by the twin method, RdG series 15, with increasing size as indicated. Twinning defects are visible already at smaller particle sizes, but difficult to distinguish (some defects are indicated by black arrows in (b)), whereas twinning defects are more pronounced for the larger particles.

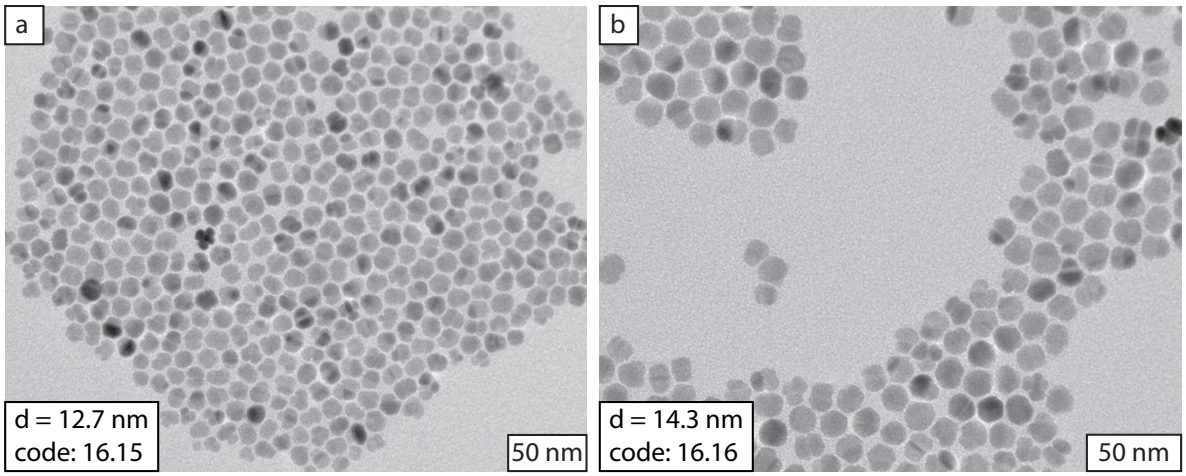

Figure 4.5. The twinning defects are also visible in the TEM images of iron oxide nanoparticles prepared by the twin method, RdG series 16.

synthesis during the growth steps compared to the original procedure [139], which can have a significant effect on the synthesis of nanocrystals as discussed in Section 4.3.1.

A major difference between the synthesis methods is the use of a degassing step in our synthesis. In the original synthesis, glassware was dried under vacuum by using a Bunsen burner at the outside of the set up. The synthesis as reported by Klokkenburg *et al.* [63,64] was based on a publication by Sun and Zeng [61]. However, in a subsequent publication a few years later, that same group reported that "*the key to the success of making monodisperse nanoparticles is to heat the mixture to 200 °C first and remain at that temperature for some time before it is heated to reflux at 265 °C in phenyl ether...*" [62]. This degassing procedure step was investigated by us in preliminary experiments and seemed to decrease polydispersity.

Several changes were made in the chemicals used, primarily to avoid the high costs of the chemicals used in ref [64]. First, instead of oleic acid with 99% purity as used by Klokkenburg *et al.*, here technical grade oleic acid was used since no influence of the somewhat lower purity was observed previously (Section 4.3.1). Second, 1,2-dodecanediol was used as a reductor instead of 1,2-hexadecanediol. Both are mild reducing agents in the reaction, and according to Sun *et al.* both react well with iron(III) acetylacetonate to form magnetite nanoparticles [62]. Since preliminary experiments showed no difference, 1,2-dodecanediol was used in all experiments. However, in a recent report [142] on the preparation of gold-copper nanocubes, it was found that the length of the carbon chain of the diol is important in the preparation of the nanocubes: if hexanediol was used instead of 1,2-hexadecanediol no cubes were formed, and if 1,2-dodecanediol was used, branched particles with a only small amount of nanocubes were obtained. Apparently a small difference in hydrocarbon chain length

can make a significant difference. Moreover, when the co-reducing agent in their synthesis, 1-dodecanethiol, was not used, nanocrystals with multiple twinning defects were found [142]. Thus, the change of reductor may very well be at the origin of the observed twinning defects in our magnetite nanocrystals.

Another important parameter in the synthesis of nanocrystals is the amount of surfactants. It is well known from the literature that the type and amount of surfactants can have a significant influence on the shape of nanocrystals [138, 143, 144]. Here, the amounts of surfactants in the growth steps were lowered by a factor of 3 compared to literature [63], although in the first growth steps Klokkenburg used even smaller amounts of surfactants to prevent secondary nucleation [139]. Moreover, after synthesis the particles were rinsed extensively using ethanol, which is known to desorb surfactant molecules from the nanoparticles [140]. This may cause aggregation between two particles insufficiently stabilized by the steric surfactant barrier. Such particles might result in the particles with twinning defects upon growth.

In conclusion, particles with twinning defects can be reproducibly made using our twin method. These twinning defects arise from differences with the original synthesis by Klokkenburg and are most likely due to the change in reductor or the surfactant concentration. To clarify the origin and precise nature of these twinning defects more systematic investigation would be required.

4.3.3. Klokkenburg method

To prepare a size series of iron oxide nanoparticles without twinning defects, the Klokkenburg method was repeated in the same way as originally done by Klokkenburg, including the cleaning of glassware and the order of addition of chemicals [64, 139]. Several series were started, and the resulting particle sizes obtained from TEM are shown in Figure 4.6. Here, a particle size of 20 nm is obtained after 14 growth steps, the same number of steps required by Klokkenburg [64]. Interestingly, RdG series 18 seemed to grow much faster, which can be explained by the larger seeds formed in the first synthesis step: the same amount of material was used, so the number of seeds had to be considerably smaller, which increased the growth rate in subsequent steps. However, this also implies that less surfactant per particle was required, whereas similar amounts were used. The larger excess of surfactant may explain the secondary nucleation observed in the fourth growth step (see Figure 4.8b).

A representative selection of TEM images of RdG series 17 is shown in Figure 4.7, and TEM images of RdG series 18–20 are shown in Figure 4.8. Clearly, these particles look different than the twins in Figures 4.4 and 4.5. The shape of the particles prepared by the Klokkenburg method is faceted, resembling the particles prepared previously [64], contrary to the more rounded shapes of the twins. This shows that the Klokkenburg

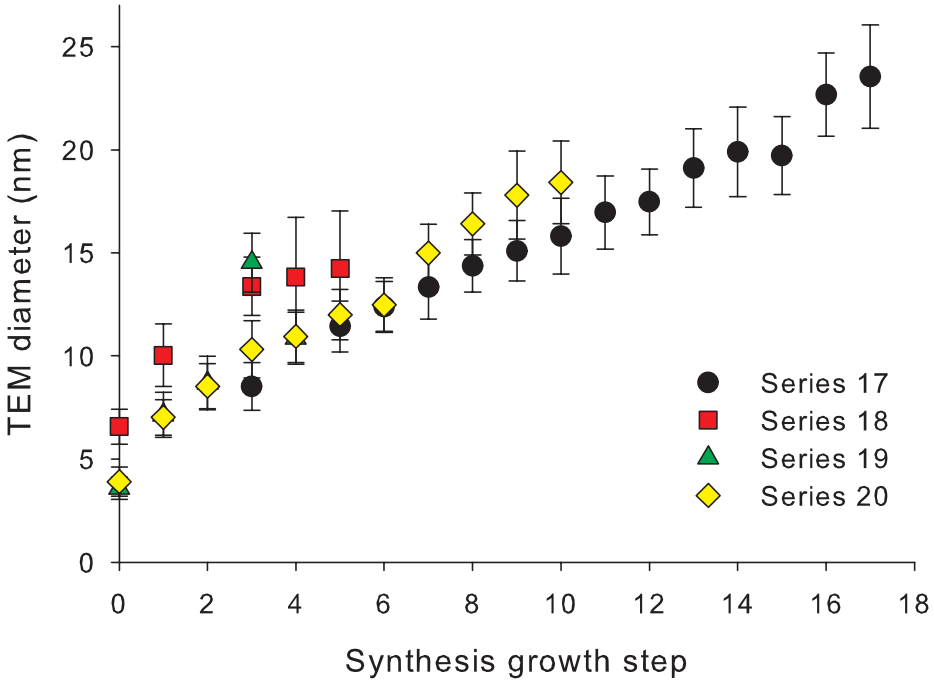

Figure 4.6. Average diameter from TEM versus the synthesis growth step for magnetite synthesis series 17 (dots), series 18 (squares), series 19 (triangles) and series 20 (diamonds). The error bars indicate the standard deviation in TEM size.

method has been reproduced. Nevertheless, the TEM images suggest that some particles in these series may have twinning defects as well. In most cases this is seen as a line that goes through the middle of the particle, which may also be explained by the faceted shape where such a line represents the edge of 2 facets, not a twinning defect. Since the total absence of defects cannot be excluded from these pictures, the crystallinity of these particles was investigated by XRD. From XRD the average crystalline size can be determined, which will be significantly reduced if twinning defects are present. XRD measurements were performed using particles of 23.5 nm from RdG series 17. From the diffraction pattern (see Chapter 5, Figure 5.7) an average crystallite size of 18 nm was determined, which is close to the TEM size, confirming the single crystalline nature of the particles.

Although the Klokkenburg method has been successfully reproduced, it was observed that upon increasing the size of the nanocrystals, colloidal stability decreased. This may result from the increasing interactions between the nanoparticles, although this cannot be quantified by magnetic measurements due to the lack of stable colloidal dispersions of the largest particle sizes. In the synthesis of RdG series 17, a strong 1.3 T magnet was used to destabilize the particles during washing steps, possibly resulting in irreversible aggregation. Therefore, in the purification steps of RdG series 18–20 a 0.1 T magnet was

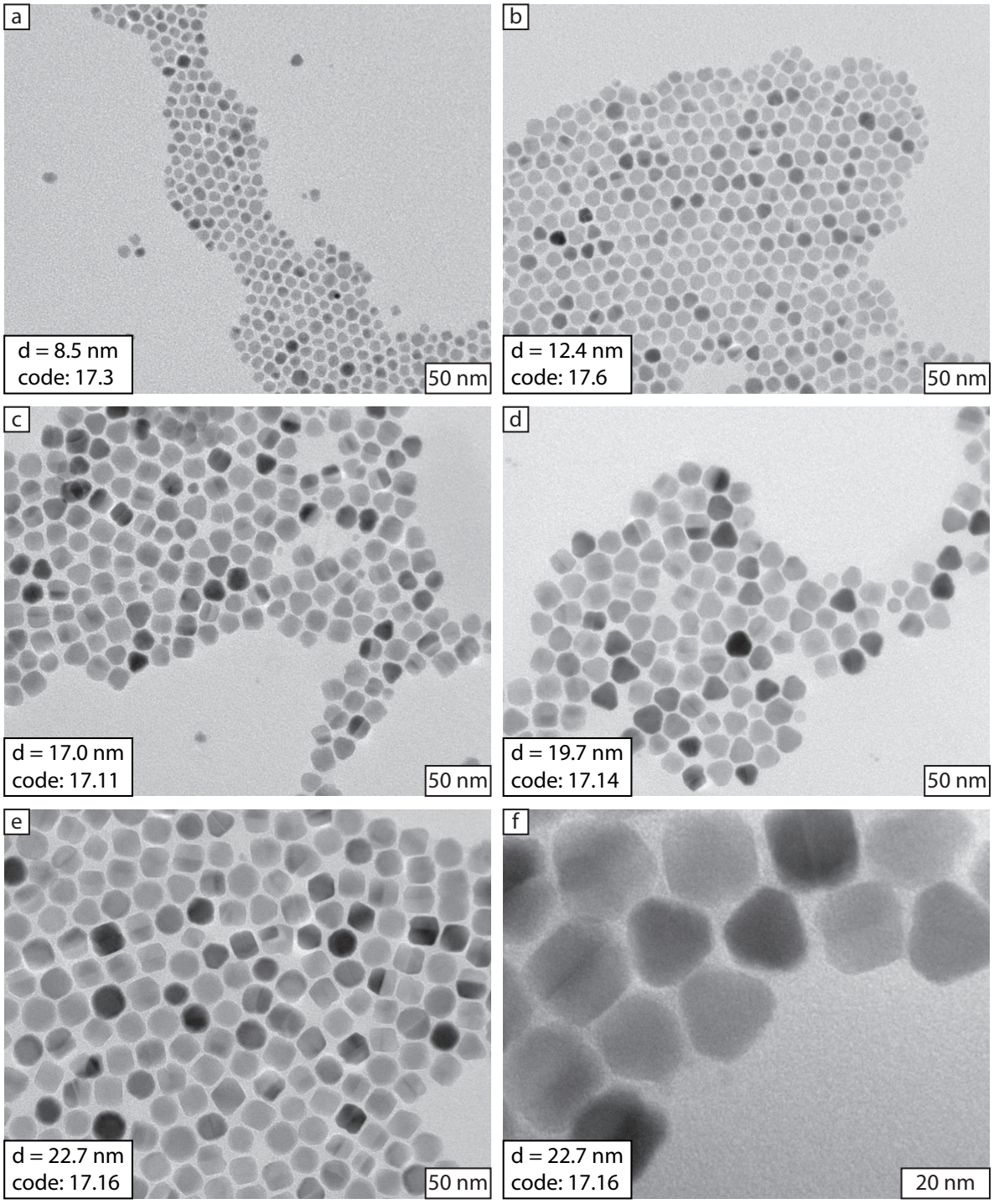

Figure 4.7. TEM pictures of iron oxide nanoparticles prepared by the Klokkenburg method, RdG series 17, with increasing diameters as indicated in the figure.

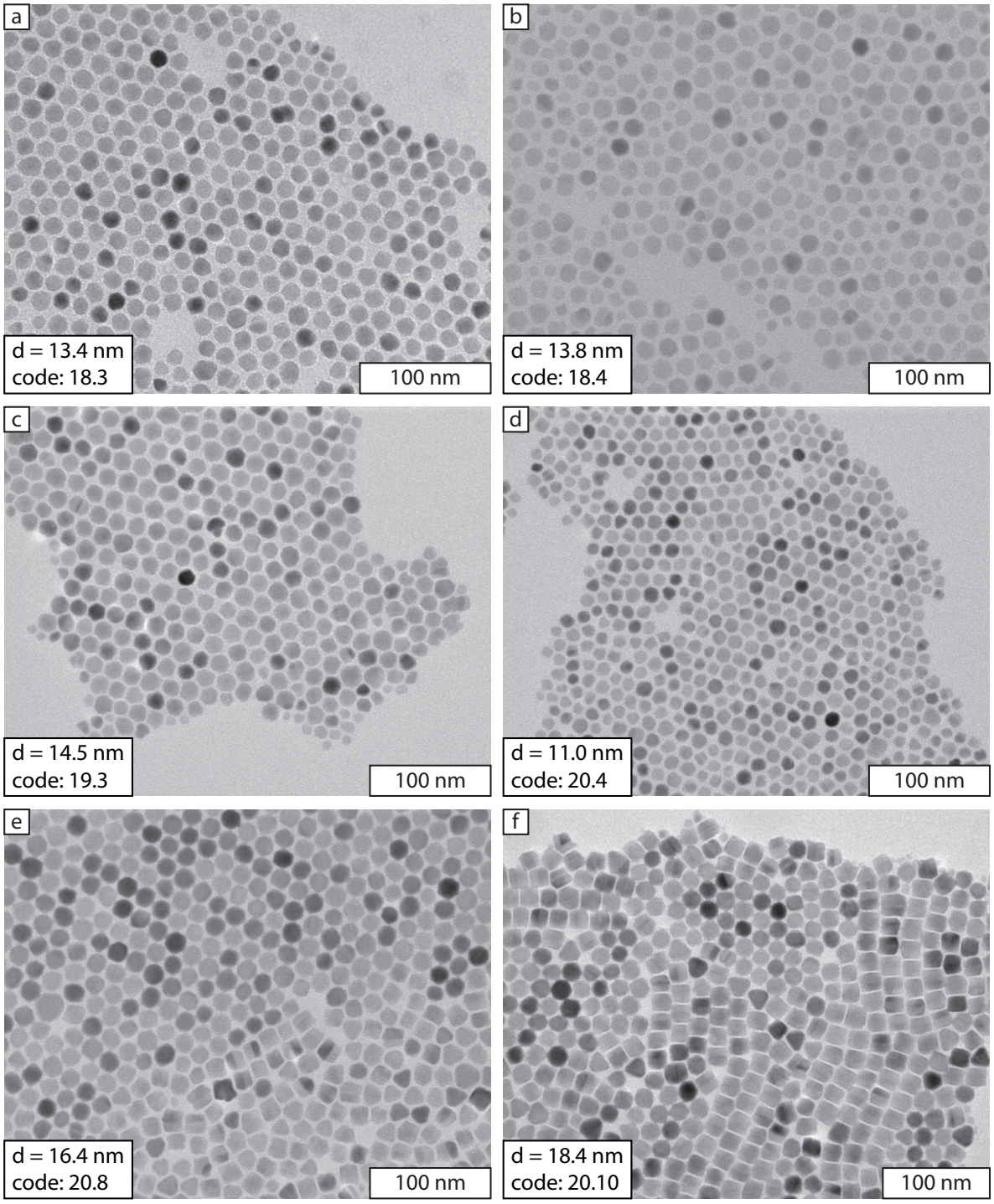

Figure 4.8. TEM pictures of iron oxide nanoparticles prepared by the Klokkenburg method, RdG series 18 (**a**–**b**), 19 (**c**), and 20 (**d**–**f**).

used for destabilization, except in the washing of the seeds. Despite the use of a weaker magnet, also the larger particles of RdG series 20 were unstable. Different attempts to redisperse the aggregates, such as ultrasonication, addition of an excess of surfactant,

heating in decalin and even an additional growth step, were all ineffective. In the latter series all samples were stored in decalin containing oleic acid to prevent desorption of the oleic acid from the surface of the particles. However, during purification of the particles, part of the surfactants could still have been washed away, which may have resulted in irreversible aggregation due to the large magnetic interactions.

Altogether, the synthesis of faceted magnetic nanoparticles is clearly reproduced, although the largest particles are not colloidally stable. This may very well be the result of magnetic interactions, since the dipole moment increases with the radius of the particles cubed. Therefore, it is important to purify the particles carefully, and store them in a solvent with an excess of the stabilizing surfactants. Despite the aggregation of the largest nanocrystals, several samples of magnetic nanoparticles could be used for further experiments, as shown in Chapters 6, 7, and 8.

4.4. Conclusions

Different synthesis methods to prepare size series of monodisperse magnetic nanoparticles have been investigated. Monodisperse iron oxide nanoparticles with different average sizes could be prepared in a single thermal decomposition step using the Hyeon method, but the reported [58] accurate control of the average particle diameter could not be reproduced. The degassing step first reported in a later publication by Hyeon *et al.* [59] appears to be very important to obtain a low polydispersity. The crystal defects discussed in Chapter 5 may find their origin in the rapid growth of the particles of the particles prepared by this synthesis method.

The twin method, an upscaled seed-mediated growth procedure, yielded series of iron oxide particles which contain twinning defects. These twinning defects are most likely the result of the change in reductor (the diol) or the different surfactant concentrations. Further investigations would be required to elucidate the origin of the twinning defects.

Finally, the synthesis of size series of faceted iron oxide particles by the Klokkenburg method [63, 64] could be reproduced. However, for increasing particle size, colloidal stability significantly decreases, which may result from the strong magnetic interactions, especially if adsorbed surfactants are removed during purification. It is concluded that the Klokkenburg method remains the best way to prepare size series of well crystallized magnetic iron oxide nanoparticles.

4.5. Acknowledgements

Rick de Groot (RdG), Suzanne Woudenberg (SW), Aldo Brinkman (AB), and Raluca Somoghi are thanked for the many syntheses contributing to this chapter. Mark Klokkenburg is acknowledged for useful discussions.

5

Diverging Geometric and Magnetic Size Distributions of Iron Oxide Nanocrystals

Abstract

An important reason to prepare magnetic nanoparticles of uniform size and shape is to ensure uniform magnetic properties. However, here, we demonstrate that magnetic iron oxide crystals of 20 nm or less with a low polydispersity of the geometric size can nevertheless have a strikingly broad distribution of the magnetic dipole moment. A comparative study was performed on nanoparticles with near-perfect crystallinity, twinning defects, or a high density of dislocations. Size, shape, and crystal defects were characterized with electron microscopy and X-ray diffraction, and magnetic dipole moments were determined from magnetization curves of dilute colloidal dispersions. The largest divergence was found for spherical particles with 3.5% geometric size polydispersity and 35% magnetic size polydispersity due to crystal lattice defects that disrupt single-domain magnetic spin coupling. This is in stark contrast with the usual implicit assumption that uniform size and shape guarantee well-defined magnetic properties of the individual particles.

5.1. Introduction

Magnetic nanoparticles have generated much interest, thanks to their suitability for many applications in the fields of magnetic data storage, catalysis, and biomedicine [10, 11, 14, 16, 20, 22–27, 130, 131]. For applications that require uniform magnetic properties of the individual particles, a uniform size is critical because the magnetic properties of nanoparticles are strongly size-dependent [145]. Fortunately, it is possible to prepare nanoparticles with a low polydispersity, down to a few percent. However, we will demonstrate that due to crystal defects, particles of 20 nm or less with a low polydispersity of the geometric size can, nevertheless, have a high polydispersity of the magnetic properties.

An example of an application in which uniform magnetic properties are critical is the use of magnetic nanoparticles to obtain locally targetted therapeutic hyperthermia [20, 25, 146–148]. The particles are introduced into a patient, in the vicinity of biological cells to be destroyed, and they are selectively heated using an alternating magnetic field. In theory, the most effective heating is produced when the characteristic frequency for magnetic relaxation is the same for each particle and the alternating field is applied at precisely that frequency. In practice, polydispersity of nanoparticle sizes diminishes the magnetic heating that can be achieved [148], and the theoretical limit seems almost impossible to reach because small differences in size can already cause large differences in the magnetization dynamics. For instance, an increase in the radius of magnetite nanoparticles (Fe_3O_4) from 7 to 8 nm theoretically slows down the Néel mobility of the magnetic dipole by a factor of 50 [147], a size sensitivity confirmed by frequency-dependent magnetic susceptibility measurements [149]. Another application of nanoparticles for which uniform magnetic properties are crucial [150] is as tracer material for magnetic particle imaging [151], an emerging technique that gives the prospect of performing rapid tomographic imaging using relatively inexpensive single-sided scanners [152].

Nanoparticles with a low geometric size polydispersity can be prepared by thermal decomposition of organometallic precursors [10, 11, 14, 52, 53, 130, 153]. Obtaining size uniformity relies on the separation of nucleation and growth processes. A brief nucleation event yields initial particles that subsequently all grow at the same rate under conditions that no new nuclei are formed. We expect magnetic iron oxide crystals of 20 nm or less to have a single magnetic domain [154, 155], in which case particles of the same size should all have the same permanent magnetic dipole moment. Nevertheless, due to crystal defects, the magnetic polydispersity is likely to be greater than expected from the geometric size polydispersity.

The most widely invoked type of defect has only a moderate effect: it consists of a "magnetically dead" surface layer on the order of 1 nm that effectively does not

contribute to the magnetic dipole moment of the particle [145, 156–159]. Here, we focus on internal defects whose effect on the magnetic properties is more detrimental. Magnetic measurements are performed on iron oxide nanoparticles with twinning defects or a high density of dislocations, and a comparison is made with iron oxide particles of the same size but with near-perfect single crystallinity.

In Section 5.2, the chemical synthesis and characterization methods are described. This includes a discussion of our approach to determine magnetic dipole moment distributions, by analyzing magnetization curves measured on dilute colloidal dispersions (Section 5.2.3). In Section 5.3, the experimental results obtained by electron microscopy, magnetization measurements, and X-ray diffraction are presented. Finally, in Section 5.4, the results are discussed for the different types of particles studied, with a low or a high geometric size polydispersity and a low or a high magnetic polydispersity.

5.2. Experimental Methods

5.2.1. Chemical Synthesis Methods

Magnetic iron oxide nanocrystals were prepared by different methods, resulting in particles that are referred to as "facets", "precipitates", "twins", and "spheres". The main aspects of the chemical syntheses are given below. The synthesis of the "twins" is described in the most detail because it has not been published before.

Our preparation of the "facets", referred to as the Klokkenburg method in Chapter 4 [63], is similar to the method of Sun et al. [61, 62]. Briefly, initial seeds with a size of 5 nm were grown in 14 seeded growth steps to a final size of 20 nm. Iron acetylacetonate was thermally decomposed in diphenyl ether in the presence of oleic acid, oleyl amine, and 1,2-hexadecanediol. The synthesis was performed under nitrogen on a 20 mL scale, and the reaction mixture was heated to reflux without stopping to degas and then refluxed for 30 min. The "facet" particles were used previously in several studies of dipolar structure formation [81, 160–164].

The "twins" were prepared according to a variation on the procedure to prepare the "facets", in 27 seeded growth steps. First, seed particles of a few nanometers in size were prepared by mixing 7.06 g (20 mmol) of iron acetylacetonate (Acros, >99%), 20.23 g (100 mmol) of 1,2-dodecanediol (Aldrich, 90%), 16.90 g (60 mmol) of oleic acid (Sigma-Aldrich, 90%), and 16.04 g (60 mmol) of oleyl amine (Fluka, >70%) in 200 mL of phenyl ether (Acros, 99%). This reaction mixture was heated to 200 °C under nitrogen flow to degas the dispersion for 30 min, after which the mixture was heated to reflux temperature (around 260 °C) for another 30 min under nitrogen atmosphere. The resulting seed dispersion was washed by precipitation with 100 mL of ethanol and 30–40 min of centrifugation at 2000 rpm (912 g). These seed particles were redispersed in hexane (Merck, p.a.) and grown in repeated seeded growth steps using the same procedure as described above, with only the amounts of surfactants (oleic acid and

oleyl amine) reduced to 20 mmol. After 20 growth steps when the particles did not seem to grow any further, the amounts of surfactants were decreased to 10 mmol. After each growth step, 10% of the reaction mixture was taken out for storage.

The "precipitates" were prepared by Bica [165] by aqueous precipitation of iron salts according to a method similar to that of Massart [55], followed by transfer to the apolar solvent decalin after surface modification with oleic acid. The same particles were previously used in a statistical thermodynamics study that involved determining the size of 10^5 particles, confirming a log-normal shape of the distribution [166].

The "spheres" were made by single-step thermal decomposition of iron oleate using a method from the Hyeon group [58, 59]. The syntheses were performed with 20 mL of solvent, 3 mmol of iron oleate, and ∼0.8 g of oleic acid. To obtain uniform particles, it was important to perform the degassing step described by Kwon et al. [59]. To vary the average particle size, solvents with different boiling points were used (octadecene, trioctylamine, eicosene).

5.2.2. Characterization Methods

For transmission electron microscopy (TEM), Philips Tecnai 12 and 20 electron microscopes operating at 120 or 200 kV, respectively, were used. Size distribution parameters were determined from size analysis of 800 of the "precipitate" particles and 200–300 of each of the other types of particles.

To obtain magnetization curves at room temperature, a Micromag 2900 alternating gradient magnetometer from Princeton Measurements Corporation, calibrated with an yttrium iron garnet sphere calibration sample purchased from NIST, was used. Dilute dispersions of the nanoparticles in the apolar solvent decalin were contained in square capillary cups of $4\times4\times0.4$ mm^3 oriented with the 4×4 mm^2 face parallel to the magnetic field, to minimize demagnetization effects. Further experimental details are in ref [167].

To determine saturation magnetizations of the particles in emu per gram, including oleic acid layer, magnetization curves were also measured for weighed amounts of dry particles after three washing steps to remove excess oleic acid. In each step, ethanol was used to destabilize the colloidal dispersion, the system was centrifuged, the supernatant was removed, and the particles were redispersed in cyclohexane. In a final step, the cyclohexane was removed by evaporation.

X-ray diffraction measurements were performed with a Bruker AXS D8 ADVANCE diffractometer equipped with a Co Kα1 source ($\lambda = 0.178897$ nm) in a wide angle range (from 22 to 80°in 2θ). The iron oxide crystallite size was determined using the Scherrer equation [168]: $d = K\lambda/[\beta\cos\theta]$, where d is the size of the crystalline domain; K is the shape factor, which is taken to be 0.9 for unknown particle shapes; λ is the wavelength of the incident radiation; β is the line-broadening at half the maximum intensity (fwhm) of the peak in radians; and θ is the Bragg angle in radians.

5.2.3. Magnetic Analysis Approach

To determine magnetic polydispersities of nanoparticles, we follow an approach known from the field of ferrofluids: the analysis of magnetization curves of dilute colloidal dispersions of the particles in a liquid [167,169–171]. The main underlying principle is that in the liquid, nanoparticle dipoles respond independently of each other to the magnetic field, as long as the dispersion is sufficiently dilute and the dipole moments are not too large [167, 172, 173]. In this way, effective dipole moments can be obtained for the individual particles with a single magnetic domain (or the internal magnetic domains of particles with multiple domains), regardless of their shape or anisotropy. Magnetic dipole moment distributions are calculated by fitting the magnetization curves on the basis of a log-normal distribution of the dipole moments.

The Langevin function, L (dimensionless), describes the degree of alignment of a dipole of magnitude μ (in Am^2) in an external field H (in A/m):

$$L(\mu, H) = \coth\left(\frac{\mu_0 \mu H}{kT}\right) - \frac{kT}{\mu_0 \mu H} \tag{5.1}$$

where μ_0 is the permittivity of vacuum and kT is the thermal energy. A log-normal distribution function $P(\mu)$ (with units $(\mathrm{Am}^2)^{-1}$) of the magnetic dipole moment is assumed, as is often done for ferrofluids [167, 169–173],

$$P(\mu) = \frac{1}{\sqrt{2\pi}\mu\sigma_\mu}\exp\left(-\frac{\left(\ln\frac{\mu}{\mu^*}\right)^2}{2\sigma_\mu^2}\right) \tag{5.2}$$

where $\ln(\mu^*)$ and σ_μ are the mean and the standard deviation of $\ln(\mu)$. On this basis, the average magnetic dipole moment is $\langle\mu\rangle = \mu^*\exp(\sigma_\mu^2/2)$. The total magnetization, M, of the colloidal dispersion (in A/m) is given by

$$M = \chi_{\mathrm{dia}} H + \frac{N}{V}\int_0^\infty \mu P(\mu) L(\mu, H)\mathrm{d}\mu \tag{5.3}$$

where χ_{dia} is the diamagnetic susceptibility (dimensionless), N is the total number of magnetic nanoparticles, and V is the system volume (in m^3). $P(\mu)\mathrm{d}\mu$ gives the number probability to have a particle of dipole moment between μ and $\mu + \mathrm{d}\mu$, so that an additional factor of μ is required to account for the fact that a particle with a small magnetic dipole moment contributes less than a particle with a large magnetic dipole moment to the total magnetic moment of the sample [170]. The linear diamagnetic term is due to the solvent and the sample holder; whether it is negligible depends on the concentration of iron oxide in the ferrofluid. The measurements were corrected for the diamagnetic contribution, a correction whose reliability was confirmed by obtaining the same magnetic dipole moment distribution at different ferrofluid concentrations.

The magnetic sizes d_μ that we report are the diameters of hypothetical spherical particles that would have both the same magnetic dipole moment as our particles and

the theoretical bulk magnetization, m_s, of magnetite, 91 emu/g (maghemite is on the order of 80 emu/g) [174].

$$d_\mu = \sqrt[3]{6\mu/(\pi m_s)} \tag{5.4}$$

It is noted that this is an effective size and that our particles are spheres only by crude approximation, but there is insufficient detailed information about the three-dimensional shape of our particles and their magnetic domains to warrant describing them with more than one length scale parameter. Furthermore, in contrast to the work of Chen et al. [171], who took into account the magnetic effect of a defective surface shell, our objective is not to use magnetization measurements to determine the geometric particle size. Our own magnetic sizes are merely a way to express the magnetic dipole moment of the particles in nanometers after conversion using the theoretical magnetization per unit volume as a constant conversion factor.

One complication of expressing the magnetic dipole moment as an effective size is that magnetization measurements yield volume-averaged dipole moments, whereas geometric size distributions from electron microscopy are number-averaged. From Equation 5.4, a log-normal distribution of the magnetic dipole moment implies a log-normal distribution of the magnetic size. The mean, $\ln(\mu^*)$, and standard deviation, σ_μ, of the dipole moment distribution are related to the mean, $\ln(d_\mu^*)$, and standard deviation, σ_d, of the magnetic size distribution as follows:

$$d_\mu^* = \sqrt[3]{6\mu^*/(\pi m_s)} \tag{5.5}$$

$$\sigma_d = \frac{1}{3}\sigma_\mu \tag{5.6}$$

Using Equations 5.5 and 5.6, number density distributions were calculated. These can now directly be compared to the TEM size distributions, which were described by a log-normal function, yielding a mean $\ln(d_{\mathrm{TEM}}^*)$ and a standard deviation σ_{TEM}. Nevertheless, it is useful also to know the volume averages for better comparison with the volume-averaged XRD values. Therefore, volume-averaged geometric and magnetization sizes were calculated for each type of particle, as well.

5.3. Results

5.3.1. Electron Microscopy

Figure 5.1 illustrates that the various synthesis methods resulted in magnetic iron oxide nanocrystals of different shapes and sizes. The geometric size distributions obtained from TEM are log-normal number density probability functions, and their dimensionless standard deviations are used as a measure of the polydispersity to express how uniform the particles are. The "facets" are faceted particles with an average TEM size of 20 nm and a relatively low TEM polydispersity. The "precipitates" are highly polydisperse maghemite particles. The "twins" have clearly distinguishable twinning

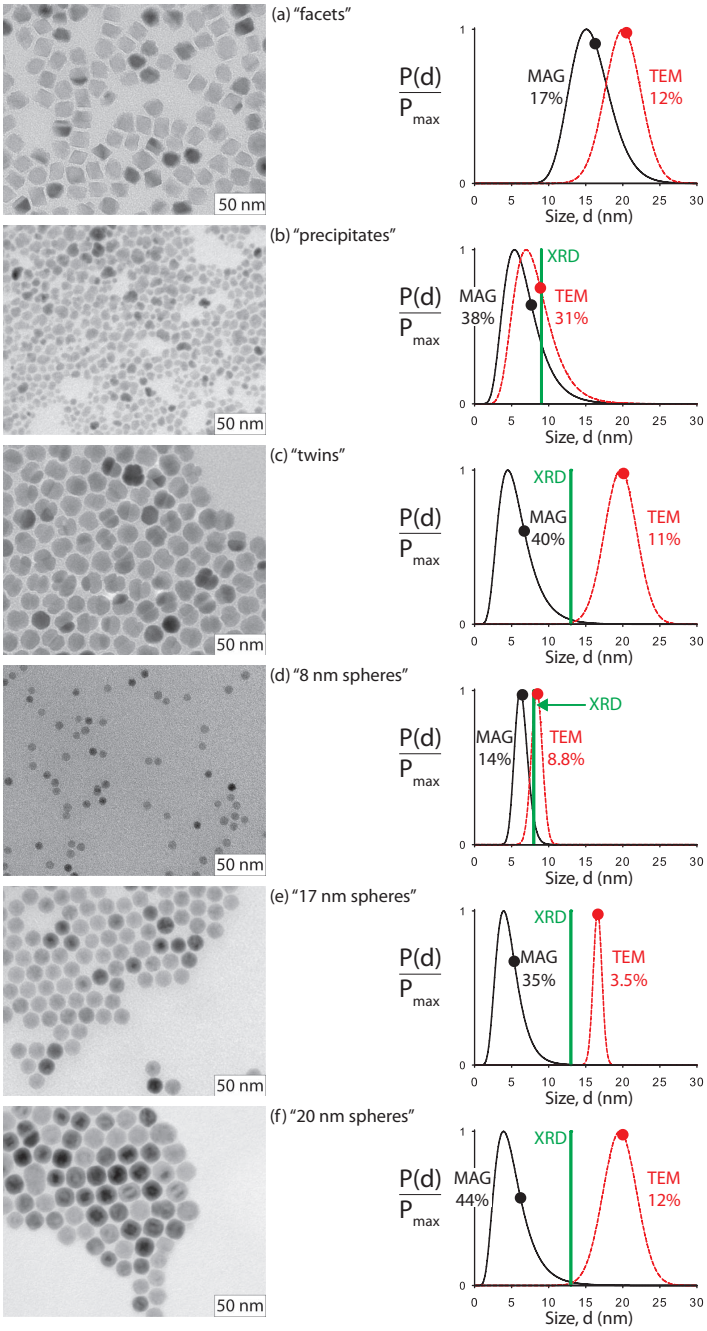

Figure 5.1. Transmission electron microscopy (TEM) images and size distributions of iron oxide nanoparticles synthesized by different methods: (**a**) thermal decomposition of iron acetylacetonate, (**b**) aqueous precipitation, (**c**) a variation on method "a" yielding twinning defects, and (**d**–**f**) thermal decomposition of iron oleate. TEM and magnetic measurements (MAG) were used to determine polydispersities (%) and log-normal size distributions, scaled to the maximum probability $P_{\max}$. Both the TEM and magnetic size distributions are shown as number density distributions. For better comparison with crystallite sizes from X-ray diffraction line-broadening (XRD), volume-averaged TEM and MAG sizes are indicated by large circular dots.

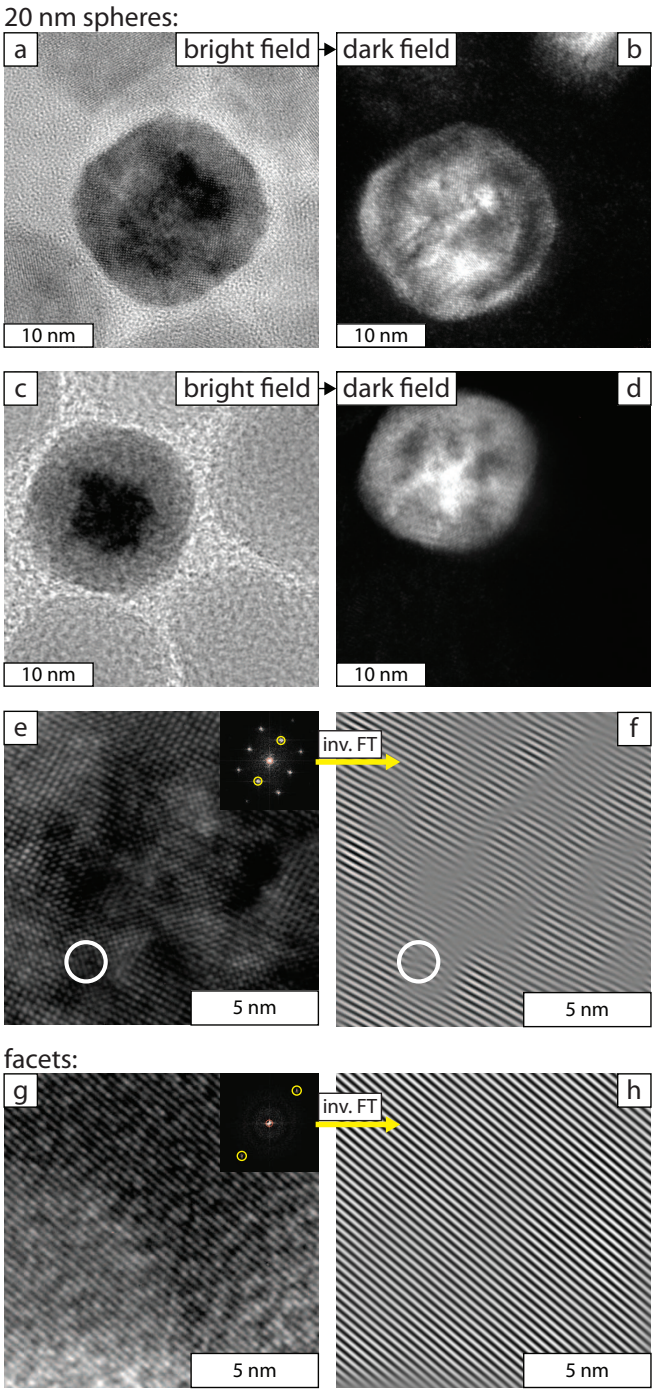

Figure 5.2. High-resolution TEM images of two 20 nm "sphere" particles (**a**–**f**) and a 20 nm "facet" particle (**g,h**). Each 20 nm "sphere" exhibits defect-induced internal contrast variations, both in bright field mode (**a,c**) and in dark-field visualization of the diffracted electrons (**b,d**). At higher magnification, the effect of crystal lattice defects in **e** and **g** is visually enhanced by Fourier transform (insets), followed by inverse Fourier transform (inv.FT) of the indicated spots in Fourier space, pertaining to only one crystallographic direction. Several dislocations are then revealed in the "sphere" (see, for instance, inside the circle) but none in the "facet".

defects, and their TEM size and polydispersity are similar to the "facets". Finally, the "spheres" are roughly spherical particles with a low TEM polydispersity.

"Facet" and "sphere" particles with the same size of 20 nm were also examined more closely using high-resolution TEM to study internal crystal defects [175–177] (see Figure 5.2). At first sight, the crystalline periodicity of the "spheres" appears to extend across the entire particles, at least for the imaged crystal planes. However, on the scale of a few nanometers, the electron contrast of each particle is inhomogeneous, both in bright field (transmitted electrons) and in dark field (diffracted electrons). Contrast depends on whether the orientations of the crystal planes fulfill electron diffraction conditions. For this reason, differently oriented "facet" particles or crystalline domains inside the "twin" particles have sharply different contrasts (Figure 5.1a,c). In the 20 nm "spheres", such contrast differences are now observed inside individual particles, which can be explained by crystal defects. The dislocation concentration in the 20 nm "spheres" is high (Figure 5.2f), whereas for comparison, no dislocation is observed for the imaged "facet" particle (Figure 5.2h).

5.3.2. Magnetic Measurements

Magnetization curves were measured for colloidal dispersions of the particles with at least two different low volume fractions, to demonstrate that interparticle interactions have a negligible effect on the magnetization curve (see Appendix). For the 20 nm "facet" particles, the volume fraction of the colloidal dispersion had to be lower than 0.5%; otherwise, significantly larger average dipole moments and polydispersities were found [167]. The reason is that at higher concentrations, the magnetization curve is no longer that of single particles but of dipolar chains [68, 81, 160, 167, 173]. For all the other particles, the results were concentration-independent below concentrations of a few percent. This agrees with the negligible effect of dipolar interactions found at room temperature and concentrations of a few volume percent or lower in previous systematic work on the concentration-dependent magnetic properties of "precipitate"-like particles [67, 68, 173] and of particles prepared by the same "heating up" method that we used to prepare the "spheres" [178].

The main results are the magnetic size distributions in Figure 5.1. For the "facets", the "precipitates", and the 8 nm "spheres", TEM and magnetic measurements give a similar average size and polydispersity. However, for the "twins" and the "spheres" of 17 and 20 nm, the magnetic sizes are much smaller and more polydisperse than the geometric sizes. Nevertheless, the saturation magnetization measured on dry particles was of the expected order of magnitude (see Table 5.1). The measurements from which the magnetic distributions in Figure 5.1 were calculated will now be further discussed.

Figure 5.3 illustrates the effect of the size of the nanoparticle dipoles on the magnetization curve. Large dipoles result in a steep initial slope because a weak field suffices to

Table 5.1. Summary of numerical results, including number-averaged sizes $\langle d \rangle$, volume-averaged sizes $\langle d^3 \rangle^{1/3}$, and size polydispersities σ_d.

sample name		20 nm facets	precipitates	20 nm twins	8 nm spheres	17 nm spheres	20 nm spheres
ref to synthesis method		[61–63]	[55, 165]		[58, 59]	[58, 59]	[58, 59]
part of Figure 5.1		a	b	c	d	e	f
internal crystal defects		∼none	∼none	twinning	∼none	dislocations	dislocations
TEM	$\langle d \rangle$ (nm)	20.0	8.0	19.7	8.4	16.6	19.6
	$\langle d^3 \rangle^{1/3}$ (nm)	20.4	8.9	20.1	8.5	16.6	20.0
	σ_d (%)	12	31	10.7	8.8	3.5	11.6
XRD	$\langle d^3 \rangle^{1/3}$ (nm)	18 [a]	9	13	8	13	13
AGM	$\langle d \rangle$ (nm)	15.8	6.7	5.7	6.3	4.7	5.2
	$\langle d^3 \rangle^{1/3}$ (nm)	16.3	7.7	6.7	6.5	5.3	6.3
	σ_d (%)	17	38	40	14	35	41
	$\langle \mu \rangle$ (10^{-20} Am^2)	107.0	11.1	7.5	6.7	3.7	6.1
	M_{sat} (emu/g) [b]	69 [a]	53	65	26	28	30

[a] Measured on a separate batch of particles prepared by the same method ($\langle d \rangle = 23.5$ nm).
[b] M_{sat} of dry particles, including oleic acid (emu/g)

align them, whereas small dipoles require a much stronger field to approach saturation magnetization. This implies that the field-dependence of the relative magnetization is sufficient information to determine the magnitude of the magnetic dipole moment of nanoparticles. No knowledge of the mass of the sample is required. However, it is necessary to know the magnetization at which the sample saturates (M_{sat}), which was determined by numerically fitting the entire curve. The M_{sat} value was verified by extrapolating the magnetization M versus reciprocal field, $1/H$, to obtain the magnetization in the limit that $1/H$ approaches zero.

The polydispersity of the magnetic dipole moment is obtained from the *shape* of the magnetization curve. To demonstrate this, we represent a low-field selection of the magnetization data using two dimensionless axes in Figure 5.4. Not only is the magnetization (corrected for diamagnetic contributions) scaled to its saturation value, as in Figure 5.3, but now also the magnetic field strength is rescaled in such a way that the initial slope is unity. This rescaling is performed using the measured initial magnetic susceptibility, that is, the slope χ_i of M versus H in the low-field limit. For a given magnetic polydispersity, σ_μ, pertaining to a specific distribution shape (for instance, log-normal), any chosen value of the dimensionless field corresponds to a unique value of the dimensionless magnetization, independent of the magnitude of the dipole moments; the reason is that from Equations 5.2 and 5.3, an increase of μ^* by a factor of x increases M by a factor $\exp[(\ln x)^2/(2\sigma_\mu^2)]$, and it can be shown that M_{sat} and χ_i are then increased by the same factor. For monodisperse dipole moments, the curve shape

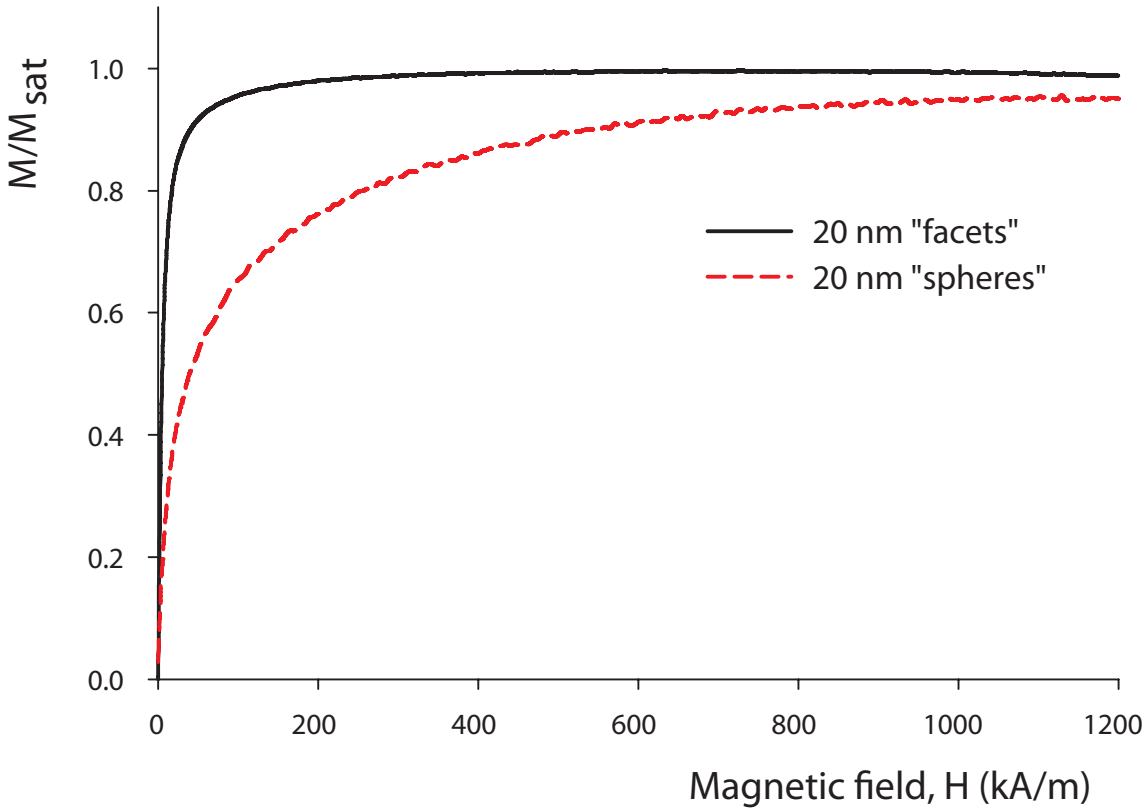

Figure 5.3. Illustration of how the average magnetic dipole moment affects the magnetization curve of ferrofluids. Magnetization curves are shown for iron oxide "facet" and "sphere" particles with a similar geometric size of 20 nm, dispersed in the apolar solvent decalin. The magnetizations are scaled to the saturation value. Clearly, the dipole moment of the "facet" particles is much larger than that of the "spheres", since the "facets" require a much weaker magnetic field to align the dipoles.

is given by the Langevin function, whereas for magnetically polydisperse ferrofluids, the dimensionless magnetization at a chosen value of the dimensionless magnetic field is lower because the small dipoles of the distribution lag behind in being aligned. To the best of our knowledge, our dimensionless representation of the magnetization data is original and a convenient way to compare the magnetic polydispersity in experimental systems without having to assume a log-normal or other type of distribution.

5.3.3. X-ray Diffraction

For all the particles studied, the positions of the XRD diffraction peaks indicate the presence of magnetic iron oxide, magnetite (Fe_3O_4) or maghemite (γ-Fe_2O_3) or both, which is difficult to distinguish from XRD (see Appendix). For the spheres,

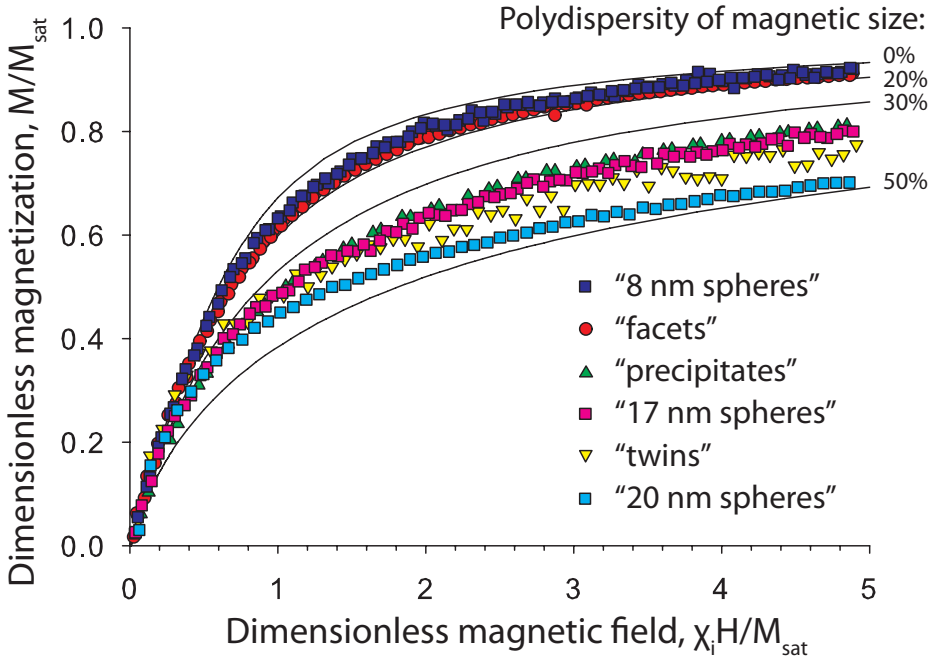

Figure 5.4. Dimensionless magnetization curves of the iron oxide nanoparticles imaged in Figure 5.1, measured on dilute dispersions to avoid the effects of nanoparticle dipole interactions. The magnetization, M, is scaled to its saturation value, M_{sat}, and the magnetic field, H, is scaled using M_{sat} and the initial magnetic susceptibility, χ_i, to yield an initial slope of unity. In this way, the curves do not depend on the average value but only on the polydispersity and distribution shape of the magnetic dipole moment. The drawn lines are simulated curves for log-normal distributions of the magnetic size with a standard deviation of 0%, 20%, 30%, and 50%. Only a low-field selection of the data is presented here.

this concurs with Park et al. [58], who reported that crystal composition gradually shifts from maghemite to magnetite for increasing particle sizes. The two crystal forms have a similar theoretical bulk magnetization [174]. The average nanoparticle sizes obtained from XRD line broadening are shown in Figure 5.1 as vertical lines. There was insufficient material of the "facet" particles to perform XRD on the same synthesis batch of particles that were studied extensively in the past by various techniques [81,160–164, 167], but a new synthesis batch of such particles yielded particles with a TEM size of 23 nm and an XRD size of 18 nm. XRD provides a volume-weighted average. Therefore, for better comparison with XRD, the volume-averaged sizes from TEM and magnetic measurements are indicated by a large circular dot on each TEM and magnetization curve analysis (MAG) distribution curve in Figure 5.1.

The numerical results from TEM, AGM, and XRD are summarized in Table 5.1.

5.4. Discussion

Magnetic iron oxide nanoparticles were prepared with different degrees of crystallinity, and the effective sizes were determined by electron microscopy, magnetization curve analysis, and X-ray diffraction. Here, first the sizes measured by different methods are compared with each other to conclude which types of particles are single crystals and single magnetic domains. This information is then used to examine how twinning defects and dislocations affect the nanoparticle magnetic dipole moment and, in particular, its polydispersity. Finally, it is discussed how the magnetic properties are related to the chemical synthesis method.

An XRD size that agrees with the volume-averaged TEM size indicates that each nanoparticle is a single crystal. This is the case for the "facets", the "precipitates", and the 8 nm "spheres" (Figure 5.1 and Table 5.1). In contrast, the XRD size of the "twins" and the largest "spheres" is significantly smaller than expected from TEM. In the case of the twinned particles, this is clearly due to the twinning defects, which split each particle into two or more crystalline domains. For the 17 and 20 nm "spheres", XRD and high-resolution TEM (Figure 5.2) suggest that the high density of dislocations perturbs the long-range periodicity to such a large extent that these particles are also split into several crystalline domains.

The magnetic sizes as calculated by us on the basis of the theoretical bulk magnetization are expected to agree with TEM and XRD when the particles are single crystalline and sufficiently small that they have a single magnetic domain. This is, indeed, what is observed for the "facets", the "precipitates", and the 8 nm "spheres". In these cases, the magnetic size is only slightly smaller than from TEM and XRD. This small difference is ascribed to surface defects [145, 156–159].

For the twinned particles and the largest "spheres", however, the volume-averaged effective magnetic size (the large circular dots in Figure 5.1) is less than half that from XRD. Nevertheless, the saturation magnetization M_{sat} of the dry particles is of the expected order of magnitude. The small magnetic size appears to be that of individual magnetic domains inside each particle, which respond separately to the external field. The magneto-crystalline anisotropy of magnetic iron oxides is sufficiently low and the magnetic domains are apparently sufficiently small that rapid Néel reorientation of the dipoles inside separate magnetic domains seems plausible [147]. The dislocations and possibly also an inhomogeneous magnetite/maghemite stoichiometry disrupt the long-range coupling of atomic magnetic spins. This agrees with the detrimental effects of crystal defects on the magnetic properties of bulk crystalline magnetite [179]. In our case with nanoparticles, a consequence of the fact that the crystalline defects are not well controlled is that the magnetic properties can be very different from one particle

to another. In other words, the magnetic polydispersity is much higher than expected from the geometric size polydispersity.

To promote uniform magnetic properties, not only must the geometric size polydispersity be low but also internal crystal defects must be avoided. One approach to obtain a low concentration of crystal defects is to grow particles in separate seeded growth steps. In the optimal case, this results in epitaxial growth in each step, as was done for the "facet" particles. However, this approach is laborious, and in each growth step, a mishap may occur, resulting, for instance, in twinning defects that are propagated in subsequent growth steps. In that respect, single-step thermal decomposition of iron oleate, with a nanoparticle size tunable via the boiling point of the solvent, is much more convenient. Our "sphere" particles of 8 nm prepared in that way are well crystallized and have a magnetic size polydispersity on the same order as the geometric size polydispersity. However, when larger spherical particles of 17 or 20 nm were prepared by the same method, high concentrations of internal crystal defects were obtained, which decreased the net magnetic moment of the particles in low field and increased the magnetic polydispersity.

A possible remedy for crystal defects is to recrystallize the particles by annealing them, as was done by Kwon et al. [59] by refluxing for 15 h at 320 °C. In that process, the magnetic moment increased by a factor of 5, approaching the theoretical bulk magnetization; at the same time, the shape of the particles changed from sphere to cube, and the geometric size polydispersity increased. One might be tempted to conclude that the shape change from sphere to cube is directly responsible for the increased dipole moment, but this is not necessarily the case. Salazar-Alvarez et al. [180] compared the magnetic properties of spherical and cubic iron oxide nanoparticles of the same volume, and they found practically the same magnetic properties, the main difference being only the blocking temperature. In light of our own results, the increased magnetic moment after the annealing of spherical iron oxide nanoparticles by Kwon et al. [59] was probably mainly due to the removal of internal crystal defects.

A possible conclusion is that better magnetic properties are to be expected from iron oxide nanoparticles whose surface is faceted rather than spherical. Facets suggest that particle growth was sufficiently slow for the preferential development of energetically favored surface crystal planes. In contrast, sphericity suggests that particle growth is too rapid to develop those facets, which may also be too rapid for good crystallization by epitaxial growth. Our own spherical particles were prepared in a single step, implying relatively rapid nucleation and growth. Good crystallinity and magnetic properties are found for the particles of 8 nm but not for the larger spherical particles of 17 or 20 nm. Their growth was probably even more rapid, resulting in a high concentration of crystal defects and poor magnetic properties. Despite their low geometric size polydispersity,

the 17 and 20 nm "spheres" have a high magnetic polydispersity on the same order as when particles are prepared by aqueous precipitation.

5.5. Conclusions

In conclusion, low TEM size polydispersity of magnetic nanoparticles does not guarantee low polydispersity of the magnetic dipole moments. During chemical synthesis, effective separation of nucleation and growth results in a low geometric size polydispersity. Assuming that each particle has a single magnetic domain, is perfectly crystallized, and has the same shape, low geometric size polydispersity would result in low polydispersity of the magnetic properties. However, it is difficult to avoid crystal defects, such as twinning and dislocations, which can have a highly detrimental effect on the strength and low polydispersity of the magnetic properties. For applications in which the magnetic properties of the individual particles are critical, TEM size monodispersity therefore does not suffice as a criterion for a successful synthesis. The magnetic properties may be much more polydisperse than expected from the physical size.

5.6. Acknowledgements

Suzanne Woudenberg and Rick de Groot are acknowledged for particle synthesis, Hans Meeldijk for performing the high-resolution TEM, Hirsa Torres Galvis and Krijn de Jong for XRD-measurements, and they are thanked for many useful discussions. John Geus, Jan Hilhorst, Andrei Petukhov, Mark Klokkenburg, Jos van Rijssel, Aldo Brinkman, Janne-Mieke Meijer, and Pedro Zeijlmans van Emmichoven are also thanked for useful discussions. This chapter is reprinted with permission from B. Luigjes *et al.*, Journal of Physical Chemistry C, 115(30):14598-14605, 2011.

Appendix

In this Appendix, further characterization results for the discussed iron oxide nanoparticles are given. Figure 5.5 shows a magnetization curve of "facet" particles in decalin at low concentration, where interactions have a negligible effect. High resolution TEM images in Figure 5.6 illustrate that the observed contrast variations are related to the faceting of the particles rather than to internal crystal defects. An XRD diffraction pattern of the particles is shown in Figure 5.7.

For the "precipitates", characterization results are presented in Figures 5.8–5.9, for the "twin" particles in Figures 5.10–5.11, and for the spheres in Figures 5.12–5.17.

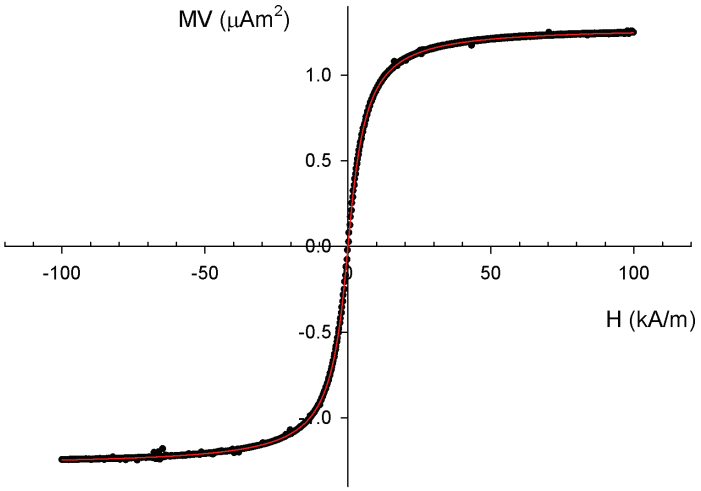

Figure 5.5. Total sample magnetic moment MV (corrected for a diamagnetic contribution $\chi_{\rm dia}VH$, with $\chi_{\rm dia}V$ of order -10^{-14} m^3) versus external field for 3.0 μL of a dispersion of "facet" particles in decalin, with an iron oxide volume fraction of 0.17% (dots) and its corresponding fit (line). From this curve the values for $\langle\mu\rangle = 1.07\times10^{-18}$ Am^2, $\sigma_d = 0.17$, and the saturation magnetic moment $MV(H \to \infty) = 1.29$ μAm^2 were obtained. The same $\langle\mu\rangle$ and σ_d were found at a volume fraction of 0.07%, confirming a negligible influence of interparticle magnetic interactions. Measurements at iron oxide volume fractions of a few percent yielded values of $\langle\mu\rangle$ and σ_d that appeared more than a factor two larger, due to magnetic interactions [167].

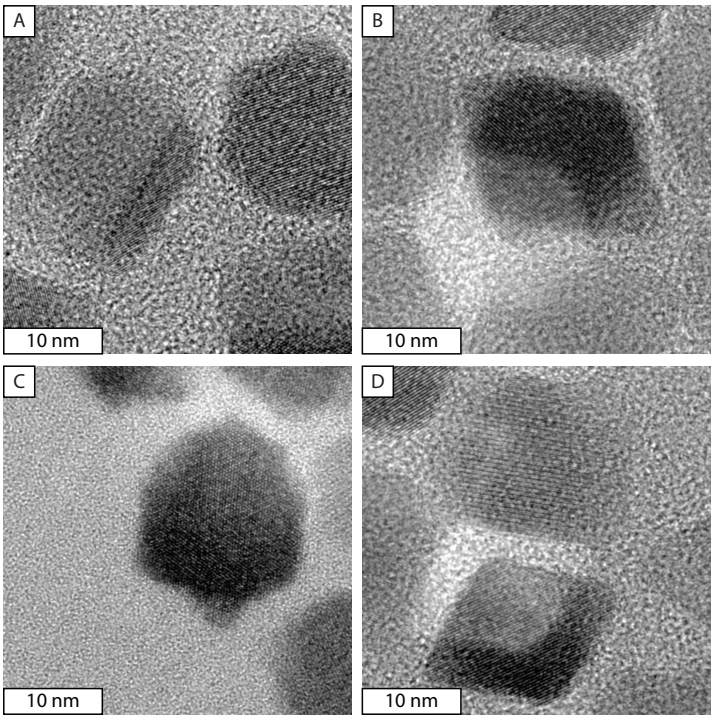

Figure 5.6. High resolution TEM images of the "facet" particles.

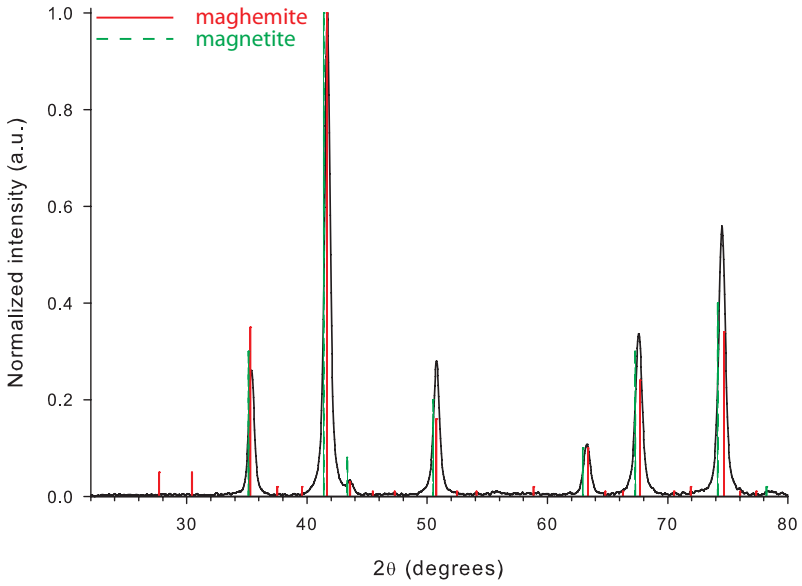

Figure 5.7. The XRD pattern of 23 nm "facet" particles can be assigned mainly to magnetite, with an average crystallite size of 18 nm (measured on a different synthesis batch than used for the magnetic measurements and TEM, particles of similar size).

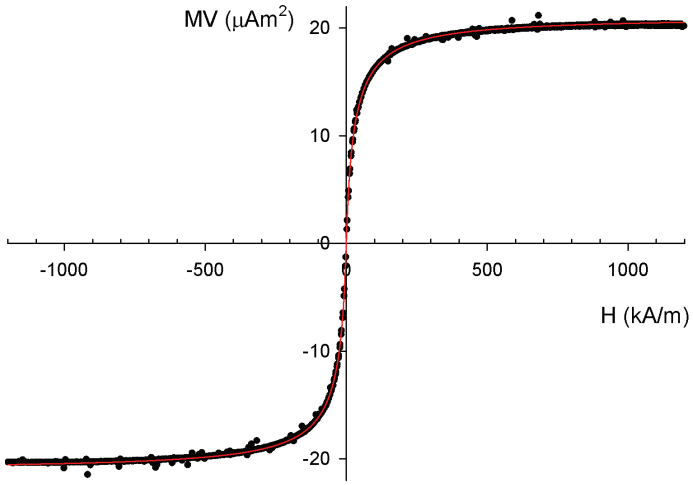

FIGURE 5.8. Total sample magnetic moment versus external field for 3.2 μL of a dispersion of "precipitates" in decalin, with an iron oxide volume fraction of 2% (dots) and its corresponding fit (line). From this curve the values $\langle\mu\rangle = 1.11\times10^{-19}$ Am^2, $\sigma_d = 0.38$, and the saturation magnetic moment $MV(H \to \infty) = 21.1$ μAm^2 were obtained and the diamagnetic contribution is negligible. The same magnetic polydispersity and low-field bulk magnetization were found for an iron oxide volume fraction of 0.2%, indicating that the concentration was sufficiently low to neglect interparticle magnetic interactions.

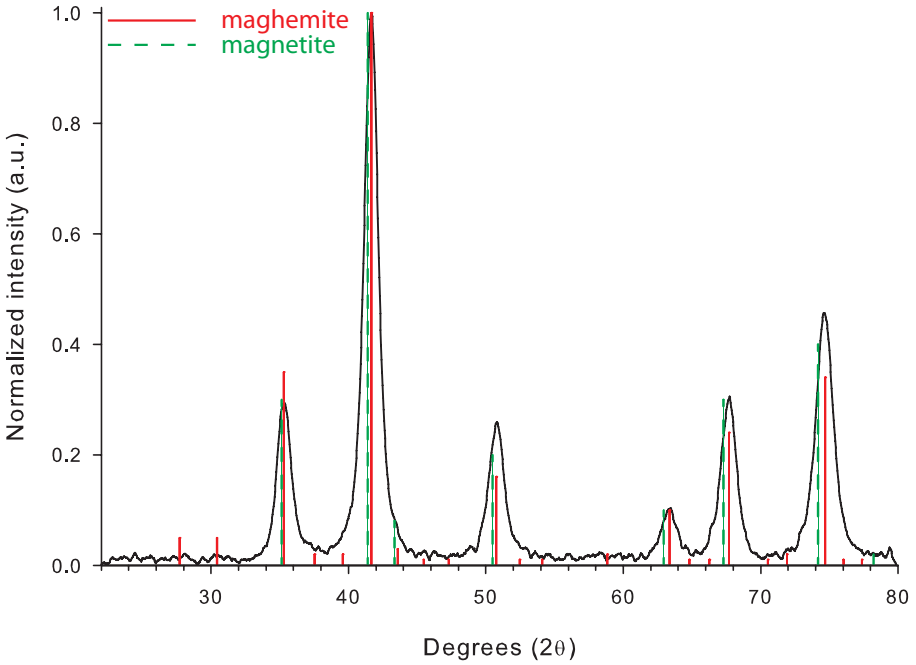

FIGURE 5.9. The XRD pattern of the "precipitates" can be assigned to maghemite or magnetite, with an average crystallite size of 9 nm.

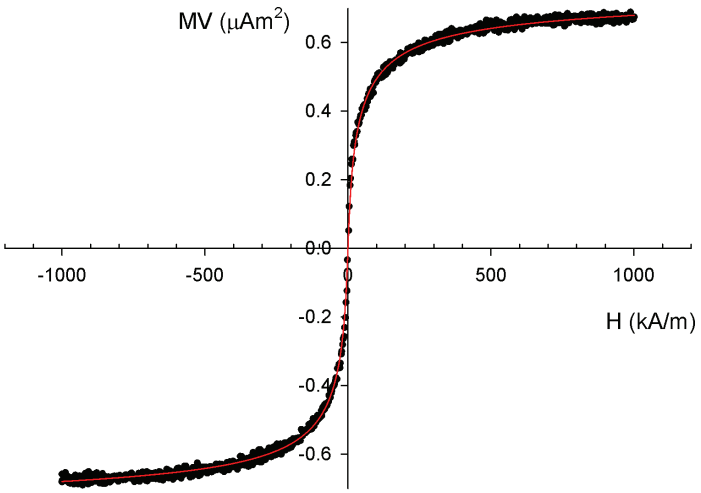

Figure 5.10. Total sample magnetic moment MV (corrected for a diamagnetic contribution $\chi_{\text{dia}}VH$, with $\chi_{\text{dia}}V$ of order -10^{-14} m^3) versus external field for a dispersion of "twin" particles in decalin (dots) and its corresponding fit (line). From this curve the values $\langle\mu\rangle = 7.46\times10^{-20}$ Am^2, $\sigma_d = 0.40$, and the saturation magnetic moment $MV(H\to\infty) = 0.70$ μAm^2 were obtained.

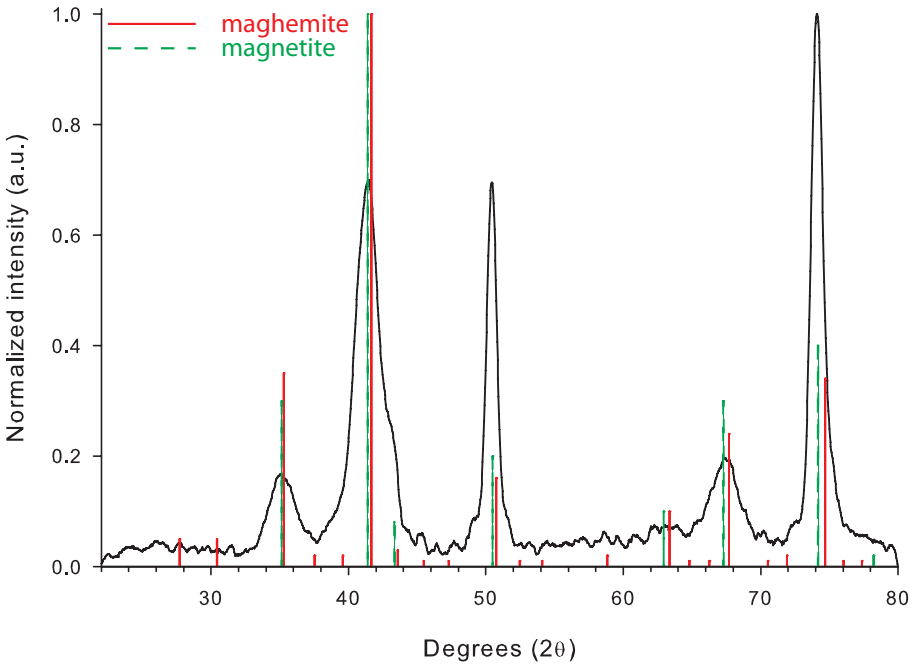

Figure 5.11. The XRD pattern of the "twins" can be assigned to maghemite or magnetite, with an average crystallite size of 13 nm.

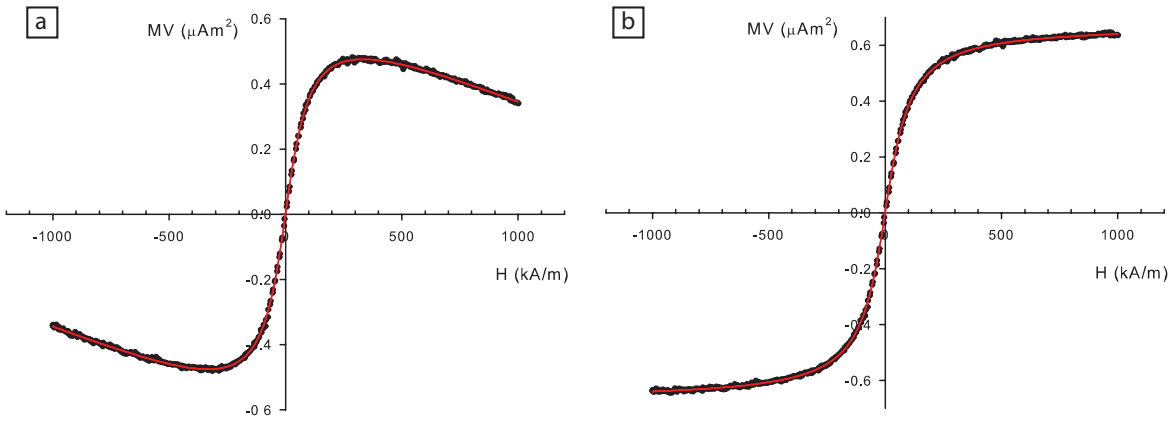

FIGURE 5.12. Field-dependence of the total sample magnetic moment MV, before (**a**) and after correction (**b**) for the diamagnetic contribution, for a colloidal dispersion of 8 nm "sphere" particles in decalin (dots) and its corresponding fit (line). From this curve the values $\langle\mu\rangle = 6.70\times10^{-20}$ Am^2, $\sigma_d = 0.14$, and the saturation magnetic moment $MV(H \to \infty) = 0.67$ μAm^2 were obtained.

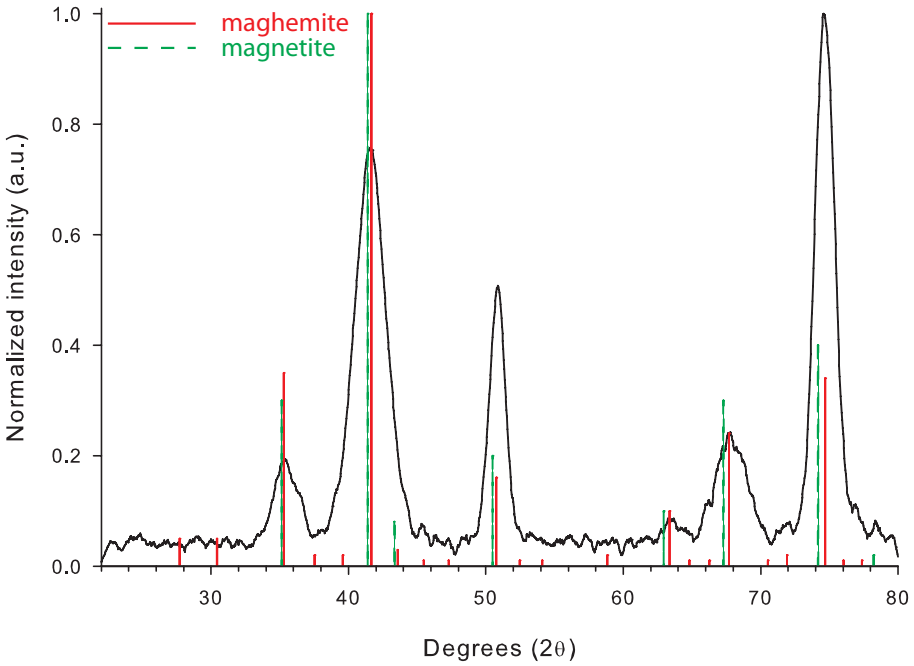

FIGURE 5.13. The XRD pattern of the 8 nm "spheres" can be assigned to maghemite or magnetite, with an average crystallite size of 8 nm.

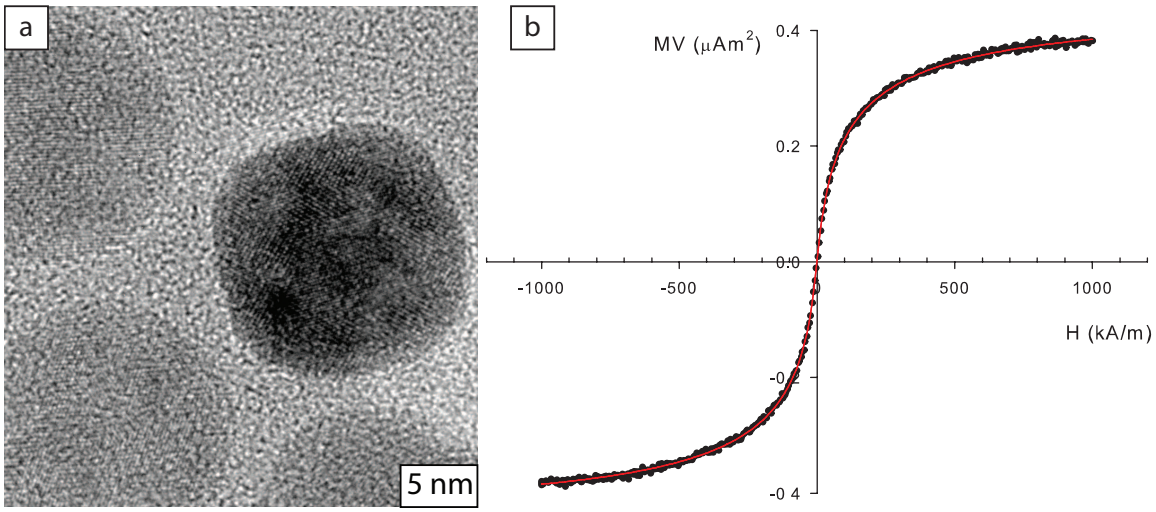

Figure 5.14. High-resolution TEM image of 17 nm "spheres" (**a**) and the total sample magnetic moment MV (corrected for a diamagnetic contribution $\chi_{\text{dia}}VH$, with $\chi_{\text{dia}}V$ of order -10^{-13} m^3) versus external field for a dispersion of these particles in decalin (dots) and its corresponding fit (line) (**b**). From this curve the values $\langle\mu\rangle = 3.73\times10^{-20}$ Am^2, $\sigma_d = 0.41$, and the saturation magnetic moment $MV(H\to\infty) = 0.42$ μAm^2 were obtained.

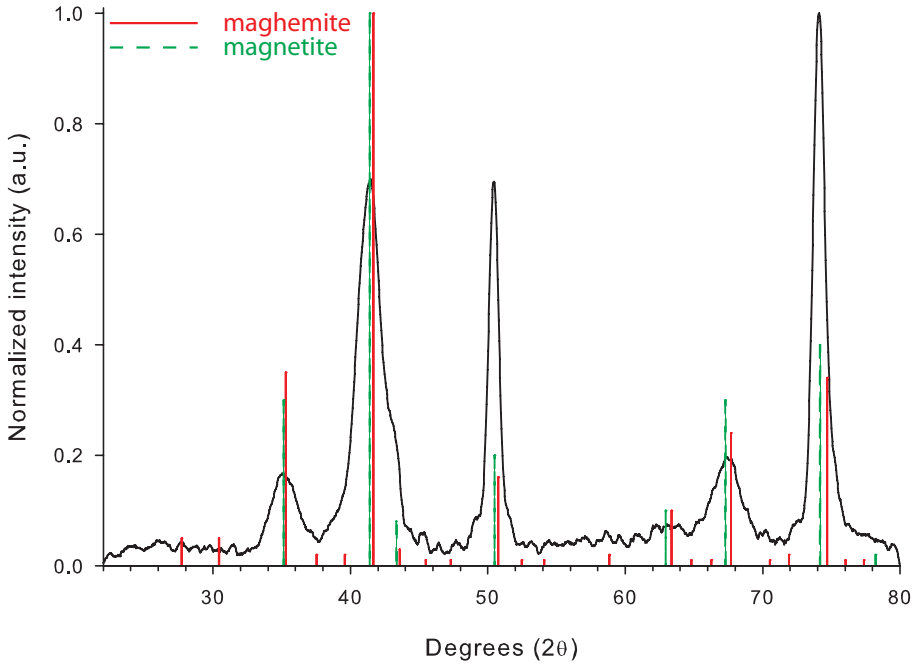

Figure 5.15. The XRD pattern of the 17 nm "spheres" can be assigned to maghemite or magnetite, with an average crystallite size of 13 nm.

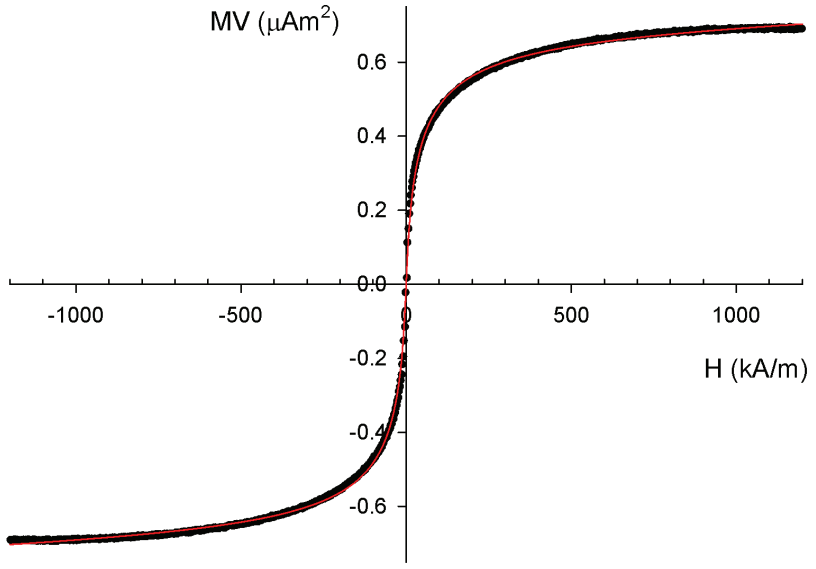

FIGURE 5.16. Total sample magnetic moment MV (corrected for a diamagnetic contribution $\chi_{\text{dia}}VH$, with $\chi_{\text{dia}}V$ of order -10^{-13} m^3) versus external field for a dispersion of 20 nm "sphere" particles in decalin (dots) and its corresponding fit (line) (iron oxide volume fraction: 2.5%). From this curve the values $\langle\mu\rangle = 6.12\times10^{-20}$ Am^2, $\sigma_d = 0.44$, and the saturation magnetic moment $MV(H\to\infty) = 0.73$ μAm^2 were obtained.

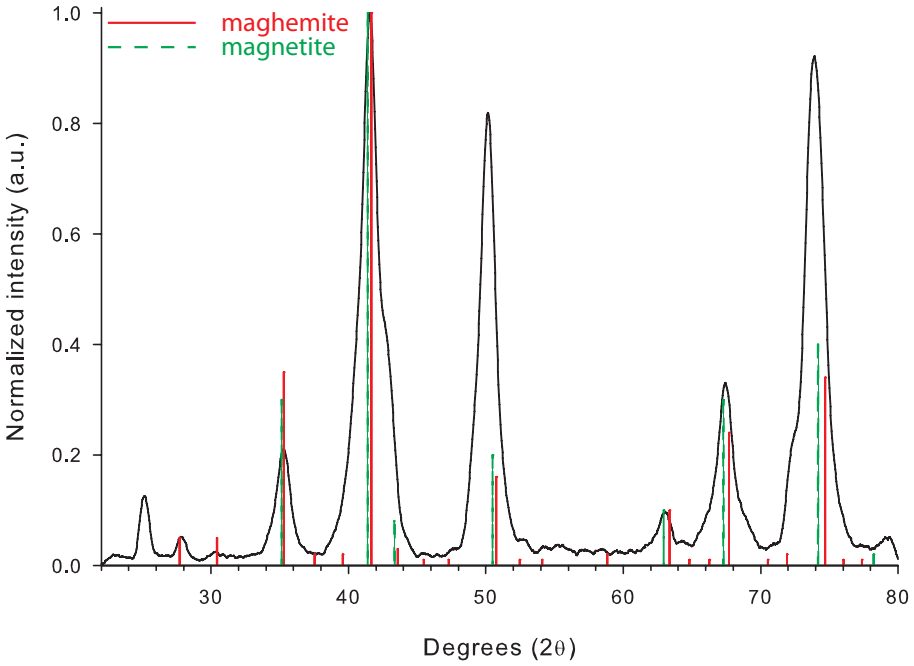

FIGURE 5.17. The XRD pattern of the 20 nm "spheres" can be assigned to maghemite or magnetite, with an average crystallite size of 13 nm.

Part 3

Analytical Centrifugation

6

Analytical Centrifugation of Concentrated Ferrofluids Using a LUMiFuge

Abstract

A LUMiFuge stability analyzer, originally designed to study sedimentation kinetics, is used for the first time to measure the osmotic equation of state of concentrated colloidal dispersions by analytical centrifugation. A liquid colloidal dispersion of strongly light absorbing magnetic nanoparticles is introduced into homebuilt measurement cells with thin glass capillaries of only 50 µm in internal thickness, so that high concentrations of hundreds of grams per liter can be measured. The LUMiFuge has several instrumental drawbacks, such as strong optical broadening of the recorded signal and a relatively short maximum measurement time compared to the time required to establish sedimentation-diffusion equilibrium. The chapter ends with a discussion of the important parameters in the data analysis and their influence on the calculated equation of state. Despite these limitations, accurate equations of state of the strongly absorbing ferrofluid are obtained, independent of rotation rate, by following the elaborate data analysis procedure detailed here.

6.1. Introduction

Analytical centrifugation is a useful technique to analyze colloidal dispersions. It is mostly used for sedimentation-velocity experiments, from which properties such as molecular weights, particle sizes, and particle shapes can be determined [99]. Less common in the colloidal field is using analytical centrifugation to determine sedimentation-diffusion equilibrium profiles. In a typical experiment, a colloidal dispersion is centrifuged and the concentration profile is measured *in situ* as it progresses towards sedimentation-diffusion equilibrium. Once the equilibrium profile is reached, the osmotic equation of state can be determined by integration of the concentration profile, as has been demonstrated both in experiments and in computer simulations [98, 181, 182]. With analytical centrifugation, very low pressures can be measured that cannot be probed via osmometric methods [89].

Only for a few colloidal systems, the equation of state has been determined by an analytical ultracentrifuge (AUC), *e.g.* [96, 98]. One of the main limitations in the use of an AUC for measuring the equilibrium concentration profile is the size of the colloids, since the size of most colloidal particles requires rotation rates lower than generally obtainable by an AUC. The AUC typically operates at rotation rates in the range of 3000–60000 rpm (724–289750 g at a radial distance of 7.2 cm), causing all colloids to be centrifuged to the bottom of the cell and, consequently, no sedimentation-diffusion profile can be measured. Another limitation is that strongly absorbing colloids can only be measured at low concentrations. Here, a LUMiFuge is employed and optimized as an analytical centrifuge to obtain the equation of state of ferrofluids at low rotation rates and high concentrations.

The Stability Analyzer LUMiFuge® was originally designed to study the sedimentation kinetics of industrial dispersions such as anti-settling agents by measuring the spatial and temporal changes in light transmission during centrifugation [102, 183]. It has the advantage that it can operate at very low rotation rates (6–2325 g), enabling the measurement of larger colloids than is possible with the AUC. Additionally, the plastic sample cells can easily be modified, allowing measurements using homebuilt sample cells. Here, thin glass capillaries with an optical path length of only 50 µm are built into the measurement cells. Another advantage is that the LUMiFuge measures at a higher wavelength than conventional AUCs, which allows measurements on concentrated colloidal dispersions that strongly absorb in the visible range and typically absorb less at longer wavelengths.

As a model system, concentrated, strongly absorbing ferrofluids are investigated. These are colloidal dispersions of magnetic nanoparticles in a liquid, and they have been studied previously at low concentration by sedimentation velocity experiments only [101,184]. The influence of particle interactions on the equation of state is expected

at high concentrations, as has been shown for other systems that do not strongly absorb light [96, 97, 182].

In the first section, it is explained theoretically how the equation of state can be obtained from sedimentation-diffusion equilibrium concentration profiles. Subsequently, the experimental methods are described in Section 6.3. In Section 6.4 the procedure to obtain an equation of state from raw LUMiFuge data is explained stepwise. The various limitations of the LUMiFuge are discussed in Section 6.5, and different aspects that are important for the data analysis and their influence on the equation of state are examined in Section 6.6. Finally, concluding remarks are given in Section 6.7.

6.2. Theory

6.2.1. Sedimentation-diffusion equilibrium

Colloidal particles dispersed in a solvent of lower density sediment towards the bottom. When the colloidal system is in equilibrium, there is a balance between sedimentation and the opposing diffusion by Brownian motion as schematically depicted in Figure 6.1a, for a sample in earth's gravity. This balance results in a concentration profile that is directly related to the osmotic equation of state. The osmotic pressure Π can be obtained by integration of this profile, since the profile follows from the force balance:

$$\mathrm{d}\Pi = -\rho(h)\Delta m g \mathrm{d}h \tag{6.1}$$

where ρ is the number concentration of the colloids, Δm is the buoyant mass of a single particle, g is the gravitational acceleration, and h the height, with $\Pi(h \to \infty) = 0$ and $\rho(h \to \infty) = 0$.

For an ideal system, the osmotic pressure is given by Van 't Hoff's law:

$$\Pi = \rho k T \tag{6.2}$$

which leads on substitution in Equation 6.1 to the barometric height distribution:

$$\rho(h) = \rho(h=0)\exp[-\Delta m g h/(kT)] = \rho(h=0)\exp[-h/L_g] \tag{6.3}$$

where k is Boltzmann's constant, T the absolute temperature; $L_g = kT/(\Delta m g)$ is the so-called sedimentational length, i.e. the height at which the number concentration has decreased by a factor 1/e. This height distribution is schematically shown in Figure 6.1b by the solid line. This figure also indicates what happens when interactions start playing a role: the profile is blown up by repulsions, whereas attractions compress the profile. In the low-concentration limit these profiles coincide, as the particles are too far apart to interact. An example of repulsive interactions at higher concentrations is the hard-sphere repulsion, which can be taken into account via the Carnahan-Starling

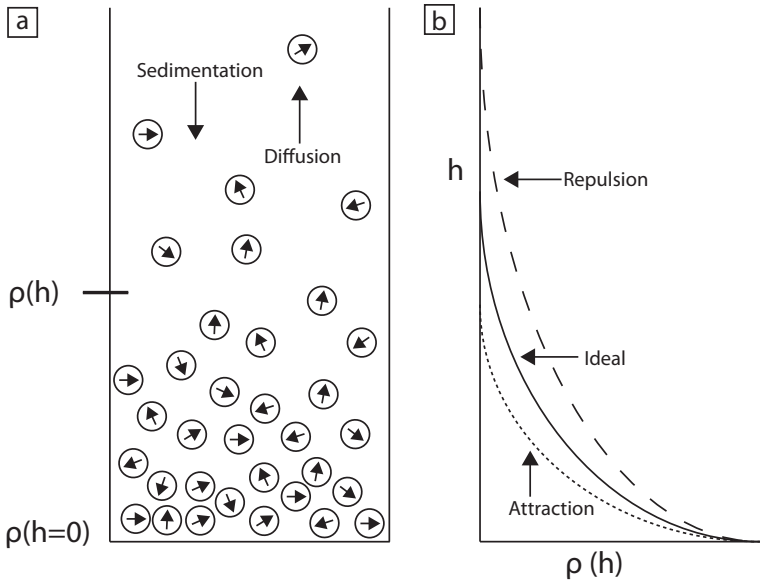

Figure 6.1. Schematic illustration of a sedimentation-diffusion equilibrium concentration profile under earth's gravity (**a**) and of the corresponding height distribution of the concentration ρ (**b**).

equation of state [185]:

$$\Pi = \rho kT \left(\frac{1 + \phi + \phi^2 - \phi^3}{(1-\phi)^3} \right) \tag{6.4}$$

with ϕ the volume fraction.

To measure the equation of state of a colloidal dispersion, analytical centrifugation can be employed. In a centrifugal field with angular velocity ω, the force balance reads, instead of Equation 6.1:

$$\mathrm{d}\Pi = \rho(r)\Delta m \omega^2 r \mathrm{d}r \tag{6.5}$$

where r is the distance from the center of the rotor. Here, $\Pi(r \to 0) = 0$ and $\rho(r \to 0) = 0$.

The osmotic pressure can be obtained by integration of Equation 6.5, without any assumption on the underlying particle interactions:

$$\Pi(\rho(r^{'})) = \Delta m \omega^2 \int_0^{r^{'}} \rho(r) r \mathrm{d}r \tag{6.6}$$

If the system behaves ideally, the concentration at position r follows from substitution of Equation 6.2 in Equation 6.5:

$$\rho(r) = \rho(r_b) \exp \left[\frac{\omega^2 \Delta m (r^2 - r_b^2)}{(2kT)} \right] \tag{6.7}$$

in which $\rho(r_b)$ is the number concentration at the bottom position r_b.

In the LUMiFuge, a signal that is proportional to the transmission T is measured as a function of the radial distance r. The transmission is related to the colloid concentration

via Lambert-Beer's law:

$$A = \epsilon c l = -\log T \tag{6.8}$$

with A the absorbance, ϵ the extinction coefficient (in m^2kg^{-1}), c the colloid concentration (in kgm^{-3}) and l the optical path length (in m). From the experiments we calculate the concentration profile using:

$$c = c_0 \frac{-\log T}{-\log T_0} \tag{6.9}$$

with c_0 and T_0 the starting concentration and transmission respectively.

When the concentration at each position is known, the osmotic pressure is obtained by integration via Equation 6.6, starting from the point where the colloid concentration is zero, and hence Π=0, using:

$$\Pi(r) = \Pi(r - \Delta r) + \rho(r)\Delta m \omega^2 r \Delta r = \Pi(r - \Delta r) + c(r) f_b \omega^2 r \Delta r \tag{6.10}$$

where Δr is the integration step width of 14 μm, determined by the resolution of the detector of the LUMiFuge. $c(r)$ is the mass concentration obtained from the measurements, which is multiplied by a factor $f_b = \Delta m/m$, with m the mass of a single particle, such that the concentration in terms of buoyant mass is used in the integration.

6.2.2. Choice of the rotation rate

The rotation rate of the LUMiFuge used in an experiment was chosen by calculating the acceleration that is required to obtain a sedimentation length of 1 mm, the liquid column height in the samples being several millimeters. From Equation 6.3 the sedimentation length is $L_g = kT/(\Delta m g)$. The required acceleration a in a centrifuge is calculated using $a = Ng = kT/(L_g \Delta m)$, with N an integer. The required accelerations for L_g = 0.5 and 1.5 mm were also calculated for control experiments, since the measured equation of state should be the same for different rotation rates. This calculation is an estimate, since it assumes ideal behavior and radial independence of the acceleration within the small radial distance in which the sample is measured.

6.2.3. Estimate of experimental time scale

The time to reach sedimentation-diffusion equilibrium in a measurement can be estimated by considering the sedimentation velocity in the low-concentration limit, given by

$$u = \frac{2}{9} \frac{R^2 \Delta \rho a}{\eta} \tag{6.11}$$

with R the core radius of the colloid, $\Delta\rho = \rho_{mag} - \rho_s$ with ρ_{mag} the density of the magnetic core and ρ_s the density of the solvent, a the acceleration, and η the viscosity of the solvent. By dividing the liquid column height of the sample by this velocity, an expected equilibration time is obtained.

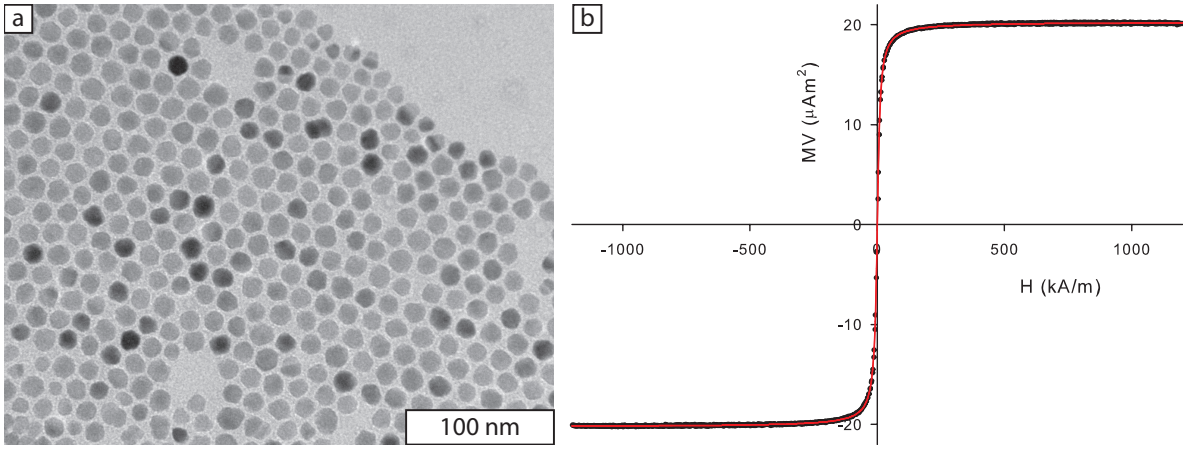

Figure 6.2. **(a)** TEM image of iron oxide nanoparticles with an average size of 13.4 nm (± 11%). **(b)** Total magnetic moment MV versus the external field H of an 8 wt% dispersion of the particles in decalin (dots) and corresponding fit (line). The average magnetic dipole moment of 4.3×10^{-19} Am^2 was obtained from a more dilute sample where interparticle magnetic interactions are negligible.

6.3. Experimental

6.3.1. Magnetite system

Magnetic iron oxide nanoparticles dispersed in a solution of 15.6 mM oleic acid in decalin were used as a colloidal model system and studied by analytical centrifugation. These particles were prepared by a seeded growth method, as described in Chapter 4. Here, particles from series 18 were used, which are magnetite particles with an average size of 13.4 nm (± 11%) from TEM. A TEM image and magnetization curve of these particles are shown in Figure 6.2. The average dipole moment of these particles is 4.3×10^{-19} Am^2, determined by measuring and fitting the magnetization curve using an alternating gradient magnetometer, as described in Chapter 5.

6.3.2. LUMiFuge

Sedimentation-diffusion equilibrium concentration profiles were measured using a Stability Analyzer LUMiFuge®. This is a centrifuge in which the change of transmission as a function of radial position can be measured in time. A pulsed NIR-LED illuminates the sample cell at a wavelength of 880 nm and the transmitted light is detected by a CCD-line of 2048 elements positioned every 14 μm, as displayed schematically in Figure 6.3a. The rotation rate ranges from 200 to 4000 rpm, corresponding to 6 to 2325 times earth's gravity at the bottom of the sample cell, 0.13 m from the rotor axis. The rotor can contain up to 8 measurement cells. The type of measurement cells used here is shown in Figure 6.3b, and these are modified for concentrated samples as discussed in the next section. The standard maximum measurement time of the LUMiFuge of

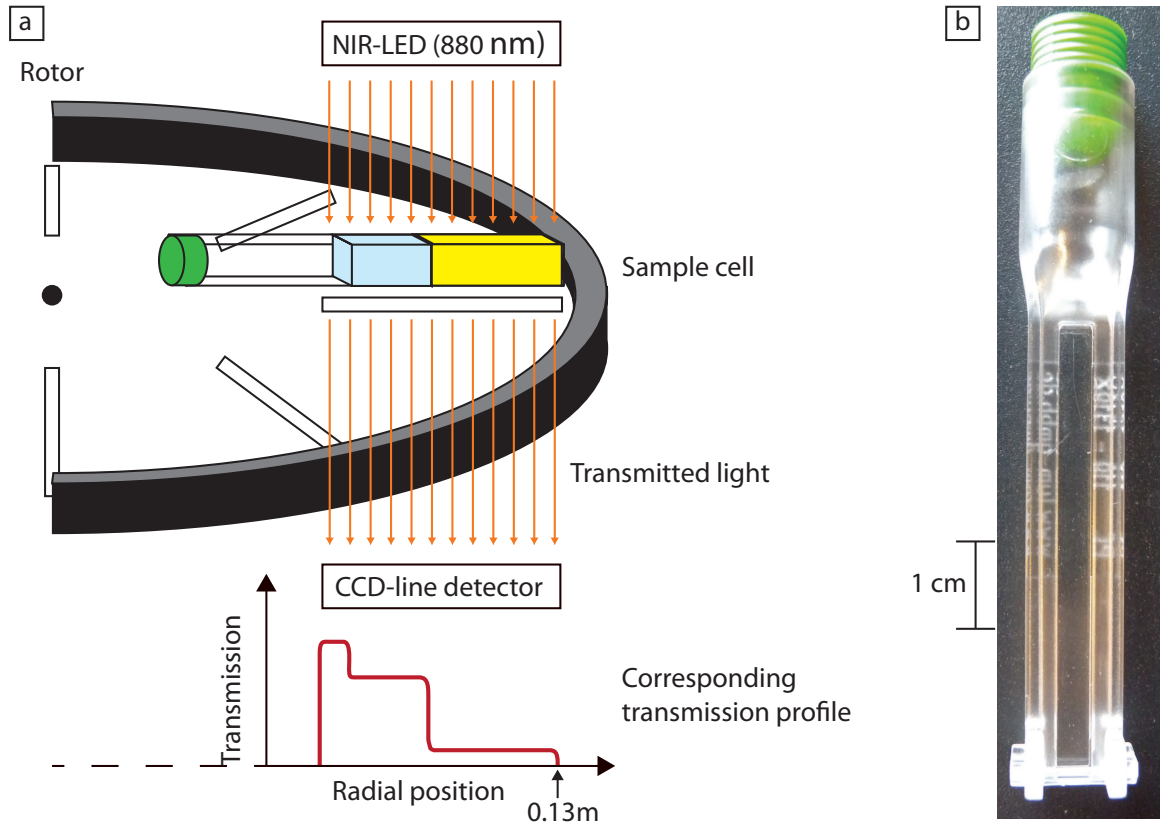

Figure 6.3. **(a)** Schematic illustration of the LUMiFuge and how a transmission scan is obtained. **(b)** Empty LUMiFuge measurement cell.

48 hours was upgraded to a maximum of 99 hours. For equilibration measurements taking a longer time, new measurements were started at intervals shorter than 99 hours, keeping the time between two measurements as short as possible (maximum a few minutes).

6.3.3. Preparation of sample cells

To enable the measurement of highly concentrated samples, flat capillaries with a maximum length of 20 mm, only 50 µm in internal thickness, and 1 mm in width were built into the LUMiFuge sample cells, by first preparing homebuilt metal capillary holders as depicted stepwise in Figure 6.4. Transparent two-component epoxy glue was used (Bison Kombi Snel®), that could be manipulated for about 5 minutes before becoming too viscous. First, two metal plates with a slit are glued on top of each other, by applying the glue only at the spherical holes. One of these slits was slightly wider than the capillary (1.2 mm), whereas the other was slightly more narrow (0.9 mm), to enable the positioning of the capillary in the middle of the sample cell where the transmission was measured (see Figure 6.4a). After drying of the glue, the metal slits were glued on top of a thin glass plate of 0.15 mm in thickness with the thin slit on

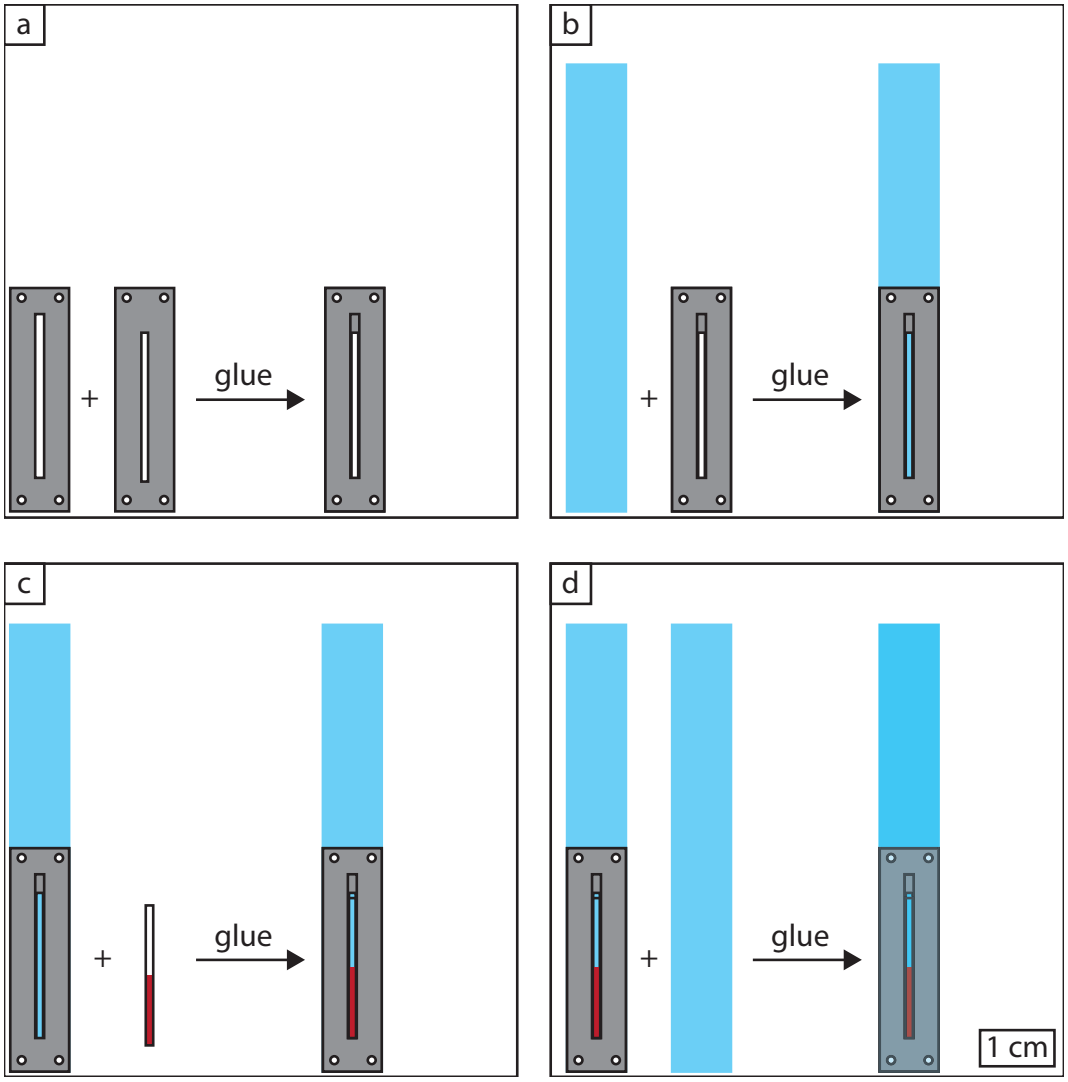

Figure 6.4. Preparation of the metal capillary holder containing a concentrated sample for LUMiFuge measurements: First two metal plates with slits of slightly different widths are glued on top of each other (**a**). This metal unit is glued on a thin piece of glass (**b**), after which the capillary with sample is placed in the glue (**c**). Finally, another thin glass plate is glued on top (**d**).

the bottom side (Figure 6.4b), and a small piece of cardboard was used to apply the glue by smoothing. On top of this metal holder, more glue was applied in the same way. Subsequently, a capillary was filled with the colloidal dispersion, wiped clean on the outside, and placed into the glue in the middle of the metal holder (Figure 6.4c). More glue was applied, and air bubbles were removed by smoothing using the piece of cardboard, which is important because such bubbles scatter light and greatly decrease the measured signal. Finally, a second thin glass plate was glued on top (Figure 6.4d).

Alternatively, the capillary could be sealed by glue first and then glued within the metal capillary holder via its two extremities only. This method was applied to the

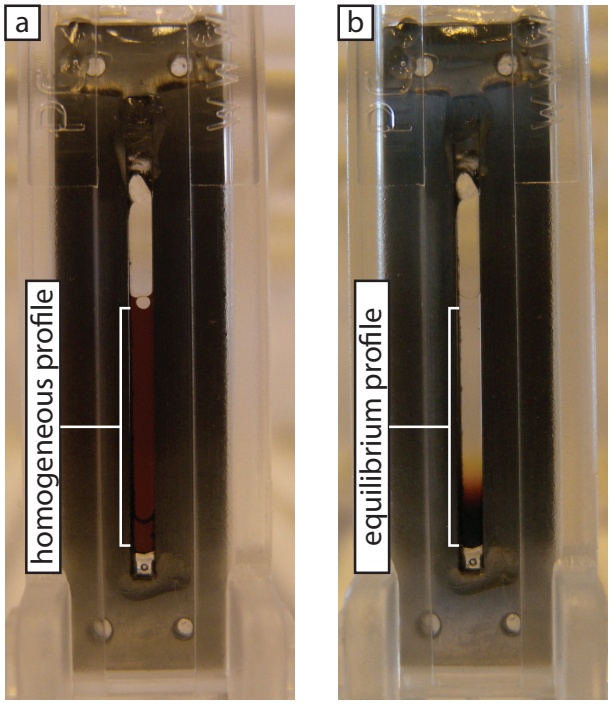

Figure 6.5. Homebuilt LUMiFuge capillary sample cell, with a concentrated dispersion of magnetite colloids in a 50 μm thin capillary. Before equilibration in the LUMiFuge, the sample color is homogeneous **(a)**, and after equilibration, the sedimentation-diffusion equilibrium concentration profile is visible by the increasing absorption towards the bottom of the sample **(b)**.

sample discussed in this chapter. This way, no glue is on the faces of the capillary itself, enabling measurement of a more homogeneous transmission profile. However, care should be taken when glueing the capillary into the metal holder that glue does not flow into the metal slits, since it is not possible to smooth (homogenize) the glue anymore.

After drying, the edges of the metal capillary holder unit were filed to remove excess glue. Finally, the metal holder with the sample capillary was glued into a standard plastic LUMiFuge sample cell (Figure 6.3b), which has an internal thickness of 2 mm, and an internal width of 1 cm. The resulting model sample discussed in this chapter is shown in Figure 6.5. The metal plates can be reused after dissolution of the sample cell in dimethylformamide.

6.3.4. Sedimentation-diffusion equilibrium measurements

Oppositely positioned sample cells were balanced to less than 0.1 g difference by adding pieces of parafilm at the top caps of the measurement cells before placing them in the LUMiFuge. All measurements were performed at 22.0 ± 0.5 °C, using a light factor (a measure for the lamp intensity) of 1.00. A measurement, the way it is described here, consists of 255 transmission scans, in which the time interval programmed

between 2 subsequent scans determines the total time that the total measurement of 255 scans takes. Two types of measurements were performed: long equilibration measurements with the maximum amount of time of 1400 seconds between the recording of two transmission scans, and short measurements with the minimum amount of time of 10 seconds between the recording of two transmission scans. In both cases, the maximum of 255 scans was measured, hence a short measurement took about 42 minutes, whereas a long measurement took almost 99 hours, unless it was interrupted sooner.

First, 11 short measurements of 255 scans each were performed to be able to average enough data of the starting transmission profile. Subsequently, long measurements were performed, interrupted at different times to start a new long measurement. In between almost every long measurement a short measurement was performed. These short measurements were compared to each other to determine when sedimentation-diffusion equilibrium had been established. When equilibrium was reached at a certain rotation rate, 11 short measurements were performed before increasing the rotation rate. The rotation rates discussed in this chapter are 500, 625, and 1000 rpm corresponding to 36, 57, and 145 times the gravitational acceleration, respectively.

6.3.5. Absorption measurements

For the measurement of UV-Vis absorption spectra of very concentrated samples, flat capillaries with an internal thickness of 50 μm (as described in Section 6.3.3) were filled with a dispersion of iron oxide nanoparticles of 17 nm in diameter. These particles were prepared using the Hyeon method described in Chapter 4 and dispersed in a 15.6 mM solution of oleic acid in decalin. These capillaries were sealed by glue, after which they were attached to a metal slit with a slit width of 0.9 mm using sticky tape. As a reference, a capillary was filled with the 15.6 mM solution of oleic acid in decalin. Subsequently, the absorption spectra were measured with a PerkinElmer Lambda 35 UV-Vis Spectrometer in the range of 200 to 1100 nm, using a slit width of 4 nm.

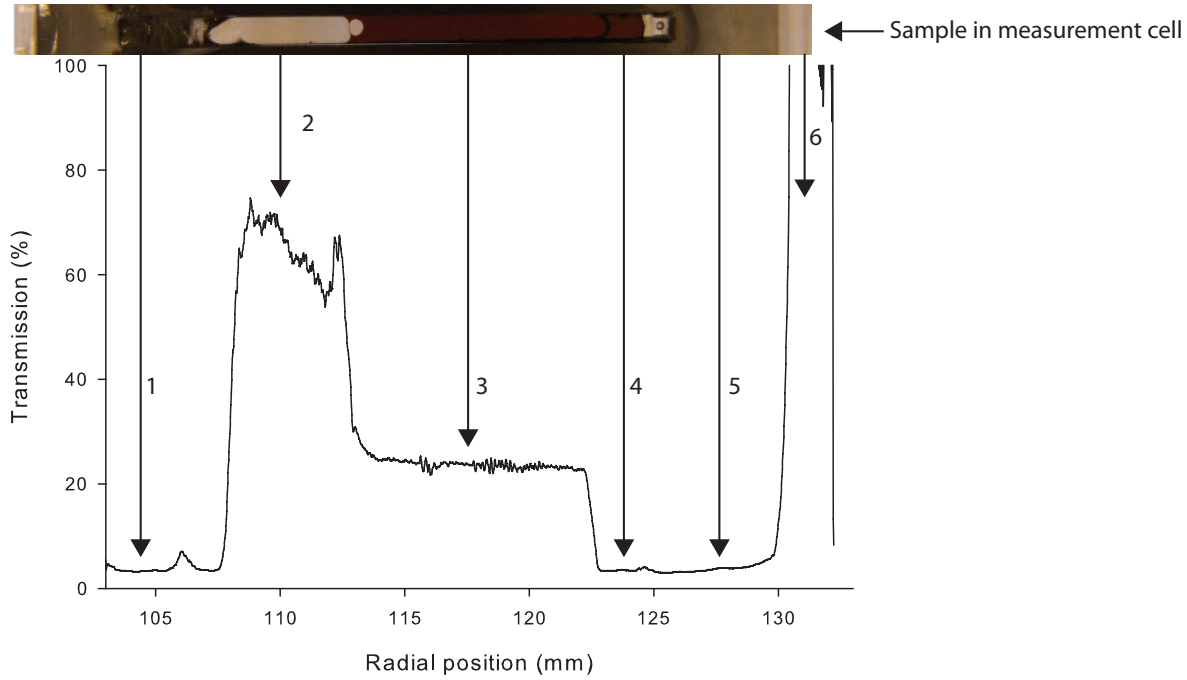

Figure 6.6. Raw transmission data at the start of the measurement, with a picture of the sample at the position approximately corresponding to the measured data. The arrows with a number indicate the different regions: **1.** No transmission due to the metal. **2.** High transmission where the capillary is empty. **3.** Significant decrease in transmission due to the magnetic fluid. **4.** Although sample and air can still be visibly observed in the measurement cell, transmission at the measured wavelength is zero due to the presence of glue bubbles. **5.** No transmission due to the metal. **6.** The bottom of the plastic LUMiFuge sample cell, where higher transmission is observed.

6.4. Data analysis

In this section, the analysis procedure is described step by step, from the primary data as obtained from the LUMiFuge to the equation of state of the colloidal dispersion. The uncertainties of the data analysis will be discussed in Section 6.6.

The LUMiFuge records the relative transmission of the sample as a function of radial position. It can record a maximum of 255 transmission scans per measurement. To reduce digital noise, 11 of such measurements were performed and averaged. All data shown below were obtained after averaging 11 measurements, each measurement containing 255 transmission scans. In Figure 6.6 the raw data at the start of the measurement series are shown, together with the sample cell to indicate the different regions that can be found in the transmission profile. At the top of the transmission profile there should be no transmission due to the metal plates (1). The signal recorded here is a background signal that is subtracted from the data in further analysis. It is a

spurious signal of the equipment that is also recorded when the sample space is filled with non-transmitting material, such as the metal in this case. Next, the transmission at the top of the capillary where no sample is present is observed (2). This transmission decreases significantly at the position where the ferrofluid is present (3). The transmission is constant over the range where magnetic particles are present, since no glue was applied on this part of the capillary. However, there is glue present at the bottom of the capillary, with bubbles that cause significant attenuation of the transmission signal (4), and no signal from the sample in this bottom region can be detected. The transmission is as low as where the metal plates are present (5). At the bottom of the plastic sample cell itself, the transmission increases dramatically (6).

The same primary data at the start of the experiment are shown in Figure 6.7, after subtraction of the background. Transmission profiles are shown for sedimentation-diffusion equilibrium at 3 rotation rates (500, 625, and 1000 rpm). Upon centrifugation of the sample, the transmission at the top of the sample increases, as the particles move towards the bottom. Likewise, the concentration of the particles at the bottom of the sample increases and hence the transmission decreases. From the transmission profiles it can be seen that the concentration towards the bottom increases more for higher rotation rates. It is also noteworthy that the bottom part of the capillary is not measured, as the transmission profile for 1000 rpm does not display a decrease in concentration compared to the starting profile: this occurs at the radial position that is not measurable due to the glue bubbles (see Figure 6.6).

To calculate the concentration profile using Equation 6.9, the starting concentration c_0 and the starting transmission T_0 of the dispersion need to be known. The latter can determined from the region that is depleted of colloids using

$$T_0 = \frac{T_{\text{start}}}{T_{\text{end}}} \tag{6.12}$$

with T_{start} the transmission of the cell (including optical imperfections) at the start of the measurement and T_{end} the transmission of the cell at equilibrium, in the region depleted of colloids. This region is given by the plateau in a graph of the $T_{\text{start}}/T_{\text{end}}$ ratio versus radial position, as indicated in Figure 6.8. The value of T_0 obtained at 1000 rpm is used in further analysis, since at lower rotation rates the dispersion may not yet be fully depleted of colloids in this range.

Now that T_0 is known, the absorption can be calculated also at all other radial positions, using:

$$A = -\log\left(T_0 \frac{T_{\text{end}}}{T_{\text{start}}}\right) \tag{6.13}$$

The resulting absorption profile is shown in Figure 6.9.

In principle the average size of the particles is known from TEM measurements, and a buoyant mass could be calculated. However, this would necessitate assumptions about

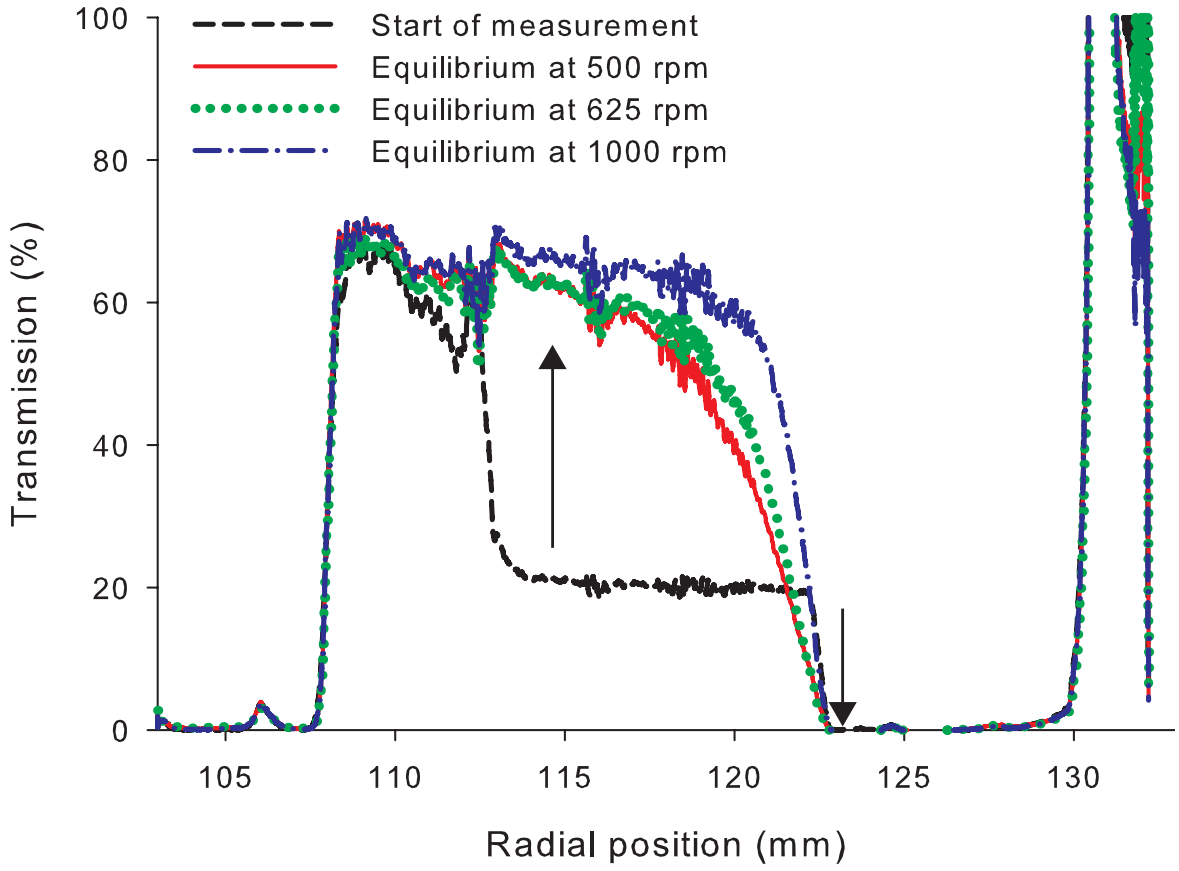

Figure 6.7. Primary transmission data after subtraction of the background for 13 nm magnetite particles at the start of the measurement (dashed line), and after reaching equilibrium after centrifugation at 500 rpm (solid line), 625 rpm (dotted line), and 1000 rpm (dash-dotted line). Higher in the sample (lower radial position), the transmission increases (left arrow) due to sedimentation of the particles towards the bottom. At the bottom the concentration of particles increases, and hence the transmission decreases (right arrow).

the three-dimensional shape and the density of the particles. Hence, it is better to obtain the buoyant mass directly from the measured data. From Equation 6.7 we know the mass concentration $c(r)$:

$$c(r) = c(r_b)\exp\left[\frac{\omega^2 \Delta m}{2kT}(r^2 - r_b^2)\right] \tag{6.14}$$

Replacing the concentration by absorbance using Lambert-Beer's law and rearranging gives:

$$\mathrm{Ln}\frac{A(r)}{A(r_b)} = \frac{\omega^2 \Delta m}{2kT}(r^2 - r_b^2) \tag{6.15}$$

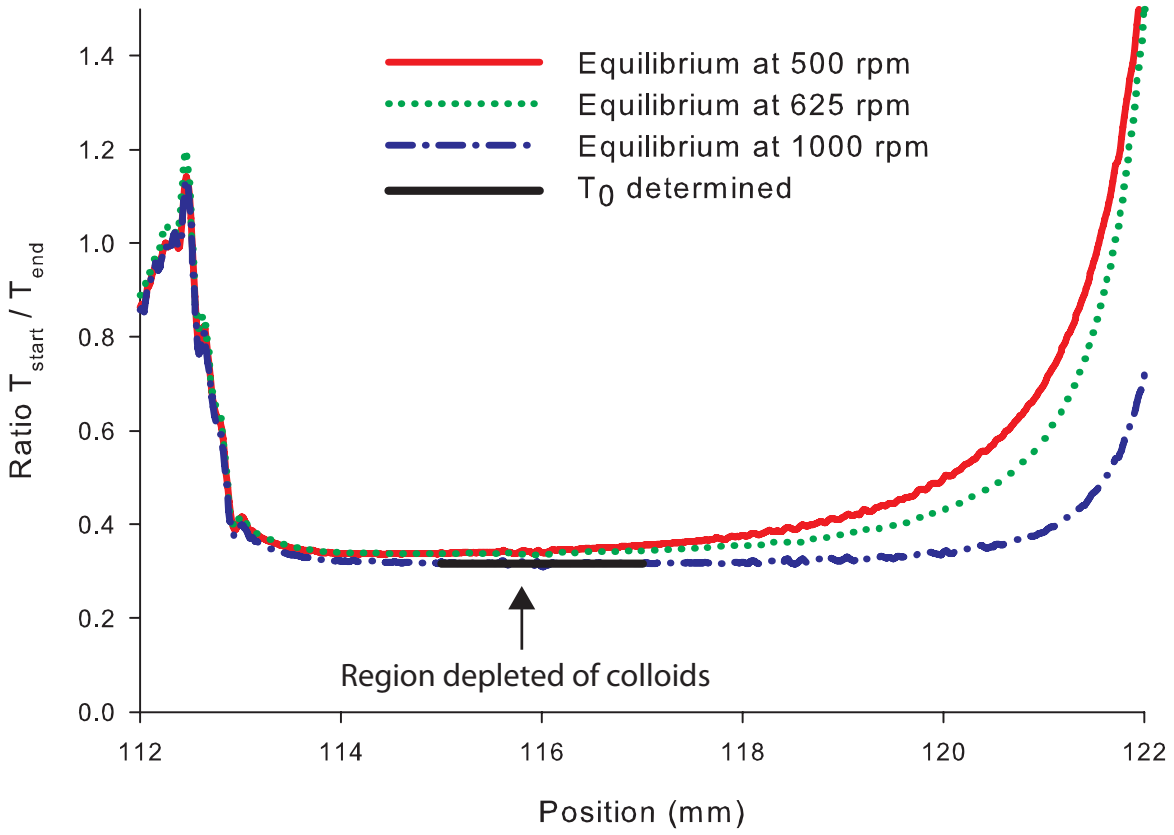

Figure 6.8. Ratio of the transmission at the start of the equilibration measurement divided by the transmission at equilibrium for 3 rotation rates. In the region where this ratio reaches a plateau, the sample is depleted of colloids and the starting transmission T_0 can be determined, as indicated by the thick line.

Therefore, by plotting $\mathrm{Ln}A(r)$ as a function of r^2, we can obtain the buoyant mass from the slope given by:

$$\text{slope} = \frac{\omega^2 \Delta m}{2kT} = \frac{\omega^2 \frac{4}{3}\pi R_{core}^3 (\rho_{mag} - \rho_s)}{2kT} \tag{6.16}$$

From this buoyant mass, the size of the particles can also be obtained if a spherical shape is assumed, as shown in the right-hand side of the equation. Here, R_{core} is the radius of the core of the particle, ρ_{mag} is the density of the magnetite core and ρ_s is the density of the solvent.

In Figure 6.10 the slopes of $\mathrm{Ln}A(r)$ versus r^2 are shown, with their fits indicated by the solid lines for the three rotation rates. Ideally, at low r^2 a straight line should be obtained. However, due to noise this is not the case. Therefore the fit was performed in a range of low concentration, but not yet too noisy. It can already be seen by eye that the slopes are not the same at different rotation rates. The buoyant masses obtained from the fits at 500, 625, and 1000 rpm are 5.6×10^{-21} kg, 4.0×10^{-21} kg, and 3.3×10^{-21}

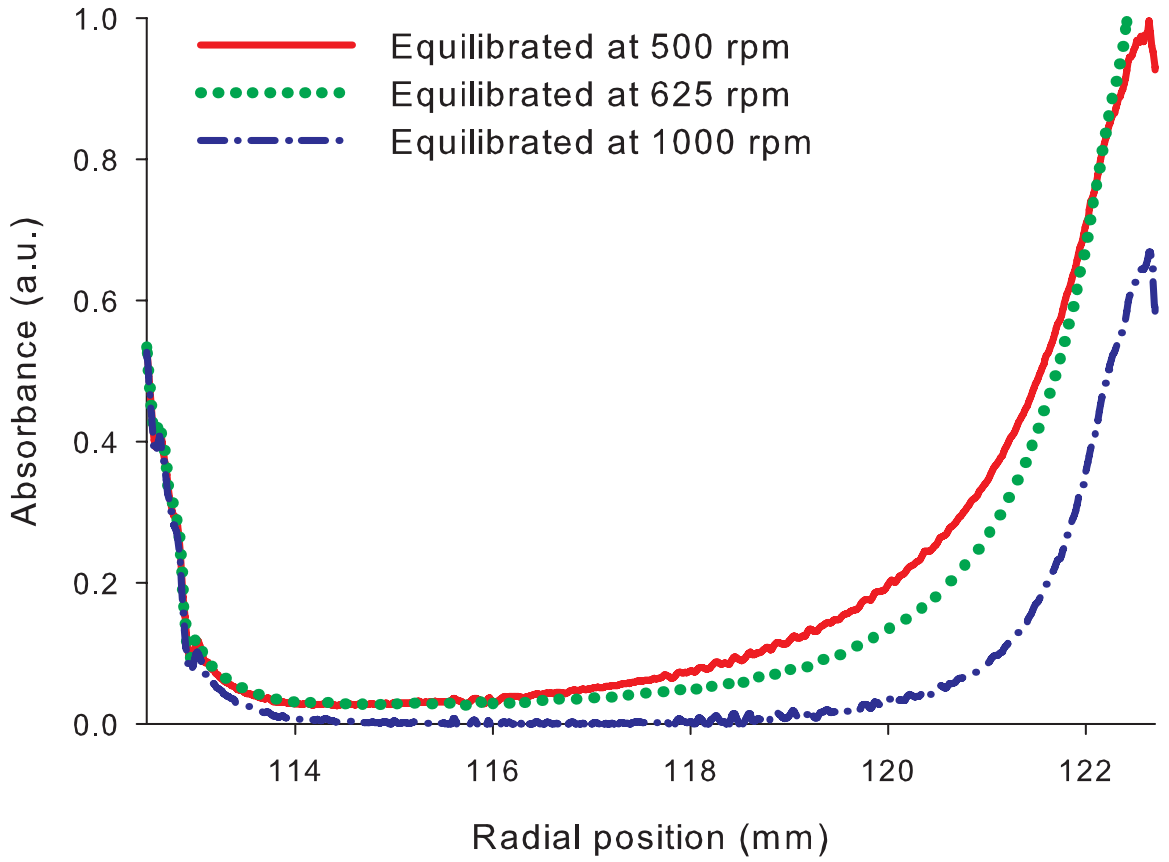

Figure 6.9. The absorbance of 13 nm magnetite particles versus radial position for three different rotation rates: 500 rpm (solid line), 625 rpm (dotted line) and 1000 rpm (dash-dotted line).

kg, corresponding to diameters of 13.6 nm, 12.1 nm, and 11.3 nm, respectively. Clearly, fractionation is taking place due to the polydispersity of the sample, despite it being only 11%. Larger particles end up lower in the profile, an effect which is more pronounced at higher rotation rates.

Polydispersity can also cause a further deviation in the plot of $\mathrm{Ln}A(r)$ versus r^2, an effect discussed in Chapter 8.

At the lowest concentrations high in the profiles, noise is significant, and optical reflections from the liquid-air meniscus hamper an accurate determination of the concentration profile. Nevertheless, to determine the equation of state, integration of the concentration profile must be started at a very low concentration, assuming that the osmotic pressure is zero at that point. To obtain a more accurate low concentration regime, the fitted line in Figure 6.10 is extrapolated to much lower absorptions, since in this very dilute regime the colloids behave ideally.

The concentration profile is calculated using Equation 6.9 and multiplied by the factor $f_b = \Delta m/m$ to correct for buoyancy. For each rotation rate, the buoyant mass, Δm, is

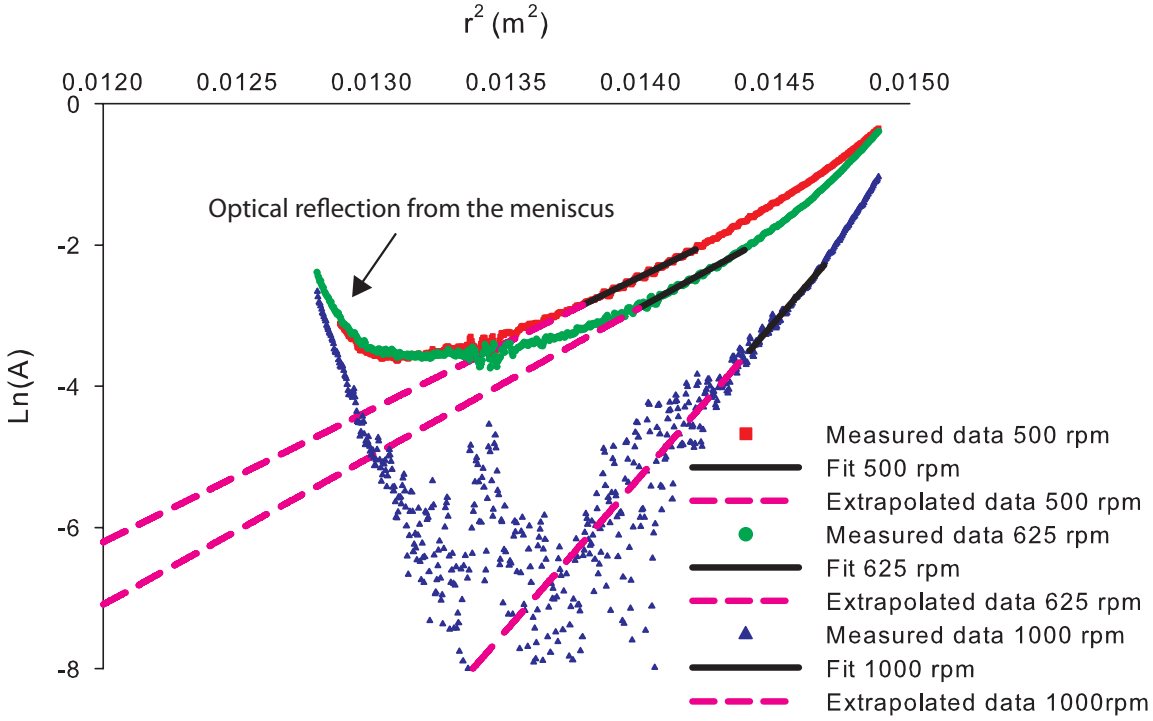

Figure 6.10. Graph of Ln(A) as a function of r^2 for magnetite particles equilibrated at 500 rpm (squares), 625 rpm (spheres) and 1000 rpm (triangles). The regions that are fitted are indicated by solid lines, whereas the extrapolated data from this fit are indicated by dashed lines.

calculated from the slope of Ln$A(r)$ versus r^2, using the left-hand side of Equation 6.16. To calculate the non-buoyant mass, m, the size obtained from the right-hand side of Equation 6.16 is used and an oleic acid shell thickness of 2 nm is assumed. The masses and sizes obtained at the specific rotation rate are used to calculate the concentration profile. The data in the low concentration range are replaced by the extrapolated data points. The concentration profiles for the three rotation rates are shown in Figure 6.11. For equilibrium at 500 rpm, the concentration profile calculated from the raw data is also shown, without the extrapolation at low concentrations, where the concentration clearly does not reach zero.

The osmotic pressure is calculated from the buoyant concentration using Equation 6.10, starting at the lowest concentration, where Π is set to 0. The resulting equations of state are shown in Figure 6.12 where the non-buoyant mass concentration is used on the horizontal axis to indicate that this sample was measured up to concentrations of 300 kg/m^3. Clearly, these equations of state differ from each other, which is due to the use of different buoyant masses for the calculations at different rotation rates. A better way to compare these equations of state is in terms of the number concentration, calculated

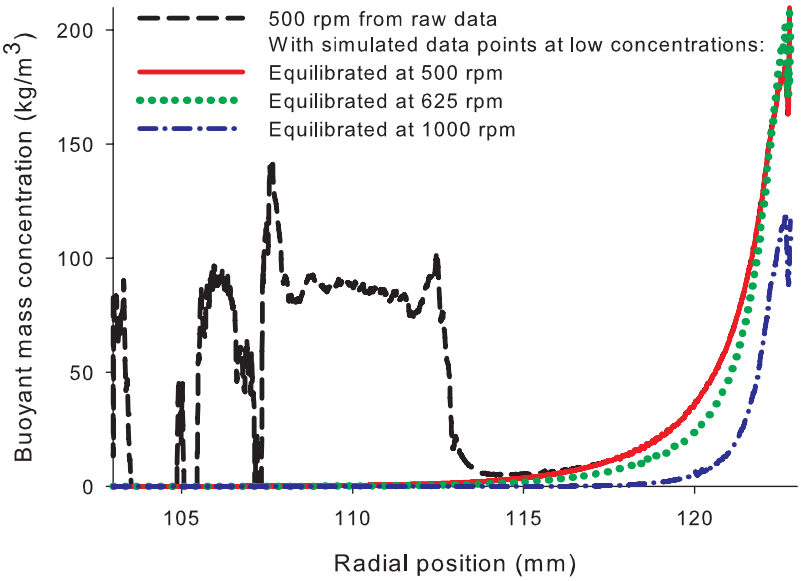

Figure 6.11. The concentration profiles of 13 nm magnetite particles as a function of radial position at 500 rpm (solid line), 625 rpm (dotted line) and 1000 rpm (dash-dotted line). Data at low concentrations (positions closest to the center of the rotor) are obtained from the extrapolated absorption data (see text). For comparison the concentration profile at 500 rpm as obtained from raw data (dashed line) is shown.

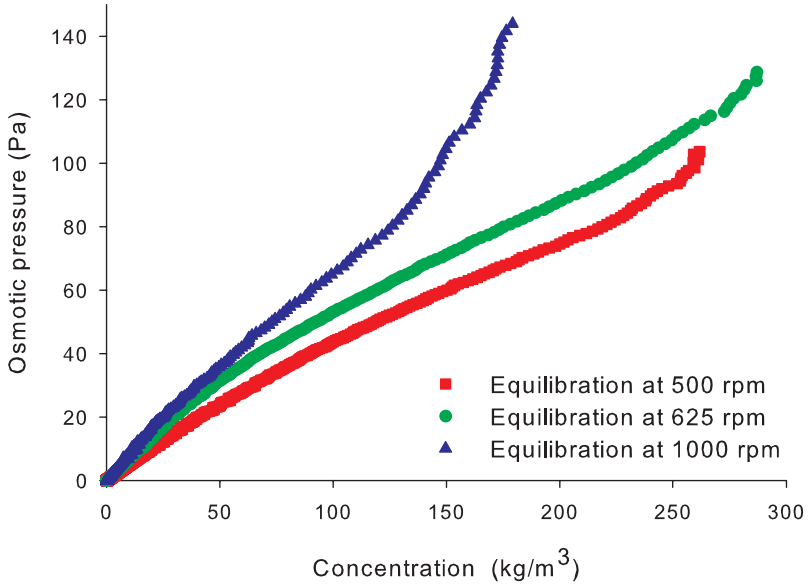

Figure 6.12. Osmotic pressure of 13 nm particles as a function of the (non-buoyant) mass concentration for equilibration at 500 rpm (squares), 625 rpm (spheres) and 1000 rpm (squares). The non-buoyant mass concentration is used on the horizontal axis to indicate that this sample was measured up to concentrations of 300 kg/m^3.

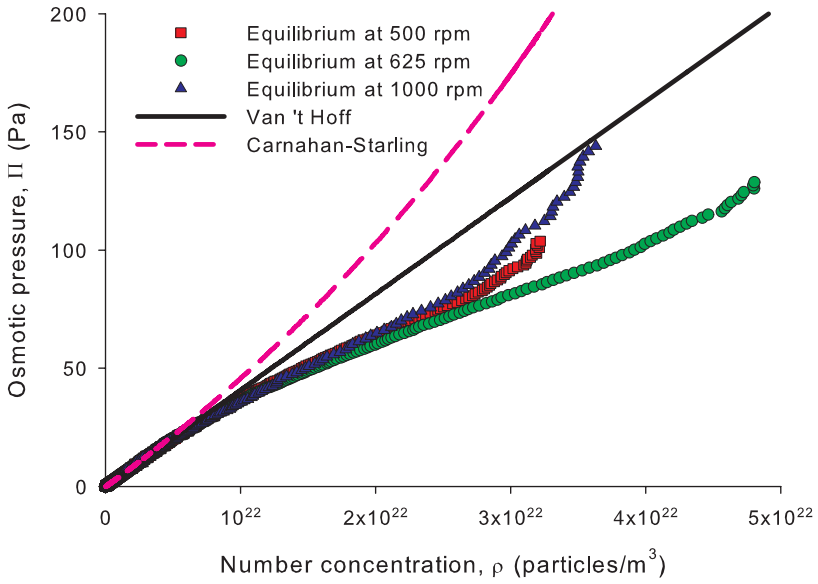

FIGURE 6.13. Osmotic pressure of 13 nm magnetite particles as a function of the number concentration for equilibration at 500 rpm (squares), 625 rpm (spheres), and 1000 rpm (squares). The corresponding Van 't Hoff equation (solid line, Equation 6.2) as well as the Carnahan-Starling equation for hard spheres (dashed line, Equation 6.4) are shown. The equations of state determined at 500, 625, and 1000 rpm agree with each other up to about 2.5×10^{22} particles per m^3.

by dividing the mass concentration $c(r)$ by the mass m, or the buoyant concentration, $c_{buoyant}(r)$, by the buoyant mass, Δm:

$$\rho(r) = \frac{c(r)}{m} = \frac{c_{buoyant}(r)}{\Delta m} \tag{6.17}$$

The volume fraction, ϕ, required for the calculation of Carnahan-Starling's equation of state (Equation 6.4), is obtained using:

$$\phi = \frac{c_{buoyant}(r)}{\rho_{buoyant}} = \frac{c_{buoyant}(r)}{\frac{\frac{4}{3}\pi R_{core}^3(\rho_{mag}-\rho_s)}{V_{tot}}} = \frac{c_{buoyant}(r)}{\frac{\frac{4}{3}\pi R_{core}^3(\rho_{mag}-\rho_s)}{\frac{4}{3}\pi(R_{core}+d_{shell})^3}} \tag{6.18}$$

with $\rho_{buoyant}$ the 'buoyant' density, calculated using the radius of the core of the particle, R_{core}, the thickness d_{shell} of the oleic acid shell taken to be 2 nm, and ρ_{mag} and ρ_s the densities of the core and shell respectively.

The osmotic equations of state in terms of number concentration are shown in Figure 6.13 where all 3 rotation rates overlap for a wide measurement range. All samples follow Van 't Hoff's law (Equation 6.2) at low concentrations, which is expected in the diluted regime. Importantly, the simulated data run up to pressures of 7–10 Pa, which enforces Van 't Hoff's law for the initial part of the graph. The fact that all samples follow Van

't Hoff's law up to pressures of at least 20 Pa justifies this assumption. At pressures above 30 Pa, the equations of state start deviating from ideal behavior. For hard sphere repulsions, the particles should follow the Carnahan-Starling equation of state as given by Equation 6.4. However, the opposite is found: the equations of state even fall below Van 't Hoff's law, which indicates attractions due to the magnetic properties of the particles, assuming that Van der Waals forces are negligible. Also polydispersity may contribute to the curves in Figure 6.13, as further discussed in Chapter 8. Nevertheless, whether polydispersity, magnetic interactions or even other factors are contributing to this effect, the rotation rate-independent equations of state in Figure 6.13 demonstrate that the equations of state of concentrated ferrofluids can be accurately measured using a LUMiFuge according to the described procedure.

6.5. Instrumental limitations

6.5.1. Measurement timing

In principle, the LUMiFuge was not designed for long-term measurements, which has several disadvantages. Firstly, due to the maximum of 99 hours of measurement time, several consecutive 99 hour measurements are required for most sedimentation-diffusion equilibrium measurements. Consequently, the samples are not kept at the same rotation rate, since it drops to zero between each new measurement. Rotation at the required equilibration speed also has to be interrupted to obtain more than 255 transmission scans for averaging to decrease the digital noise. Although the time period between two measurements can be limited to a few minutes only, this may cause disturbance of the concentration profile; fortunately this is limited by the confined geometry of the narrow glass capillaries used.

Moreover, the LUMiFuge requires a temperature equilibration step at the start of each measurement. It performs this measurement at a predefined rotation rate of 2000 rpm. This step can be stopped manually, but only after reaching this rotation rate. In principle it is assumed that the samples are inserted after the temperature equilibration step, but in our case the samples have to be left in the rotor. The disadvantage is that with consecutive measurements, the samples that have to be kept in the rotor will briefly be accelerated to 2000 rpm. It is important to stop this temperature equilibration step as soon as possible. The first measured transmission scans may be slightly different from equilibrium due to this acceleration at 2000 rpm.

Another disadvantage with the LUMiFuge is that the acceleration rate and deceleration rates cannot be controlled. A slower deceleration can be programmed by decreasing the set rotation speed stepwise for the last few measured scans, but it was found that this does not change the effect of deceleration.

The time that it takes to reach sedimentation-diffusion equilibrium is shown in Figure 6.14 for equilibration at 500 rpm, by showing the change in the radial position at an

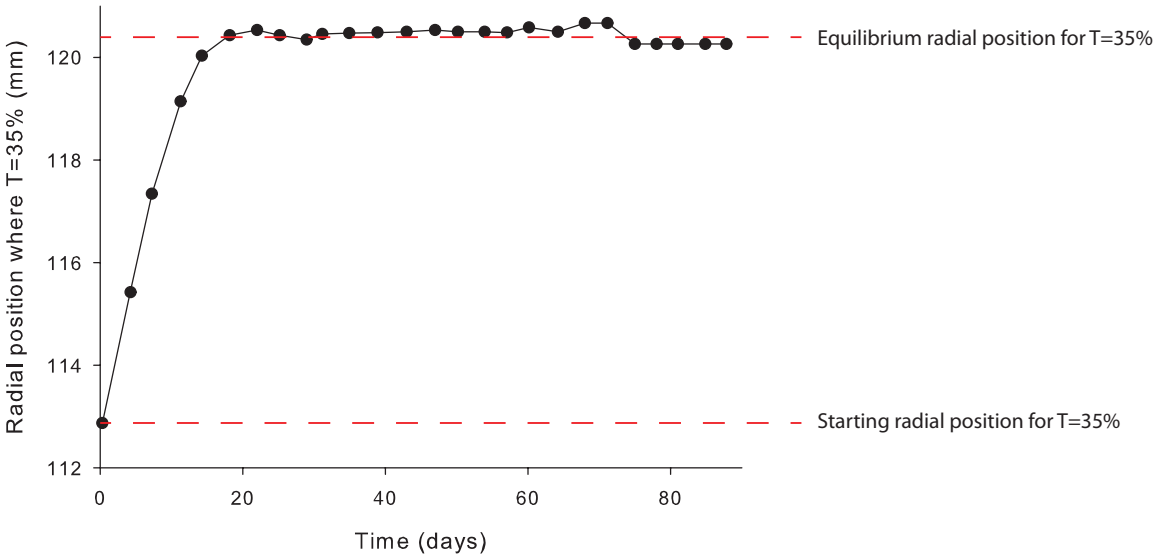

Figure 6.14. The radial position where the transmission is 35 % as a function of measurement time for a rotation rate of 500 rpm. The radial position increases until sedimentation-equilibrium is reached, which takes about 20 days.

arbitrary chosen transmission of 35 % as a function of time. On the basis of Equation 6.11, the required time to reach equilibrium was expected to be about 18 days. This is of the same order as found in Figure 6.14, where it takes about 20 days to reach equilibrium. As concentration increases, the dynamics slow down and equilibration takes longer. After 20 days, most of the transmission profile remains unchanged, only in some specific regions, especially at low transmission values, small changes could be observed. To check whether sedimentation-diffusion equilibrium was reached, the data of several measurements were divided by the latest measurement, until a value of 1 was reached for all radial positions.

6.5.2. Digital noise

It is evident from the primary data, such as in Figure 6.7, that the transmission fluctuates, even where it should remain constant. Firstly, there are time-independent factors that contribute to this, such as imperfections in the sample cell and irregularities in the glue that do not change over time. These effects are in principle corrected for, since the transmission profiles at the start and end of a measurement are divided by each other.

Second, there is time-dependent noise, which can be reduced by averaging an increased number of measured scans. This is done by the recording of 255 scans or more. In Figure 6.15 the effect of averaging is shown by comparison of a single scan to the average of 255 scans. In Figure 6.15a it can be seen that the averaging reduces the

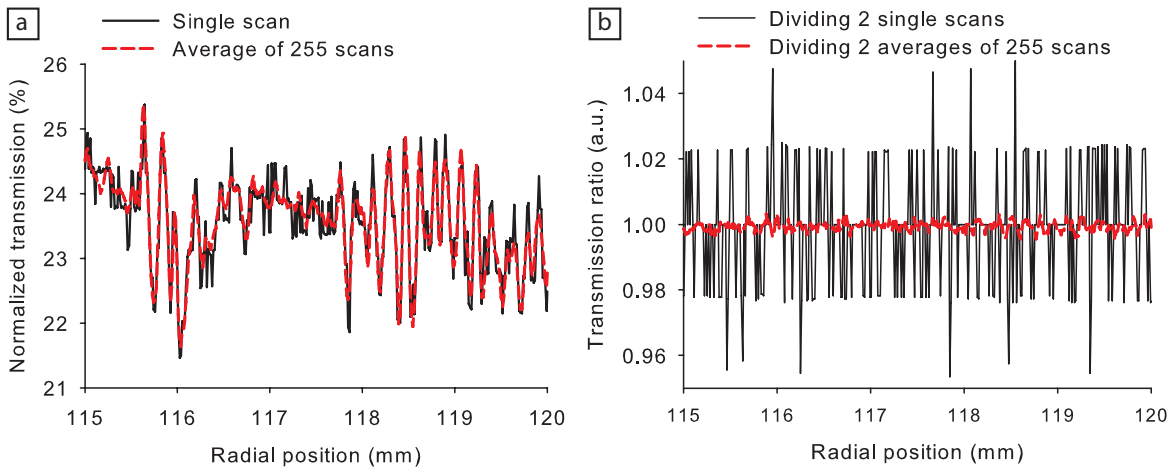

Figure 6.15. Comparison of the average of 255 transmission scans (dashed line) to a single scan (solid line) by comparison of the transmission data (**a**) and by dividing the transmission ratio of 2 consecutive single scans or the averages of two consecutive sets of 255 scans (**b**).

noise, which is visualized more clearly by dividing 2 subsequent scans or averages of scans in Figure 6.15b. Clearly, the averaging of 255 scans reduces the noise significantly. To reduce the noise even more, 11 measurements of 255 scans were averaged in the experiments described in this chapter.

The noise level in the raw data of LUMiFuge measurements is found to depend on the rotation speed: the noise is the highest at 200 rpm (lowest rotation rate) and the smallest at 4000 rpm (highest rotation rate). This is probably caused by the fact that the recording time of a single scan is the same for all rotation rates, whereas a larger part of the sample passes the detector at higher rotation rates. By measurement of a black mask with a transparent line running diagonally across the mask, it was indeed found that the signal at higher rotation rate is recorded over a larger lateral range, as shown in Figure 6.16. Hence, at higher rotation rates where the signal is recorded over a larger lateral width, the noise is more averaged. To investigate how much this affects our measurements in the range of 500–1000 rpm, 255 transmission scans of an empty LUMiFuge measurement cell measured at 500 rpm are averaged and compared to the average of 255 transmission scans measured at 1000 rpm. From Figure 6.17a it can be seen that the noise-level is indeed slightly lower for the measurement at 1000 rpm.

In the data analysis, the transmission at the start and at the end of a measurement are divided by each other, which reduces time-independent noise. Since the time-independent noise is slightly rotation rate dependent, this was done at 500 rpm for all samples. Therefore, for samples that reached equilibrium at a certain rotation rate, 11 short measurements at 500 rpm were performed to be able to divide this data with the 11 starting measurements at 500 rpm. However, during these short measurements

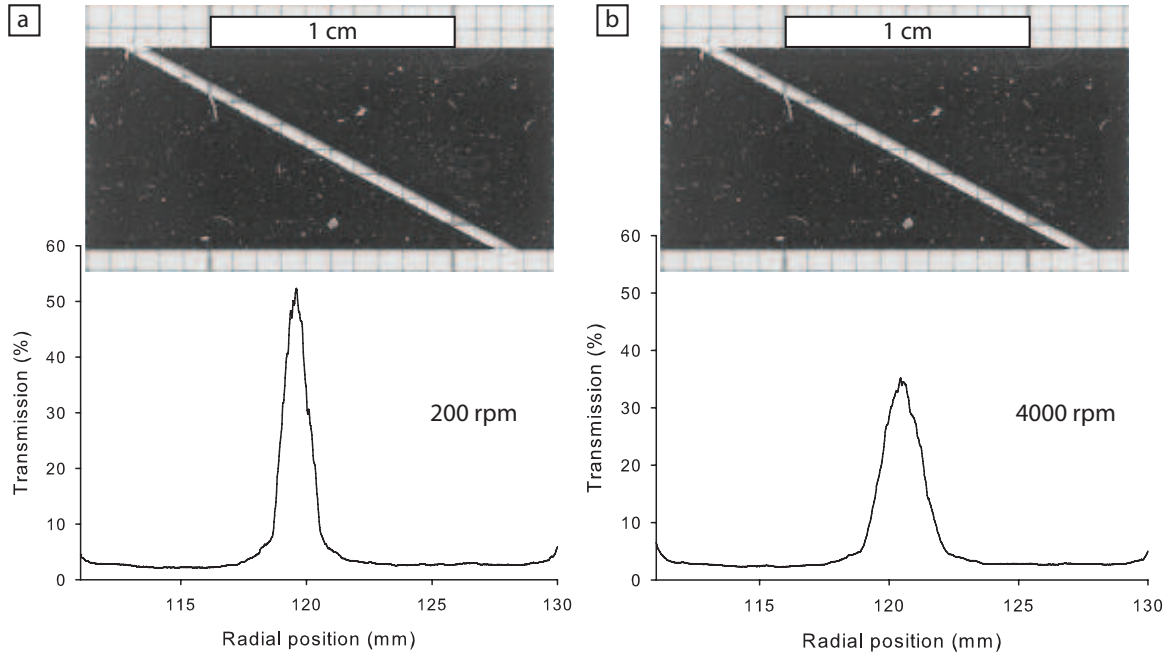

Figure 6.16. Average of 255 scans of a black mask with a transparent diagonal line measured at 200 rpm (**a**) and 4000 rpm (**b**). A picture of the mask is shown above the graphs at approximately the same scale. The measured lateral range is larger for the mask measured at 4000 rpm.

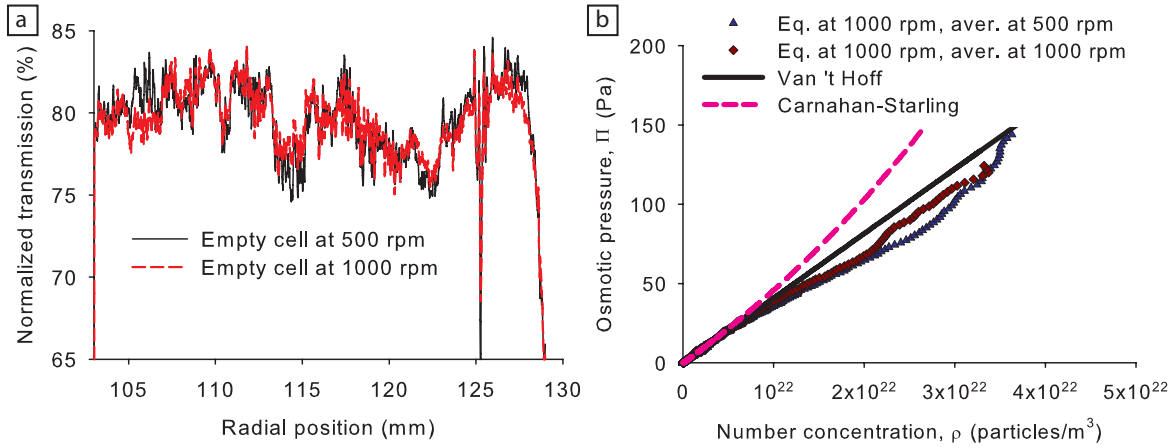

Figure 6.17. (**a**) Average of 255 scans of an empty sample cell measured at 500 rpm (solid line) and 1000 rpm (dashed line). (**b**) Equation of state from an equilibrated sample of magnetite particles at 1000 rpm measured by averaging short measurements at 500 rpm (triangles) and 1000 rpm (diamonds). The corresponding Van 't Hoff equation (solid line) and the Carnahan-Starling equation for hard spheres (dashed line) are also shown.

the sedimentation-diffusion equilibrium obtained at 625 rpm or 1000 rpm may slightly expand towards the profile at 500 rpm. To investigate whether an influence of this expansion can be found in the resulting equation of state, equilibrium at 1000 rpm was investigated: first 11 short measurements were performed at 1000 rpm after which 11 short measurements of this equilibrium were measured at 500 rpm. The resulting equations of state are compared in Figure 6.17b. At low concentrations no significant difference is observed. However, at higher concentrations the equation of state obtained at 1000 rpm shifts towards higher pressures. In the concentration profiles (not shown) it can be seen that this corresponds to slightly higher concentrations when averaging at 500 rpm takes place, which can be explained by expansion of the profile towards the equilibrium profile corresponding to 500 rpm.

6.5.3. Normalization

The recorded transmission depends on the response of the individual pixels on the CCD detector, which causes variations in the recorded light transmission as a function of position. This is corrected for by a normalization procedure in the equipment software, by assigning a weighing factor to each reading to obtain a normalized setting of 100 percent transmission for all pixels in the absence of a sample that affects transmission [183]. These weighing factors are automatically applied by the software on the measured data, depending on several factors. The most important factor of influence is the light factor, which is an indicator for the intensity of the light source. The light factor is kept at the default, optimal value of 1.0 in all our measurements. Another factor is the temperature. The rotation speed is only of minor influence on the weighing factors. For our measurements, a normalization was performed at 22 °C with a light factor of 1.0 and a rotation speed of 660 rpm. Our own colloidal systems are not sensitive to the temperature fluctuations of about ± 0.5 °C of the LUMiFuge.

The procedure of normalization is not mentioned in Section 6.4 on data analysis, since it is applied automatically by the software. Moreover, by dividing the transmission profile at the start and end of a measurement, it is automatically corrected for in our analysis procedure. Therefore, as long as all measurements are performed at the same light factor and temperature, the normalization procedure is unimportant.

6.5.4. Fluctuations in background signal and signal strength

From the primary transmission data of the LUMiFuge it is clear that a transmission of zero is not reached, even when there is supposed to be no transmission at all by applying a mask. Moreover, this background level may change per measurement, even though it remains constant during a measurement itself. This is illustrated in Figure 6.18, which compares 11 short measurements when the sample is in equilibrium at 625

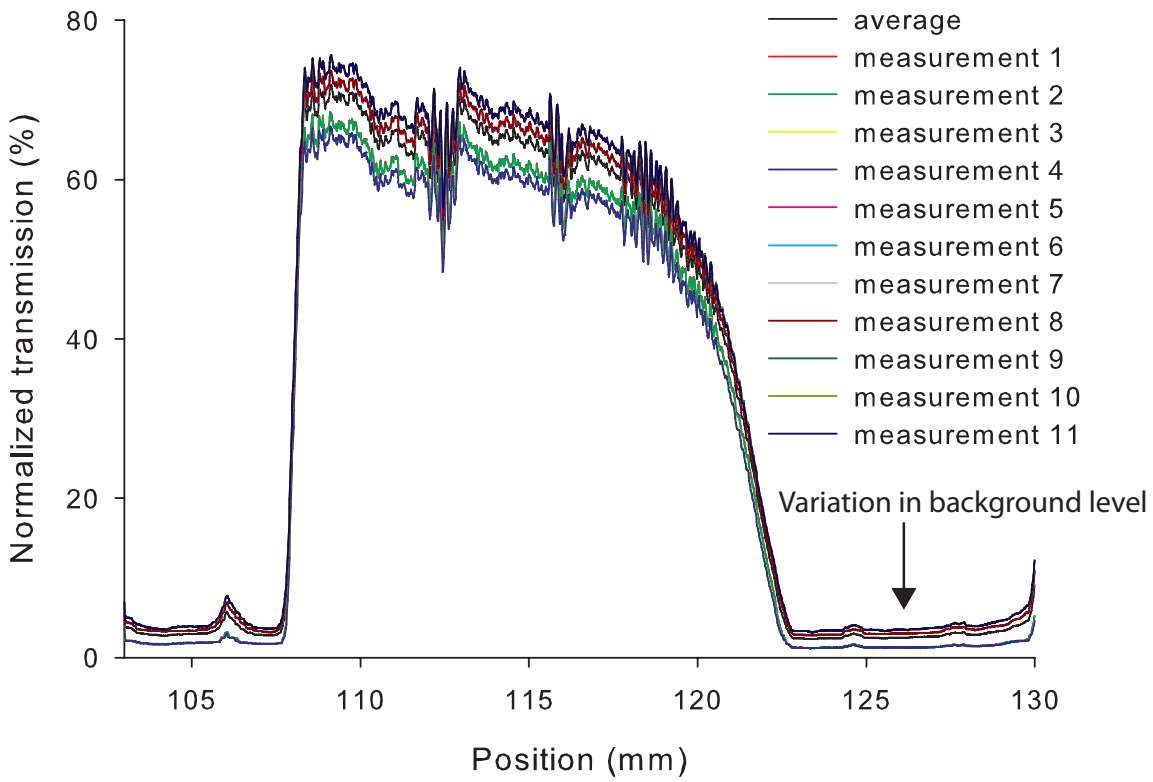

Figure 6.18. Raw transmission data of magnetite particles when sedimentation-diffusion equilibrium is reached at 625 rpm. 11 short measurements at this equilibrium as well as its average are shown. The arrow indicates one of the positions where the transmission should be zero, even though the equipment reports a finite transmission, which can vary from one measurement to the other.

rpm. Therefore a background correction needs to be applied. The simplest correction is the subtraction of the background in each measurement. Although this does result in a level of 0% transmission, the higher transmission values then do not yet overlap for different measurements that should be identical. A possible method would be to apply a correction factor from a reference cell for which the transmission should be constant over time, but this also does not result in a satisfactory correction, and is not used here. The origin of these variations between consecutive measurements that should be identical is not known. It is probably not due to small variations in light intensity of the LED-array, since in that case applying a reference cell correction factor should have been sufficient. It may be due to slight erratic shifts in the timing of the CCD-array recording compared to the position of the rotor.

The background correction that is applied in our current data analysis is the subtraction of the background, as the error in the high transmission values is probably

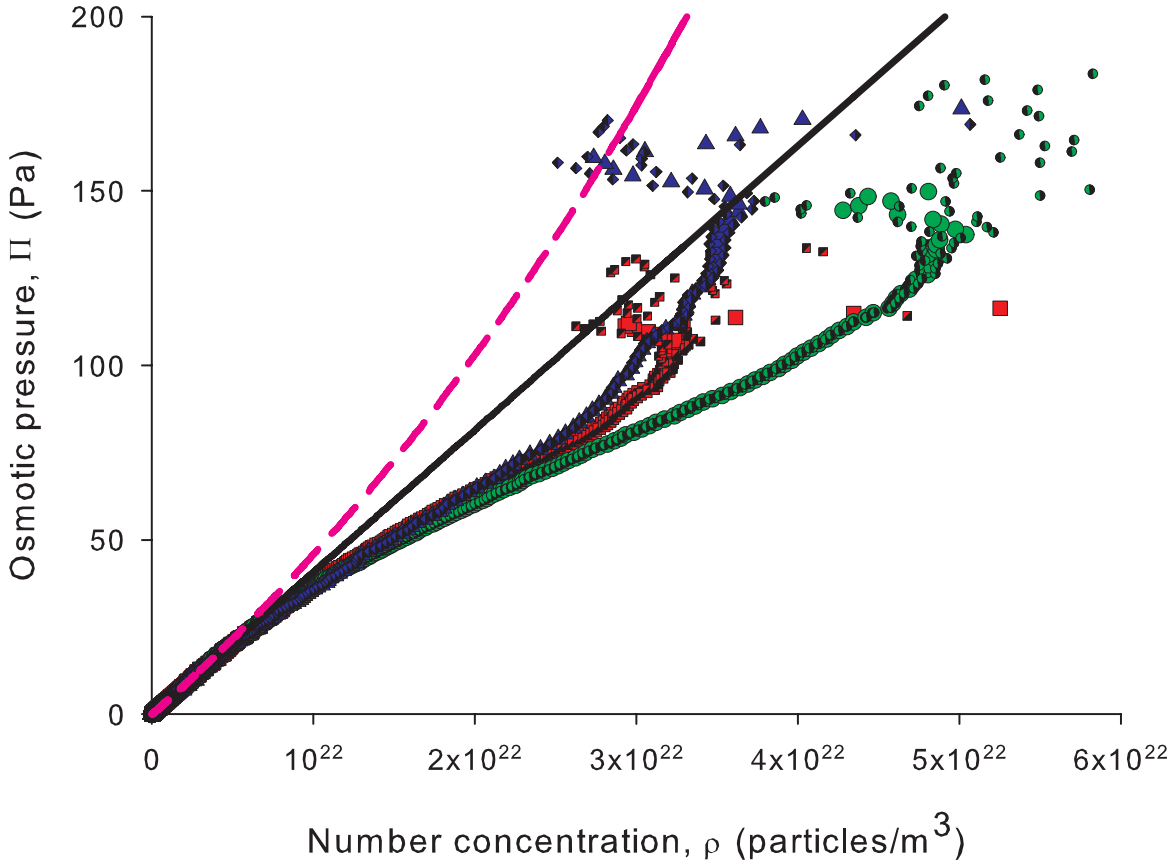

Figure 6.19. Osmotic pressure of a dispersion of magnetite particles as a function of the number concentration for equilibration at 500 rpm (squares), 625 rpm (spheres), and 1000 rpm (triangles). The data is corrected by subtracting the average background transmission. This value was varied by its standard deviation and the resulting equations of state were calculated (semi-filled squares, semi-filled spheres and semi-filled diamonds for 500, 625, and 1000 rpm respectively). Only at the highest osmotic pressures the data points start to spread and the equations of state become unreliable. The corresponding Van 't Hoff equation (solid line) as well as the Carnahan-Starling equation for hard spheres (dashed line) are also shown.

small. The correction is performed by averaging the data in a region where the transmission should be zero and subtracting this average value from the data. If this value is inaccurate, it may have a large effect on the transmission data close to zero, thus where the concentration of particles is high. This is investigated by varying the value for the background correction by the standard deviation in its average and calculation of the corresponding equations of state. The resulting equations of state are compared in Figure 6.19. Clearly, the effect on the equation of state is only notable at the highest

pressures for a certain rotation rate. This occurs at the concentrations where the pressure starts to vary noisily along the horizontal axis, which is why this data was already left out in the equations of state shown in Section 6.4.

As mentioned, the background subtraction is not entirely sufficient for correcting the high transmission values. If this has a significant influence, it will be reflected in the obtained starting transmission value, T_0, which will be further discussed in Section 6.6.1.

6.5.5. Optical Broadening

One of the main disadvantages of the LUMiFuge, not being designed like an analytical ultracentrifuge, is in its optics. Due to the relatively poor optics, the signal measured at a certain position is convoluted by contributions from nearby radial positions, as schematically depicted in Figure 6.20a. Hence, where the change in transmission should be abrupt, it in fact is not: the data is convoluted by the optical broadening response function as the optical signal from a certain position is broadened. This is schematically illustrated in Figure 6.20b.

If the transmission is constant over the whole radial range, optical broadening has effectively no influence. The steeper the transmission profile, the stronger the effect of optical broadening. Importantly, this implies that optical broadening will have a stronger effect on samples at higher rotation rates, as the concentration profile is more compressed and the corresponding transmission profiles have steeper slopes.

For the same reason, it is important in the sample preparation to obtain homogeneous initial transmission profiles. In principle the irregularities due to the sample cell will be divided out, but if the profile is not homogeneous the effect of optical broadening becomes larger.

The optical broadening function was determined by the measurement of a known abrupt profile: a 100 μm slit in a metal mask, obtained from CVI Melles Griot. In Figure 6.21 the effect of optical broadening on the slit is shown; the measured transmission profile is much broader than the indicated 100 μm.

Since the width of the slit is well defined, the corresponding transmission profile that should result can be artificially constructed. By deconvolution of the measurement of this slit with the artificial transmission profile, the actual optical broadening function is determined.

The optical broadening function can also be determined from the measurement of an abrupt profile by differentiation of the transmission to the radial position. This gives approximately the same function as determined by deconvolution of the 100 μm slit. It was also found that the broadening function is independent of radial position and rotation rate.

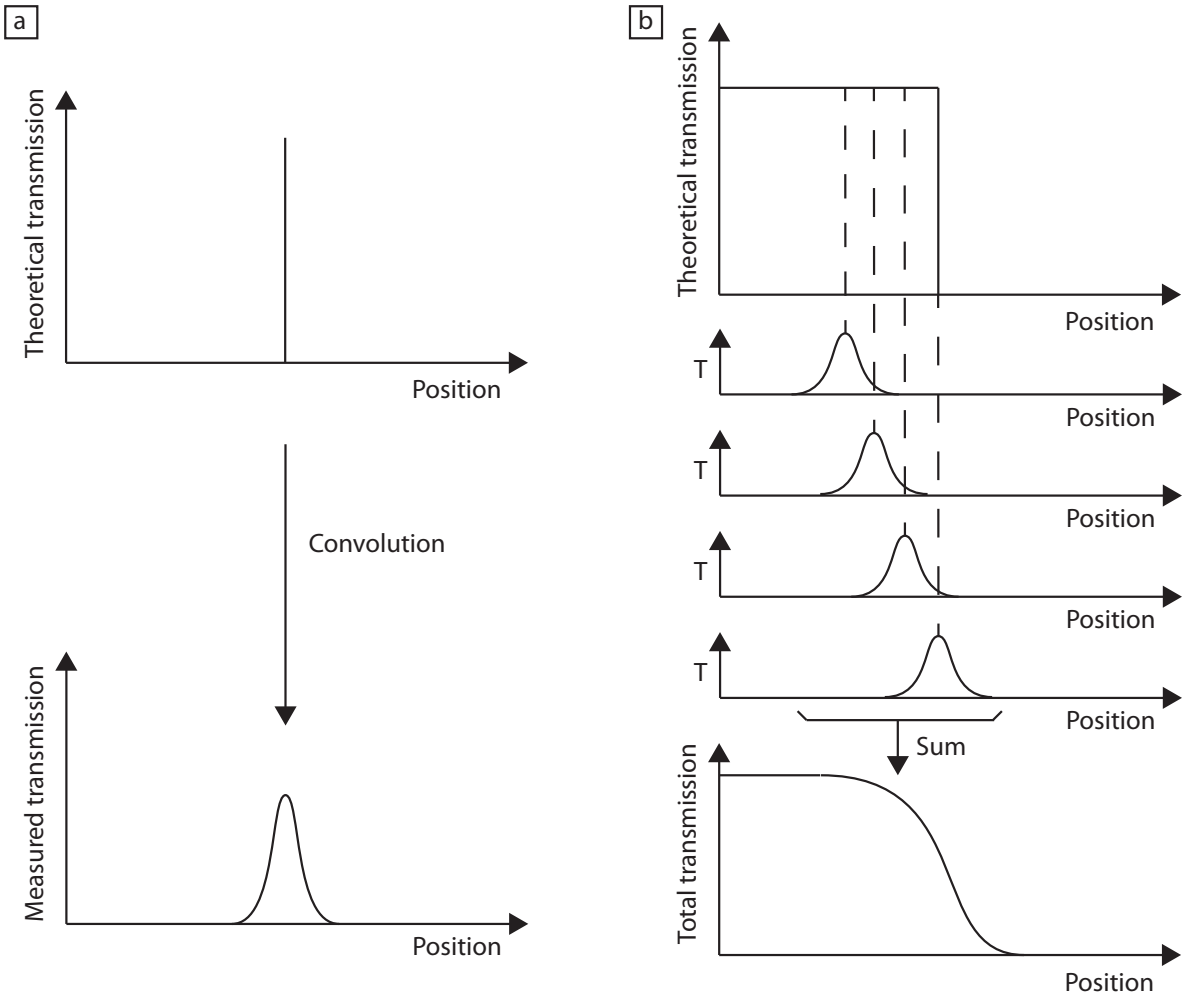

Figure 6.20. Schematic illustration of the effect of convolution on the transmission at a certain position (**a**) and how this affects the total transmission profile in the case of an abrupt transition of transmission (**b**).

Deconvolution can in principle be performed using a program that makes an estimate for the deconvoluted transmission profile, subsequently convolutes it again and compares the result with the measurement. Based on the difference a new estimate of the deconvoluted profile is made, and the process is repeated iteratively until the convoluted profile from the program fits with the measured convoluted profile, hence the deconvoluted transmission profile is now known.

The optical broadening function that was determined using the 100 μm slit is shown in Figure 6.22a. The three peaks in this broadening function are probably due to an optical interference effect. In Figure 6.22b, the measured transmission profile of the slit is compared to the measurement after deconvolution. The slit should ideally give a single peak in the form of a block of 100 μm in width, but convolution by the optics of the LUMiFuge results in a profile with 3 peaks in the raw data. After deconvolution,

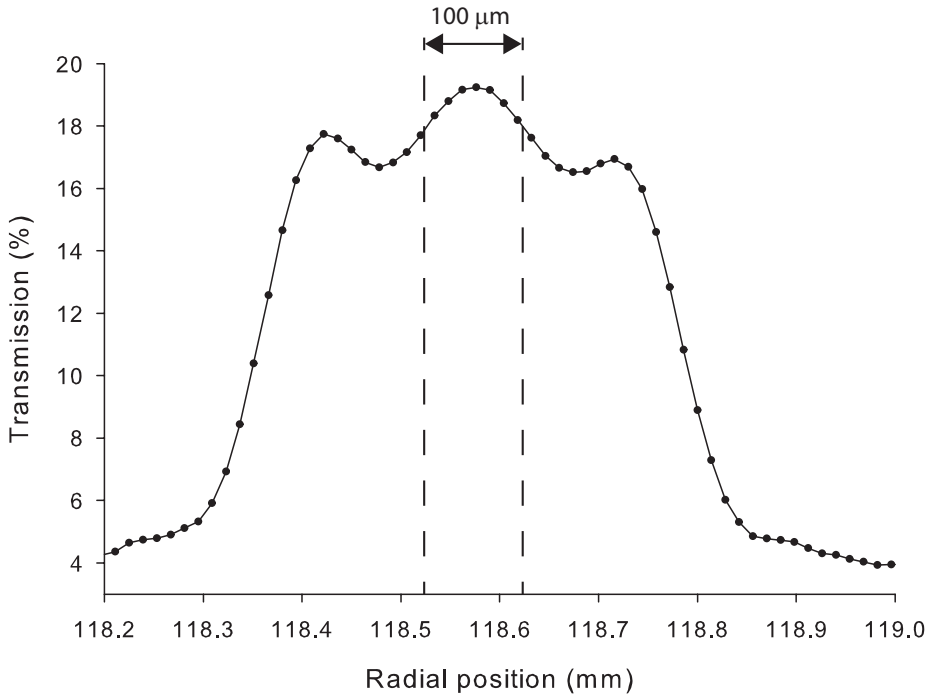

Figure 6.21. Transmission profile of the 100 µm slit, which is convoluted by optical broadening. The actual distance of 100 µm is indicated by the dashed lines.

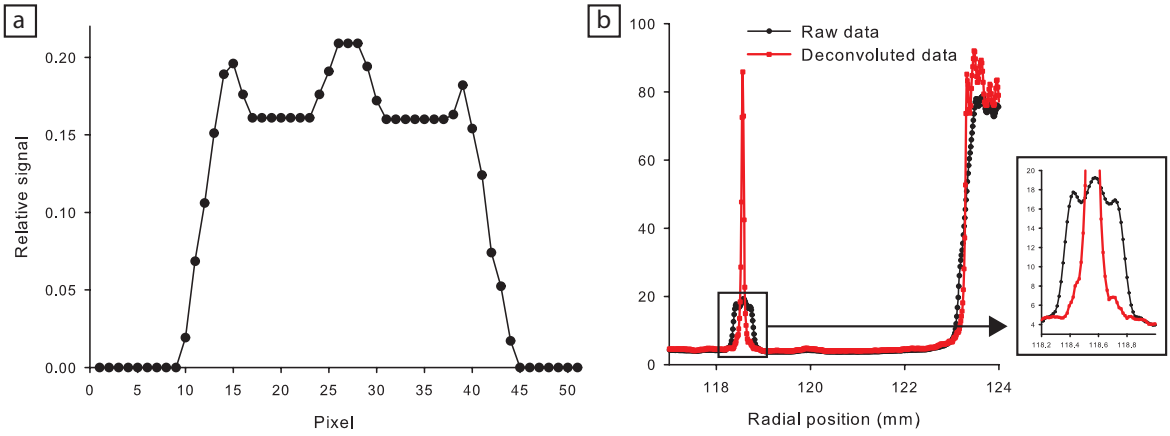

Figure 6.22. (**a**) The optical broadening function determined from a 100 µm slit in a metal mask. (**b**) Transmission data of the metal mask with 100 µm slit before deconvolution (spheres) and after deconvolution using the optical broadening function shown in (**a**) (squares). The inset magnifies the position of the 100 µm slit, showing how the 3 peaks before deconvolution transform to one peak after deconvolution.

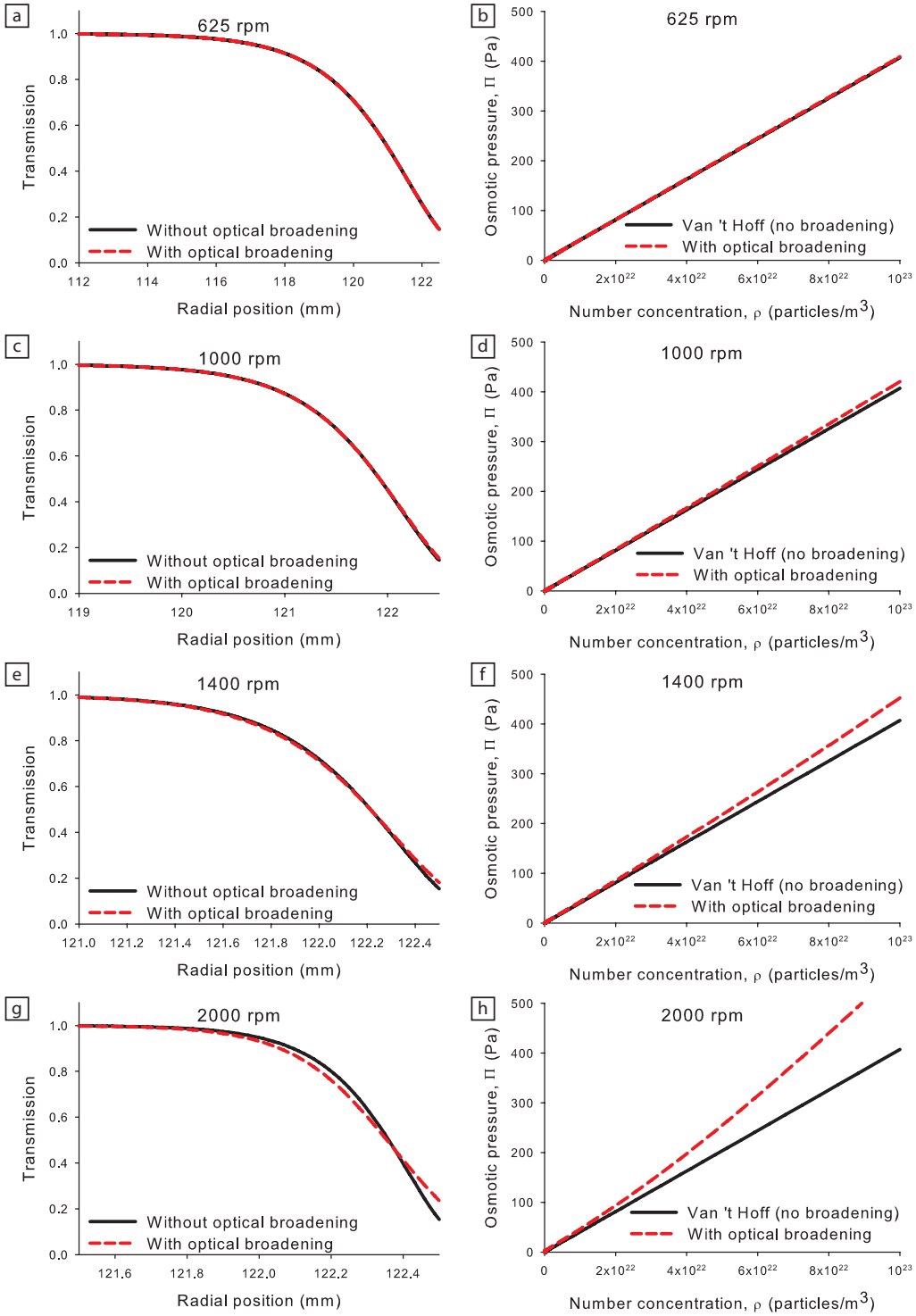

FIGURE 6.23. **Left**: Calculated transmission profiles with (dashed line) and without the influence of optical broadening (solid line) and the corresponding equations of state (**right**). The influence of optical broadening increases with increasing rotation rate: at low rotation rates (**a**–**b**) no significant influence of optical broadening is observed, For 1000 rpm (**c**–**d**) slight deviation from ideal behavior is observed at high concentrations, whereas for higher rotation rates (**e**–**h**) the effect is significant.

these 3 peaks have become one single peak, although it is not a perfect block. This is probably due to the removal of some inaccurate data points at the edge of the optical broadening function. Nevertheless, the change of transmission is now more abrupt, also visible at a radial position of 123 mm. It can also be seen that the transmission through the slit has the same value as the transparent part of the cell at positions below the metal mask (radial positions 124 mm and higher), as it should.

The influence of the optical broadening on the equation of state was calculated for several rotation rates. This was done by calculating concentration profiles assuming ideal behavior of the colloids using Equation 6.7, assuming the same particle size as in the experiments. A bottom concentration of 1×10^{23} particles per m^3 at a radial position of 122.5 mm was used for all calculations. The concentration profiles were checked to obey van 't Hoff's law without convolution. From the calculated concentration profiles, the transmission profiles were calculated and convoluted by the optical broadening function. These transmission profiles before and after optical broadening are shown in the left column of Figure 6.23. The equations of state were calculated and compared to van 't Hoff's law, which corresponds to the equations of state without optical broadening (right column Figure 6.23). The effect of optical broadening increases with increasing rotation rate as the concentration profiles are more compressed and the corresponding transmission profiles have steeper slopes. At rotation rates 500 and 625 rpm, no influence of optical broadening is found. At 1000 rpm the osmotic pressure is slightly overestimated at the highest concentrations. For rotation rates of 1400 and 2000 rpm optical broadening starts to have a significant influence on the equations of state. For the experiments described in this chapter, the highest rotation rate described is 1000 rpm, and the measured concentrations only reach 0.5×10^{23} particles per m^3, where the influence of optical broadening is negligible (Figure 6.23d). This is in agreement with the rotation rate independence of the equations of state. However, at higher rotation rates and concentrations the effects of optical broadening can be very significant and should be taken into account.

In calculating the equations of state from theoretical concentration profiles it was also found that if the number of data points is too small, the integration steps become too large and pressures may be overestimated.

6.6. Data analysis errors

6.6.1. Starting transmission, T_0

Important for the data analysis is a correct value of the starting transmission of the dispersion, since it is used to determine the concentration through Equation 6.13. As explained in Section 6.4, the starting transmission should be determined from the region that is depleted of colloids after reaching equilibrium, in principle at the highest employed rotation rate. As mentioned in Section 6.5.4, the background correction that

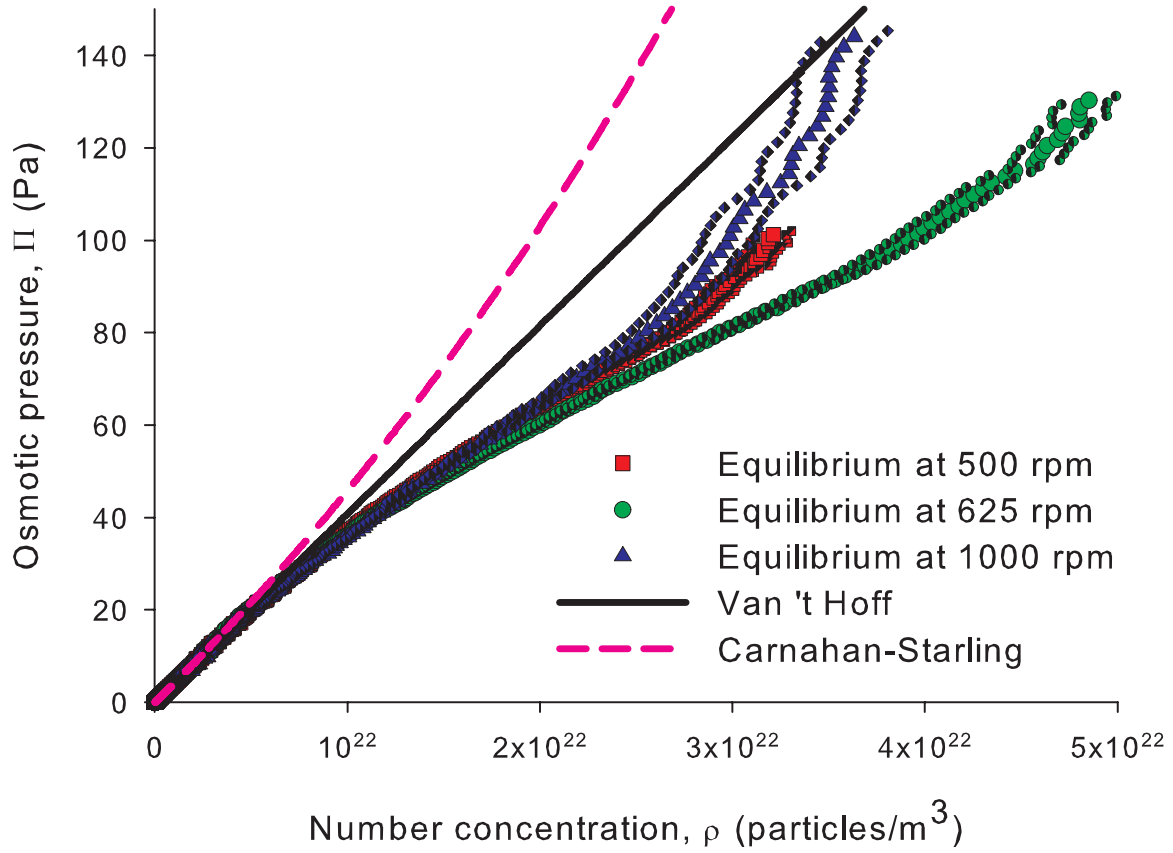

Figure 6.24. Osmotic pressure as a function of the number concentration of magnetite particles for equilibration at 500 rpm (squares), 625 rpm (spheres) and 1000 rpm (triangles). The influence of the choice of the starting transmission, T_0, is shown by calculation of the equations of state with the standard deviation in starting transmission subtracted or added to the average value of T_0 (semi-filled squares, semi-filled spheres and semi-filled diamonds for 500, 625 and 1000 rpm respectively). The corresponding Van 't Hoff equation (solid line) as well as the Carnahan-Starling equation for hard spheres (dashed line) are also shown.

is applied to the raw data slightly underestimates the effect of the background on high transmission values, hence it is instructive to see what influence variations in T_0 have on the equation of state.

The starting transmission is determined from the average in the $T_{\text{start}}/T_{\text{end}}$ ratio in the region depleted of colloids at equilibrium (Figure 6.8). To investigate the influence of T_0 on the equation of state, the standard deviation in the average of the $T_{\text{start}}/T_{\text{end}}$ ratio is subtracted or added to the average value of T_0. The resulting equations of state are compared in Figure 6.24. At low concentrations and pressures, the variations in T_0 do not have any significant influence on the equations of state as all the data coincide. However, at higher osmotic pressures, a variation of the magnitude of the standard

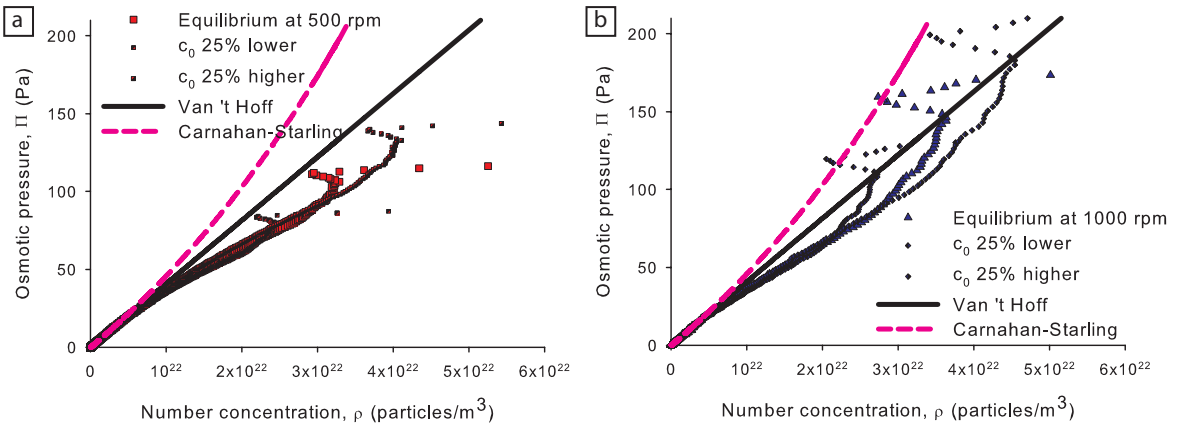

FIGURE 6.25. Influence of the choice of starting concentration c_0 on the osmotic equations of state of magnetite particles after equilibration at 500 rpm (**a**) and 1000 rpm (**b**). The starting concentration was varied by subtracting or adding 25% of its value of 134 g/L. The inaccurate data points at high pressures are left in to illustrate that essentially the shape of the curve remains unchanged; only its relative concentrations and pressures are changed. The corresponding Van 't Hoff equation (solid line) as well as the Carnahan-Starling equation for hard spheres (dashed line) are also shown.

deviation in T_0 does affect the equations of state. Although in absolute numbers it varies for the different rotation rates, it seems that the effect starts to become significant approximately in the region where the pressure starts bending towards repulsive behavior. Although it may very well be that hard sphere repulsions start to contribute more significantly at these high concentrations, the increasing inaccuracy should be kept in mind in interpreting these data.

6.6.2. Starting concentration, c_0

Another important variable in the calculations of the osmotic equations of state is the starting concentration, c_0. To investigate the impact of the starting concentration, it is varied by 25% of its value, as shown in Figure 6.25. Clearly, the starting concentration has a large influence, as it is concentration that is on the horizontal axis and that is integrated to obtain the osmotic pressure along the vertical axis. The extent of the graph is decreased or increased by 25% if c_0 is respectively lowered or increased by 25%. It is clearly essential to ensure an accurate value for the starting concentration to quantitatively analyze the equations of state. Nevertheless, if the starting concentrations are not very accurate, still the general trends can be obtained from the data as the main features displayed by the shape of the curves remain unchanged. Both the x-axis and the y-axis are affected to a similar extent by errors in the starting concentration.

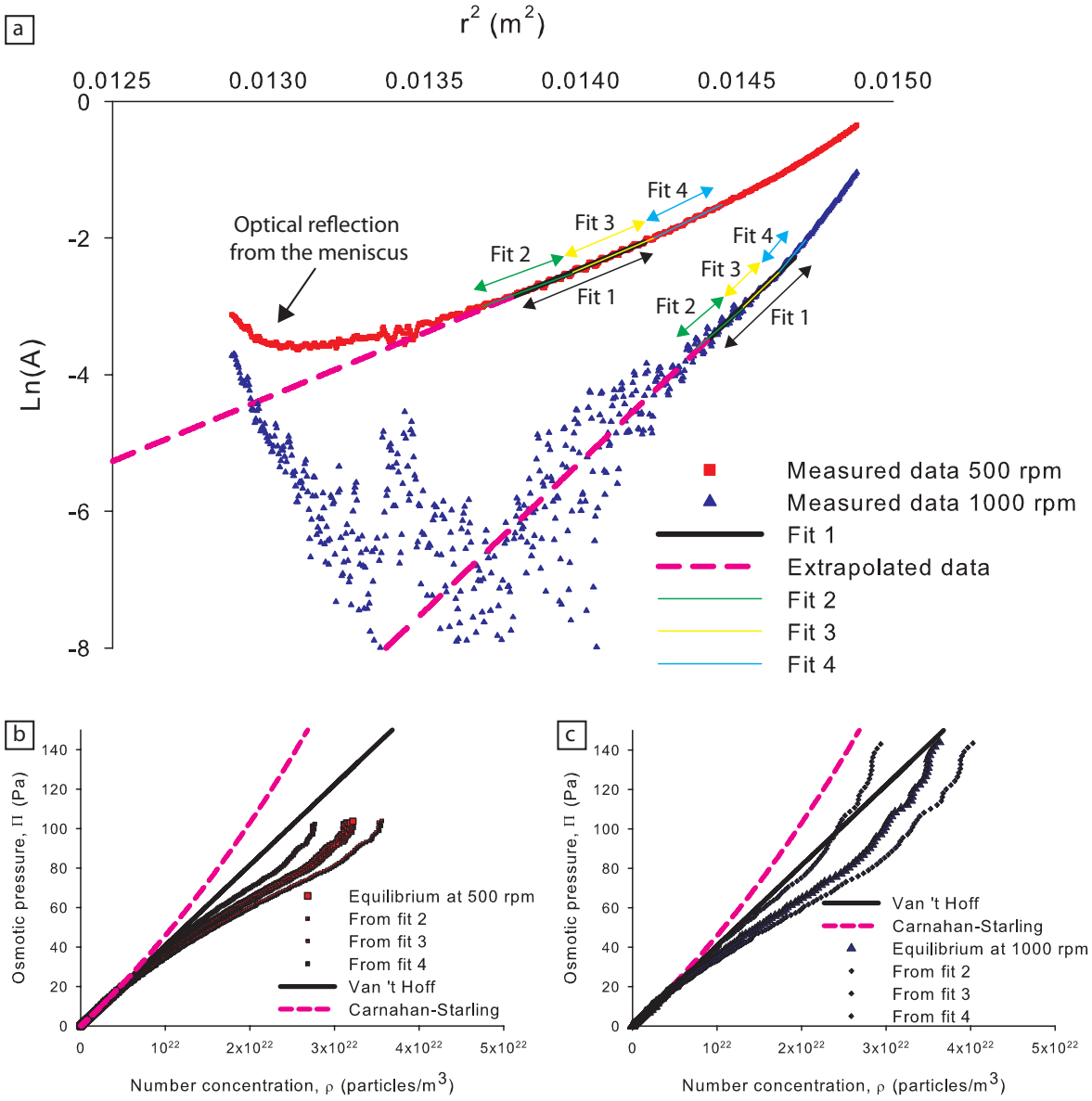

FIGURE 6.26. (**a**) $\ln(A)$ as a function of r^2 for equilibration of magnetite nanoparticles at 500 rpm (squares) and 1000 rpm (triangles), in which the fit used in the data analysis (Fit 1) as well as 3 other fits in different regions (Fit 2 – Fit 4) are indicated. In (**b**) the resulting equation of state for 500 rpm is shown (squares) with the variations due to 3 other fits (semi-filled squares). In (**c**) the equation of state for 1000 rpm is shown (triangles), with the variations due to the 3 other fits (semi-filled diamonds).

6.6.3. Influence of the fitting range of ln(A) versus r^2

To determine the buoyant mass of the particles that are measured, the slope of $\ln(A)$ as a function of r^2 is fitted, as discussed in Section 6.4. For monodisperse, non-interacting colloids, this should yield a straight line. In the more concentrated region,

deviations may be expected when interactions start to play a role. In the dilute regime, at low values for r^2, ideal behavior should be obtained, but the lower the values of r^2, the more effects of noise as well as the optical reflections from the meniscus can be observed. Hence, the data used for fitting are chosen in the dilute regime where these effects are not too dominant.

The choice of this fitting region has an influence on the equation of state, as shown in Figure 6.26. In Figure 6.26a the data of $\ln(A)$ as a function of r^2 is shown, where the fitting region is varied as indicated. The resulting equations of state change considerably at higher concentrations, as shown in Figure 6.26b and 6.26c. Therefore, it is important to choose the fitting region carefully, and several fitting regions should be tried to have an indication of what the most reliable range is. The fitting region is chosen in the region where not too much noise or influence of the meniscus is present, but also not at too high concentrations, where deviations from the straight slope may very well be the result of interactions. The region of fitting is chosen in such a way that a reasonable amount of data is included in the fit. It should be mentioned that polydispersity also affects the slope of the curve, which will be further discussed in Chapter 8.

The fit of $\ln(A)$ versus r^2 is also used to extrapolate the data to very low absorptions that are not measurable due to noise. By using this method, the integration by Equation 6.10 is started at a sufficiently low concentration to set Π=0. If the concentration without extrapolation is used, the osmotic equation of state starts with an offset instead of going through zero. This is exemplified by integration of the concentration profile given by the black dashed line in Figure 6.11. The resulting equation of state is shown in Figure 6.27, and compared to the equation of state where extrapolated data is used, for the system equilibrated at 500 rpm. When the concentration is not close enough to zero at the point where integration is started, an offset is found, which causes the equation of state to be systematically at too low pressures. Moreover, the concentration at which integration is to be started has to be determined manually, which may be prone to error as well. Using the extrapolated data at very low absorptions circumvents the problem of having an offset as well as a manual choice of the starting point of integration. The rotation rate independence of the final results and the agreement of the equations of state with Van 't Hoff 's law up to higher concentrations than the extrapolated data justify this approach.

6.6.4. Linearity of absorption

In the analysis of the LUMiFuge measurements, Lambert-Beer's law is used (Equation 6.8), which assumes that concentration depends linearly on absorption. The validity of Lambert-Beer's law at high concentrations was investigated by measurements of the absorption of capillaries with varying concentrations of ferrofluid. In Figure 6.28 the

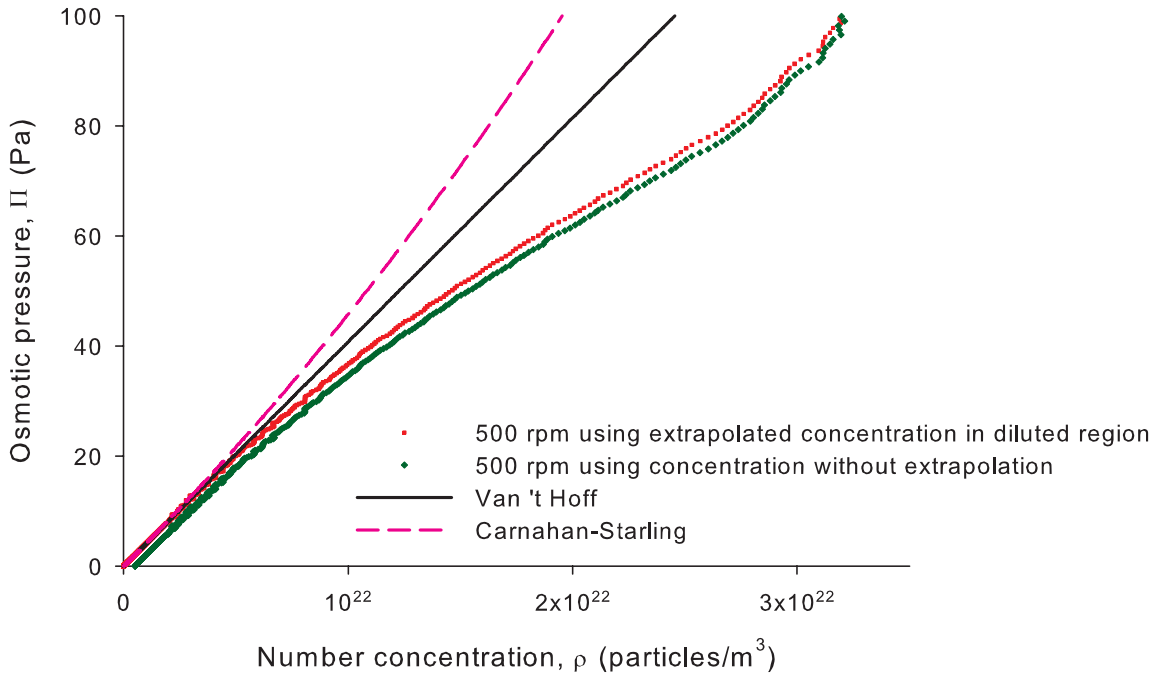

Figure 6.27. Equation of state of magnetite particles after equilibration at 500 rpm using the concentration obtained by extrapolating the data in Figure 6.26 to very low absorptions (squares) and using the measured concentration only (diamonds). If the concentration where integration is started is not low enough, an offset at zero pressure is found, as indicated by the black arrow. The resulting equation of state is then systematically too low.

absorption at a wavelength of 880 nm as a function of concentration is shown. This figure shows that Lambert-Beer's law holds for concentrations over 300 g/L, at least at 880 nm, the wavelength of the LED used in the LUMiFuge measurements. At concentrations of 400 g/L and higher, the absorption was too high to measure even in these thin capillaries. The sample discussed in this chapter has a starting concentration of 134 g/L and is measured up to 300 g/L, which is within the linear Lambert-Beer regime.

6.7. Conclusions

The LUMiFuge, originally designed as a stability analyzer, can be used as an analytical centrifuge to measure sedimentation-diffusion equilibria of colloidal dispersions and obtain their equations of state. Nevertheless, it has several instrumental limitations.

First, the measurement time required is beyond the maximum measurement time of the LUMiFuge, hence consecutive measurements have to be performed. This has disadvantages as the LUMiFuge has to be briefly accelerated to 2000 rpm at the start

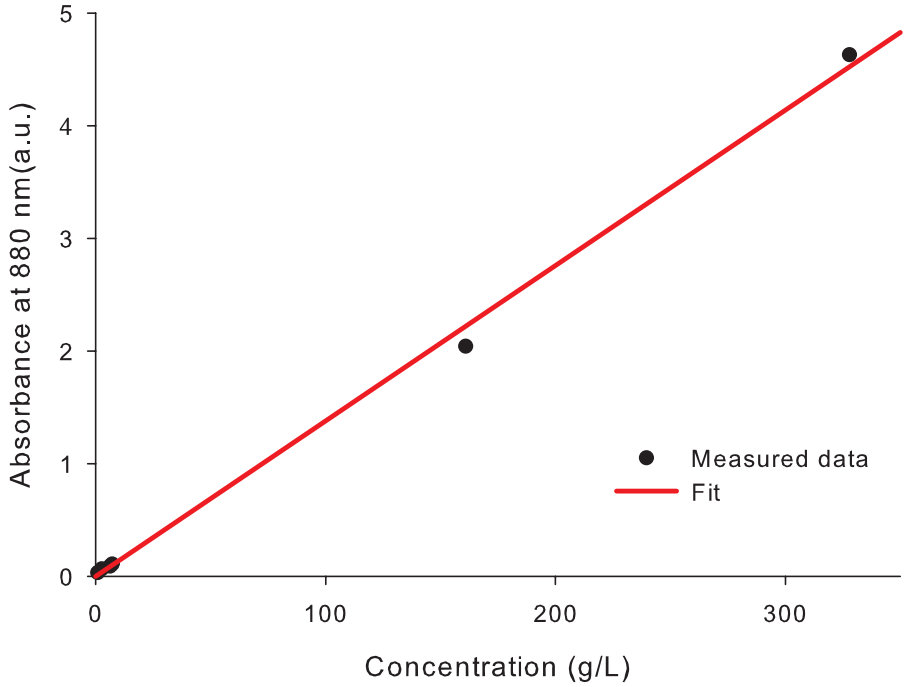

Figure 6.28. Absorbance of 17 nm iron oxide nanoparticles measured at 880 nm, the wavelength used by the LUMiFuge, as a function of concentration in a 50 μm thin capillary. The slope of the corresponding fit is 0.014 L/g.

of each measurement. Moreover, the background level varies per measurement, which requires correction. Therefore, it would be highly desirable to increase the maximum measurement time of the instrument.

The optics and digitization of the LUMiFuge are not as sophisticated as in a typical AUC, therefore, noise reduction procedures are required. The time-independent noise is significantly reduced by dividing the transmission profiles at the start and the end of a measurement. Time-dependent noise can be reduced by averaging of a large number of transmission scans. A significant disadvantage of the LUMiFuge is the optical broadening of the transmitted signal. It was calculated that this can have an important influence on the equation of state, overestimating pressures at high rotation rates and concentrations. For the measurements described in this chapter, this influence is negligible though, as the rotation rates employed are still low enough at the measured concentrations.

Several parameters in the data analysis are important to obtain an accurate equation of state, and it was shown that accurate values of the starting transmission and starting concentrations are required. Another important step in the data analysis is the determination of the buoyant mass from the slope of $\ln(A)$ as a function of r^2. From this analysis it was found that the buoyant mass varies for different rotation rates, *i.e.* size fractionation takes place within the measurement cell, despite a low polydispersity of

only 11 %. It is important to choose an appropriate range to fit the slope of $\ln(A)$ versus r^2: in a dilute concentration range where interactions do not play a role, though not in the most dilute range where noise and the influence of the meniscus are important. To increase the dilute concentration range it is recommended to increase the column height of the colloidal dispersion in the sample cells, which also shifts the region where the meniscus distorts the data.

An accurate concentration profile at low concentrations is required, which can be can be obtained by extrapolation towards zero concentration using the fit of $\ln(A)$ as a function of r^2. The validity of this approach is confirmed, as the colloidal dispersion still obeys Van 't Hoff's law beyond the extrapolated data.

Finally, it was found that Lambert-Beer's law holds for concentrations up to at least 300 g/L for iron oxide nanoparticles.

Despite several limitations in the use of the LUMiFuge, the model system investigated, a concentrated, strongly absorbing ferrofluid could be measured and its equation of state could be determined for the first time by analytical centrifugation. The coincidence of a large part of the equations of state at three different rotation rates validates our approach. At low concentrations, Van 't Hoff's law is obeyed, whereas at higher concentrations the osmotic pressure is lower than expected from Van 't Hoff's law, or the Carnahan-Starling equation of state for hard spheres. Whether deviations from ideal behavior are due to attraction between the colloids or due to polydispersity is discussed in Chapter 8.

In summary, using the LUMiFuge as an analytical centrifuge for concentrated ferrofluids is possible, though demanding. It takes a significant amount of time in terms of sample preparation and data analysis, and it takes a long time to reach sedimentation-diffusion equilibrium. The limitations in the optics of the LUMiFuge complicate the data analysis, and optical broadening of the transmission signal can have a significant influence at higher rotation rates. Nevertheless, this technique is suitable for measuring osmotic pressures of strongly absorbing, concentrated, colloidal dispersions due to the small optical path lengths in the homebuilt capillary cells and the use of light wavelength of 880 nm. Thus, this technique may prove very useful in the analysis of colloidal particles which are too heavy for measurement with an AUC, or for very concentrated, highly absorbing samples.

6.8. Acknowledgements

Claire van Lare is thanked for initial experiments and investigations on the experimental limitations of the LUMiFuge. Rick de Groot and Suzanne Woudenberg are acknowledged for particle synthesis. Dominique Thies-Weesie is thanked for useful

discussions. Peter Horsman, Gert de Jong and co-workers are acknowledged for constructing the metal slits, and Hans van der Kraan for cutting the glass plates and capillaries.

7

Analytical Ultracentrifugation of Concentrated Ferrofluids Using Ultra-Thin Sedimentation Centerpieces

Abstract

An analytical ultracentrifuge (AUC) is employed to determine the osmotic equation of state of ferrofluids. Accurate osmotic pressures below 1 pascal are obtained at magnetite concentrations below 1.0 g/L using conventional AUC measurement cells with an optical path length of 3 mm, which is the shortest path length that is commercially available. However, to measure osmotic pressures at concentrations beyond this dilute regime, smaller optical path lengths are required, realized here in homebuilt AUC centerpieces with optical path lengths as low as 50 micrometers. Our novel centerpieces allow accurate osmotic pressure measurements on ferrofluids with initials concentrations above 100 g/L, following the analysis procedure described in this chapter.

7.1. Introduction

Analytical ultracentrifugation is a versatile technique, widely applied to biological macromolecules to determine sizes, shapes and molecular weights using both sedimentation velocity and sedimentation-diffusion equilibrium measurements [100, 186]. In colloid science, the analytical ultracentrifuge (AUC) has mainly been used to perform sedimentation velocity experiments, whereas reports on sedimentation-diffusion equilibrium measurements via an AUC are scarce [4, 96–98]. At equilibrium between sedimentation and opposing diffusion of colloids, the concentration profile can be integrated to obtain the equation of state of the colloids, as has been demonstrated both in experiments and in computer simulations. [98, 181, 182]. The advantage of an AUC is that very low osmotic pressures can be measured that are very difficult to probe with other methods, such as light scattering [5] and osmometry [89].

Here, an AUC is used to measure the equation of state of a concentrated, strongly light absorbing ferrofluid. Colloidal dispersions of magnetic nanoparticles in a liquid have been studied previously by sedimentation velocity measurements at low concentrations [101, 184]. To obtain particle interactions more directly from the equation of state, higher concentrations are required, as indicated by sedimentation-diffusion equilibrium measurements on weakly absorbing colloidal dispersions [96, 97, 182]. However, for ferrofluids, measuring the equation of state of concentrated dispersions is unfeasible using conventional AUC measurement cells with an optical path length of 3–12 mm, due to the strong light absorption of the colloids. In the previous chapter it was shown how concentrated ferrofluids can be analyzed by building thin glass capillaries into the sample cells of a LUMiFuge stability analyzer. The advantages of a LUMiFuge compared to an AUC are its low rotation rates, allowing measurements of larger colloids, and the use of a wavelength of 880 nm, where these colloids absorb less light. However, the optics of the LUMiFuge is not as sophisticated as in a typical AUC. In this chapter, an AUC is used for sedimentation-diffusion measurements at relatively low rotation rates. Homebuilt AUC sample cells are developed to decrease the optical path length of the light down to 50 μm, enabling measurements of more concentrated colloidal dispersions.

In the next section, the general formulas required to obtain the equation of state from equilibration AUC data are reviewed. The experimental methods, including a description of the new sample cells, are detailed in Section 7.3. Subsequently, the analysis of raw AUC data to obtain the equation of state is shown, and the resulting equations of state using different optical path lengths are discussed in Section 7.4. Finally, conclusions are given in Section 7.5.

7.2. Theory

For a colloidal dispersion which rotates at an angular frequency ω, the centripetal acceleration at a distance r from the rotation axis at $r = 0$ equals $\omega^2 r$. The force balance for the colloids is then given by [187]:

$$\frac{\mathrm{d}\Pi}{\mathrm{d}r} = \rho(r)\Delta m\omega^2 r \tag{7.1}$$

where $\rho(r)$ is the number density of colloids with a buoyant mass Δm. For non-interacting colloids Van 't Hoff's law for the osmotic pressure, Π, reads:

$$\Pi = \rho kT \tag{7.2}$$

in which k is Boltzmann's constant and T is the absolute temperature. The corresponding number concentration follows from substitution of Equation 7.2 into Equation 7.1:

$$\rho(r) = \rho(r_b)\exp[\omega^2\Delta m(r^2 - r_b^2)/(2kT)] \tag{7.3}$$

with $\rho(r_b)$ the concentration at the bottom position $r = r_b$. For interacting particles the osmotic pressure can be obtained by integration of Equation 7.1:

$$\Pi(\rho(r^{'})) = \Delta m\omega^2 \int_0^{r^{'}} \rho(r) r \mathrm{d}r \tag{7.4}$$

where $\Pi(r \to 0) = 0$ and $\rho(r \to 0) = 0$. This equation shows that the osmotic pressure exerted by a number density $\rho(r^{'})$ equals the total buoyant weight of colloids in the region from $r = 0$ to $r = r^{'}$. The experimental equation of state can be compared to theoretical predictions, such as the Carnahan-Starling equation of state for hard spheres [185]:

$$\Pi = \rho kT \left(\frac{1 + \phi + \phi^2 - \phi^3}{(1 - \phi)^3} \right) \tag{7.5}$$

with ϕ the colloidal volume fraction. The experimental equation of state can also be compared to expressions for the osmotic pressure of dipolar hard spheres [88], as further discussed in Chapter 8.

In an analytical ultracentrifuge, the equilibrium concentration profile of the colloids is determined by measuring the absorbance, A, as a function of the radial position. The absorbance is related to the concentration of the colloids via Lambert-Beer's law:

$$A = \epsilon c l = -\log T \tag{7.6}$$

with ϵ the extinction coefficient (in $\mathrm{m^2 kg^{-1}}$), c the colloid concentration (in $\mathrm{kgm^{-3}}$), l the optical path length (in m), and T the transmission. After converting the obtained mass concentration profile to a number concentration profile, the osmotic pressure can be determined by integration via Equation 7.4, which for a finite integration step width, Δr, determined by the resolution of the detector, yields:

$$\Pi(r) = \Pi(r - \Delta r) + \rho(r)\Delta m\omega^2 r\Delta r \tag{7.7}$$

Importantly, the light absorption A determines the experimentally accessible upper value of r of the integral in the concentration profile in Equation 7.4. Thus, the smaller the optical path for the light transmission, the larger the osmotic pressure that can be retrieved via Equation 7.7.

7.3. Experimental

7.3.1. Magnetite colloids

Magnetic iron oxide nanoparticles were prepared by seeded growth, as described in Chapter 4. As in Chapter 6, particles from series 18 were used, with an average core diameter of 13.4 nm (± 11%) from TEM and dispersed in a solution of 15.6 mM oleic acid in decalin. Absorption measurements as a function of wavelength were performed to determine the extinction coefficient, using a Varian Cary 1E UV-Vis spectrophotometer and measurement cells with an optical path length of 2 mm.

7.3.2. Analytical centrifugation

Equilibrium measurements on iron oxide nanoparticles at low concentrations were performed using a Beckman Coulter Optima XL-I AUC (absorbance optics). Measurements of samples with concentrations of 103 and 134 g/L were performed with a Beckman Coulter Optima XL-A AUC (absorbance optics). In both cases an An-60 Ti rotor containing 3 samples and 1 counterbalance was used.

Conventional centerpieces have an optical path length of 3 or 12 mm, which is too large for strongly absorbing magnetite colloids. Homebuilt 2-compartment centerpieces with a much smaller optical path length were developed as schematically illustrated in Figure 7.1. The precise optical path length was determined for each centerpiece; it varied between 50–70 μm, depending on the thickness of the layer of glue.

For different concentrations a wavelength scan was recorded and compared to a measurement of the emission spectrum of the Xenon flash lamp of the AUC through an empty hole in the rotor. From this comparison, the most suitable wavelength of the lamp was chosen to match an optimal signal-to-noise ratio with an absorbance in the range of 0.2–0.5. For concentrated samples the absorbance was higher than this range, and the maximum wavelength of 541 nm was used.

For sedimentation-diffusion equilibrium measurements, equilibrium scans were made at a temperature of 20.0 ± 0.1 °C. A rotation rate of 1600 rpm was used, corresponding to 206 times the gravitational acceleration at a radial position of 7.2 cm near the bottom of the cell. This is below the lowest rotation rate of the instrument recommended by the manufacturer Beckman, as at lower rates rotor stability may be lost. However, it was previously found that lower rotation rates are still feasible [96, 97], and we found

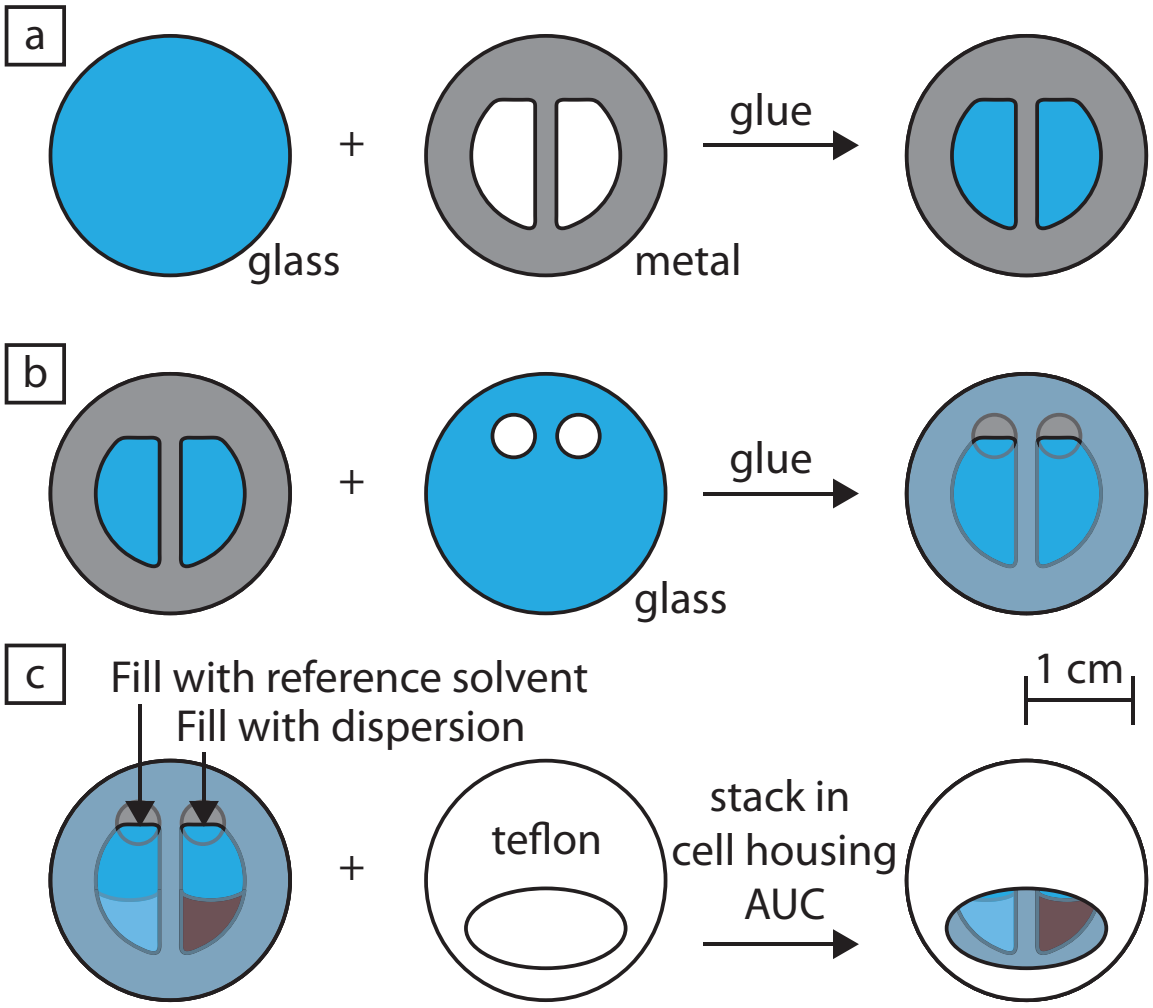

Figure 7.1. Schematic illustration of the preparation of a homebuilt AUC sample cell. First a metal spacer with a thickness of 50 µm is glued on a 1 mm thick, 22.5 mm diameter quartz glass plate (**a**). This is covered by a similar glass plate with 2 spherical holes of 4 mm in diameter (**b**). The two compartments can be filled with the colloidal dispersion and reference solvent through these spherical holes. A 0.1 mm thick piece of Teflon with an oval hole in the optical analysis zone is used to cover the holes in the stacking of all standard parts of the AUC sample cell (**c**).

that sedimentation-diffusion profiles are still reliable down to 1200 rpm. Equilibrium scans were made at various time intervals, and if the subtraction of two scans with an 8 hour interval resulted in a difference of less than 1 %, the sample was considered to be in equilibrium.

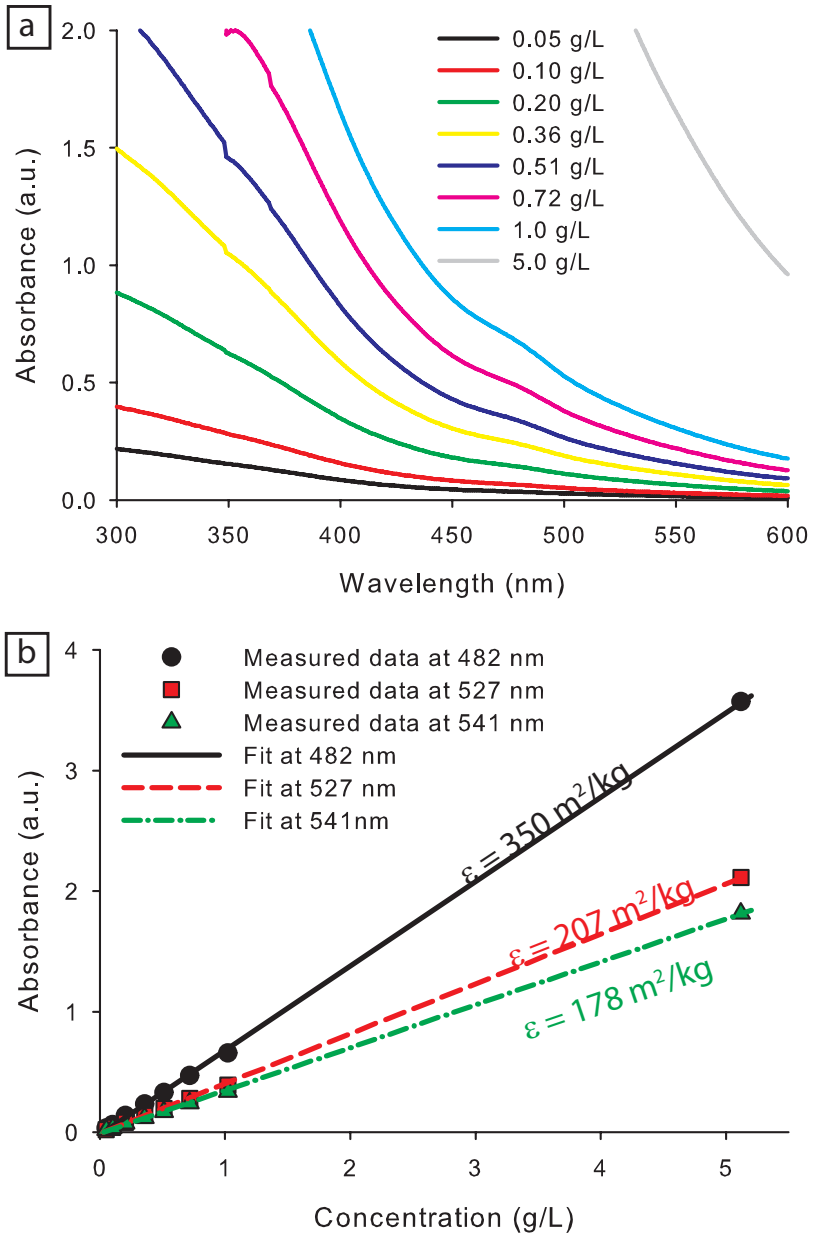

FIGURE 7.2. (**a**) Absorption spectra of magnetite particles measured with a spectrophotometer as a function of wavelength for several concentrations. (**b**) The absorbance as a function of concentration with their corresponding fits for three wavelengths: 482 nm (dots), 527 nm (squares) and 541 nm (triangles). The slopes of these fits yield the extinction coefficients indicated in the graph.

7.4. DATA ANALYSIS AND RESULTS

7.4.1. Absorption measurements with the spectrophotometer

UV-Vis absorption spectra of the magnetite dispersion were measured for several concentrations, as shown in Figure 7.2a. The absorbance as a function of concentration

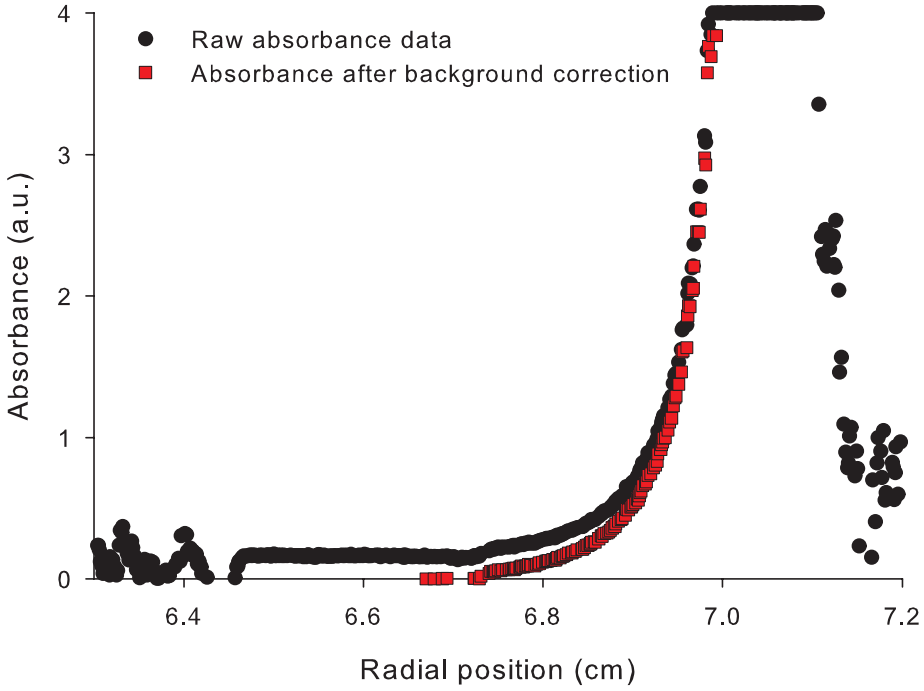

Figure 7.3. Absorbance as a function of radial position of raw AUC data (dots) and after background subtraction (squares).

is shown for three wavelengths in Figure 7.2b. From linear fits to this data, the extinction coefficients were calculated to be 350, 207, and 178 m^2/kg for a wavelength of 482, 527, and 541 nm, respectively. The extinction coefficients were used to determine concentrations from the absorption profiles obtained in AUC measurements at these wavelengths.

7.4.2. Data analysis for the AUC

In this section, the data analysis from AUC absorption data to the equation of state is described. The data analysis of the sample with a starting concentration of 134 g/L equilibrated at 1600 rpm and measured at a wavelength of 541 nm is shown, to illustrate the different steps. First, raw absorption data from the AUC are corrected for the background signal, as displayed in Figure 7.3.

The buoyant mass, Δm, of a particle can be obtained directly from the sample without assumptions regarding particle size or particle shape. From Equation 7.3 we know the mass concentration $c(r)$:

$$c(r) = c(r_b)\exp\left[\frac{\omega^2 \Delta m}{2kT}(r^2 - r_b^2)\right] \tag{7.8}$$

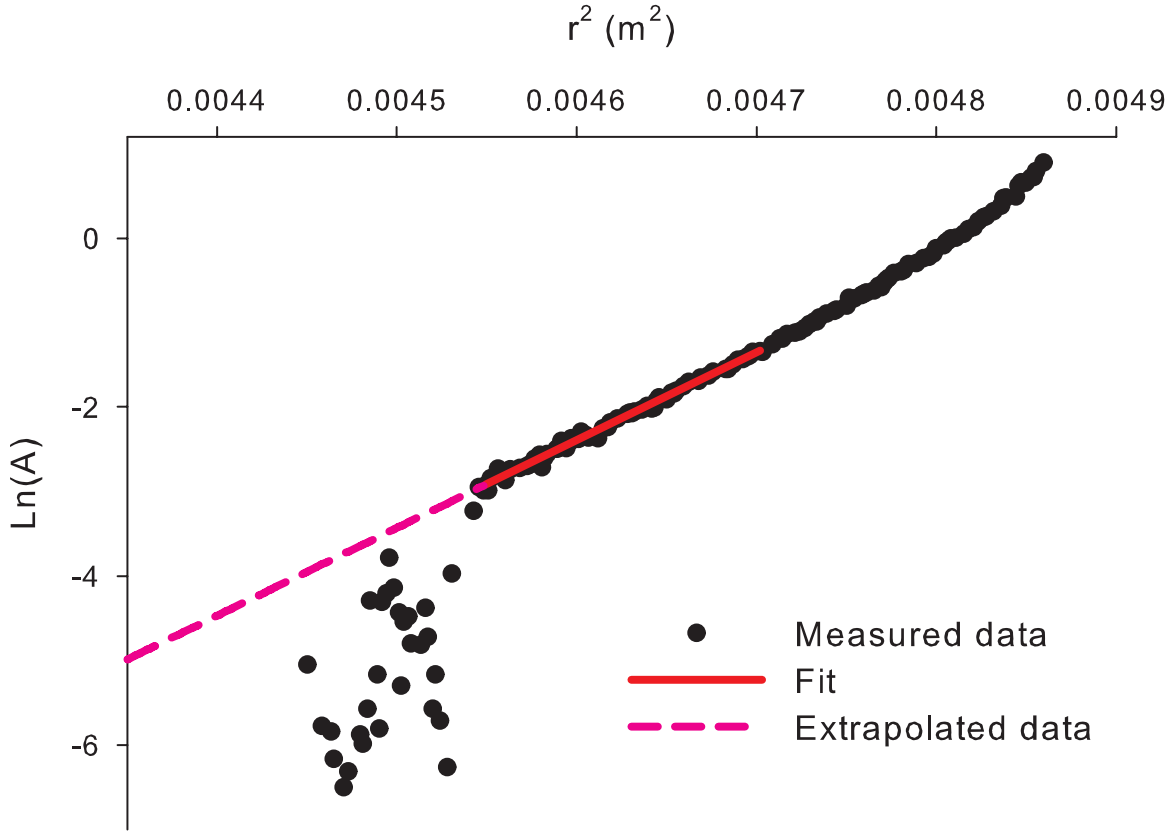

FIGURE 7.4. Ln(A) of the measured magnetite particles as a function of r^2 (spheres) with its fit (solid line) and the extrapolated data from the fit (dashed line).

Replacing the concentration by absorbance using Lambert-Beer's law (Equation 7.6) and rearranging gives:

$$\mathrm{Ln}\frac{A(r)}{A(r_b)} = \frac{\omega^2 \Delta m}{2kT}(r^2 - r_b^2) \tag{7.9}$$

The absorbance at the bottom position, r_b, cannot be determined since the absorbance is too high, but this is not important for obtaining the buoyant mass from the slope of a graph with Ln$A(r)$ as a function of r^2:

$$\text{slope} = \frac{\omega^2 \Delta m}{2kT} = \frac{\omega^2 \frac{4}{3}\pi R_{core}^3 (\rho_{mag} - \rho_s)}{2kT} \tag{7.10}$$

where the right-hand side of the equation shows how the size of the particles can be obtained, assuming a spherical shape. Here, R_{core} is the radius of the core of the particle, ρ_{mag} is the density of the magnetite core and ρ_s is the density of the solvent.

In Figure 7.4 the graph of Ln$A(r)$ as a function of r^2 as well as its fit are shown, from which a buoyant mass of 3.2×10^{-21} kg and a corresponding diameter of 11 nm are obtained. This diameter is smaller than the average of the TEM distribution, which indicates that some fractionation has taken place due to the polydispersity of the

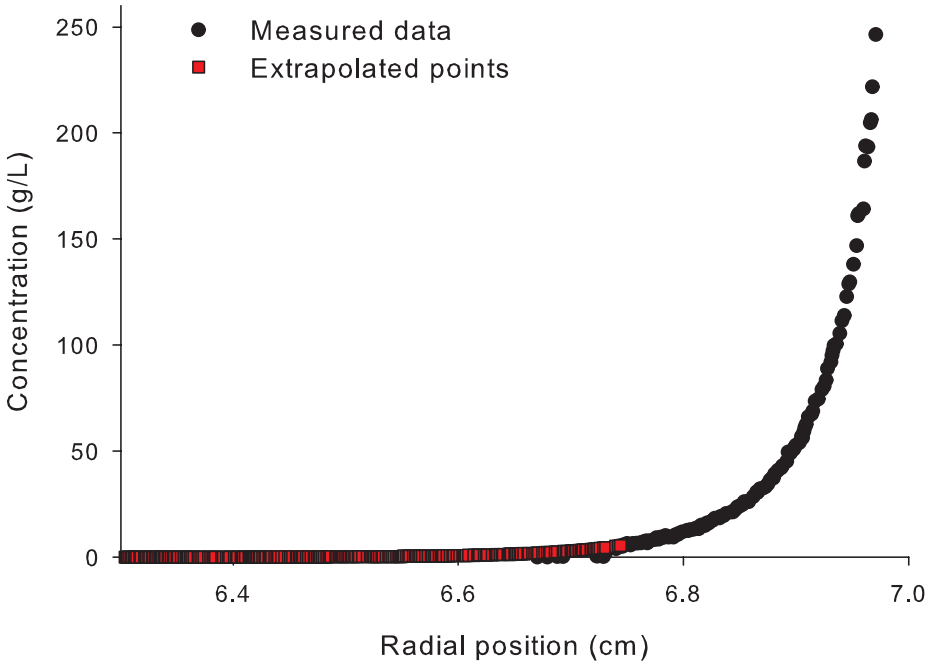

Figure 7.5. The concentration profile of 13 nm magnetite particles in g/L as a function of radial position for the measured data (spheres) and the extrapolated points (squares).

sample, despite it being only 11%. The larger particles sediment towards the bottom of the cell more rapidly than the average particles detected in the dilute range used to determine the buoyant mass. The effects of polydispersity are further discussed in Chapter 8.

The concentration at every radial position is obtained from the absorbance using Lambert-Beer's law (Equation 7.6). To determine the equation of state it is important to start the integration of the concentration profile at very low concentrations, which are difficult to measure. Therefore, the fit from Figure 7.4 is extrapolated to an even more dilute regime (lower radial positions). In Figure 7.5 the concentration profile as a function of radial position is shown for the measured data and the extrapolated data points.

From this concentration profile the number concentration profile is calculated using the size obtained from Figure 7.4. Subsequently, the osmotic pressure is obtained by integration of the concentration profile using Equation 7.7. In this integration, the osmotic pressure is set to zero at the lowest concentration, and the buoyant mass obtained from the slope of Ln(A) versus r^2 is used. The resulting equation of state is shown in Figure 7.6 and compared to Van't Hoff's law (Equation 7.2) and Carnahan-Starling's equation of state for hard spheres (Equation 7.5). At low concentrations, Van 't Hoff's law is obeyed, as expected in the dilute regime. The data up to an osmotic

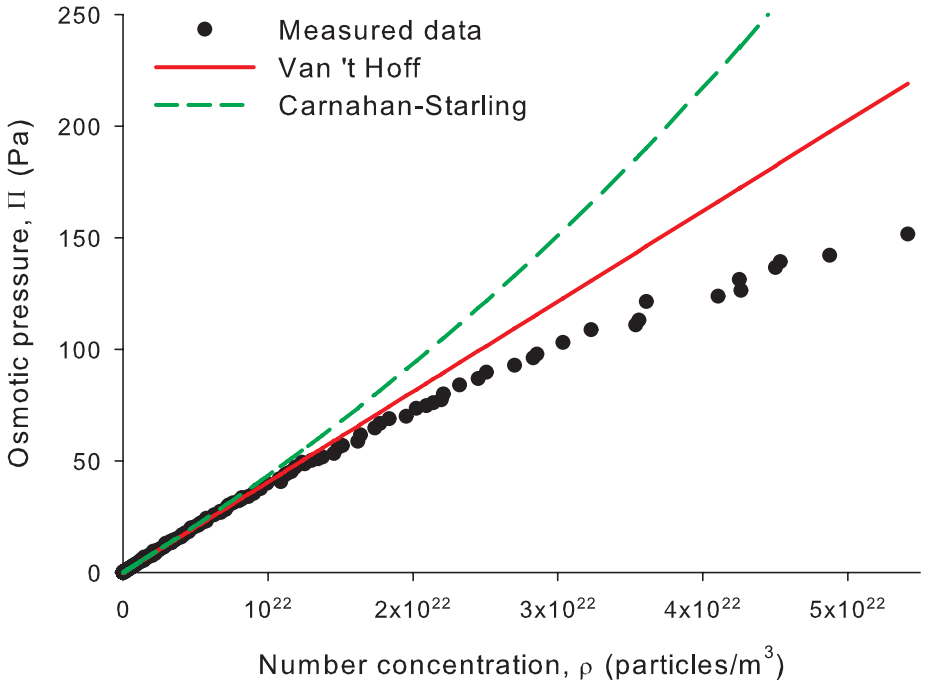

Figure 7.6. Osmotic pressure of 13 nm magnetic particles as a function of the number concentration (dots), together with Van 't Hoff's equation of state (solid line, Equation 7.2) and Carnahan-Starling's equation for hard spheres (dashed line, Equation 7.5).

pressure of a few pascals (less than 4 Pa) were obtained by extrapolation in the dilute regime. This approach is validated by the fact that Van 't Hoff's law is obeyed up to pressures above 40 Pa.

7.4.3. Influence of optical path length on the calculated equation of state

In the previous section it was shown how the equation of state can be determined from sedimentation-diffusion equilibrium measurements using the analytical ultracentrifuge. In this section, the results using the standard double sector centerpieces of the AUC with an optical path length of 3 mm and our homebuilt centerpieces with optical path lengths of only 50–70 μm are compared to each other.

In Figure 7.7a the osmotic equation of state is shown for dilute samples, where the standard centerpiece with an optical path length of 3 mm was used. Clearly, very low osmotic pressures can be measured. In this low concentration regime Van 't Hoff's law is obeyed, and from Carnahan-Starling's equation of state it is evident that the measurements are performed in a concentration regime where hard sphere repulsions do not play a role yet. However, beyond a pressure of 1 pascal the sample starts to become too concentrated, and the absorption saturates. Therefore, the deviations at the highest concentrations are most likely due to noise in the data at the highest

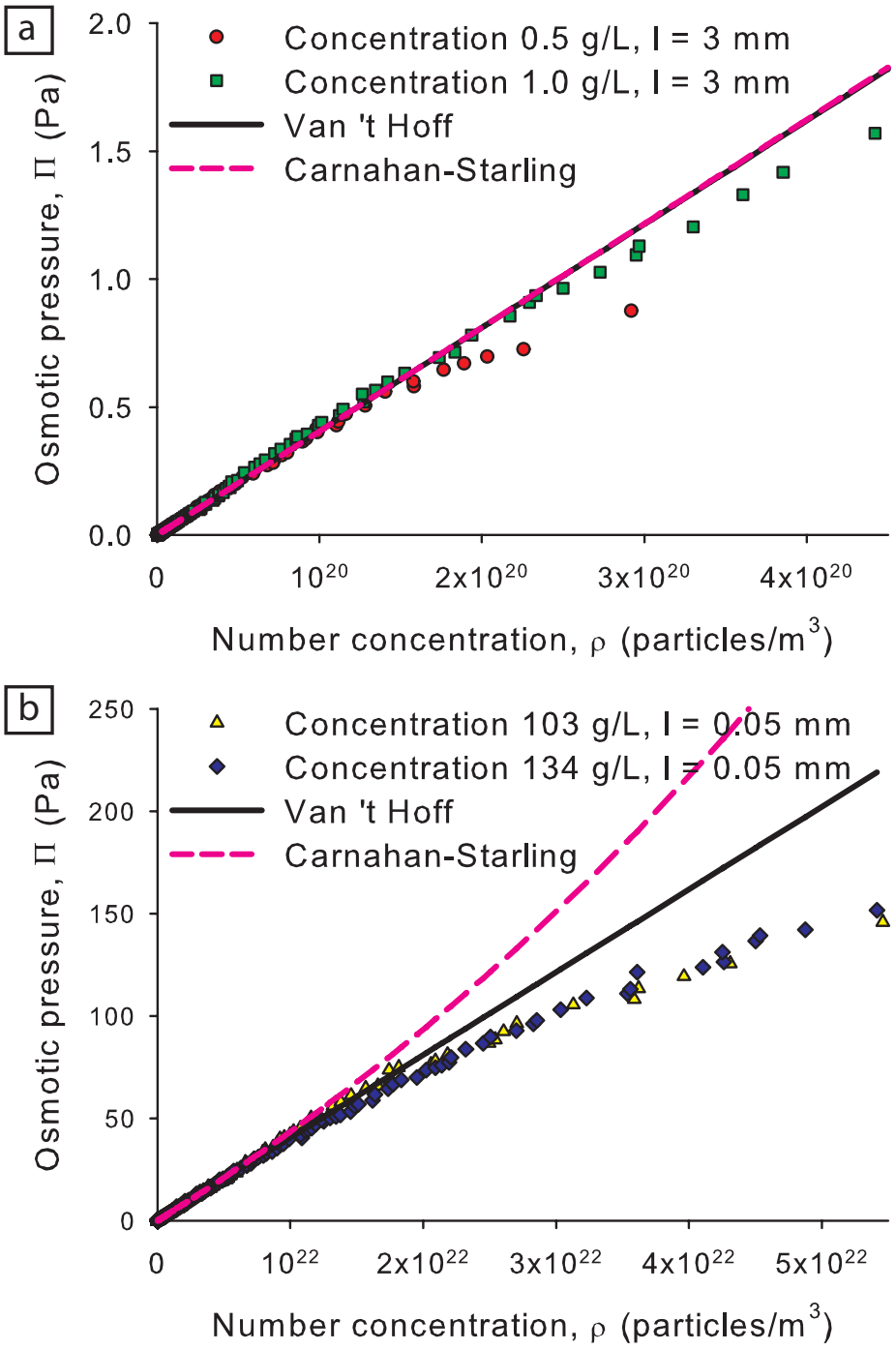

Figure 7.7. Equations of state of 13 nm iron oxide nanoparticles measured at different concentrations and using different optical path lengths: 0.5 and 1.0 g/L with an optical path length of 3 mm (**a**), and 103 and 134 g/L with an optical path length of 50 μm (**b**). The corresponding Van 't Hoff equation (solid line, Equation 7.2) as well as the Carnahan-Starling equation for hard spheres (dashed line, Equation 7.5) are shown in both figures.

absorbance measured here, also suggested by the lack of an accurate trend in the curve in this region.

In order to measure these strongly absorbing colloids in higher concentrations, the optical path length needs to be reduced. This was done by the preparation of homebuilt centerpieces with optical path lengths down to only 50 μm. The resulting equations of state in Figure 7.7b show that the difference is very large compared to Figure 7.7a: pressures of two orders of magnitudes higher can now be measured. Hence, these cells allow measurements up to concentrations where significant deviations from Van 't Hoff's law can be expected. For example, excluded volume effects, accounted for by the Carnahan-Starling equation for hard spheres, start to become important in this region as indicated in the figure. Interestingly, for these concentrated samples the osmotic pressure falls below Van 't Hoff's law at higher concentrations. Contrary to the deviations in Figure 7.7a, here the data do follow a clear trend. Moreover, different starting concentrations result in the same equation of state, which confirms the reliability of the measurements. The deviation from ideal behavior is likely the result of magnetic interactions between the particles, which is analyzed and discussed in more detail in Chapter 8.

Clearly, our homebuilt centerpieces for AUC offer a significant advantage for strongly absorbing colloids. Not only can higher concentrations be measured; in addition, volumes of sample of only 1–2 microliters of sample are required for the measurements, compared to about 100 μL for the conventional cells. It should be noted though, that in some samples evaporation of the solvent started to take place after long equilibration times due to faulty cell sealing, which is easily detected by the changes in the liquid-air meniscus, such that the measurements can be excluded from analysis. Another remark that should be made is that when larger iron oxide colloids are measured (diameter $>$ 16 nm), the extinction coefficient (in m^2kg^{-1}) becomes more than twice as high, and the accessible concentration regime is reduced significantly.

7.5. Conclusions

The equation of state of concentrated ferrofluids can be accurately determined from sedimentation-diffusion equilibrium measurements using an analytical ultracentrifuge. Using conventional centerpieces with an optical path length of 3 mm, extremely low osmotic pressures can be accurately determined. However, for strongly absorbing colloids this is insufficient to assess any deviations from ideal behavior of the colloids. By using homebuilt centerpieces with an optical path length down to 50 μm, this concentration regime does become accessible. Hence, analytical ultracentrifugation can be used to measure osmotic pressures even below 1 Pa as well as pressures over 100 Pa, and the osmotic equation of state up to first-order deviations from Van 't Hoff's law can be obtained, as further studied in Chapter 8.

7.6. Acknowledgements

Dominique Thies-Weesie is thanked for performance of the measurements and many useful discussions. Peter de Graaf, Wim Nieuwenhuis, and Henk Jan Siekman are acknowledged for the construction of the homebuilt AUC cells. Rick de Groot is acknowledged for particle synthesis.

8

Osmotic Second Virial Coefficient of Apolar Ferrofluids Measured Via Analytical Centrifugation

Abstract

To study the thermodynamics of dipolar hard spheres experimentally, apolar ferrofluids are very useful as a model system. The osmotic equation of state of concentrated ferrofluids is obtained for the first time by analytical centrifugation using a LUMiFuge and an analytical ultracentrifuge. Sterically stabilized magnetic iron oxide nanoparticles with a diameter of 13 nm dispersed in an apolar solvent show a significant deviation from Van 't Hoff's law, due to magnetic interparticle attractions. The osmotic second virial coefficient, B_2, can be obtained from the equation of state, and it can be correlated to the dipolar coupling parameter, λ, as described in ref [88]. From our measured equations of state, a second virial coefficient is found that corresponds to an effective dipolar coupling parameter in the range $\lambda = 2.0$–2.4. If there is an isotropic phase separation for dipolar hard spheres, it is expected at a value of $\lambda \approx 2.5$, close to our experimentally obtained value, yet no indications for such a phase transition are found. The dipolar coupling parameter obtained by analytical centrifugation is in reasonable agreement with the coupling parameter calculated from independent magnetic measurements of the nanoparticles, providing clear validation of the analytical centrifugation method to determine interactions between colloidal particles.

8.1. Introduction

The dipolar hard-sphere (DHS) potential is widely employed to model dipolar interactions. It can be used to describe simple polar liquids, such as ethanol, and ferrofluids, i.e. colloidal dispersions of magnetic nanoparticles in a liquid. Despite the model's simplicity, the phase behavior of DHS-fluids is still under debate [65–68]. An important unresolved issue concerns the liquid-gas criticality. It was conjectured by de Gennes and Pincus that the orientational average of weak dipolar interactions yields an isotropic attraction that enables the coexistence of a gas and a liquid phase as in Van der Waals fluids [69]. However, Monte Carlo computer simulations from the early nineties failed to find any liquid-gas transition; this failure was attributed to the formation of chain-like structures [72–75], which was supported by theoretical work [76, 77]. This chain formation was also predicted by de Gennes and Pincus [69], and has been confirmed via direct imaging in cryogenic TEM experiments from our group [63, 79, 80]. Interestingly, Tlusty and Safran argued that coexistence of two phases with different chain morphologies is possible [82]. Simulations by Camp *et al.* of dipolar hard spheres, or rather particles that approach the limit of dipolar hard spheres, confirm that such a phase separation of different chain morphologies is indeed plausible if the magnetic interaction is large enough [83, 84, 86].

In this chapter, we investigate the thermodynamics of dipolar hard spheres experimentally. The equation of state of a ferrofluid is determined via measurement of the osmotic pressure over a concentration range that is large enough to probe deviations from Van 't Hoff's osmotic pressure law for ideal particles. Measurements of the osmotic pressure of ferrofluids have been reported previously, not using analytical centrifugation, and only for aqueous systems of small magnetic particles, in which electrical double-layer interactions and Van der Waals forces are significant if not dominant [89–92]. In this chapter, a dispersion of magnetite nanoparticles with a coating of oleic acid in decalin is used as a model system for dipolar hard spheres.

The measurement of the osmotic pressure of a ferrofluid over a large concentration range is challenging. Direct measurements using an osmometer or the osmotic stress method [93] are difficult, especially for low pressures [89], and the required dialysis tubes for apolar solvents do not exist. Light scattering can also be used to determine osmotic pressures [5], which has been applied to determine the second virial coefficient of attractive, non-magnetic particles [5, 94, 95]. The use of light scattering for our ferrofluids is unfeasible, since they strongly absorb light, although X-ray scattering would, in principle, be an option [90]. Our own approach is to use analytical centrifugation to obtain the osmotic pressure from sedimentation-diffusion equilibrium concentration profile measurements.

It has been shown previously that an analytical ultracentrifuge (AUC) can be used to obtain the osmotic equation of state of colloidal dispersions [96–99]. In a typical experiment, a colloidal dispersion is centrifuged and the concentration profile of the colloids is recorded *in situ* as it evolves towards sedimentation-diffusion equilibrium. The integration of the concentration profile of a colloidal dispersion in equilibrium directly yields the osmotic equation of state, as has been shown both in experiments and computer simulations [98, 181, 182]. However, measuring the equation of state of concentrated ferrofluids is unfeasible using conventional AUC measurement cells with an optical path length of the light of 3–12 mm, due to the strong light absorption of the iron oxide colloids. This problem is resolved by us in two separate ways.

Firstly, homebuilt AUC centerpieces with an optical path length of 50–70 μm, described in Chapter 7, are used to enable the measurement of concentrated dispersions with the AUC. Secondly, it was shown in Chapter 6 how a LUMiFuge stability analyzer can be used as an analytical centrifuge to obtain the osmotic equation of state of concentrated ferrofluids. In this chapter, osmotic equations of state of ferrofluids acquired in these two ways are reported and discussed in terms of the deviations from ideal behavior.

The first-order deviation from ideal behavior is characterized by the osmotic second virial coefficient, B_2. Recently, the relation between this B_2 and the dipolar coupling parameter, λ, has been calculated for a wide range of λ's [88]. Sedimentation velocity experiments by Planken *et al.* [101] yielded accelerated sedimentation for magnetite nanoparticles with an increasing dipolar coupling constant, which can be correlated to the second virial coefficient using a dimer model. In this chapter, the second virial coefficient is obtained in a more direct way, from the measured equation of state.

This chapter is organized as follows. In Section 8.2, it is reviewed how the second virial coefficient is related to the dipolar coupling constant for dipolar hard spheres. The experimental details of the ferrofluids and analytical centrifugation measurements are described in Section 8.3. In Section 8.4, the obtained equations of state are discussed, followed by an analysis of the corresponding B_2. Finally, conclusions are drawn in Section 8.5.

8.2. Theory

The equation of state for dilute, non-interacting colloids is given by Van 't Hoff's law:

$$\Pi = \rho k T \tag{8.1}$$

Here, Π is the osmotic pressure, k is Boltzmann's constant, T is the absolute temperature, and ρ is the particle number density. To include hard-sphere repulsions at higher

concentrations, Carnahan-Starling's equation of state can be used [5, 185]:

$$\Pi = \rho kT \left(\frac{1 + \phi + \phi^2 - \phi^3}{(1-\phi)^3} \right) \tag{8.2}$$

with ϕ the colloidal volume fraction.

The non-ideality of the equation of state of a colloidal dispersion can be expressed in terms of a virial expansion:

$$\frac{\Pi}{kT} = \rho + B_2\rho^2 + B_3\rho^3 + \ldots \tag{8.3}$$

where B_2 and B_3 are the second and third virial coefficient, respectively. Here, the first term corresponds to Equation 8.1, and the first deviation from ideal behavior is expressed by the second virial coefficient, B_2. For dipolar hard spheres (DHS), the pair potential at a center-to-center distance r is [188]:

$$\begin{aligned} \frac{u(r)}{kT} &= \infty; \qquad 0 \leq r < \sigma \\ \frac{u(\vec{r},\Omega)}{kT} &= \lambda \Big(\frac{\sigma}{r}\Big)^3 f(\Omega); \qquad r \geq \sigma \end{aligned} \tag{8.4}$$

where σ is the hard sphere diameter, and $f(\Omega)$ is the orientational part of the dipolar interaction, given by:

$$f(\Omega) = \hat{\mu_1} \cdot \hat{\mu_2} - 3(\hat{\mu_1} \cdot \hat{r})(\hat{\mu_2} \cdot \hat{r}) \tag{8.5}$$

where Ω denotes orientations of both dipoles, and the carets indicate the unit vectors of the dipole moment $\vec{\mu}$. In Equation 8.4, λ is the dipolar coupling parameter, which gives the amplitude of the magnetic interaction:

$$\lambda = \frac{\mu_0 \mu^2}{4\pi kT\sigma^3} \tag{8.6}$$

with μ_0 the permeability of vacuum and μ the magnitude of the dipole moment. The dipole moment scales with σ^3, thus from Equation 8.6, λ scales as $\lambda \sim \sigma^3$ as well. The maximal dipolar attraction for two spheres at contact ($r = \sigma$) with their dipoles in the head-to-tail configuration is $\mathrm{u_{max}}/(kT) = -2\lambda$.

The pair correlation function, $g(r, \rho)$, can be calculated from the potential of mean force, $V(r, \rho)$, which represents the average reversible work to bring a colloid to a position $\vec{r}$, relative to the other colloid centered at the origin $r = 0$ [5]:

$$g(r, \rho) = \exp\left[-\frac{V(r, \rho)}{kT} \right] \tag{8.7}$$

For sufficiently low number densities, ρ, the colloids only interact simultaneously with one other colloid. Then only the orientations of their two dipole moments need to be

averaged and the potential of mean force can be calculated from [88, 188]:

$$\exp\left[-\frac{V(r,\rho\to 0)}{kT}\right] = \left\langle \exp\left[-\frac{u(\vec{r},\Omega)}{kT}\right]\right\rangle_{\Omega} \tag{8.8}$$

where the brackets denote the averaging of the Boltzmann exponent of the pair potential over all orientations of the two dipoles at a certain distance $r = |\vec{r}|$. Using the analytical solution for the averaging in Equation 8.8 found by Chan *et al.* [188], the pair correlation function for two dipolar hard spheres is obtained:

$$g(x) = \begin{cases} 0; & 0 \le r < \sigma \\ \displaystyle\sum_{n=0}^{\infty}(-1)^n i_n\left(\frac{x}{2}\right) i_n\left(\frac{3x}{2}\right); & r \ge \sigma \end{cases} \tag{8.9}$$

with i_n the modified spherical Bessel function [189], and

$$x = \lambda\left(\frac{\sigma}{r}\right)^3 \tag{8.10}$$

The weak-coupling limit of the dipolar attraction is defined by $x \ll 1$ and the strong-coupling limit by $x \gg 1$. As long as center-to-center distances are large enough ($r^3 \gg \lambda\sigma^3$), two dipoles will enter the weak-coupling regime even for large coupling parameters ($\lambda \gg 1$).

For spherical particles, the second virial coefficient, B_2, is a function of the isotropic pair correlation function, $g(r)$ [5]:

$$B_2 = 2\pi\int_0^{\infty}[1-g(r)]r^2\mathrm{d}r \tag{8.11}$$

For $0 \le r < \sigma$, $g(r) = 0$ and the hard-sphere repulsion part of the second virial coefficient, B_2^{HS}, is given by:

$$B_2^{HS} = \frac{2}{3}\pi\sigma^3 \tag{8.12}$$

Using Equation 8.9, the second virial coefficient for dipolar hard spheres in the weak-coupling limit ($x \ll 1$) is found to be [88]:

$$\frac{B_2}{B_2^{HS}} = 1 - \frac{1}{3}\lambda^2 - \frac{1}{75}\lambda^4 - \frac{29}{55125}\lambda^6 \tag{8.13}$$

The higher order terms are included to improve the accuracy near $\lambda \approx 1$.

In the strong-coupling limit ($x \gg 1$) the following asymptotic result is obtained [88]:

$$\frac{B_2}{B_2^{HS}} \sim -\frac{\mathrm{e}^{2\lambda}}{12\lambda^3}; \qquad \lambda\to\infty \tag{8.14}$$

The result for the weak-coupling limit (Equation 8.13) has been compared to full numerical simulations, and the resulting graph from [88] is shown in Figure 8.1. This shows that Equation 8.13 is accurate up to $\lambda \approx 2.5$.

The described theory provides a way to calculate the dipolar coupling parameter λ from an experimental value of B_2. For single-domain magnetic nanoparticles, the λ

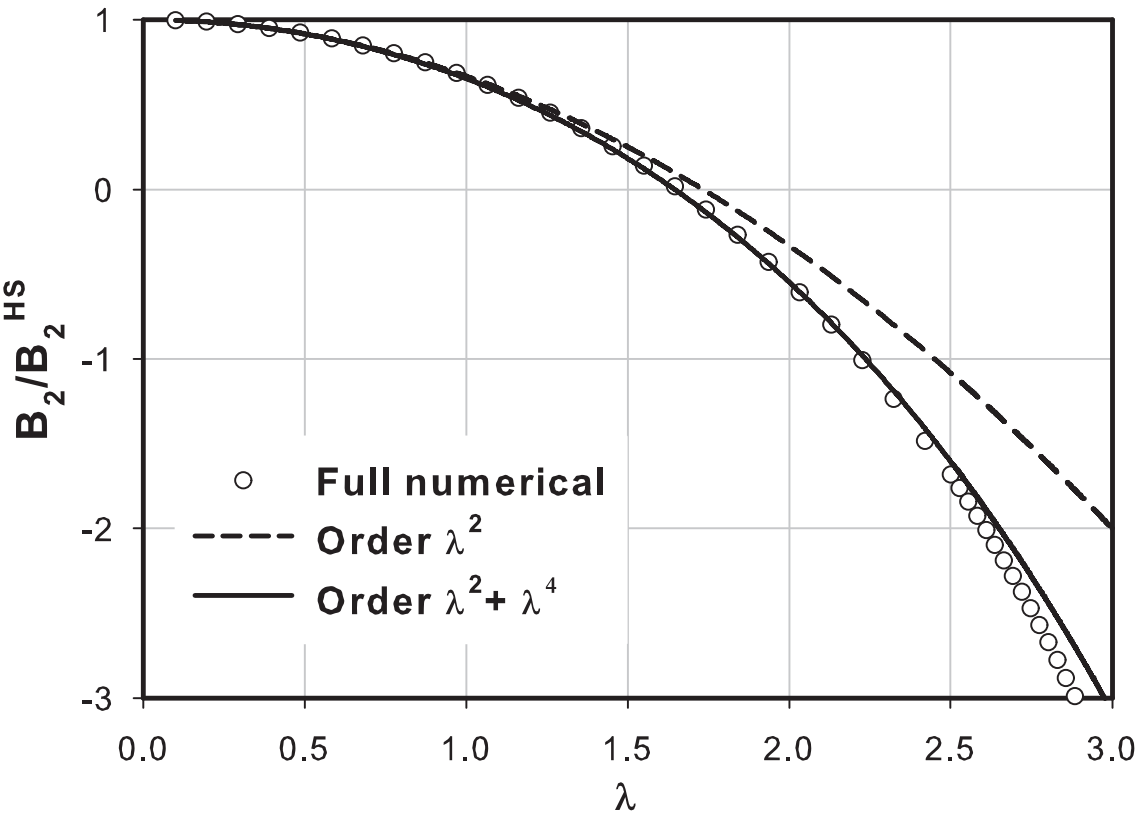

Figure 8.1. Second virial coefficient B_2 (scaled on the hard-sphere value B_2^{HS}), as a function of the dipolar coupling parameter, λ, taken from ref [88]. Numerical integration of Equation 8.11 for the pair correlation function in Equation 8.9 (open circles) is compared to the weak-coupling limit from Equation 8.13 using only the λ^2 term (dashed line) and adding the λ^4 term (solid line). If the λ^4 term is included, Equation 8.13 is quite accurate up to $\lambda \approx 2.5$.

obtained from analytical centrifugation can then be compared to the λ from independent magnetization measurements, calculated using Equation 8.6.

8.3. Experimental

8.3.1. Magnetite nanoparticles

As a model system for dipolar hard spheres, a colloidal dispersion of oleic acid-coated magnetic iron oxide nanoparticles in a solution of 15.6 mM oleic acid in decalin was used. These magnetite particles were prepared by seeded growth, as described in Chapter 4. Two different particle sizes were investigated by analytical centrifugation: particles with an average core diameter of 13.4 nm (± 10.5%) and 11.0 nm (± 11.7%), from series 18 and 20, respectively, of which the synthesis is described in Chapter 4. The magnetization curves of the particles (Figure 8.2) were measured using an alternating gradient magnetometer, and fitted using the method described in Chapter 5. For the 13

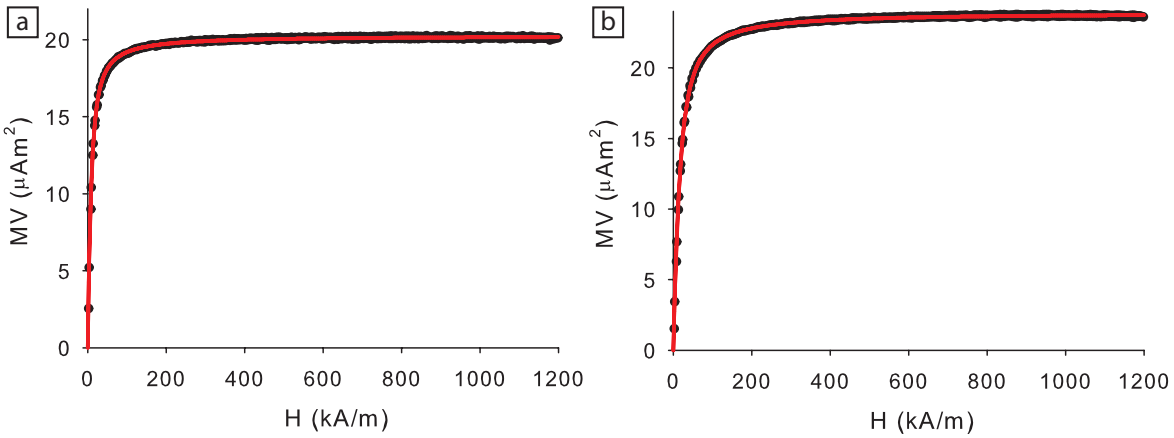

Figure 8.2. Total magnetic moment MV versus the external field H of a dispersion of 13.4 nm (**a**) and 11.0 nm (**b**) particles in decalin (dots) and the corresponding fits (lines). The average magnetic dipole moments of 4.3×10^{-19} Am^2 (**a**) and 2.7×10^{-19} Am^2 (**b**) were obtained from more dilute samples where interparticle magnetic interactions are negligible.

and 11 nm particles, the determined average dipole moments are 4.3×10^{-19} Am^2 and 2.7×10^{-19} Am^2, respectively. The corresponding dipolar coupling parameters obtained by inserting these average dipole moments in Equation 8.6 are $\lambda = 0.9$ and $\lambda = 0.5$ for, respectively, 13 and 11 nm particles. However, Equation 8.6 assumes monodispersity of the particles, whereas in the dipole moments that are obtained from fitting the magnetization curves, polydispersity is taken into account. If monodispersity is assumed in the analysis, the calculated coupling parameters are $\lambda = 1.8$ and $\lambda = 0.8$ for, respectively, 13 and 11 nm particles.

8.3.2. Analytical centrifugation using an analytical ultracentrifuge

Equilibrium measurements on iron oxide nanoparticles were performed using a Beckman Coulter Optima XL-I AUC (absorbance optics) and a Beckman Coulter Optima XL-A AUC (absorbance optics). In both cases, an An-60 Ti rotor containing 3 samples and 1 counterbalance was used. Ultra-thin centerpieces were prepared to obtain optical light paths of 50–70 μm, as described in Chapter 7. The 13 nm particles were measured using starting concentrations of 36, 103, and 134 g/L, at a wavelength of 541 nm. For sedimentation-diffusion equilibrium measurements, equilibrium scans were recorded at a temperature of 20.0 ± 0.1 °C. Rotation rates of 1200, 1400, and 1600 rpm were used, corresponding to 116, 158, and 206 times the gravitational acceleration at a radial position of 7.2 cm, near the bottom of the cell. Equilibrium scans were made at various time intervals, and when the subtraction of 2 scans with an 8 hour interval resulted in a difference of less than 1 %, the sample was considered to be in equilibrium.

8.3.3. Analytical centrifugation using a LUMiFuge

Sedimentation-diffusion equilibrium measurements were performed using a Stability Analyzer LUMiFuge®, which measures the transmission at a wavelength of 880 nm. All measurements were performed at 22.0 ± 0.5 °C, using a light factor (a measure for the lamp intensity) of 1.00 with starting concentrations of 150 and 134 g/L for 11 and 13 nm particles, respectively. The particles were measured at rotation rates of 500, 625, and 1000 rpm, corresponding to 36, 57, and 145 times the gravitational acceleration at the bottom of the cell, respectively. Further details about the measurements and analysis procedure are given in Chapter 6.

8.4. Results and discussion

8.4.1. Osmotic pressure for magnetic particles

Osmotic equations of state can be obtained by integration of the concentration profile that is calculated from the absorption and transmission data acquired by analytical centrifugation. The procedures are described in detail in Chapter 6 and Chapter 7 for the use of a LUMiFuge and analytical ultracentrifuge, respectively.

In Figure 8.3a, the equations of state of 13 nm particles obtained using a LUMiFuge are shown. The equations of state overlap for all 3 rotation rates for a wide measurement range. At low concentrations, Van 't Hoff's law is obeyed. For particles with only hard-sphere repulsions, the Carnahan-Starling equation of state (Equation 8.2) should describe the pressures at increasing concentrations, which exceed the value given by Van 't Hoff's law. However, in Figure 8.3 the opposite is found: at higher concentrations, pressures are even lower than expected from either the Carnahan-Starling or Van 't Hoff's equation of state. At the highest concentrations, the pressures in Figure 8.3a start to increase again. Possibly, hard sphere repulsions increasingly manifest themselves in this region. In Chapter 6 it was shown that inaccuracies, for example in the determined starting transmission, had the most effect at the highest concentrations, where, consequently, the interpretation of the data in Figure 8.3a is problematic.

The equations of state of 13 nm magnetite particles obtained with an AUC are shown in Figure 8.3b, measured at different starting concentrations as well as different rotation rates. The coincidence of these curves clearly shows the reliability of analytical centrifugation to determine the equation of state. Despite the relatively low pressures that are measured up to high concentrations, the equation of state can be accurately determined.

The equations of state obtained from the LUMiFuge and the AUC are shown with the same concentration and pressure axis in Figures 8.3a and 8.3b, respectively, to facilitate their comparison. Both techniques yield very similar results for the equation of state, although deviations from Van 't Hoff's law start at somewhat lower pressures of about

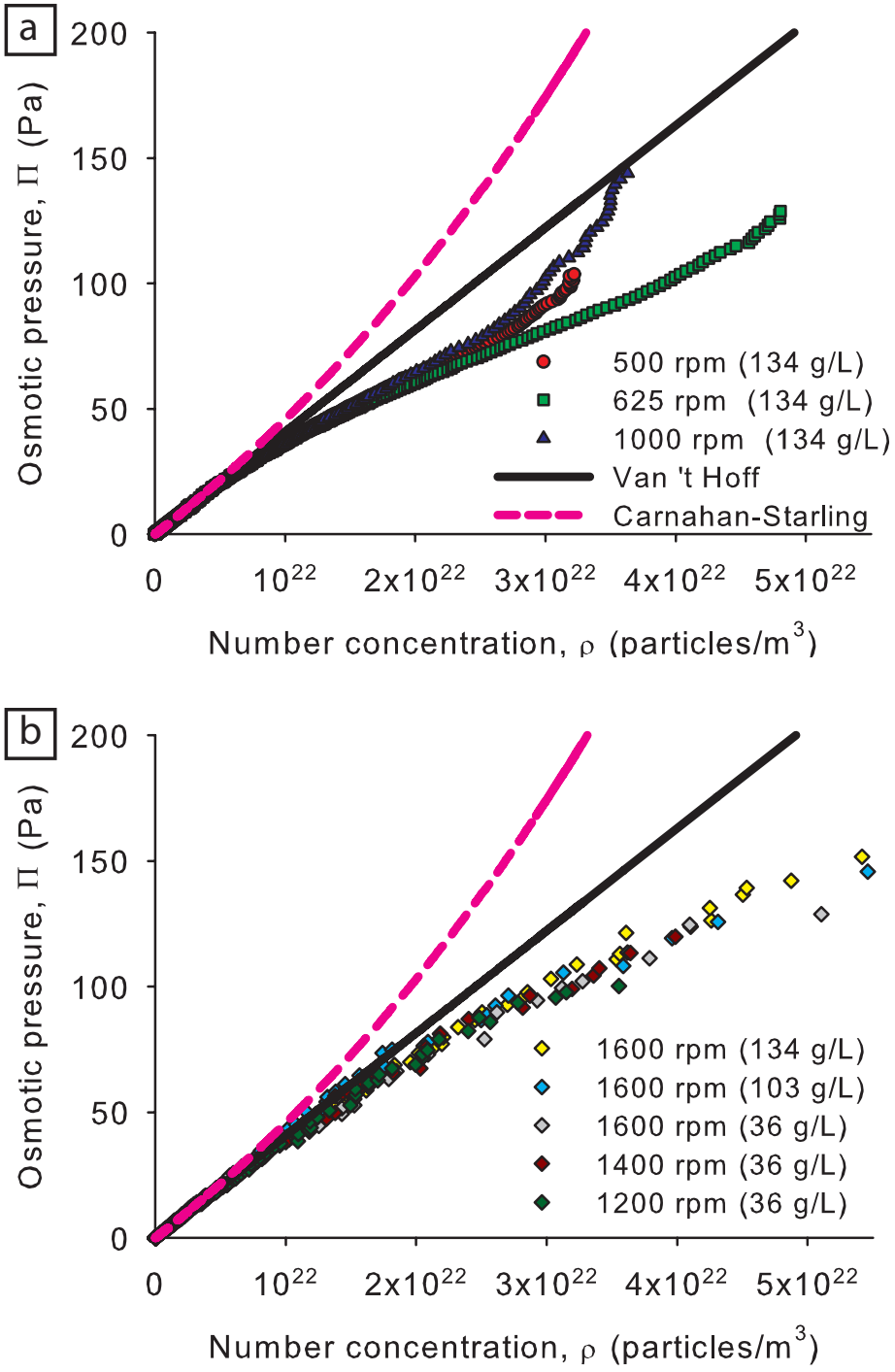

Figure 8.3. Osmotic pressure as a function of number concentration of 13 nm magnetite nanoparticles, measured using a LUMiFuge (**a**) and an AUC (**b**). Different initial concentrations and rotation rates were used as indicated, and the corresponding equations of state overlap in a wide concentration range. In both figures, Van 't Hoff's law (solid line, Equation 8.1) and Carnahan-Starling's equation of state (dashed line, Equation 8.2) are shown.

30 Pa for LUMiFuge data, compared to about 50 Pa for AUC data, for reasons that are unclear. Nevertheless, it is evident that the equation of state of 13 nm magnetite particles shows a significant deviation below Van 't Hoff's law, as could be expected for particles with (magnetic) attraction. However, it was shown in Chapters 6 and 7 that despite the polydispersity being relatively low (11 %), an effect of fractionation can be observed in the low concentration region of the profile. Therefore, the influence of polydispersity on the equation of state is now examined.

8.4.2. Polydispersity

To determine the effect of polydispersity on the osmotic equation of state, theoretical concentration profiles are calculated assuming an ideal mixture of non-interacting particles, and subsequently analyzed as follows. First, the measured size distribution from TEM of the 13 nm particles is divided into different size batches (9–10 nm, 10–11 nm, ... etc.) for which the average sizes and their relative contributions to the size distribution (number fractions) are calculated. Assuming a fixed total concentration based on the measured concentrations at the bottom of the sample cell in the LUMiFuge experiments, the corresponding number concentration profile for each batch is calculated using:

$$\rho(r) = \rho(r_b)\exp\left[\frac{\omega^2 \Delta m(r^2 - r_b^2)}{2kT}\right] \tag{8.15}$$

in which $\rho(r)$ and $\rho(r_b)$ are the number concentration at position r and the bottom position r_b, respectively, ω is the angular velocity, and Δm is the buoyant mass. For each size batch, the concentration profile is multiplied by its buoyant mass to obtain mass concentrations, and by its number fraction to assign the appropriate contribution to the total concentration. The total concentration profile is then the sum of the concentration profiles for each size batch. This total concentration profile is first converted to an absorption profile, such that the same analysis method described in Chapter 6 for the analysis of LUMiFuge data can be used to obtain the equation of state.

An important step in the analysis of measured data is the determination of the buoyant masses and corresponding sizes of the particles in the low concentration region. These are obtained from the slope of a graph of the natural logarithm of the absorbance, $\ln(A)$, as a function of the radial position squared, r^2. For simulated profiles assuming ideal behavior of the colloids this should be a straight line, as was found for the individually calculated concentration profiles of each size batch (not shown). However, for the total concentration profile a straight line in the $\ln(A)$ versus r^2 graph is clearly not found, as shown in Figure 8.4 for the 3 calculated rotation rates. The simulated data show that a deviation from a straight line in a $\ln(A)$ versus r^2 graph can be caused by polydispersity. The buoyant mass of the particles is obtained from a linear fit in the same radial region as in the experiments, as indicated by the black solid lines in

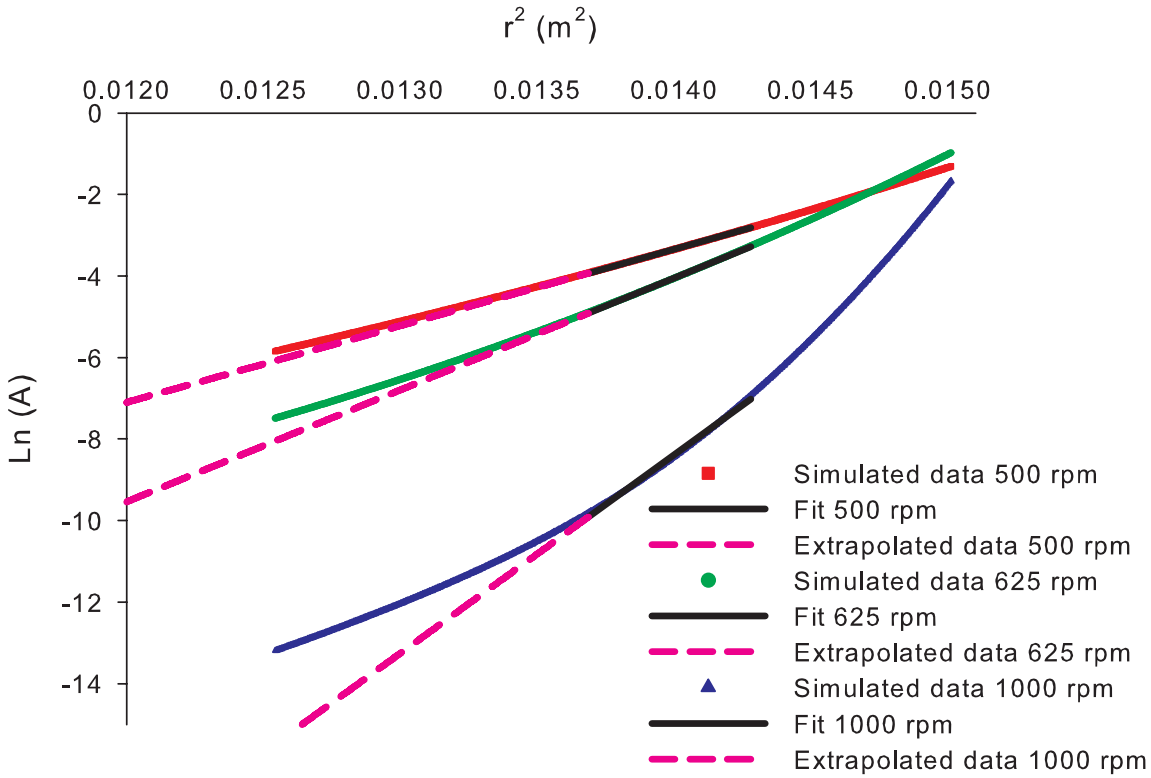

FIGURE 8.4. Graph of $\ln(A)$ as a function of r^2 from the simulated profiles taking into account the experimental polydispersity simulated for 500 rpm (squares), 625 rpm (spheres) and 1000 rpm (triangles). The regions that are fitted are indicated by solid lines, which are the same regions fitted in the LUMiFuge experiments. The extrapolated data from these fits are indicated by dashed lines.

Figure 8.4. For rotation rates of 500, 625, and 1000 rpm, buoyant masses of 5.6×10^{-21}, 5.2×10^{-21}, and 3.6×10^{-21} kg were found, respectively. These values are close to the experimental values (5.6–3.3×10^{-21} kg), confirming that in this low-concentration region used for the fit, fractionation due to polydispersity takes place.

In the analysis of the experimental data, the data at low concentrations are influenced by noise and the position of the meniscus of the sample. Therefore, the data in the dilute region are extrapolated from the fit, and the same procedure is applied for the calculated profiles. The concentration profiles that are obtained from this procedure are integrated to obtain the osmotic pressures. The resulting equations of state are compared to the experimental data in Figure 8.5.

The equations of state calculated using the TEM distribution to incorporate polydispersity are shown by the dotted lines in Figure 8.5. For all three rotation rates, the calculated equations of state fall below Van 't Hoff's law, which suggests that polydispersity can indeed cause the deviations from ideal behavior. However, the calculated

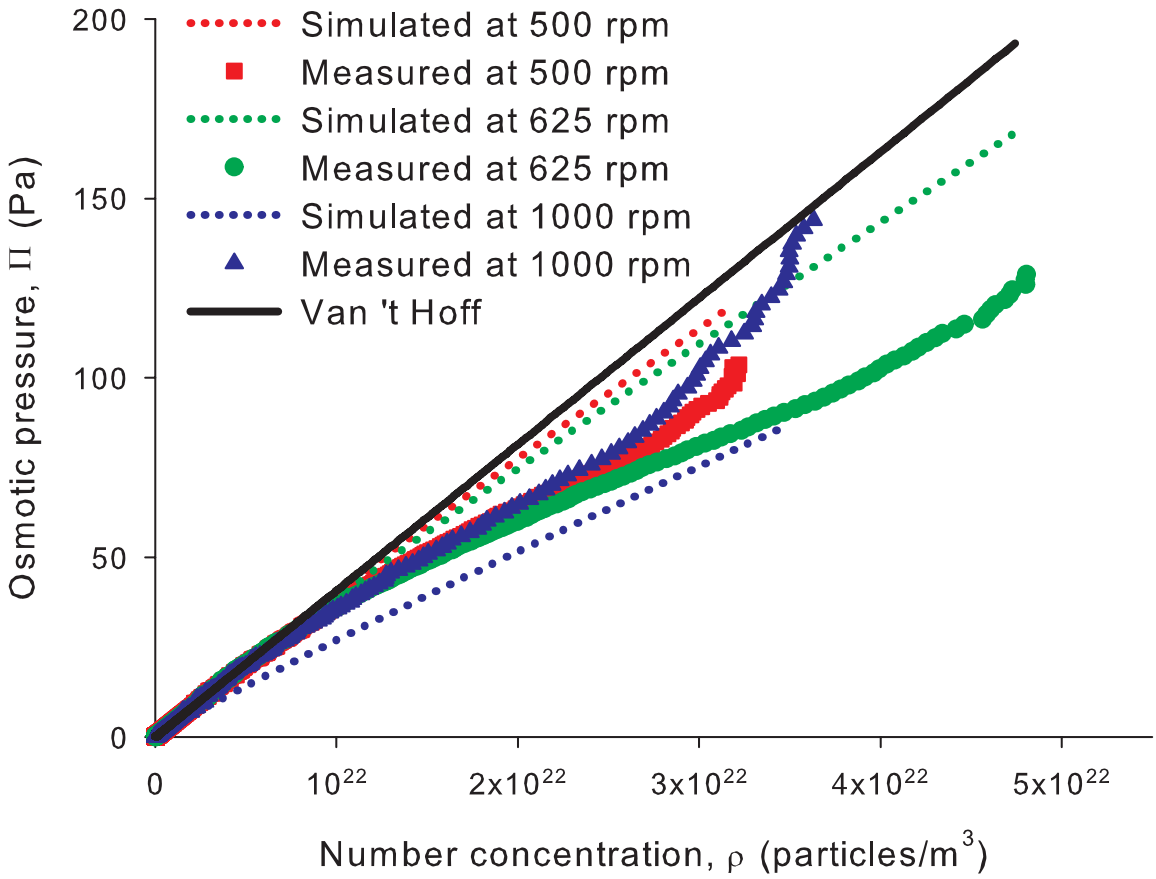

Figure 8.5. Comparison of the simulated (dotted lines) and measured equations of state for 13 nm particles with an polydispersity of 11%, measured at 500 rpm (squares), 625 rpm (spheres) and 1000 rpm (triangles). Van't Hoff's law is shown for comparison (solid line).

equations of state also show that these deviations depend on the rotation rate: larger rotation rates cause larger deviations, showing very large deviations at 1000 rpm. This is in contradiction with the experiments, where results from all three rotation rates coincide over a large measurement range. Therefore, it is unlikely that the deviations from Van 't Hoff's law for the measured data are caused by polydispersity.

Thus, on the one hand, the deviations from ideal behavior at high concentrations are unlikely to be due to polydispersity, yet in the dilute regime some fractionation is clearly observed. This apparent contradiction may be explained by the differences in concentrations along the radial position of the sample. In the dilute range, some fractionation takes place as the larger particles sediment more rapidly, and smaller particles are measured with increasing rotation rate. However, at larger radial positions, as concentration increases, the particle distribution becomes more homogeneous. Here, hydrodynamic interactions between particles apparently prevent a measurable

size fractionation for these low polydispersities. It has in fact been reported that it is very difficult to separate particles with a similar size by centrifugation. For example, Johnson *et al.* attempted to separate silica dumbbells from single silica spheres, which required more than 20 repeated centrifugation steps [190]. In our case, the size difference between the magnetic colloids is significantly smaller, hence it should come as no surprise that at increasing concentrations no effects of fractionation can be observed. Therefore, we can conclude that the deviations from ideal behavior are predominantly due to attractions between the particles.

8.4.3. Osmotic pressures for weakly magnetic particles

For comparison with the 13.4 nm particles, the equation of state was also determined for smaller particles (11.0 nm in diameter) which have a weaker magnetic interaction, but similar polydispersity (11.7%). The equations of state at different rotation rates are shown in Figure 8.6a. A smaller magnetic attraction is indeed what is observed: the samples obey Van 't Hoff's law up to high concentrations. If only hard-sphere repulsions would be present, the colloids should follow Carnahan-Starling's equation of state, however for these small colloids, still some (magnetic) attraction is present which reduces the pressure with respect to the hard-sphere value.

It should be noted, though, that the analysis of the data as well as the calculation of the Carnhan-Starling equation of state depend on the assumed thickness of the oleic acid shell, which will have a larger effect for smaller particles. To investigate this influence on the equation of state, the measured data were analyzed for an oleic acid shell thickness of 2 nm (Figure 8.6a) as well as for a shell thickness of 1 nm (Figure 8.6b). Changing this shell thickness changes the mass concentration and number densities, and with that the pressure, such that the graph in Figure 8.6b is slightly extended. The effect on the calculated Carnahan-Starling curve is larger, though, and the effective difference between Van 't Hoff's law and Carnahan-Starling is less pronounced for a shell thickness of 1 nm. Since the data are more noisy for this sample, it is difficult to determine quantitatively whether the data really follow Van 't Hoff's law or whether it starts to deviate towards the Carnahan-Starling equation of state.

Nevertheless, two important conclusions can be drawn by comparing the equations of state of 13 nm particles (Figure 8.3) to 11 nm particles (Figure 8.6a). First, the comparison confirms that the deviation below Van 't Hoff's law for 13 nm particles is not due to polydispersity, since the 11 nm particles with a similar polydispersity do not show this deviation. Second, the comparison indicates that this deviation is indeed due to (magnetic) attractions between the particles: the smaller particles with a smaller dipolar coupling parameter exert higher osmotic pressures than the more attractive 13 nm colloids.

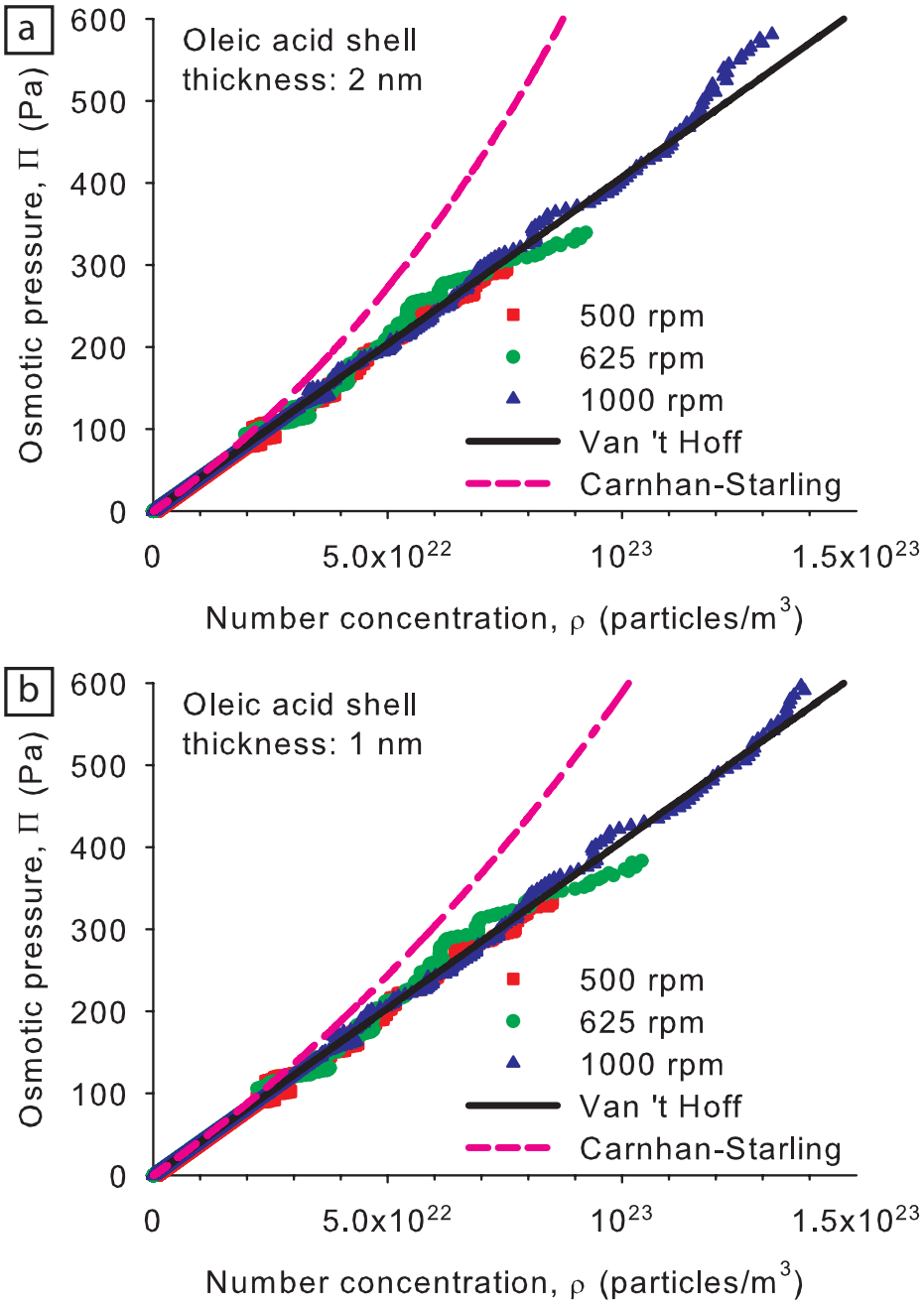

Figure 8.6. Osmotic pressure as a function of number concentration of 11 nm magnetite nanoparticles, measured using a LUMiFuge at 500 rpm (squares), 625 rpm (spheres), and 1000 rpm (triangles). Van 't Hoff's law (solid line, Equation 8.1) and Carnahan-Starling equation of state (dashed line, Equation 8.2) are also indicated. The analysis of the measured data and calculation of Carnahan-Starling's equation of state with an oleic acid shell of 2 nm (**a**) and 1 nm (**b**) are compared.

8.4.4. Osmotic second virial coefficient

A convenient way of expressing the virial series (Equation 8.3) is in terms of the volume fraction ϕ:

$$\frac{\Pi}{\rho kT} = 1 + B_2^{'}\phi + \cdots \tag{8.16}$$

In this way, a dimensionless $B_2^{'}$ can directly be obtained from the slope of a graph of $\Pi/(\rho kT)$ versus ϕ. This $B_2^{'}$ is related to B_2 (in m^3) from Section 8.2 by the volume v of the particle: $B_2^{'} = B_2/v$. The ratio $B_2^{'}/B_2^{HS'}$, with $B_2^{HS'}$ the dimensionless virial coefficient for hard spheres, is equal to the ratio B_2/B_2^{HS} in Equations 8.13 and 8.14 as the particle volume drops out. Thus, an effective dipolar coupling parameter λ can be determined for the weak-coupling limit using Equation 8.13, repeated below with the ratio $B_2^{'}/B_2^{HS'}$ included:

$$\frac{B_2^{'}}{B_2^{HS'}} = \frac{B_2}{B_2^{HS}} = 1 - \frac{1}{3}\lambda^2 - \frac{1}{75}\lambda^4 - \frac{29}{55125}\lambda^6 \tag{8.17}$$

The equations of state are displayed in a graph of $\Pi/(\rho kT)$ versus ϕ in Figure 8.7a and 8.7b for the measurements with the LUMiFuge and AUC, respectively. For an ideal system, Van 't Hoff's law is obeyed, and $B_2^{'} = 0$, resulting in the horizontal line at $\Pi/(\rho kT) = 1$. If repulsions dominate, $B_2^{'}$ is positive; for example, $B_2^{HS'} = 4$ in Carnahan-Starling's equation of state. As attractions between colloids are increasing, $B_2^{'}$ decreases and eventually becomes negative for $\lambda \gtrsim 1.6$ (the Boyle point, see Figure 8.1 and ref [88]).

In principle, at the lowest volume fractions, all data points should originate from $\Pi/(\rho kT) = 1$, as ideal behavior is imposed at the lowest concentrations. The fact that the measured data points start at zero and quickly increase to $\Pi/(\rho kT) = 1$ is an (almost unavoidable) artifact of our analysis method. Integration of the concentration profile is started at a chosen distance r from the rotor, where concentrations are very low and the osmotic pressure is set to be zero. This integration should, in principle, start at the center of the rotor, where $r = 0$. Although for the resulting equations of state shown in Figure 8.3 starting the integration at $r > 0$ has negligible influence, the obtained pressure at these positions does differ from the calculated values of ρkT at the lowest volume fractions. Hence, the graph starts at $\Pi/(\rho kT) = 0$, but rapidly increases to $\Pi/(\rho kT)$ =1. The data points at the lowest volume fractions correspond to values calculated from the extrapolated points from the $\ln(A)$ versus r^2 fit used in the data analysis (see also Chapters 6 and 7). The measured data starts at $\phi = 0.005$ or lower, as is evident by the significant increase in noise.

The second virial coefficient can be obtained from a linear fit to the data in Figure 8.7. The lowest volume fractions are not included in the fit, due to the relatively high noise levels. Nevertheless, the calculated intercept of the fitted lines with the y-axis

($\phi = 0$) is close to $\Pi/(\rho kT) = 1$ for most samples, as it should be. The regions that are fitted are indicated by the solid lines in Figure 8.7. Several fitting regions were investigated, of which an example is shown for 625 rpm in Figure 8.7a, where three fits of the 600 rpm data are indicated.

The second virial coefficients follow from the slope of these fits. The B_2' values obtained by the fits, including the values from the variation of the fitting range at 625 rpm, range from B_2' = -3.1 to -5.9 for LUMiFuge data. For the AUC data, the range of B_2' values obtained is B_2'= -2.6 to -4.8. Although this seems to be a rather wide range, in fact, a B_2' range of -2.3 to -5.9 is equivalent to dipolar coupling parameters λ in the range of 2.0–2.4 only, calculated from Equation 8.17. This λ-range is within the validity range of the weak-coupling calculation in Equation 8.17. Moreover, these λ-values are plausible: on the one hand, values of λ of 2.0–2.4 are large enough to induce significant deviations from ideal behavior, whereas on the other hand these values of λ are just too small to induce significant dipolar chain formation [63, 81]. In addition, since λ scales with σ^3, one can easily verify that if λ = 2.0–2.4 for 13.4 nm particles, λ should be in the range 1.1–1.3 for 11.0 nm particles, corresponding to values of B_2' in the range of 2.8–1.5. Thus, the equation of state should be much closer to ideal behavior, and intermediate between the Carnahan-Starling equation of state and Van 't Hoff's law, a trend which is indeed observed (Figure 8.6). The 13.4 nm particles studied here are in between weakly magnetic, almost ideal particles and strongly magnetic particles that display significant chain formation.

In Table 8.1, values of B_2' are listed for several values of λ calculated from Equation 8.17 and compared to the experimental values. The second virial coefficients corresponding to the λ values obtained from magnetization curves of these particles are given and compared to representative values of B_2' and corresponding λ's from LUMiFuge and AUC measurements. The coupling parameter that corresponds to the average dipole moment obtained from a polydisperse fit of the magnetization curve is only 1.3, whereas assuming monodispersity gives a λ of 1.8, closer to the value of $\lambda = 2.2$ from analytical centrifugation.

The dipole moment, and thus the coupling parameter λ, strongly depends on the diameter of the particles ($\lambda \sim \sigma^3$). Hence, the corresponding value of B_2' will be considerably different depending on whether two of the smaller particles in the sample or two of the larger particles interact. To estimate the range of B_2' values that may be expected, two values of λ are calculated, based on particle diameters of 12.3 and 14.6 nm, corresponding to the average TEM diameter with its standard deviation subtracted and added, respectively. Using Equation 8.17, B_2' is calculated to be 2.0 and -4.5 for a λ of 1.2 and 2.3, respectively, as given in Table 8.1 (rows 3–4). The comparison with experimental data is illustrated in Figure 8.8, in which the representative LUMiFuge and AUC samples from Table 8.1 are shown, with their fits extrapolated to $\phi = 0$. Clearly,

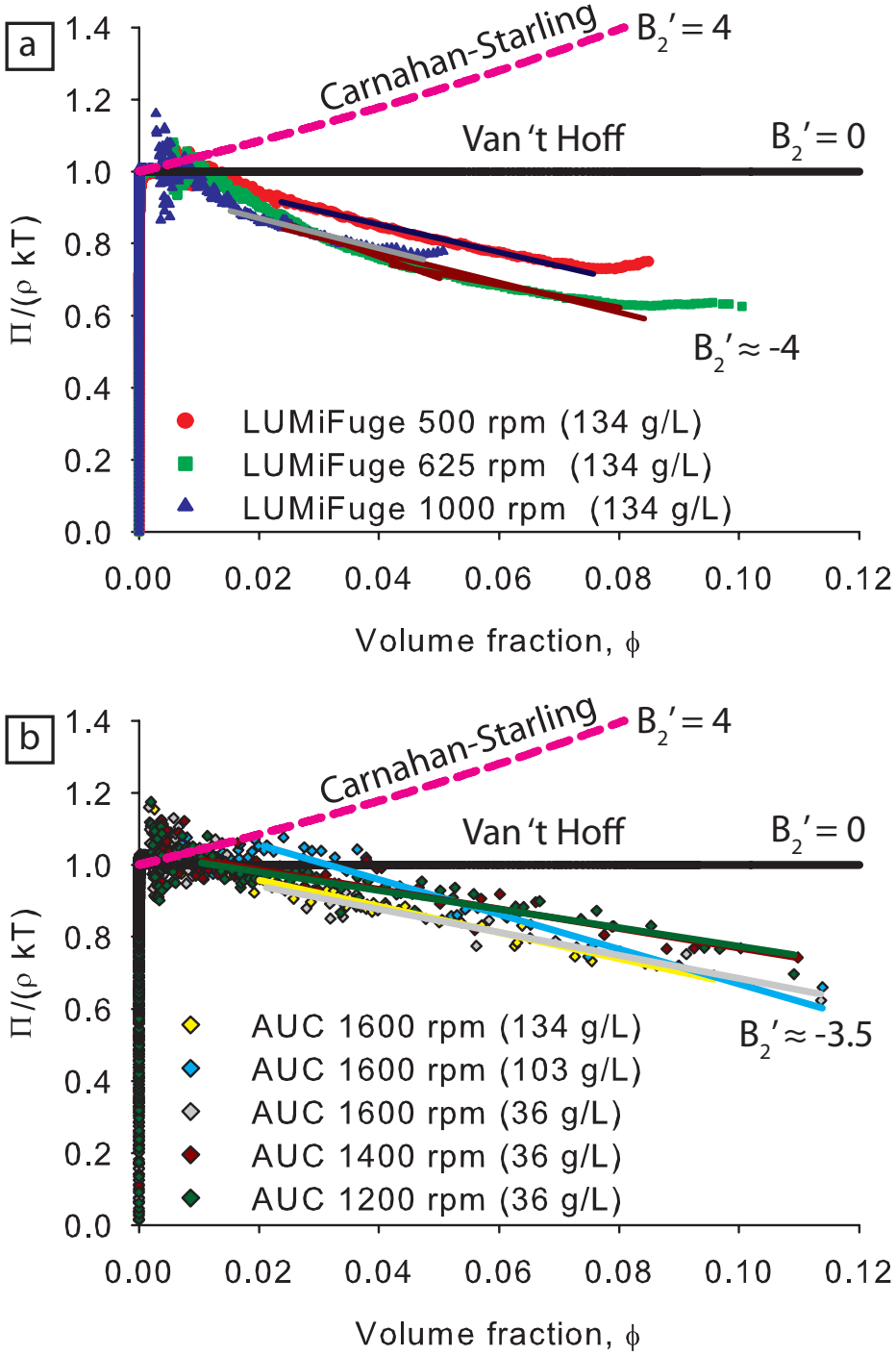

Figure 8.7. $\Pi/(\rho kT)$ versus ϕ of 13 nm magnetite particles from the measured LUMiFuge data (**a**) and AUC data (**b**). Van 't Hoff's law (black solid line, Equation 8.1) as well as Carnahan-Starling's equation state (pink dashed line, Equation 8.2) are also shown. In (**a**) the blue, brown, and grey solid lines correspond to the data at 500, 625, and 1000 rpm, respectively. For 625 rpm three different fitting ranges were tested. In (**b**) the fitting ranges for AUC data are indicated by solid lines of the same color as the data points.

Table 8.1. Values of the dimensionless B_2' (see Equation 8.16) corresponding to the λ's obtained from magnetic measurements (rows 1–2), calculated using Equation 8.17. Calculated values of λ and corresponding B_2' are shown for the smaller (row 3) and larger (row 4) fraction of the size distribution from TEM, calculated by subtracting or adding the standard deviation, σ_d, to the average TEM diameter, d_{TEM}, respectively. Experimental values of B_2' and their corresponding λ are shown for representative data measured by the LUMiFuge (row 5) and AUC (row 6).

	λ	B_2'
1. Calculated from polydisperse fit magnetization curves	1.3	1.6
2. Calculated from magnetization curves assuming monodispersity	1.8	-1.0
3. Calculated for $d_{\mathrm{TEM}} - \sigma_d$	1.2	2.0
4. Calculated for $d_{\mathrm{TEM}} + \sigma_d$	2.3	-4.5
5. From representative LUMiFuge data	$\sim$ 2.2	$\sim$ -3.9
6. From representative AUC data	$\sim$ 2.2	$\sim$ -3.6

the experimental data are within the range of plausible values for B_2' calculated from theory (Equation 8.17). The measured data are close to the coupling parameter corresponding to the larger particles interaction, suggesting that the interactions between the largest particles have the largest contribution to the deviations from ideal behavior measured by analytical centrifugation. The largest dipoles also contribute the most to the average value of the dipole moment extracted from magnetization curves when monodispersity is assumed, which explains the relatively good agreement of B_2' with that value of the dipole moment.

It is also relevant to determine how much Van der Waals interactions contribute to the attractions between the particles. Using recently published values of the Hamaker constant for iron oxides in various apolar solvents [191] and Hamaker's expression for two identical spheres [1,192], the Van der Waals interactions for particles of 13.4 nm in diameter are calculated to be a few tenths of kT. Thus, the Van der Waals interactions only have a minor contribution to the attraction between the particles.

Interestingly, for isotropic interactions, the onset of liquid-gas phase separation is expected for a second virial coefficient of about $B_2'/B_2^{HS'} \approx$ -1.5 [193]. This corresponds according to Figure 8.1 to an effective coupling parameter of $\lambda \approx 2.5$ [88]. Our experimentally obtained second virial coefficient and coupling parameter are very close to these values, yet no signs of phase separation, such as a plateau in the measured osmotic pressure [98], have been observed. One could argue that, perhaps, particles should be more attractive to observe such liquid-gas coexistence. However, since magnetite particles with a dipolar coupling of $\lambda \approx 2.0$ are clearly on the brink of chain

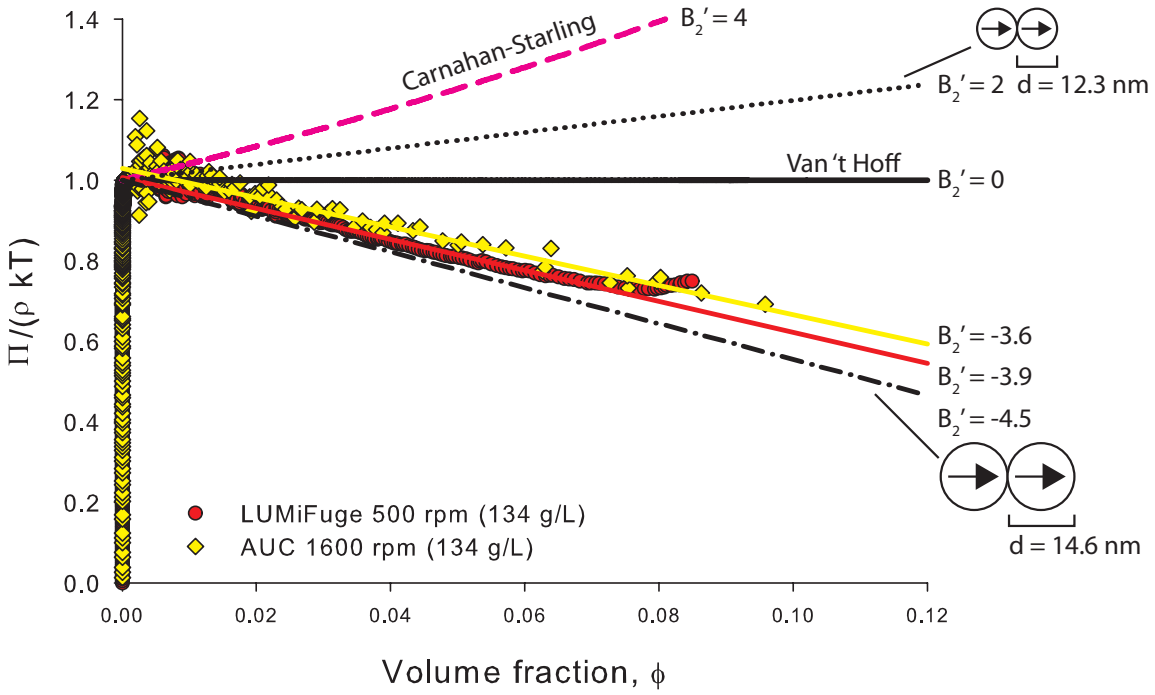

FIGURE 8.8. $\Pi/(\rho kT)$ versus ϕ of 13 nm magnetite particles, comparing representative LUMiFuge data (red spheres) and AUC data (yellow diamonds). Their corresponding fits are extrapolated to $\phi = 0$. The data is compared to calculations of particle sizes 12.3 and 14.6 nm, corresponding to the average TEM diameter of the particles with its standard deviation subtracted and added, respectively. Van 't Hoff's law (black solid line) as well as Carnahan-Starling's equation state (pink dashed line) are also shown.

formation [81], a Van der Waals-like phase behavior is a very unlikely scenario. This does not exclude the possibility of a phase separation involving dipolar structures, such as chains and rings, that has been predicted for higher values of λ [84, 86].

8.5. Conclusions

The equations of state of concentrated apolar ferrofluids have been measured for the first time, by analytical centrifugation, from sedimentation-diffusion equilibria obtained with a LUMiFuge as well as an analytical ultracentrifuge (AUC). With both techniques, high concentrations of the strongly absorbing dispersions could be measured using homebuilt ultra-thin centerpieces and thin capillary measurement cells for the AUC and LUMiFuge, respectively.

The measured equation of state of 13 nm magnetite nanoparticles is independent of rotation rate or the starting concentration, indicating the consistency of our analysis method used. The data from AUC and LUMiFuge measurements agree reasonably well,

although deviations from ideal behavior start at somewhat different pressures. From both AUC and LUMiFuge data, it is evident that the osmotic pressures fall below values from Van 't Hoff's law. Moreover, the obtained effective dipolar coupling parameters are in good agreement for the two techniques and comparable to those calculated from the dipole moments determined by independent magnetic measurements.

Despite fractionation effects found in the low-concentration range of the experiments, the deviations below ideal behavior for 13 nm particles are unlikely to be due to polydispersity, as indicated by equations of state calculated using the TEM distribution as input. This is confirmed by the equation of state of 11 nm particles, in which pressures do not fall below Van 't Hoff's law, despite a similar polydispersity as the 13 nm particles. Since the dipole moment of the particles is size dependent, the increased deviations from ideal behavior of 13 nm particles compared to 11 nm particles confirms that these deviations are caused by magnetic attractions.

The osmotic second virial coefficient, $B_2^{'}$, can be extracted from the equation of state and converted to an effective dipolar coupling constant using the formula for $B_2^{'}$ in the weak-coupling limit [88]. The value of $B_2^{'}$ is about -3.7 ($\lambda = 2.2$), although the range of $B_2^{'}$ values found varies depending on the fit parameters between -2.6 to -5.9. Nevertheless, all these values are within a range of an effective dipolar coupling parameter of $\lambda = 2.0$–2.4, and data from the LUMiFuge and AUC are in good agreement with each other. These values of λ are slightly larger than obtained from magnetic measurements, and they seem to correspond to the interactions between the larger particles in the sample. The contribution from Van der Waals interactions is negligible. The observed values of the effective λ are close to those expected for Van der Waals-like phase separation, whereas no indications of such a liquid-gas transition are found. The effective coupling parameter $\lambda \approx 2.2$ for our ferrofluids is close to, or at the onset of dipolar chain formation [63, 81], which makes it unlikely that Van der Waals-like phase coexistence can be observed in magnetic ferrofluids.

The fact that these values for $B_2^{'}$ and λ can be fairly accurately measured shows that analytical centrifugation is a suitable technique to study the thermodynamics and particle interactions in colloidal dispersions, and can be utilized for other types of nanoparticles as well, as will be explored in the future.

8.6. Acknowledgments

Dominique Thies-Weesie is gratefully acknowledged for performing the AUC measurements and for many useful discussions. Rick de Groot is thanked for particle synthesis, and Jos van Rijssel for useful discussions. Bonny Kuipers is thanked for providing the numerical calculations in Figure 8.1.

Bibliography

[1] J. Lyklema. *Fundamentals of Interface and Colloid Science, Vol. I.* Academic Press Limited, 1993.

[2] D. H. Everett. *Basic Principles of Colloid Science*. Royal Society of Chemistry, 1988.

[3] W. B. Russel, D. A. Saville, and W. R. Schowalter. *Colloidal Dispersions*. Cambridge University Press, 1995.

[4] A. P. Philipse. *Fundamentals of Interface and Colloid Science, Vol. IV*, chapter Particulate Colloids: Aspects of Preparation and Characterization. Elsevier, 2005.

[5] A. Vrij and R. Tuinier. *Fundamentals of Interface and Colloid Science, Vol. IV*, chapter Structure of Concentrated Colloidal Dispersions. Elsevier, 2005.

[6] W. Poon. Colloids as big atoms. *Science*, 304(5672):830–831, 2004.

[7] A. van Blaaderen. Colloidal molecules and beyond. *Science*, 301(5632):470–471, 2003.

[8] A. van Blaaderen. Materials science - colloids get complex. *Nature*, 439(7076):545–546, 2006.

[9] S. C. Glotzer and M. J. Solomon. Anisotropy of building blocks and their assembly into complex structures. *Nature Materials*, 6(8):557–562, 2007.

[10] U. Jeong, X. W. Teng, Y. Wang, H. Yang, and Y. N. Xia. Superparamagnetic colloids: Controlled synthesis and niche applications. *Advanced Materials*, 19(1):33–60, 2007.

[11] A. H. Lu, E. L. Salabas, and F. Schuth. Magnetic nanoparticles: Synthesis, protection, functionalization, and application. *Angewandte Chemie-International Edition*, 46(8):1222–1244, 2007.

[12] D. Horak, M. Babic, H. Mackova, and M. J. Benes. Preparation and properties of magnetic nano- and microsized particles for biological and environmental separations. *Journal of Separation Science*, 30(11):1751–1772, 2007.

[13] B. Berkovski and V. Bashtovoy, editors. *Magnetic fluids and applications handbook*. Begell House, inc., New York, 1996.

[14] D. V. Talapin, J. S. Lee, M. V. Kovalenko, and E. V. Shevchenko. Prospects of colloidal nanocrystals for electronic and optoelectronic applications. *Chemical Reviews*, 110(1):389–458, 2010.

[15] M. E. Dry. The Fischer-Tropsch process: 1950-2000. *Catalysis Today*, 71(3-4):227–241, 2002.

[16] S. Shylesh, V. Schunemann, and W. R. Thiel. Magnetically separable nanocatalysts: Bridges between homogeneous and heterogeneous catalysis. *Angewandte Chemie-International Edition*, 49(20):3428–3459, 2010.

[17] V. Polshettiwar, R. Luque, A. Fihri, H. Zhu, M. Bouhrara, and J. M. Bassett. Magnetically recoverable nanocatalysts. *Chemical Reviews*, 111(5):3036–3075, 2011.

[18] K. Butter. *Iron(oxide) ferrofluids: synthesis, structure and catalysis*. PhD thesis, Utrecht University, 2003.

[19] E. M. Claesson, N. C. Mehendale, R. J. M. Klein Gebbink, G. van Koten, and A. P. Philipse. Magnetic silica colloids for catalysis. *Journal of Magnetism and Magnetic Materials*, 311(1):41–45, 2007.

[20] Q. A. Pankhurst, J. Connolly, S. K. Jones, and J. Dobson. Applications of magnetic nanoparticles in biomedicine. *Journal of Physics D: Applied Physics*, 36(13):R167–R181, 2003.

[21] P. Tartaj, M. P. Morales, T. Gonzalez-Carreno, S. Veintemillas-Verdaguer, and C. J. Serna. Advances in magnetic nanoparticles for biotechnology applications. *Journal of Magnetism and Magnetic Materials*, 290:28–34, 2005.

[22] A. K. Gupta and M. Gupta. Synthesis and surface engineering of iron oxide nanoparticles for biomedical applications. *Biomaterials*, 26(18):3995–4021, 2005.

[23] S. Laurent, D. Forge, M. Port, A. Roch, C. Robic, L. V. Elst, and R. N. Muller. Magnetic iron oxide nanoparticles: Synthesis, stabilization, vectorization, physicochemical characterizations, and biological applications. *Chemical Reviews*, 108(6):2064–2110, 2008.

[24] J. H. Gao, H. W. Gu, and B. Xu. Multifunctional magnetic nanoparticles: Design, synthesis, and biomedical applications. *Accounts of Chemical Research*, 42(8):1097–1107, 2009.

[25] Q. A. Pankhurst, N. K. T. Thanh, S. K. Jones, and J. Dobson. Progress in applications of magnetic nanoparticles in biomedicine. *Journal of Physics D: Applied Physics*, 42(22):224001, 2009.

[26] K. M. Krishnan. Biomedical nanomagnetics: A spin through possibilities in imaging, diagnostics, and therapy. *IEEE Transactions On Magnetics*, 46(7):2523–2558, 2010.

[27] R. Hao, R. J. Xing, Z. C. Xu, Y. L. Hou, S. Gao, and S. H. Sun. Synthesis, functionalization, and biomedical applications of multifunctional magnetic nanoparticles. *Advanced Materials*, 22(25):2729–2742, 2010.

[28] S. Laurent, S. Dutz, U. O. Hafeli, and M. Mahmoudi. Magnetic fluid hyperthermia: Focus on superparamagnetic iron oxide nanoparticles. *Advances in colloid and interface science*, 166(1-2):8–23, 2011.

[29] D. Jiles. *Introduction to Magnetism and Magnetic Materials*. Chapman & Hall / CRC, Taylor & Francis Group, 1998.

[30] P. Debye. *Polar Molecules*. Dover Publications, reprint of Reinhold Publishing Corporation edition, 1929.

[31] P. J. Flanders. An alternating-gradient magnetometer. *Journal of Applied Physics*, 63(8):3940–3945, 1988.

[32] A. P. Philipse, M. P. B. Vanbruggen, and C. Pathmamanoharan. Magnetic silica dispersions - preparation and stability of surface-modified silica particles with a magnetic core. *Langmuir*, 10(1):92–99, 1994.

[33] Y. Lu, Y. D. Yin, B. T. Mayers, and Y. N. Xia. Modifying the surface properties of superparamagnetic iron oxide nanoparticles through a sol-gel approach. *Nano Letters*, 2(3):183–186, 2002.

[34] J. Lee, Y. Lee, J. K. Youn, H. Bin Na, T. Yu, H. Kim, S. M. Lee, Y. M. Koo, J. H. Kwak, H. G. Park, H. N. Chang, M. Hwang, J. G. Park, J. Kim, and T. Hyeon. Simple synthesis of functionalized superparamagnetic magnetite/silica core/shell nanoparticles and their application as magnetically separable high-performance biocatalysts. *Small*, 4(1):143–152, 2008.

[35] E. M. Claesson and A. P. Philipse. Monodisperse magnetizable composite silica spheres with tunable dipolar interactions. *Langmuir*, 21(21):9412–9419, 2005.

[36] J. Q. Zhuang, H. M. Wu, Y. A. Yang, and Y. C. Cao. Supercrystalline colloidal particles from artificial atoms. *Journal of the American Chemical Society*, 129(46):14166–14167, 2007.

[37] J. Q. Zhuang, H. M. Wu, Y. G. Yang, and Y. C. Cao. Controlling colloidal superparticle growth through solvophobic interactions. *Angewandte Chemie-International Edition*, 47(12):2208–2212, 2008.

[38] H. Deng, X. L. Li, Q. Peng, X. Wang, J. P. Chen, and Y. D. Li. Monodisperse magnetic single-crystal ferrite microspheres. *Angewandte Chemie-International Edition*, 44(18):2782–2785, 2005.

[39] J. P. Ge, Y. X. Hu, M. Biasini, W. P. Beyermann, and Y. D. Yin. Superparamagnetic magnetite colloidal nanocrystal clusters. *Angewandte Chemie-International Edition*, 46(23):4342–4345, 2007.

[40] Y. Deng, D. Qi, C. Deng, X. Zhang, and D. Zhao. Superparamagnetic high-magnetization microspheres with an Fe_3O_4@SiO_2 core and perpendicularly aligned mesoporous SiO_2 shell for removal of microcystins. *Journal of the American Chemical Society*, 130(1):28–29, 2008.

[41] B. Luo, X. J. Song, F. Zhang, A. Xia, W. L. Yang, J. H. Hu, and C. C. Wang. Multi-functional thermosensitive composite microspheres with high magnetic susceptibility based on magnetite colloidal nanoparticle clusters. *Langmuir*, 2009.

[42] P. Qiu, C. Jensen, N. Charity, R. Towner, and C. Mao. Oil phase evaporation-induced self-assembly of hydrophobic nanoparticles into spherical clusters with controlled surface chemistry in an oil-in-water dispersion and comparison of behaviors of individual and clustered iron oxide nanoparticles. *Journal of the American Chemical Society*, 132(50):17724–17732, 2010.

[43] L. Li, E. S. G. Choo, J. B. Yi, J. Ding, X. S. Tang, and J. M. Xue. Superparamagnetic silica composite nanospheres (SSCNs) with ultrahigh loading of iron oxide nanoparticles via an oil-in-DEG microemulsion route. *Chemistry of Materials*, 20(20):6292–6294, 2008.

[44] A. Xia, J. H. Hu, C. C. Wang, and D. L. Jiang. Synthesis of magnetic microspheres with controllable structure via polymerization-triggered self-positioning of nanocrystals. *Small*, 3(10):1811–1817, 2007.

[45] S. Sacanna, W. K. Kegel, and A. P. Philipse. Thermodynamically stable Pickering emulsions. *Physical Review Letters*, 98(15), 2007.

[46] S. Sacanna, W. K. Kegel, and A. P. Philipse. Spontaneous oil-in-water emulsification induced by charge-stabilized dispersions of various inorganic colloids. *Langmuir*, 23(21):10486–10492, 2007.

[47] D. J. Kraft, J. W. J. de Folter, B. Luigjes, S. I. R. Castillo, S. Sacanna, A. P. Philipse, and W. K. Kegel. Conditions for equilibrium solid-stabilized emulsions. *Journal of Physical Chemistry B*, 114(32):10347–10356, 2010.

[48] S. Sacanna and A. P. Philipse. Preparation and properties of monodisperse latex spheres with controlled magnetic moment for field-induced colloidal crystallization and (dipolar) chain formation. *Langmuir*, 22(24):10209–10216, 2006.

[49] S. Sacanna and A. P. Philipse. A generic single-step synthesis of monodisperse core/shell colloids based on spontaneous Pickering emulsification. *Advanced Materials*, 19(22):3824–3826, 2007.

[50] E. M. Claesson. *Magnetic core-shell silica colloids*. PhD thesis, Utrecht University, 2007.

[51] B. H. Erné, E. M. Claesson, S. Sacanna, M. Klokkenburg, E. Bakelaar, and B. W. M. Kuipers. Low-frequency complex magnetic susceptibility of magnetic composite microspheres in colloidal dispersion. *Journal of Magnetism and Magnetic Materials*, 311(1):145–149, 2007.

[52] J. Park, J. Joo, S. G. Kwon, Y. Jang, and T. Hyeon. Synthesis of monodisperse spherical nanocrystals. *Angewandte Chemie-International Edition*, 46(25):4630–4660, 2007.

[53] S. G. Kwon and T. Hyeon. Colloidal chemical synthesis and formation kinetics of uniformly sized nanocrystals of metals, oxides, and chalcogenides. *Accounts of Chemical Research*, 41(12):1696–1709, 2008.

[54] J. Liu, S. Z. Qiao, Q. H. Hu, and G. Q. M. Lu. Magnetic nanocomposites with mesoporous structures: Synthesis and applications. *Small*, 2011.

[55] R. Massart. Preparation of aqueous magnetic liquids in alkaline and acidic media. *IEEE Transactions on Magnetics*, 17(2):1247–1248, 1981.

[56] F. A. Tourinho, R. Franck, and R. Massart. Aqueous ferrofluids based on manganese and cobalt ferrites. *Journal of Materials Science*, 25(7):3249–3254, 1990.

[57] A. P. Philipse and D. Maas. Magnetic colloids from magnetotactic bacteria: Chain formation and colloidal stability. *Langmuir*, 18(25):9977–9984, 2002.

[58] J. Park, K. J. An, Y. S. Hwang, J. G. Park, H. J. Noh, J. Y. Kim, J. H. Park, N. M. Hwang, and T. Hyeon. Ultra-large-scale syntheses of monodisperse nanocrystals. *Nature Materials*, 3(12):891–895, 2004.

[59] S. G. Kwon, Y. Piao, J. Park, S. Angappane, Y. Jo, N. M. Hwang, J. G. Park, and T. Hyeon. Kinetics of monodisperse iron oxide nanocrystal formation by "heating-up" process. *Journal of the American Chemical Society*, 129:12571–12584, 2007.

[60] N. R. Jana, Y. F. Chen, and X. G. Peng. Size- and shape-controlled magnetic (Cr, Mn, Fe, Co, Ni) oxide nanocrystals via a simple and general approach. *Chemistry of Materials*, 16(20):3931–3935, 2004.

[61] S. H. Sun and H. Zeng. Size-controlled synthesis of magnetite nanoparticies. *Journal of the American Chemical Society*, 124(28):8204–8205, 2002.

[62] S. H. Sun, H. Zeng, D. B. Robinson, S. Raoux, P. M. Rice, S. X. Wang, and G. X. Li. Monodisperse MFe_2O_4 (M = Fe, Co, Mn) nanoparticles. *Journal of the American Chemical Society*, 126(1):273–279, 2004.

[63] M. Klokkenburg, C. Vonk, E. M. Claesson, J. D. Meeldijk, B. H. Erné, and A. P. Philipse. Direct imaging of zero-field dipolar structures in colloidal dispersions of synthetic magnetite. *Journal of the American Chemical Society*, 126(51):16706–16707, 2004.

[64] M. Klokkenburg. *Dipolar structures in colloidal magnetite dispersions*. PhD thesis, Utrecht University, 2007.

[65] V. Cabuil. Phase behavior of magnetic nanoparticles dispersions in bulk and confined geometries. *Current Opinion In Colloid & Interface Science*, 5(1-2):44–48, 2000.

[66] P. I. C. Teixeira, J. M. Tavares, and M. M. T. da Gama. The effect of dipolar forces on the structure and thermodynamics of classical fluids. *Journal of Physics-Condensed Matter*, 12(33):R411–R434, 2000.

[67] B. Huke and M. Lücke. Magnetic properties of colloidal suspensions of interacting magnetic particles. *Reports On Progress In Physics*, 67(10):1731–1768, 2004.

[68] C. Holm and J. J. Weis. The structure of ferrofluids: A status report. *Current Opinion in Colloid & Interface Science*, 10(3-4):133–140, 2005.

[69] P. G. de Gennes and P. A. Pincus. Pair correlations in a ferromagnetic colloid. *Physik der Kondensierten Materie*, 11(3):189, 1970.

[70] G. S. Rushbrooke, G. Stell, and J. S. Høye. Theory of polar liquids I. dipolar hard spheres. *Molecular Physics*, 26(5):1199–1215, 1973.

[71] K. C. Ng, J. P. Valleau, G. M. Torrie, and G. N. Patey. Liquid-vapor coexistence of dipolar hard-spheres. *Molecular Physics*, 38(3):781–788, 1979.

[72] J. M. Caillol. Search of the gas-liquid transition of dipolar hard-spheres. *Journal of Chemical Physics*, 98(12):9835–9849, 1993.

[73] J. J. Weis and D. Levesque. Chain formation in low-density dipolar hard-spheres - a Monte-Carlo study. *Physical Review Letters*, 71(17):2729–2732, 1993.

[74] M. E. van Leeuwen and B. Smit. What makes a polar liquid a liquid? *Physical Review Letters*, 71(24):3991–3994, 1993.

[75] D. Levesque and J. J. Weis. Orientational and structural order in strongly interacting dipolar hard-spheres. *Physical Review E*, 49(6):5131–5140, 1994.

[76] R. P. Sear. Low-density fluid phase of dipolar hard spheres. *Physical Review Letters*, 76(13):2310–2313, 1996.

[77] R. van Roij. Theory of chain association versus liquid condensation. *Physical Review Letters*, 76(18):3348–3351, 1996.

[78] R. W. Chantrell, A. Bradbury, J. Popplewell, and S. W. Charles. Particle cluster configuration in magnetic fluids. *Journal of Physics D: Applied Physics*, 13(7):L119–L122, 1980.

[79] K. Butter, P. H. H. Bomans, P. M. Frederik, G. J. Vroege, and A. P. Philipse. Direct observation of dipolar chains in iron ferrofluids by cryogenic electron microscopy. *Nature Materials*, 2(2):88–91, 2003.

[80] K. Butter, P. H. Bomans, P. M. Frederik, G. J. Vroege, and A. P. Philipse. Direct observation of dipolar chains in ferrofluids in zero field using cryogenic electron microscopy. *Journal of Physics-Condensed Matter*, 15(15):S1451–S1470, 2003.

[81] M. Klokkenburg, R. P. A. Dullens, W. K. Kegel, B. H. Erné, and A. P. Philipse. Quantitative real-space analysis of self-assembled structures of magnetic dipolar colloids. *Physical Review Letters*, 96(3), 2006.

[82] T. Tlusty and S. A. Safran. Defect-induced phase separation in dipolar fluids. *Science*, 290(5495):1328–1331, 2000.

[83] P. J. Camp, J. C. Shelley, and G. N. Patey. Isotropic fluid phases of dipolar hard spheres. *Physical Review Letters*, 84(1):115–118, 2000.

[84] G. Ganzenmuller and P. J. Camp. Vapor-liquid coexistence in fluids of charged hard dumbbells. *Journal of Chemical Physics*, 126(19), 2007.

[85] J. C. Shelley, G. N. Patey, D. Levesque, and J. J. Weis. Liquid-vapor coexistence in fluids of dipolar hard dumbbells and spherocylinders. *Physical Review E*, 59(3):3065–3070, 1999.

[86] Y. V. Kalyuzhnyi, I. A. Protsykevytch, G. Ganzenmuller, and P. J. Camp. Liquid-vapour coexistence in the dipolar Yukawa hard-sphere fluid. *EPL*, 84(2), 2008.

[87] G. Ganzenmuller, G. N. Patey, and P. J. Camp. Vapour-liquid phase transition of dipolar particles. *Molecular Physics*, 107(4-6):403–413, 2009.

[88] A. P. Philipse and B. W. M. Kuipers. Second virial coefficients of dipolar hard spheres. *Journal of Physics-Condensed Matter*, 22(32):325104, 2010.

[89] F. Cousin and V. Cabuil. Osmotic pressure of electrostatically stabilized magnetic liquids. *Journal of Molecular Liquids*, 83(1-3):203–215, 1999.

[90] E. Dubois, R. Perzynski, F. Boue, and V. Cabuil. Liquid-gas transitions in charged colloidal dispersions: Small-angle neutron scattering coupled with phase diagrams of magnetic fluids. *Langmuir*, 16(13):5617–5625, 2000.

[91] F. Cousin, E. Dubois, and V. Cabuil. Approach of the critical point of gas-liquid transitions in an electrostatically stabilized colloidal suspension. *Journal of Chemical Physics*, 115(13):6051–6057, 2001.

[92] F. Cousin, E. Dubois, and V. Cabuil. Tuning the interactions of a magnetic colloidal suspension. *Physical Review E*, 68(2), 2003.

[93] V. A. Parsegian, N. Fuller, and R. P. Rand. Measured work of deformation and repulsion of lecithin bilayers. *Proceedings of the National Academy of Sciences of the United States of America*, 76(6):2750–2754, 1979.

[94] P. W. Rouw and C. G. de Kruif. Adhesive hard-sphere colloidal dispersions .1. diffusion-coefficient as a function of well depth. *Journal of Chemical Physics*, 88(12):7799–7806, 1988.

[95] P. W. Rouw, A. Vrij, and C. G. de Kruif. Adhesive hard-sphere colloidal dispersions. iii. stickiness in n-dodecane and benzene. In V. Degiorgio, editor, *Trends in Colloid and Interface Science II*, volume 76 of *Progress in Colloid and Polymer Science*, pages 1–15. Springer Berlin / Heidelberg, 1988.

[96] M. Rasa and A. P. Philipse. Evidence for a macroscopic electric field in the sedimentation profiles of charged colloids. *Nature*, 429(6994):857–860, 2004.

[97] M. Rasa, B. H. Erne, B. Zoetekouw, R. van Roij, and A. P. Philipse. Macroscopic electric field and osmotic pressure in ultracentrifugal sedimentation-diffusion equilibria of charged colloids. *Journal of Physics-Condensed Matter*, 17(15):2293–2314, 2005.

[98] M. G. Page, T. Zemb, M. Dubois, and H. Colfen. Osmotic pressure and phase boundary determination of multiphase systems by analytical ultracentrifugation. *ChemPhysChem*, 9(6):882–890, 2008.

[99] H. Cölfen. *Analytical Centrifugation: Techniques and Methods*, chapter Analytical Ultracentrifugation of Colloids, pages 501–583. Royal Society of Chemistry, 2005.

[100] K. L. Planken. *Analytical ultracentrifugation of inorganic colloids - sedimentation velocity of interacting and non-interacting particles*. PhD thesis, Utrecht University, 2008.

[101] K. L. Planken, M. Klokkenburg, J. Groenewold, and A. P. Philipse. Ultracentrifugation of single-domain magnetite particles and the de Gennes-Pincus approach to ferromagnetic colloids in the dilute regime. *Journal of Physical Chemistry B*, 113(12):3932–3940, 2009.

[102] T. Sobisch and D. Lerche. Application of a new separation analyzer for the characterization of dispersions stabilized with clay derivatives. *Colloid and Polymer Science*, 278(4):369–374, 2000.

[103] W. Ramsden. Separation of solids in the surface-layers of solutions and 'Suspensions' (Observations on surface-membranes, bubbles, emulsions, and mechanical coagulation). Preliminary account. *Proceedings of the Royal Society of London*, 72(479):156–164, 1903.

[104] S. U. Pickering. Emulsions. *Journal of the Chemical Society*, 91:2001–2021, 1907.

[105] R. Aveyard, B. P. Binks, and J. H. Clint. Emulsions stabilised solely by colloidal particles. *Advances In Colloid and Interface Science*, 100:503–546, 2003.

[106] F. Leal-Calderon and V. Schmitt. Solid-stabilized emulsions. *Current Opinion In Colloid & Interface Science*, 13(4):217–227, 2008.

[107] W. K. Kegel and J. Groenewold. Scenario for equilibrium solid-stabilized emulsions. *Physical Review E*, 80(3), 2009.

[108] J. Zwanikken. *Looking deeper into emulsions and suspensions - ionic screening, fractionation, and adsorption*. PhD thesis, Utrecht University, 2009.

[109] W. Ostwald. On the assumed isomerism of red and yellow mercury oxide and the surface-tension of solid bodies. *Zeitschrift Fur Physikalische Chemie–stochiometrie Und Verwandtschaftslehre*, 34(4):495–503, 1900.

[110] I. M. Lifshitz and V. V. Slyozov. The kinetics of precipitation from supersaturated solid solutions. *Journal of Physics and Chemistry of Solids*, 19(1-2):35–50, 1961.

[111] A. P. Philipse and A. Vrij. Preparation and properties of nonaqueous model dispersions of chemically modified, charged silica spheres. *Journal of Colloid and Interface Science*, 128(1):121–136, 1989.

[112] E. P. Plueddemann. *Silane Coupling Agents*. Plenum Press: New York, 1982.

[113] B. Arkles. Tailoring surfaces with silanes. *Chemtech*, 7(12):766–778, 1977.

[114] M. C. B. Salon, P. A. Bayle, M. Abdelmouleh, S. Boufi, and M. N. Belgacem. Kinetics of hydrolysis and self condensation reactions of silanes by NMR spectroscopy. *Colloids and Surfaces A-Physicochemical and Engineering Aspects*, 312(2-3):83–91, 2008.

[115] H. N. W. Lekkerkerker. Contribution of the electric double-layer to the curvature elasticity of charged amphiphilic monolayers. *Physica A*, 159(3):319–328, 1989.

[116] R. Krishnamoorti. Strategies for dispersing nanoparticles in polymers. *MRS Bulletin*, 32(4):341–347, 2007.

[117] M. E. Mackay, A. Tuteja, P. M. Duxbury, C. J. Hawker, B. Van Horn, Z. B. Guan, G. H. Chen, and R. S. Krishnan. General strategies for nanoparticle dispersion. *Science*, 311(5768):1740–1743, 2006.

[118] R. A. Vaia and J. F. Maguire. Polymer nanocomposites with prescribed morphology: Going beyond nanoparticle-filled polymers. *Chemistry of Materials*, 19(11):2736–2751, 2007.

[119] A. B. R. Mayer. Colloidal metal nanoparticles dispersed in amphiphilic polymers. *Polymers for Advanced Technologies*, 12(1-2):96–106, 2001.

[120] P. Bian and T. J. McCarthy. Polymerization of monomer-based ferrofluids. *Langmuir*, 26(9):6145–6148, 2010.

[121] R. De Palma, S. Peeters, M. J. Van Bael, H. Van den Rul, K. Bonroy, W. Laureyn, J. Mullens, G. Borghs, and G. Maes. Silane ligand exchange to make hydrophobic superparamagnetic nanoparticles water-dispersible. *Chemistry of Materials*, 19(7):1821–1831, 2007.

[122] N. T. S. Phan, C. S. Gill, J. V. Nguyen, Z. J. Zhang, and C. W. Jones. Expanding the utility of one-pot multistep reaction networks through compartmentation and recovery of the catalyst. *Angewandte Chemie-International Edition*, 45(14):2209–2212, 2006.

[123] A. S. Lubbe, C. Alexiou, and C. Bergemann. Clinical applications of magnetic drug targeting. *Journal of Surgical Research*, 95(2):200–206, 2001.

[124] U. O. Hafeli. Magnetically modulated therapeutic systems. *International Journal of Pharmaceutics*, 277(1-2):19–24, 2004.

[125] W. Stöber, A. Fink, and E. Bohn. Controlled growth of monodisperse silica spheres in micron size range. *Journal of Colloid and Interface Science*, 26(1):62–69, 1968.

[126] D. J. Kraft, B. Luigjes, J. W. J. de Folter, A. P. Philipse, and W. K. Kegel. Evolution of equilibrium pickering emulsions-a matter of time scales. *Journal of Physical Chemistry B*, 114(38):12257–12263, 2010.

[127] L. N. Donselaar, P. M. Frederik, P. Bomans, P. A. Buining, B. M. Humbel, and A. P. Philipse. Visualisation of particle association in magnetic fluids in zero-field. *Journal of Magnetism and Magnetic Materials*, 201:58–61, 1999.

[128] M. E. Leunissen, A. van Blaaderen, A. D. Hollingsworth, M. T. Sullivan, and P. M. Chaikin. Electrostatics at the oil-water interface, stability, and order in emulsions and colloids. *Proceedings of the National Academy of Sciences of the United States of America*, 104(8):2585–2590, 2007.

[129] M. E. Leunissen, J. Zwanikken, R. van Roij, P. M. Chaikin, and A. van Blaaderen. Ion partitioning at the oil-water interface as a source of tunable electrostatic effects in emulsions with colloids. *Physical Chemistry Chemical Physics*, 9(48):6405–6414, 2007.

[130] S. H. Sun, C. B. Murray, D. Weller, L. Folks, and A. Moser. Monodisperse FePt nanoparticles and ferromagnetic FePt nanocrystal superlattices. *Science*, 287(5460):1989–1992, 2000.

[131] H. Zeng, J. Li, J. P. Liu, Z. L. Wang, and S. H. Sun. Exchange-coupled nanocomposite magnets by nanoparticle self-assembly. *Nature*, 420(6914):395–398, 2002.

[132] S. A. Safran. Ferrofluids: Magnetic strings and networks. *Nature Materials*, 2(2):71–72, 2003.

[133] V. K. LaMer and R. H. Dinegar. Theory, production and mechanism of formation of monodispersed hydrosols. *Journal of the American Chemical Society*, 72(11):4847–4854, 1950.

[134] H. Reiss. The growth of uniform colloidal dispersions. *Journal of Chemical Physics*, 19(4):482–487, 1951.

[135] C. B. Murray, D. J. Norris, and M. G. Bawendi. Synthesis and characterization of nearly monodisperse CdE (E = S, Se, Te) semiconductor nanocrystallites. *Journal of the American Chemical Society*, 115(19):8706–8715, 1993.

[136] X. G. Peng, J. Wickham, and A. P. Alivisatos. Kinetics of II-VI and III-V colloidal semiconductor nanocrystal growth: "Focusing" of size distributions. *Journal of the American Chemical Society*, 120(21):5343–5344, 1998.

[137] C. D. Donega, P. Liljeroth, and D. Vanmaekelbergh. Physicochemical evaluation of the hot-injection method, a synthesis route for monodisperse nanocrystals. *Small*, 1(12):1152–1162, 2005.

[138] Y. Yin and A. P. Alivisatos. Colloidal nanocrystal synthesis and the organic-inorganic interface. *Nature*, 437(7059):664–670, 2005.

[139] M. Klokkenburg. *Personal communication*, 2010.

[140] M. Klokkenburg, J. Hilhorst, and B. H. Erné. Surface analysis of magnetite nanoparticles in cyclohexane solutions of oleic acid and oleylamine. *Vibrational Spectroscopy*, 43(1):243–248, 2007.

[141] L. M. Bronstein, X. L. Huang, J. Retrum, A. Schmucker, M. Pink, B. D. Stein, and B. Dragnea. Influence of iron oleate complex structure on iron oxide nanoparticle formation. *Chemistry of Materials*, 19(15):3624–3632, 2007.

[142] Y. L. Liu and A. R. H. Walker. Monodisperse gold copper bimetallic nanocubes: Facile one-step synthesis with controllable size and composition. *Angewandte Chemie-International Edition*, 49(38):6781–6785, 2010.

[143] S. Kumar and T. Nann. Shape control of II-VI semiconductor nanomaterials. *Small*, 2(3):316–329, 2006.

[144] Y. Xia, Y. J. Xiong, B. Lim, and S. E. Skrabalak. Shape-controlled synthesis of metal nanocrystals: Simple chemistry meets complex physics? *Angewandte Chemie-International Edition*, 48(1):60–103, 2009.

[145] X. Batlle and A. Labarta. Finite-size effects in fine particles: magnetic and transport properties. *Journal of Physics D: Applied Physics*, 35(6):R15–R42, 2002.

[146] M. Gonzales-Weimuller, M. Zeisberger, and K. M. Krishnan. Size-dependant heating rates of iron oxide nanoparticles for magnetic fluid hyperthermia. *Journal of Magnetism and Magnetic Materials*, 321(13):1947–1950, 2009.

[147] R. E. Rosensweig. Heating magnetic fluid with alternating magnetic field. *Journal of Magnetism and Magnetic Materials*, 252(1-3):PII S0304–8853(02)00706–0, 2002.

[148] A. P. Khandhar, R. M. Ferguson, and K. M. Krishnan. Monodispersed magnetite nanoparticles optimized for magnetic fluid hyperthermia: Implications in biological systems. *Journal of Applied Physics*, 109(7):07B310, 2011.

[149] P. C. Fannin. An experimental-observation of the dynamic behavior of ferrofluids. *Journal of Magnetism and Magnetic Materials*, 136(1-2):49–58, 1994.

[150] R. M. Ferguson, K. R. Minard, A. P. Khandhar, and K. M. Krishnan. Optimizing magnetite nanoparticles for mass sensitivity in magnetic particle imaging. *Medical Physics*, 38(3):1619–1626, 2011.

[151] B. Gleich and R. Weizenecker. Tomographic imaging using the nonlinear response of magnetic particles. *Nature*, 435(7046):1214–1217, 2005.

[152] T. F. Sattel, T. Knopp, S. Biederer, B. Gleich, J. Weizenecker, J. Borgert, and T. M. Buzug. Single-sided device for magnetic particle imaging. *Journal of Physics D: Applied Physics*, 42(2):022001, 2009.

[153] C. B. Murray, C. R. Kagan, and M. G. Bawendi. Synthesis and characterization of monodisperse nanocrystals and close-packed nanocrystal assemblies. *Annual Review of Materials Science*, 30:545–610, 2000.

[154] R. Hergt, S. Dutz, R. Mueller, and M. Zeisberger. Magnetic particle hyperthermia: nanoparticle magnetism and materials development for cancer therapy. *Journal of Physics-condensed Matter*, 18(38):S2919–S2934, 2006.

[155] M. Andrés Vergés, R. Costo, A. G. Roca, J. F. Marco, G. F. Goya, C. J. Serna, and M. P. Morales. Uniform and water stable magnetite nanoparticles with diameters around the monodomain-multidomain limit. *Journal of Physics D: Applied Physics*, 41(13):134003, 2008.

[156] R. H. Kodama. Magnetic nanoparticles. *Journal of Magnetism and Magnetic Materials*, 200(1-3):359–372, 1999.

[157] A. J. Barker, B. Cage, S. Russek, and C. R. Stoldt. Ripening during magnetite nanoparticle synthesis: Resulting interfacial defects and magnetic properties. *Journal of Applied Physics*, 98(6):063528, 2005.

[158] G. F. Goya, T. S. Berquó, F. C. Fonseca, and M. P. Morales. Static and dynamic magnetic properties of spherical magnetite nanoparticles. *Journal of Applied Physics*, 94(5):3520–3528, 2003.

[159] A. G. Roca, M. P. Morales, K. O'Grady, and C. J. Serna. Structural and magnetic properties of uniform magnetite nanoparticles prepared by high temperature decomposition of organic precursors. *Nanotechnology*, 17(11):2783–2788, 2006.

[160] M. Klokkenburg, B. H. Erné, J. D. Meeldijk, A. Wiedenmann, A. V. Petukhov, R. P. A. Dullens, and A. P. Philipse. In situ imaging of field-induced hexagonal columns in magnetite ferrofluids. *Physical Review Letters*, 97(18):185702, 2006.

[161] M. Klokkenburg, B. H. Erné, A. Wiedenmann, A. V. Petukhov, and A. P. Philipse. Dipolar structures in magnetite ferrofluids studied with small-angle neutron scattering with and without applied magnetic field. *Physical review. E, Statistical, nonlinear, and soft matter physics*, 75(5 Pt 1):051408, 2007.

[162] A. Wiedenmann, U. Keiderling, M. Meissner, D. Wallacher, R. Gaehler, R. P. May, S. Prevost, M. Klokkenburg, B. H. Erné, and J. Kohlbrecher. Low-temperature dynamics of magnetic colloids studied by time-resolved small-angle neutron scattering. *Physical Review B*, 77(18):184417, 2008.

[163] M. Georgescu, M. Klokkenburg, B. H. Erné, P. Liljeroth, D. Vanmaekelbergh, and P. A. Zeijlmans van Emmichoven. Flux closure in two-dimensional magnetite nanoparticle assemblies. *Physical Review B*, 73(18):184415, 2006.

[164] M. Klokkenburg and B. H. Erné. Comparison of reversible and irreversible dipolar assemblies in a ferrofluid. *Journal of Magnetism and Magnetic Materials*, 306(1):85–91, 2006.

[165] D. Bica. Preparation of magnetic fluids for various applications. *Romanian Reports in Physics*, 47:272–3, 1995.

[166] B. H. Erné, E. van den Pol, G. J. Vroege, T. Visser, and H. H. Wensink. Size fractionation in a phase-separated colloidal fluid. *Langmuir*, 21(5):1802–1805, 2005.

[167] M. Klokkenburg, B. H. Erné, V. Mendelev, and A. O. Ivanov. Magnetization behavior of ferrofluids with cryogenically imaged dipolar chains. *Journal of Physics-Condensed Matter*, 20(20), 2008.

[168] A.D. Krawitz. *Introduction to Diffraction in Materials Science and Engineering*. John Wiley: New York, 2001.

[169] R. W. Chantrell, J. Popplewell, and S. W. Charles. Measurements of particle-size distribution parameters in ferrofluids. *IEEE Transactions on Magnetics*, 14(5):975–977, 1978.

[170] M. Rasa. Magnetic properties and magneto-birefringence of magnetic fluids. *European Physical Journal E*, 2(3):265–275, 2000.

[171] D. X. Chen, A. Sanchez, E. Taboada, A. Roig, N. Sun, and H. C. Gu. Size determination of superparamagnetic nanoparticles from magnetization curve. *Journal of Applied Physics*, 105(8):083924, 2009.

[172] S. Taketomi and R. D. Shull. Experimental study of magnetic interactions between colloidal particles in magnetic fluids. *Journal of Applied Physics*, 91(10):8546–8548, 2002.

[173] A. O. Ivanov and O. B. Kuznetsova. Magnetogranulometric analysis of ferrocolloids: Second-order modified mean field theory. *Colloid Journal*, 68(4):430–440, 2006.

[174] S. Chikazumi. *Physics of Magnetism*. Wiley: New York, 1964.

[175] D. B. Williams and C. B. Carter. *Transmission Electron Microscopy: A Textbook for Materials Science*. Plenum: New York, 1996.

[176] D. Hull and D. J. Bacon. *Introduction to Dislocations*. Butterworth-Heinemann: Woburn, MA, 2001.

[177] K. Arakawa, K. Ono, M. Isshiki, K. Mimura, M. Uchikoshi, and H. Mori. Observation of the one-dimensional diffusion of nanometer-sized dislocation loops. *Science*, 318(5852):956–959, 2007.

[178] C. J. Bae, S. Angappane, J. G. Park, Y. Lee, J. Lee, K. An, and T. Hyeon. Experimental studies of strong dipolar interparticle interaction in monodisperse Fe3O4 nanoparticles. *Applied Physics Letters*, 91(10):102502, 2007.

[179] O. Ozdemir and D. J. Dunlop. Effect of crystal defects and internal stress on the domain structure and magnetic properties of magnetite. *Journal of Geophysical Research-solid Earth*, 102(B9):20211–20224, 1997.

[180] G. Salazar-Alvarez, J. Qin, V. Sepelak, I. Bergmann, M. Vasilakaki, K. N. Trohidou, J. D. Ardisson, W. A. A. Macedo, M. Mikhaylova, M. Muhammed, M. D. Baro, and J. Nogues. Cubic versus spherical magnetic nanoparticles: The role of surface anisotropy. *Journal of the American Chemical Society*, 130(40):13234–13239, 2008.

[181] T. Biben, J. P. Hansen, and J. L. Barrat. Density profiles of concentrated colloidal suspensions in sedimentation equilibrium. *Journal of Chemical Physics*, 98(9):7330–7344, 1993.

[182] R. Piazza, T. Bellini, and V. Degiorgio. Equilibrium sedimentation profiles of screened charged colloids - a test of the hard-sphere equation of state. *Physical Review Letters*, 71(25):4267–4270, 1993.

[183] *L.U.M. GmbH. Manual Dispersion Analyser LUMiSizer and Stability Analyser LUMiFuge*, 2007.

[184] A. Seifert and N. Buske. Analytical ultracentrifugation of magnetic fluids. *Journal of Magnetism and Magnetic Materials*, 122(1-3):115–118, 1993.

[185] N. F. Carnahan and K. E. Starling. Equation of state for nonattracting rigid spheres. *Journal of Chemical Physics*, 51(2):635–636, 1969.

[186] D. J. Scott, S. E. Harding, and A. J. Rowe, editors. *Analytical Centrifugation: Techniques and Methods*. Royal Society of Chemistry, 2005.

[187] A. P. Philipse. Remarks on the Donnan condenser in the sedimentation-diffusion equilibrium of charged colloids. *Journal of Physics-Condensed Matter*, 16(38):S4051–S4062, 2004.

[188] D. Y. C. Chan, D. Henderson, J. Barojas, and A. M. Homola. The stability of a colloidal suspension of coated magnetic particles in an aqueous-solution. *IBM Journal of Research and Development*, 29(1):11–17, 1985.

[189] M. Abramowitz and I. Stegun. *Handbook of Mathematical Functions*. New York: Dover, 1972.

[190] P. M. Johnson, C. M. van Kats, and A. van Blaaderen. Synthesis of colloidal silica dumbbells. *Langmuir*, 21(24):11510–11517, 2005.

[191] B. Faure, G. Salazar-Alvarez, and L. Bergström. Hamaker constants of iron oxide nanoparticles. *Langmuir*, 27(14):8659–8664, 2011.

[192] H. C. Hamaker. The London - Van der Waals attraction between spherical particles. *Physica*, 4:1058–1072, 1937.

[193] G. A. Vliegenthart and H. N. W. Lekkerkerker. Predicting the gas-liquid critical point from the second virial coefficient. *Journal of Chemical Physics*, 112(12):5364–5369, 2000.

Summary

This thesis is a study on the preparation and thermodynamic properties of magnetic colloids. Two types of magnetic model colloids are investigated: composite colloids and single-domain nanoparticles. Thermodynamics of magnetic colloids is studied using analytical centrifugation, including a specially adapted centrifuge for measuring heavy and strongly light absorbing colloids. **Chapter 1** is an introduction into the synthesis and characterization of magnetic colloids, and it also briefly reviews the phase behavior of dipolar fluids. Following this introduction, the thesis is divided into three parts.

Part 1 examines a preparation route for magnetic composite colloids. This route comprises polymerization of thermodynamically stable Pickering emulsions, consisting of 3-methacryloxypropyl trimethoxysilane (TPM) oil in water stabilized by magnetite (Fe_3O_4) or cobalt ferrite ($CoFe_2O_4$) nanoparticles. In **Chapter 2** the tunability of these emulsions is investigated, and it is shown that the emulsion droplet size increases (a) with the relative volume of oil, (b) with the amount of salt, and (c) by evolution of the droplets over time. With respect to the latter (c), we demonstrate that interfacial nanoparticles gradually transfer to the oil phase; the emulsion droplets grow to adapt to the equilibrium size belonging to the changing chemical conditions at that specific time, until eventually the emulsion demixes into the water and oil phases, with the nanoparticles suspended in the oil. This transfer of the nanoparticles to the TPM oil phase is utilized in **Chapter 3**, which describes a convenient method to transfer aqueous magnetite and cobalt ferrite to the TPM phase, by the grafting of TPM onto the surface of the nanoparticles. Polymerization of the resulting, stable TPM ferrofluids is of potential interest for the preparation of functional gels, magnetic coatings, and composite particles with an increased loading.

In **Part 2** of this thesis we investigate single-domain nanoparticles as model colloids for the study of dipolar fluids. **Chapter 4** comprises a detailed description of three methods to synthesize size series of magnetic iron oxide nanoparticles. The various methods yield particles that either have good crystallinity, contain twinning defects, or have a high density of dislocations. These crystal lattice defects can have a detrimental influence on the magnetic properties of the particles, which is demonstrated in **Chapter 5** via electron microscopy, X-ray diffraction, and magnetization measurements. An important insight from **Chapter 5** is that a low geometric size polydispersity of magnetic nanoparticles does not guarantee low polydispersity of the magnetic dipole moments.

Part 3 concerns the analytical centrifugation of concentrated dispersions of magnetic colloids to study their thermodynamics. In **Chapter 6**, a LUMiFuge stability analyzer is used for the first time to measure the osmotic equation of state of concentrated dispersions of magnetic nanoparticles. The LUMiFuge is equipped with homebuilt measurement cells with glass capillaries with an internal thickness of only 50 μm that allow measurement of concentrated, strongly light absorbing colloidal dispersions. We outline in detail the appropriate analysis procedure of the LUMiFuge results that lead to accurate osmotic pressures of magnetic fluids.

For sufficiently small colloids also an analytical ultracentrifuge (AUC) can be used to determine the osmotic equation of state, as is described in **Chapter 7**. Accurate osmotic pressures even below 1 pascal are obtained at concentrations below 1.0 g/L using conventional AUC measurement cells with an optical path length of 3 mm. However, to measure osmotic pressures at concentrations beyond this dilute regime, smaller optical path lengths are required, that we have realized in homebuilt AUC centerpieces with optical path lengths as low as 50 micrometers.

The osmotic equations of state of concentrated ferrofluids obtained by the LUMiFuge and AUC are compared in **Chapter 8**. We focus on sterically stabilized magnetic iron oxide nanoparticles with a diameter of 13 nm dispersed in an apolar solvent. These particles are used as an experimental realization of the dipolar hard spheres from theory and computer simulations. The experimental osmotic pressures of the magnetite fluids are significantly below Van 't Hoff's law due to magnetic interparticle attractions. The osmotic second virial coefficient obtained from the experimental osmotic pressures corresponds to a dipolar coupling constant in the range $\lambda = 2.0$–2.4. An isotropic, Van der Waals-like phase separation, if any, is expected at a value of $\lambda \approx 2.5$, close to our experimentally obtained value, yet no indications for such a phase transition are found.

The dipolar coupling parameter obtained by analytical centrifugation is in reasonable agreement with the coupling parameter calculated from independent magnetic measurements of the nanoparticles. This agreement clearly confirms that analytical centrifugation is an accurate method to quantify interactions between colloidal particles.

Samenvatting voor breder publiek

Magnetische colloïden

Dit proefschrift beschrijft onderzoek aan magnetische colloïden. Colloïden zijn kleine deeltjes met minimaal een van de afmetingen tussen ongeveer 1 nanometer (1 miljoenste millimeter) en 1 micrometer (1 duizendste millimeter). Colloïden zijn fijn verdeeld in een ander medium, zoals een gas, vloeistof of vaste stof. Een oplossing van colloïden in een vloeistof wordt ook wel een colloïdale dispersie genoemd. De deeltjes zijn dusdanig klein dat hun thermische energie zorgt voor "Brownse beweging"; dat is de willekeurige beweging van colloïden die je door een optische microscoop kunt zien. Door deze Brownse beweging zakken de colloïden niet naar de bodem, maar blijven ze rond bewegen in de oplossing.

Magnetische colloïden zijn colloïden met een magnetisch dipoolmoment. Ze zijn in veel toepassingen terug te vinden, zoals in magnetische vloeistoffen die gebruikt worden om harde schijven in computers stofdicht af te sluiten. Daarnaast worden magnetische colloïden veel onderzocht met het oog op medische toepassingen, bijvoorbeeld als contrastmiddel voor MRI scans, of om ze als middel tegen kanker te gebruiken. In het laatste geval worden de deeltjes ingebracht bij de tumor, waarna een wisselend magneetveld ervoor zorgt dat de magnetische nanodeeltjes zoveel warmte genereren dat tumorweefsel wordt vernietigd.

Naast de vele commerciële doeleinden, zijn colloïden ook heel geschikt als modelsysteem om atomen en moleculen na te bootsen, omdat ze groter zijn en daardoor beter te bestuderen zijn met microscopische technieken. Zo kunnen magnetische colloïden gebruikt worden als modelsysteem voor dipolaire harde bollen, zoals uitgelegd wordt in de volgende paragraaf.

Dipolaire harde bollen: miniscule magnetische knikkers

Een harde bol is een rond deeltje dat een oneindig grote afstotende kracht ondervindt als het een andere bol raakt. Anders gezegd, de bollen kunnen nooit overlappen. Een dipolaire harde bol heeft daar bovenop een aantrekkende kracht: de dipolaire attractie. In feite zijn de dipolaire harde bollen dus miniscule magnetische knikkers.

De wisselwerking tussen dipolaire harde bollen is wiskundig relatief eenvoudig te beschrijven, en de dipolaire harde bol wordt daarom veel toegepast in computersimulaties en berekeningen aan dipolaire vloeistoffen, zoals water of ethanol. Ook al bestaan

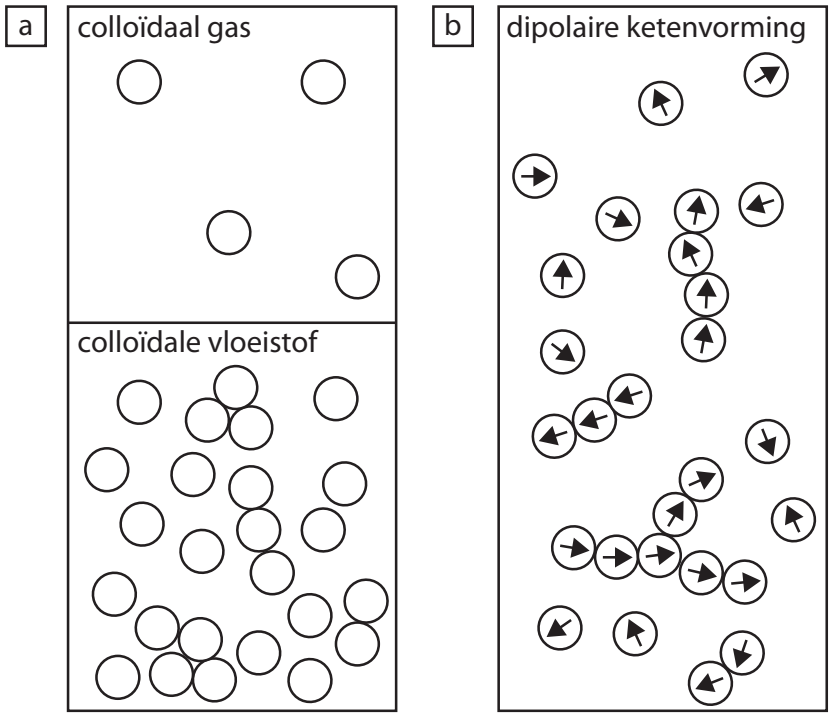

FIGUUR 1. **(a)** Schematische illustratie van een isotrope fasescheiding in een colloïd-arme fase (colloïdaal gas) en een colloïd-rijke fase (colloïdale vloeistof). **(b)** Dipolaire attracties zorgen voor ketenvorming, de vraag is of een fasescheiding van het type in (a) dan nog wel mogelijk is.

er strikt gezien geen moleculaire dipolaire harde bollen, dit model wordt vaak gebruikt om eigenschappen van dipolaire vloeistoffen te voorspellen.

Hoewel het model van een bol met een magneetje erin relatief eenvoudig is, zijn er nog onbeantwoorde fundamentele vragen. Een belangrijke vraag is: kan er in een systeem van dipolaire harde bollen een gas-vloeistof fasescheiding plaatsvinden? Met andere woorden, kan er onder bepaalde condities een scheiding plaatsvinden in een geconcentreerdere fase (colloïdale vloeistof) en een verdunde fase (colloïdaal gas) van dipolaire harde bollen, analoog aan bijvoorbeeld vloeibaar water in evenwicht met waterdamp? Normaal gesproken hebben moleculen altijd een attractieve interactie (aantrekkingskracht), de zogenaamde 'Van der Waals'-interactie. Deze Van der Waals attractie is isotroop, dat wil zeggen, richtingsonafhankelijk, en daarom is de bijbehorende gas-vloeistof fasescheiding ook isotroop (Figuur 1a). Voor deeltjes met alleen een dipolaire attractie is het echter onduidelijk of zo'n fasescheiding wel plaats kan vinden, omdat de interactie anisotroop (richtingsafhankelijk) is. Hierdoor kunnen er ketens en andere dipolaire structuren gevormd worden die zo'n isotrope fasescheiding zouden kunnen voorkomen (Figuur 1b).

Omdat computersimulaties en theoretische modellen niet met een eenduidig antwoord komen op de vraag of er in een systeem van dipolaire harde bollen fasescheiding mogelijk

is, is het van evident belang om experimenten te doen. Daarvoor zijn modeldeeltjes nodig die, volgens sommige van de voorspellingen, genoeg magnetische interactie hebben om zo'n fasescheiding te kunnen veroorzaken, als die fasescheiding al plaats zou kunnen vinden. Een groot deel van dit proefschrift is gewijd aan het maken van magnetische colloïden, om een modelsysteem te verkrijgen met een voldoende groot magnetisch dipoolmoment. Twee mogelijke routes voor het maken van magnetische colloïden zijn onderzocht en beschreven in **Deel 1** en **Deel 2** van het proefschrift. Het meten van de thermodynamische eigenschappen van deze deeltjes, die het fasegedrag bepalen, wordt beschreven in **Deel 3**.

Deel 1: Magnetische emulsies

De eerste route voor het maken van magnetische colloïden is via een specifiek soort emulsies. Emulsies bestaan uit een mengsel van twee verschillende vloeistoffen die in principe niet met elkaar mengen, zoals water en olie. Door veel energie te gebruiken, bijvoorbeeld door hard te schudden, kunnen emulsiedruppels van de ene vloeistof in de andere vloeistof gevormd worden. In de loop van de tijd zullen de twee vloeistoffen echter weer scheiden; de emulsie is niet thermodynamisch stabiel. Elk systeem wil namelijk terug naar de energetisch meest gunstige toestand, in dit geval de ongemengde staat. Een manier om emulsies toch te stabilizeren is met behulp van colloïden aan het grensvlak van de twee vloeistoffen, zogenaamde Pickering emulsies. Normaal gesproken verhogen Pickering emulsies tijdelijk de stabiliteit; uiteindelijk willen de twee vloeistoffasen het liefst weer scheiden.

Recent is er echter een specifieke groep Pickering emulsies ontdekt die wel thermodynamisch stabiel is, dus waarbij het energetisch gunstiger is om emulsiedruppels te vormen. Het voordeel hiervan is dat de emulsiedruppels spontaan vormen, en bovendien een relatief goed gedefiniëerde grootte hebben. Deze emulsies bestaan uit een specifiek soort olie (TPM) in water en ze worden gestabiliseerd door colloïden, bijvoorbeeld magnetische nanodeeltjes. Een belangrijke eigenschap van deze olie is dat deze te polymeriseren is: er kan een proces, de polymerisatie, in gang gezet worden dat de losse oliemoleculen aan elkaar verbindt, waardoor er vaste deeltjes ontstaan. Op deze manier kunnen van de emulsiedruppels met magnetische deeltjes aan het oppervlak composietdeeltjes gemaakt worden (Figuur 2). In **Hoofdstuk 2** wordt aangetoond hoe de grootte van deze emulsiedruppels te beïnvloeden is. De emulsiedruppels worden groter door meer olie of zout toe te voegen. Ook groeien de emulsiedruppels in de tijd, doordat de magnetische nanodeeltjes langzaam bedekt worden met TPM-moleculen. De emulsiedruppels passen hun grootte aan aan deze nieuwe chemische omstandigheden, zodat ze zich weer in de energetisch meest gunstige toestand bevinden. Uiteindelijk verplaatsen de nanodeeltjes zich volledig naar de oliefase.

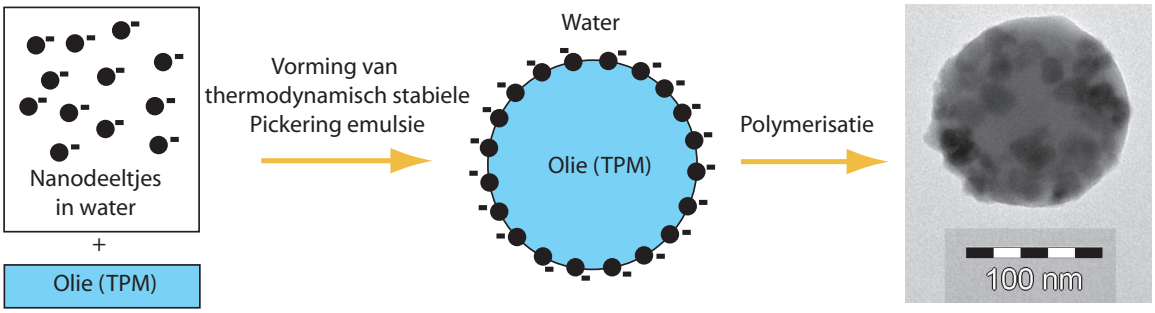

FIGUUR 2. Schematische illustratie van de vorming van een Pickering emulsie (links) en een elektronenmicroscopie plaatje van het resulterende composiet-deeltje (rechts).

De bedekking van de nanodeeltjes met de TPM-moleculen kan gebruikt worden om de deeltjes gecontroleerd van de waterfase naar de TPM-fase over te brengen, en zo een magnetische olie te verkrijgen, een TPM-ferrofluid. Deze nieuwe methode wordt beschreven in **Hoofdstuk 3**. Daarin wordt ook gekeken naar verschillende toepassingen van deze TPM-ferrofluids, waaronder het magnetischer maken van de emulsiedruppels, doordat er nu ook magnetische deeltjes in de olie zitten, en niet alleen aan het olie-water grensvlak.

DEEL 2: MAGNETISCHE NANODEELTJES

In **Deel 2** wordt een ander soort magnetische modelcolloïden beschreven: magnetische nanodeeltjes. Wanneer deze deeltjes klein genoeg zijn hebben ze in principe één magnetisch dipoolmoment. Dit dipoolmoment neemt sterk toe met de grootte van de deeltjes, dus is het van groot belang om de nanodeeltjes even groot te maken zodat ze allemaal dezelfde eigenschappen hebben. In **Hoofdstuk 4** worden verschillende chemische synthesemethoden beschreven om deze deeltjes te maken. Afhankelijk van de synthesemethode kunnen deeltjes gemaakt worden die ofwel goede kristallijne eigenschappen hebben, of tweelingen bevatten, of waar een grote hoeveelheid defecten in de kristalstructuur te vinden is. In **Hoofdstuk 5** wordt aangetoond dat deze kristaldefecten een desastreus effect kunnen hebben op de magnetische eigenschappen van de deeltjes. Hoewel er nanodeeltjes gemaakt kunnen worden met een zeer uniforme fysieke grootte, blijkt dat dus geen garantie te zijn voor uniforme magnetische eigenschappen.

DEEL 3: ANALYTISCHE CENTRIFUGATIE

Deel 3 gaat over analytische centrifugatie als methode om de thermodynamische eigenschappen van colloïden te meten. Hiermee kan de osmotische toestandsvergelijking, de osmotische druk van de colloïden als functie van de concentratie, bepaald worden. Om dit principe uit te leggen is het nuttig om te kijken naar een verschijnsel

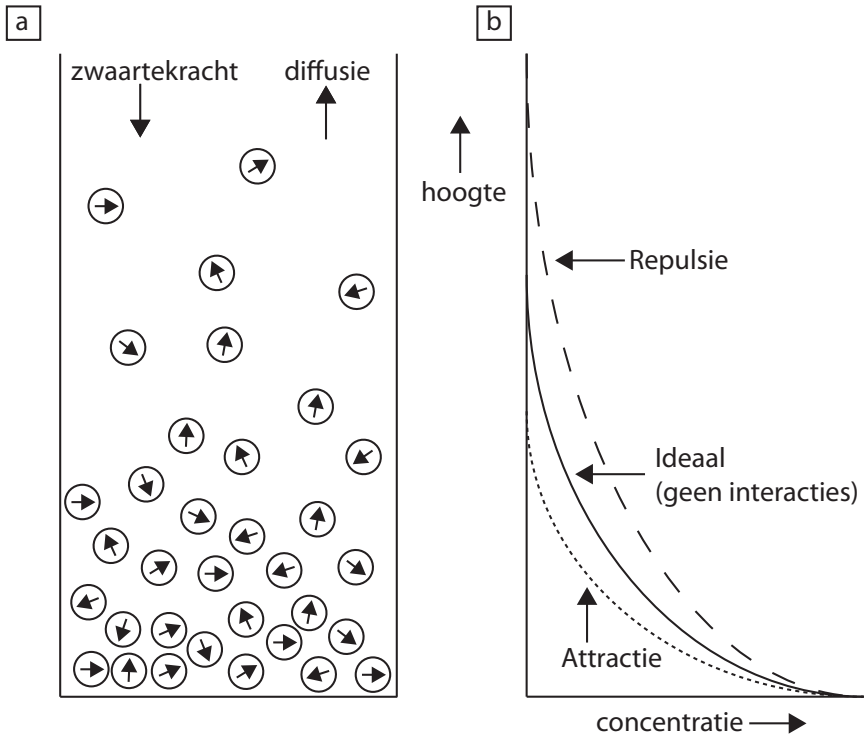

Figuur 3. **(a)** Schematische illustratie van de hoogteverdeling in normale zwaartekracht, als gevolg van een balans tussen de zwaartekracht en diffusie van de deeltjes. **(b)** Bijbehorend concentratieprofiel als functie van de hoogte. Het profiel krimpt wanneer de deeltjes attractief zijn, en zet uit als ze elkaar afstoten.

waar elke bergbeklimmer mee te maken krijgt. De luchtdruk neemt af naarmate hij hoger klimt: de dichtheid van de luchtmoleculen neemt af met de hoogte, en dus neemt de druk ook af. Zo'n hoogteverdeling kunnen we ook beschrijven voor colloïden in een oplosmiddel, waarbij de druk 'osmotische druk' genoemd wordt. Waar de verdeling van luchtmoleculen uitgespreid is over een aantal kilometer, is zo'n verdeling van colloïden uitgespreid over slechts enkele millimeters tot centimeters, afhankelijk van de deeltjesgrootte en de interacties tussen de colloïden (Figuur 3). Door de osmotische druk te meten als functie van de concentratie colloïden in het oplosmiddel zijn deze interacties te bepalen. Het instellen van thermodynamisch evenwicht kan echter lang duren, en de drukken zijn zo laag dat een speciale techniek nodig is om de osmotische druk te kunnen meten: analytische centrifugatie.

Een analytische centrifuge is een centrifuge waarin de colloïdale dispersie continu wordt rondgedraaid met grotere g-krachten dan de normale zwaartekracht om het evenwicht sneller te bereiken. Tijdens het centrifugeren kan de transmissie (doorlating) van het licht door de dispersie gemeten worden, zoals weergegeven in Figuur 4. Hoe hoger de concentratie colloïden, hoe minder licht er door de dispersie gaat. De transmissie van

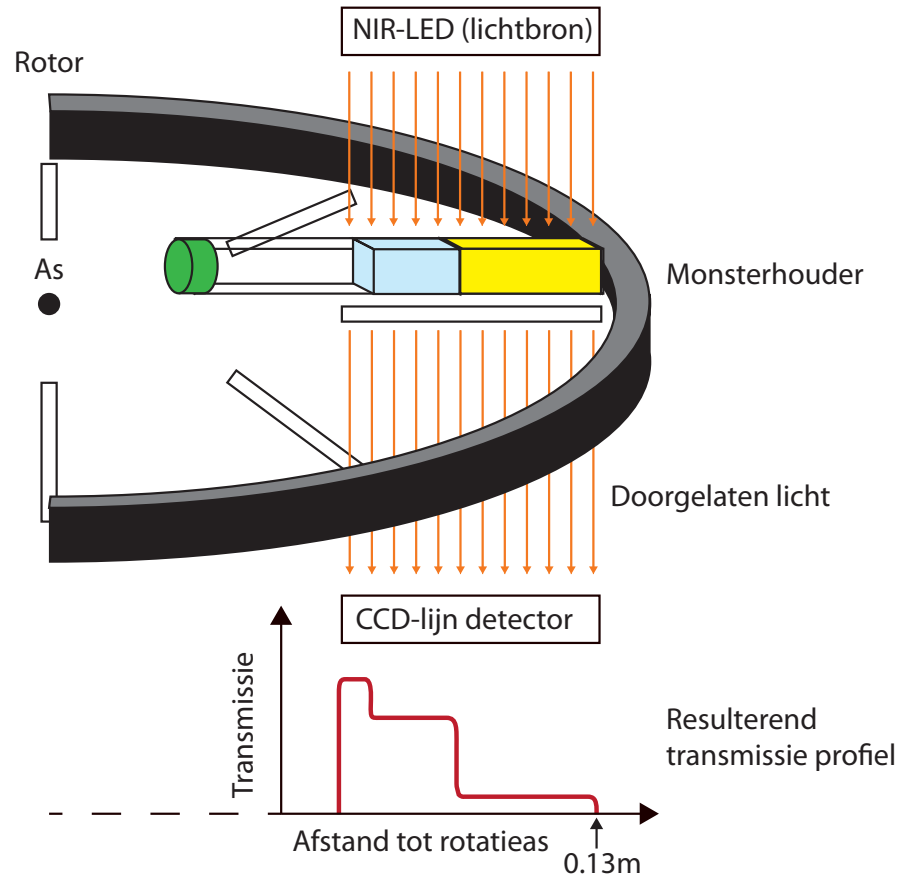

FIGUUR 4. Schematische illustratie van een LUMiFuge, waarmee een concentratieprofiel zoals in Figuur 3 gemeten kan worden. Dit gebeurt door de transmissie van het licht door de dispersie te meten en vervolgens om te rekenen naar concentratie. Door het meten in een centrifuge wordt het concentratieprofiel in Figuur 3b dus een kwartslag gedraaid.

het licht is evenredig met de concentratie colloïden, dus het concentratieprofiel wordt verkregen uit het gemeten transmissieprofiel. Wanneer het evenwicht bereikt is, kan de osmotische druk berekend worden vanuit het concentratieprofiel.

Het probleem van het meten van magnetische colloïden met een conventionele analytische ultracentrifuge (AUC) is de hoge lichtabsorptie van de donkergekleurde dispersie. Daardoor kan er niet meer gemeten worden bij hogere concentraties, terwijl daar de meeste effecten van interacties tussen de colloïden verwacht worden. Bovendien is de minimale draaisnelheid van een AUC te hoog voor de meeste colloïden, waardoor ze allemaal op de bodem van de monsterhouder terecht komen. Daarom wordt in **Hoofdstuk 6** een zogenaamde LUMiFuge, die oorspronkelijk ontworpen is om de stabiliteit van bijvoorbeeld voedselproducten zoals yoghurt en ketchup te bepalen, gebruikt als analytische centrifuge. Hiervoor zijn zelfgemaakte monsterhouders ontworpen

die capillairen, dunne glazen buisjes, bevatten, waardoor het licht maar door een klein deel van de dispersie hoeft te gaan en hoge concentraties gemeten kunnen worden. De data-analyse procedure en de bijbehorende valkuilen zijn uitgezocht, en vervolgens is de osmotische toestandsvergelijking van een geconcentreerde dispersie van magnetische colloïden bepaald.

De magnetische colloïden die gemeten zijn in Hoofdstuk 6, zijn nog dusdanig klein dat ook een conventionele analytische ultracentrifuge gebruikt kan worden. Ook hiervoor zijn nieuwe monsterhouders ontworpen, en de resultaten staan beschreven in **Hoofdstuk 7**.

De resultaten uit Hoofdstuk 6 en 7 worden met elkaar vergeleken in **Hoofdstuk 8**. Bij hoge concentraties is er duidelijk een afwijking van ideaal gedrag (gedrag zonder interacties tussen de deeltjes) te vinden in de osmotische toestandsvergelijking. Deze afwijking wordt veroorzaakt door de magnetische attracties. Met behulp van een recent gepubliceerde theorie is hieruit een dipolaire interactieparameter bepaald; de dipolaire interactieparameters die bepaald zijn met de LUMiFuge (Hoofdstuk 6) en de AUC (Hoofdstuk 7) blijken goed met elkaar overeen te komen.

Deze dipolaire interactieparameter heeft ongeveer de waarde waarbij er een isotrope, Van der Waals-achtige gas-vloeistof fasescheiding verwacht wordt. Er is echter geen enkele aanwijzing gevonden in de metingen dat deze fasescheiding plaatsvindt. Bovendien wordt vanaf ongeveer deze dipolaire interactieparameter ketenvorming verwacht, wat zo'n fasescheiding ook zou voorkomen. Dit wijst er sterk op dat er geen Van der Waals-achtige gas-vloeistof scheiding bestaat voor dipolaire harde bollen. Of er een fasescheiding mogelijk is van ketenachtige structuren is echter nog niet te zeggen; om dit te meten zijn colloïden met een groter magnetisch dipoolmoment nodig.

Het feit dat de magnetische interactieparameter nauwkeurig bepaald kan worden, en redelijk in overeenstemming is met onafhankelijke magnetische metingen, bevestigt dat analytische centrifugatie een veelbelovende techniek is voor het meten van interacties in andere colloïdale systemen.

Dankwoord

Het mooie aan het doen van een promotieonderzoek is dat je het uiteindelijk (gelukkig) niet alleen doet. Daarom wil ik hier een aantal mensen bedanken die op de een of andere manier hebben bijgedragen aan het tot stand komen van dit proefschrift.

Allereerst wil ik mijn co-promotor, Ben Erné, bedanken: het was een voorrecht om jou als mijn dagelijks begeleider te hebben. Je bent een onuitputtelijke bron van ideeën, ook als dingen niet gaan zoals verwacht. Hoewel je met veel ideeën allerlei kanten op kunt gaan, zorgt jouw gestructureerde manier van werken juist voor een heldere aanpak. Na 4 jaar was het geen verrassing meer om feedback binnen 24 uur terug te krijgen, maar dat maakt het niet minder bijzonder, en je oog voor detail bij elk facet van dit onderzoek bleek van grote waarde. Bedankt voor je nauwe betrokkenheid bij dit project evenals de persoonlijke interesse die je toonde, dat heb ik erg gewaardeerd.

Daarnaast wil ik ook mijn promotor Albert Philipse bedanken voor de mogelijkheid om dit project te doen, en de vrijheid om verschillende richtingen te onderzoeken. Bedankt voor je enthousiasme om altijd de nieuwste resultaten of samples uit het lab te willen zien en voor je heldere en telkens motiverende input. Ook heb ik veel geleerd van je sturing binnen het project, je feedback op het schrijven en alle overige adviezen.

In the past four years I have had the privilege to supervise a variety of bachelor and master students. Claire van Lare, Chiara Cassarini, Rick de Groot, Joen Hermans, and Aldo Brinkman: thank you for your enthusiasm and contributions to this thesis. Even though your efforts may not lead to a publication in all cases, it did not make your input less valuable to me! In deze context wil ik ook Suzanne Woudenberg en Niek Hijnen noemen. Al was ik niet jullie begeleider omdat jullie al als student begonnen waren voor ik startte, ik vond de samenwerking met jullie zeer waardevol.

Verder wil ik Dominique Thies-Weesie bedanken voor haar vele bijdragen aan dit proefschrift. Niet alleen de AUC metingen, maar juist ook de vele nuttige discussies, gespekt met de nodige humor, vond ik heel waardevol. Natuurlijk ook bedankt voor de verdere ondersteuning voor het reilen en zeilen van het lab, en daarvoor wil ik eveneens Kanvaly Lacina, Emile Bakelaar, Bonny Kuipers en Marina uit de Bulten-Weerensteijn bedanken. Hans Meeldijk en Chris Schneijdenberg, bedankt voor jullie ondersteuning met electronenmicroscopie. In het bijzonder dank aan jou, Hans, niet alleen voor je metingen die in dit proefschrift staan, maar ik waardeer het enorm hoe je altijd meedenkt en de tijd neemt om dingen uit te leggen. Ook mijn dank aan iedereen

bij de glasblazerij en de werkplaats voor het uitstekende maatwerk die de syntheses en de nauwkeurige metingen mogelijk hebben gemaakt.

Thanks to everyone involved with the emulsions (and more): Daniela Kraft, Willem Kegel, Julius de Folter, Stefano Sacanna, and Sonja Castillo. In het bijzonder dank aan Daniela en Willem, ik heb erg genoten van de vele gezamenlijke experimenten en discussies met jullie. Jos Zwanikken, bedankt voor je begrijpelijke uitleg van de theoriën van jou en René van Roij.

I also want to thank Hirsa Torres Galvis and Krijn de Jong for the fruitful collaboration on the magnetic nanoparticles; I enjoyed our discussions. In addition to the people mentioned by name somewhere in these acknowledgments, many people have somehow contributed with useful input. I realize this list is not complete, but I do want to mention Jos van Rijssel, Mark Klokkenburg, Jan Hilhorst, Andrei Petukhov, Janne-Mieke Meijer, John Geus, Pedro Zeijlmans van Emmichoven, Henk Lekkerkerker, Mikal van Leeuwen, and Karel Planken.

Many thanks to my roommates Esther van den Pol, Roberto Calderone, Rob Kortschot, Susanne van Berkum, and Roel Baars, not only for useful discussions, but especially for a great atmosphere. Of course some things go beyond science and a good atmosphere: thank you Rob for the many good cups of coffee. I also want to thank Maurice Mourad and Lia Verhoeff, as it all started in your office, and I always enjoyed our conversations. Thank you Laura Rossi and Marina uit de Bulten-Weerensteijn for allowing us to use your coffee machines from time to time, in addition of course to your contributions to the nice time I had here. And that brings me to everyone at the Van 't Hoff lab: thank you all for the great time I had with you both inside and outside the lab; I couldn't imagine a nicer place to do my PhD! I also want to thank everyone at the Soft Condensed Matter and the Theoretical Physics groups for the useful as well as fun times at Nanoseminars, conferences and other occasions.

Sander Wiegman en Gijs Luigjes, het is een eer dat jullie mijn paranimfen willen zijn! Veel dank aan Matti van Schooneveld en Sander Wiegman voor de enerverende squashpotjes die me scherp hielden, evenals de vele goede gesprekken. Voor de scherpende gesprekken kan mijn dank aan Maarten Groenenberg natuurlijk niet ontbreken. Bedankt Alex en Michelle van Laren, en de hele CCC-familie, voor jullie vriendschap, steun, bemoediging en gezelligheid de afgelopen jaren. Datzelfde geldt natuurlijk ook voor alle vrienden buiten CCC. Ik zou niet weten hoe ik jullie allemaal bij naam kan gaan noemen, maar bedankt voor wie jullie zijn!

In het bijzonder wil ik mijn familie bedanken: Pa, Ma, Janet, Gijs, en daar horen Erica en Daniël natuurlijk ook bij, bedankt voor jullie onvoorwaardelijke steun en interesse, ongeacht of jullie iets van mijn onderzoek begrepen of niet.

Tenslotte, alle dank en eer aan mijn hemelse Vader, voor meer dan ik hier kan beschrijven, en Jezus, U bent er altijd als mijn redder en mijn bron van vrede en vreugde!

List of publications

This thesis is based on the following publications:

- D. J. Kraft, B. Luigjes, J. W. J. de Folter, A. P. Philipse, and W. K. Kegel, *Evolution of equilibrium Pickering emulsions: a matter of time scales*, The Journal of Physical Chemistry B, 114 (2010), 12257-12263. (Chapter 2)
- B. Luigjes, D. J. Kraft, J. J. Hermans, B. H. Erné, A. P. Philipse, and W. K. Kegel, *Influence of salt on the droplet size of equilibrium Pickering emulsions*, in preparation. (Chapter 2)
- B. Luigjes, R. J. Baars, C. Cassarini, J. J. Hermans, B. H. Erné, and A. P. Philipse, *Preparation and properties of a polymerizable ferrofluid*, in preparation. (Chapter 3)
- B. Luigjes, S. M. C. Woudenberg, R. de Groot, J. D. Meeldijk, H. M. Torres Galvis, K. P. de Jong, A. P. Philipse, and B. H. Erné, *Diverging geometric and magnetic size distributions of iron oxide nanocrystals*, Journal of Physical Chemistry C, 115 (2011), 14598-14605. (Chapters 4 and 5)
- B. Luigjes, D. M. E. Thies-Weesie, A. P. Philipse, and B. H. Erné, *Analytical centrifugation of magnetite fluids (I): on the determination of equilibrium concentration profiles*, in preparation. (Chapters 6 and 7)
- B. Luigjes, D. M. E. Thies-Weesie, B. H. Erné, and A. P. Philipse: *Analytical centrifugation of magnetite fluids (II): the experimental second virial coefficient of dipolar particles*, in preparation. (Chapter 8)

Other papers by the author:

- D. J. Kraft, J. Hilhorst, M. A. P. Heinen, M. J. Hoogenraad, B. Luigjes, and W. K. Kegel, *Patchy polymer colloids with tunable anisotropy dimensions*, Journal of Physical Chemistry B, 115 (2011), 7175-7181.
- D. J. Kraft, J. W. J. de Folter, B. Luigjes, S. I. R. Castillo, S. Sacanna, A. P. Philipse, and W. K. Kegel, *Conditions for equilibrium solid-stabilized emulsions*, Journal of Physical Chemistry B, 114 (2010), 1034710356.
- S. dos Santos, B. Luigjes, and L. Piculell, *Associative phase behaviour and disintegration of copolymer aggregates on adding poly(acrylic acid) to aqueous solutions of a PEO-PPO-PEO triblock copolymer*, Soft Matter, 6 (2010), 4756-4767.
- R. Koole, B. Luigjes, M. Tachiya, R. Pool, T. J. H. Vlugt, C. de Mello Donegá, A. Meijerink, and D. Vanmaekelbergh, *Differences in cross-link chemistry between rigid and flexible dithiol molecules revealed by optical studies of CdTe quantum dots*, Journal of Physical Chemistry C, 111 (2007), 11208-11215.

Curriculum Vitae

Bob Luigjes was born on the 9^{th} of August, 1984 in Voorthuizen (Barneveld), The Netherlands. After graduating from high school in 2002 at the Johannes Fontanus College in Barneveld, he studied chemistry at Utrecht University from 2002 to 2007. He obtained his bachelor degree in 2005 after performing a bachelor research project at the Van 't Hoff laboratory for Physical and Colloid Chemistry. This research was conducted under supervision of Maria Claesson and Albert Philipse on the topic of fluorescent magnetic composite colloids. As a master student enrolled in the Chemistry and Physics program, he performed his master thesis at the Condensed Matter and Interfaces group under supervision of Rolf Koole, Daniel Vanmaekelbergh, and Andries Meijerink on the preparation and optical properties of quantum dots. He also performed a 6 month research project at Lund University (Sweden) in the group Physical Chemistry 1, under supervision of Salomé dos Santos and Lennart Piculell, on the phase behavior of polymers and non-ionic surfactants. He obtained his Master of Science degree with distinction (cum laude) in 2007. In November 2007 he started his PhD at the Van 't Hoff laboratory for Physical and Colloid Chemistry, in the chemistry department at Utrecht University, under supervision of Ben Erné and Albert Philipse. The results of the research are described in this thesis and several scientific publications, and have been presented by oral and poster contributions at different national and international conferences.